

Hypersonic Flows Around Complex Geometries with Adaptive Mesh Refinement and Immersed Boundary Method

Monal Patel

Department of Mechanical Engineering
Imperial College London

This dissertation is submitted for the degree of
Doctor of Philosophy

February 2023

Declaration

I declare that this thesis and the work reported has been composed by and originated entirely from me. Information derived from the work of others has been acknowledged in the text and references are given as appropriate.

Monal Patel
February 2023

The copyright of this thesis rests with the author. Unless otherwise indicated, its contents are licensed under a Creative Commons Attribution-Non Commercial 4.0 International Licence (CC BY-NC). Under this licence, you may copy and redistribute the material in any medium or format. You may also create and distribute modified versions of the work. This is on the condition that: you credit the author and do not use it, or any derivative works, for a commercial purpose. When reusing or sharing this work, ensure you make the licence terms clear to others by naming the licence and linking to the licence text. Where a work has been adapted, you should indicate that the work has been changed and describe those changes. Please seek permission from the copyright holder for uses of this work that are not included in this licence or permitted under UK Copyright Law.

Acknowledgements

I owe my gratitude to many individuals who have played a significant part in my PhD journey. This thesis simply would not have been possible without them.

Beginning with Salvador, I am grateful for your availability, patience and guidance; you allowed me to explore ideas in my own time, whilst preventing me from going astray. Thank you.

My examiners, Paul and Ralf, your meticulous feedback often highlighted shortcomings in my thinking and writing. I sincerely thank you.

My officemates, in particular Yuri, Giovanni, Panos, Omer, Kieran, Daniel and Stephen thank you for your companionship. You helped create a fun, helpful and productive office environment—the random conversations—various lunches, coffees and sporting sessions together were always a welcome distraction.

I am also grateful to all my friends for their friendship, which has often kept me going through difficult periods. Particular ones who shared large parts of the journey together: Nasos, Christina, Andre, Esther; and over the last year, Rahul. Thank you for sharing your time and affection with me.

Finally, my parents and sister—Mehul, Zarna and Khevana. Your love and support throughout all my formal education and training has been instrumental. Thank you for all that you have given.

Abstract

This thesis develops and validates a computational fluid dynamics numerical method for hypersonic flows; and uses it to conduct two novel investigations.

The numerical method involves a novel combination of structured adaptive mesh refinement, ghost-point immersed boundary and artificial dissipation shock-stable Euler flux discretisation. The method is high-order, low dissipation and stable up to Mach numbers $M \lesssim 30$ with stationary or moving complex geometries; it is shown to be suitable for direct numerical simulations of laminar and turbulent flows. The method's performance is assessed through various test cases.

Firstly, heat transfer to proximal cylinders in hypersonic flow is investigated to improve understanding of destructive atmospheric entries of meteors, satellites and spacecraft components. Binary bodies and clusters with five bodies are considered. With binary proximal bodies, the heat load and peak heat transfer are augmented for either or both proximal bodies by +20% to -90% of an isolated body. Whereas with five bodies, the cluster-averaged heat load varied between +20% to -60% of an isolated body. Generally, clusters which are thin in the direction perpendicular to free-stream velocity and long in the direction parallel to the free-stream velocity have their heat load reduced. In contrast, clusters which are thick and thin in directions perpendicular and parallel to the free-stream velocity feel an increased heat load.

Secondly, hypersonic ablation patterns are investigated. Ablation patterns form on spacecraft thermal protection systems and meteor surfaces, where their development and interactions with the boundary layer are poorly understood. Initially, a simple subliming sphere case without solid conduction in hypersonic laminar flow is used to validate the numerical method. Where the surface recession is artificially sped-up via the wall Damköhler number without introducing significant errors in the shape change. Then, a case with transitional inflow over a backward facing step with a subliming boundary is devised. Differential ablation is observed to generate surface roughness and add vorticity to the boundary layer. A maximum surface recession of $\sim 0.8\times$ and a maximum surface fluctuation of $\sim 0.2\times$ the inflow boundary layer thickness were generated over two flow times.

List of figures

1.1	Historical photographs of (a) First hypersonic man-made object flight (NASA, 2022) and (b) First hypersonic person (Energia, 2022).	1
1.2	Practical contexts involving hypersonic flows.	4
1.3	Hypersonic flight vehicle phenomenology (Urzay, 2020).	5
1.4	Hypersonic flow space in Earth's atmosphere (Urzay and Di Renzo, 2021) for man-made applications with "heat barrier" regions shaded in orange, representing flow parameters leading to extreme aerothermal heating. . . .	7
2.1	Left: harmonic oscillator and Morse potentials. Right: rovibronic energy levels in diatomic harmonic oscillator model.	13
2.2	Air-11 and carbon-dioxide-8 species translational-rotational ($c_{p,tr}$) and vibrational electronic (c_{ve}) specific heats normalised with universal gas constant (R) varying with temperatures up to 20,000 K.	25
2.3	Equilibrium mass and mole fractions of mixtures with varying temperatures and pressures. Low pressure at 10^2 Pa (—) and high pressure at 10^5 Pa (---). 26	26
2.4	Mixture equilibrium (e) to frozen (f) thermodynamic and transport properties ratio, varying with temperature and pressure (P) for Air-11 (—) and Carbon-dioxide-8 (---) mixtures.	27
2.5	WENO family methods' stencils.	36
2.6	Two-dimensional SAMR meshes. Left: patch-based, adapted from Deiterding (2003) . Right: tree-based, adapted from Bauer et al. (2021)	41
2.7	Local time stepping with two sub-steps. Single arrows indicate prolongation procedures, whereas double arrows indicate restriction and prolongation procedures.	44
2.8	Weak Riemann problem comparisons with WENO5, TENO6 and CS6-JST Euler flux computation methods; and AMR GTS and LTS time-stepping strategies.	49

2.9	Weak Riemann problem with 2 levels of AMR around the shock wave. . . .	49
2.10	CS6-JST and TENO6 comparison with high temperature Riemann problem with chemical reactions.	51
2.11	Verification of the thermochemical models' implementation—chemical non-equilibrium (CNE), thermal non-equilibrium (TNE) and thermochemical non-equilibrium (TCNE)—with the high temperature Riemann problem and WENO5.	52
2.12	Shu-Osher problem comparison with CS6-JST, WENO5 and TENO6 at $t = 1.8$ s.	53
2.13	Spacial discretisation order of accuracy assessment for CS6 and TENO6. .	55
2.14	Fast vortex propagation without AMR order of accuracy over 50 vortex flow-through times.	56
2.15	Fast vortex propagation with AMR (1 level) order of accuracy over 50 vortex flow-through times.	57
2.16	Slow vortex propagation case velocity profile comparisons with different numerical methods over 50 vortex flow-through times.	59
2.17	Supersonic turbulent channel flow scalar field variables instantaneous slices from case C.	63
2.18	Supersonic turbulent channel flow mean flow and fluctuations profiles for Case A (.....), Case B (- - -) and Case C (—) compared against reference solution by Foyasi et al. (2004) (•).	64
3.1	Ghost point immersed boundary with patch-based adaptive mesh refinement	69
3.2	Restriction and prolongation around immersed boundary with AMR mesh. .	73
3.3	Stagnation line shock stand-off distance in reacting flow, adapted from Belouaggadia et al. (2008)	79
3.4	Surface pressure coefficient (C_p) predictions in frozen flow over a sphere at $M = [4, 8, 16, 32]$ compared with modified Newtonian result in the limit $M \rightarrow \infty$	80
3.5	Contour plots of primitive variables of frozen flow around a sphere at $M = 4$ and $M = 32$	81
3.6	Refined mesh around the bow shock and sphere immersed boundary.	82
3.7	Sphere's shock stand-off distance for slow and fast cases with 5% error bars.	83
3.8	Reacting flow contours around sphere for slow and fast cases.	83
3.9	Sphere stagnation centreline profiles (from the stagnation point at $x = 0$) for slow and fast reacting flow cases.	84
3.10	Flat plate case mesh and order of convergence results.	87

3.11	Flat plate surface properties: coefficient of pressure C_p , coefficient of heat transfer C_h , coefficient of skin friction C_f and non-dimensional wall normal coordinate based on the local mesh size y_w^+	88
3.12	Single compression ramp numerical setup.	90
3.13	AMR $Re_h = 20$ mesh with successively zoomed views of the near wall mesh around the compression corner.	90
3.14	Single compression ramp surface properties: coefficient of pressure C_p , coefficient of heat transfer C_h , coefficient of skin friction C_f and non-dimensional wall normal coordinate based on the local mesh size y_w^+	92
3.15	Double ramp numerical setup.	94
3.16	Double ramp AMR mesh with uniform 5 levels of refinement around walls.	94
3.17	Double ramp schlieren images from two-dimensional numerical simulation with the finest mesh ($Re_h = 3$).	97
3.18	Double ramp schlieren images from experiments (Swantek, 2012).	98
3.19	Double ramp case time averaged surface properties.	98
3.20	Double ramp instantaneous AMR meshes at $120\mu s$ for Case A and Case B.	100
3.21	Double ramp numerical schlieren image comparison over time.	101
3.22	Double ramp case number of AMR mesh points varying over time with different meshing strategies.	102
3.23	Time averaged surface properties with 5 level AMR mesh but different meshing criteria.	102
3.24	Supersonic turbulent channel flow profiles with IBM walls (—) compared with conformal boundary (---), and with reference results (\cdot) from (Foyssi et al., 2004).	103
3.25	Transversely oscillating cylinder with 2D AMR mesh.	105
3.26	Transversely oscillating cylinder vorticity field from 2D computations.	106
3.27	Transversely oscillating cylinder Q-criterion surfaces from 3D computations.	106
3.28	Transversely oscillating cylinder C_D and C_L varying with non-dimensional time.	107
4.1	Hypersonic blunt body wake features with approximate length scales.	114
4.2	Relationship between wake Reynolds number (Re_w), free-stream Reynolds number (Re_∞) and free-stream Mach number (M_∞). Adapted from Hinman and Johansen (2018)	114
4.3	Cylinder bow shock shape.	115
4.4	Blunt body Edney shock interactions, from Fisher (2019)	117
4.5	Binary bodies arrangements in real (left) and non-dimensional space (right).	119

4.6	Medium resolution mesh with coloured AMR patches at different Mach numbers.	121
4.7	Surface properties from mesh refinement study at different Mach numbers. .	123
4.8	Mach number field and centreline profile.	124
4.9	Heat load convergence for all positions and Mach numbers over non-dimensional time.	125
4.10	Numerical schlieren for binary body arrangements at $M = 2$	127
4.11	Numerical schlieren for binary body arrangements at $M = 4$	128
4.12	Numerical schlieren for binary body arrangements at $M = 8$	129
4.13	Surface properties for binary body arrangements at $M = 2$. Where θ is positive in anti-clockwise direction and negative in clockwise direction. . .	131
4.14	Surface properties for binary body arrangements at $M = 4$. Where θ is positive in anti-clockwise direction and negative in clockwise direction. . .	131
4.15	Surface properties for binary body arrangements at $M = 8$. Where θ is positive in anti-clockwise direction and negative in clockwise direction. . .	132
4.16	Normalised heat load and peak heat for binary body arrangements.	132
4.17	Effect of Euler flux calculation method with WENO5 and CS4-JST in arrangement 4 at $M = 4$	134
4.18	Cases 2 (left) and 5 (right) instantaneous AMR mesh with 3 levels of refinement around body and 1 level of refinement around shocks.	136
4.19	Numerical schlieren of five body clusters at $M = 4$ in eight different arrangements.	137
4.20	Cluster averaged heat load ($\langle Q \rangle$) varying over 6-10 flow times in all cases. .	138
4.21	Time and ensemble averaged heat transfer profile around cylinder. Where θ is positive in anti-clockwise direction and negative in clockwise direction. .	139
4.22	Time and body ensemble averaged heat load ($\langle \bar{Q} \rangle$) scaling with body position standard deviations ($\sigma\{x\}/D, \sigma\{y\}/D, \sigma\{x\}/\sigma\{y\}$) for all cases.	139
4.23	Body time averaged heat load standard deviation ($\sigma\{\bar{Q}\}$) scaling with body position standard deviations ($\sigma\{x\}/D, \sigma\{y\}/D, \sigma\{x\}/\sigma\{y\}$) and ensemble time average heat load ($\langle \bar{Q} \rangle / Q_1$) for all cases.	140

5.1	Hypersonic ablation surface patterns with indicated length scales. (a) From left to right, ablation grooves, turbulent wedge and cross-hatching patterns on wax cone (0.1 m) (Stock, 1975). (b) Flat plate cross-hatching pattern on wax ablator (0.15 m) (Stock and Ginoux, 1973). (c) The Middlesbrough stony meteorite, a smooth nose, few large and deep ablation pits followed by regmaglypt surface (0.16 m) (Lin and Qun, 1987). (d) A smooth pear-shaped iron meteorite (0.12 m) (Hodge-Smith, 1939). (e) Bacubirito iron meteorite, world's longest meteorite, covered in regmaglypts (4.2 m) (Terán-Bobadilla et al., 2017).	145
5.2	Subsonic ablation surface patterns. (a) Pink salt block with longitudinal grooves (0.1 m) (Cohen et al., 2020). (b) Scalloped Shafts cave walls (0.15 m) (Meakin and Jamtveit, 2010) (c) Sastrugi in snow (1 m) (Amory et al., 2017). (d) Ice ablation waves (0.2 m) (Bordiec et al., 2020).	145
5.3	Surface species mass (left) and energy (right) balances with two coordinate systems, global ($\hat{x}, \hat{y}, \hat{z}$) and local ($\hat{n}, \hat{t}_1, \hat{t}_2$).	150
5.4	Slice of AMR patches around sphere with 3 refinement levels.	156
5.5	Single species subliming sphere temperature (K) plots.	156
5.6	Subliming sphere shape change with material time (τ_w).	159
5.7	Comparison of shape changes with different ablation modes. Left: Sublimation only (Current work). Right: Shear only (Ristroph et al., 2012).	159
5.8	Backward facing step geometry and computational domain.	161
5.9	Backward facing step high resolution 3 level mesh patches.	162
5.10	Backward facing step wall steady-state heat transfer with varying mesh resolution.	163
5.11	Transient (top row) and steady state (bottom row) surface heat transfer and pressure.	164
5.12	Variation of mass loss with non-dimensional flow time.	165
5.13	Surface temperature and pressure varying with time. Beginning with $\tau_f = 2$ (top row) and increasing by two flow times for every row below.	166
5.14	Surface mass fraction and flux varying with time. Beginning with $\tau_f = 2$ (top row) and increasing by two flow times for every row below.	167
5.15	Q-criterion plots at different times with temperature based colour scale. . .	168
5.16	Surface properties with ablating and moving wall boundary condition at $\tau_f = 1$ (top) and $\tau_f = 2$ (bottom).	170
5.17	Q-criterion with temperature field colouring of iso-surfaces.	171
B.1	Mesh patches with 1 level of refinement around horse body and wake. . . .	199

B.2	Velocity (m/s) field side and top projections of horse geometry in $M = 6$ flow.	200
B.3	Horse geometry handling verification surface temperature and pressure in $M = 6$ flow and in three-dimensions.	200

List of tables

1.1	Continuum hypersonic computational fluid dynamics solvers as of 2022. . .	8
2.1	Sub-problems of the system of conservation laws in Eq. (2.30).	29
2.2	Observed order of accuracy with and without AMR.	58
2.3	Mesh refinement study	62
3.1	Mesh refinement study with frozen flow over sphere at $M = 4$	80
3.2	Stand-off predictions in frozen flow over a sphere at $M = [4, 8, 16, 32]$. . .	80
3.3	Compression ramp refinement cases ($Re_h = [40, 20, 10]$) computational fluid points distribution and cost.	90
3.4	Double compression ramp case AMR mesh points count.	95
3.5	Transversely oscillating cylinder mean drag (\bar{C}_D), root-mean-squared drag fluctuations ($C'_{rms,D}$) and root-mean-squared lift ($C'_{rms,L}$) comparisons with literature.	107
3.6	Percentage (%) of run time for each code function	108
4.1	Mesh refinement cases low, medium and high resolutions for each Mach number. Number of computational points ($\times 10^6$) and number of refinement levels in brackets.	120
4.2	Stagnation point heat transfer convergence (C_h) with increasing Mesh resolution at different Mach numbers and comparison with semi-empirical correlations of Tauber (1989).	122
4.3	Flow length scales at different Mach numbers.	124
4.4	Cylinder centre coordinates (x, y) (m) for each case.	135
5.1	Hertz-Knudsen parameters values (rounded to two significant figures) for some common hypersonic ablation materials.	149
5.2	Non-dimensional single species subliming sphere parameters.	154
5.3	Single species subliming sphere mesh refinement results.	155

5.4	Single species subliming sphere body refinement.	157
5.5	Backward facing step flow conditions.	161
5.6	Backward facing step mesh refinement results.	162

Nomenclature

Roman

Symbol	Description	Units	First page
C_p	Surface pressure coefficient	-	73
Da	Damkholer number	-	27
D	Diffusion coefficient	m s^{-2}	18
Kn	Knudsen number	-	6
Le_k	Lewis number	-	16
M	Mach number	-	10
Q	Partition function	-	13
R_k	Specific gas constant	$\text{J kg}^{-1} \text{K}^{-1}$	17
Re	Reynolds number	-	27
S	Control surface	m^2	27
T	Temperature	K	16
Y	Mass fraction	-	10
\mathbf{f}_n^v	Viscous flux vector in coordinate direction n	varies	27
\mathbf{f}_n	Euler flux vector in coordinate direction n	varies	27
\mathbf{j}	Mass diffusion flux vector	$\text{kg s}^{-1} \text{m}^{-2}$	15
\mathbf{q}	Conserved variables vector	varies	27
\mathbf{q}	Thermal diffusion flux vector	W s^{-3}	15
\mathbf{s}	Source term vector	varies	27
\mathbf{u}	Velocity	m s^{-1}	10
$\hat{\mathbf{n}}_n$	Unit normal in coordinate direction n	-	27
a	Speed of sound	m s^{-1}	10
c_p	Specific heat capacity at constant pressure	$\text{J kg}^{-1} \text{K}^{-1}$	16
c_{ve}	Vibrational-electronic mode specific heat capacity	$\text{J kg}^{-1} \text{K}^{-1}$	16

Symbol	Description	Units	First page
e_0	Gas specific formation energy	J kg^{-1}	10
e_{int}	Specific internal energy	J kg^{-1}	10
e_{kin}	Specific kinetic energy	J kg^{-1}	10
e_t	Specific total energy	J kg^{-1}	10
e_{ve}	Specific vibrational-electronic energy	J kg^{-1}	15
h_t	Specific total enthalpy	J kg^{-1}	15
k_B	Partition function	J K^{-1}	13
p	Pressure	$\text{kg m}^{-1} \text{s}^{-2}$	15
t	Time	s	27
x_n	Spacial coordinate, $n \leq 3$	m	27

Greek

Symbol	Description	Units	First page
Λ	Ratio of thermal diffusivity of transistional-rotational and vibrational-electronic modes	-	16
α	Thermal diffusivity of mixture	$\text{m}^2 \text{s}^{-1}$	16
∇	Gradient operator	m^{-1}	15
τ	Momentum diffusion flux tensor	$\text{kg m}^{-1} \text{s}^{-2}$	15
ε_r	Molecular rotational energy	J	11
ε_t	Molecular transational energy	J	11
ε_v	Molecular vibrational energy	J	11
ε_e	Molecular electronic energy	J	11
ε	Molecular total energy	J	11
μ	Viscosity	$\text{kg m}^{-1} \text{s}$	18
ω	Source term	Varies	15
ρ	Density	kg m^{-3}	15
$\tilde{\Delta}$	Stagnation line shock stand-off distance	-	74

Subscripts

Symbol	Description	Units	First page
∞	Free-stream state	-	5
k	Species index	-	10
tr	Translational-Rotational mode	-	15
ve	Vibrational-Electronic mode	-	15

Table of contents

List of figures	v
List of tables	xi
Roman	xiii
Greek	xiv
Subscripts	xiv
1 Introduction	1
1.1 History	1
1.2 Applications	2
1.3 Phenomenology	5
1.4 Existing numerical approaches	8
1.5 Thesis objectives and outline	10
2 Hypersonic flow modelling	11
2.1 Gas physical modelling	11
2.1.1 Energy partitioning	11
2.1.2 Molecular internal energy	12
2.1.3 Partition function	14
2.1.4 Multi-temperature models	15
2.1.5 Conservation laws	16
2.1.6 Closures	17
2.1.7 Thermochemistry trends	23
2.2 Gas numerical modelling	28
2.2.1 Mathematical theory for conservation laws	28
2.2.2 Numerical methods	30
2.2.3 Structured adaptive mesh refinement (SAMR)	41

2.3	Numerical validations	48
2.3.1	Weak Riemann problem	48
2.3.2	High temperature Riemann problem	50
2.3.3	Shu-Osher problem	53
2.3.4	Isentropic vortex propagation	54
2.3.5	Supersonic turbulent channel flow	60
2.4	Summary	65
3	Hypersonic flow around complex geometries	67
3.1	SAMR-GPIBM Coupling	67
3.1.1	Algorithms	69
3.2	Numerical tests	77
3.2.1	Euler sphere	77
3.2.2	Flat plate	85
3.2.3	Single compression ramp	89
3.2.4	Double compression ramp	93
3.2.5	Supersonic turbulent channel flow	103
3.2.6	Transversely oscillating cylinder	104
3.3	Summary	109
4	Heat transfer to proximal circular cylinders in hypersonic flow	111
4.1	Introduction	111
4.2	Flow physics	113
4.2.1	Wake and shock shape	113
4.2.2	Stagnation-point and shock-interaction heat transfer	116
4.3	Binary bodies	118
4.3.1	Mesh refinement	119
4.3.2	Results	125
4.4	Multiple bodies	135
4.4.1	Results	136
4.5	Summary	141
5	Hypersonic ablation patterns	144
5.1	Introduction	144
5.1.1	Existing studies	146
5.2	Hypersonic ablation modelling	148
5.2.1	Multi-species sublimation boundary conditions	150

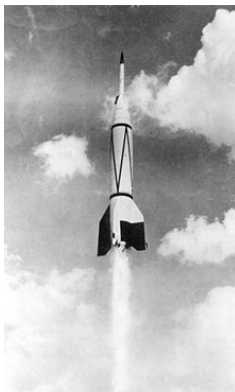
5.2.2	Simple boundary conditions	151
5.2.3	Numerical method	152
5.3	Single species subliming sphere test	154
5.3.1	Numerical setup	154
5.3.2	Stationary wall ablation	155
5.3.3	Moving wall ablation	157
5.4	Search for ablation patterns	160
5.4.1	Backward facing step numerical setup	160
5.4.2	Results	164
5.5	Summary	172
6	Conclusions	174
6.1	Main contributions	174
6.2	Future works	177
	References	179
	Appendix A Conservation equations and non-dimensional numbers	195
A.1	Knudsen number	195
A.2	Energy equation heat flux term	196
A.3	Non-dimensional conservation equations	197
	Appendix B Three-dimensional immersed geometry handling verification	199

1. Introduction

1.1 History

First hypersonic object. On Thursday, the 24th February 1949, in the largest overland military test range embedded in the deserts of New Mexico, United States—radio signals from the fastest and furthest man-made object buzz the automatic trajectory plotting pens. They show a maximum speed of 2.3 km/s, Mach number of more than five and 400 km altitude (same altitude as the International Space Station today). At this moment, the first object of human design achieved hypersonic flight. It was a two-stage rocket built upon the spoils of World War II by the United States and was called RTV-G4 Bumper, as shown in Fig. 1.1a.

First hypersonic person. On Wednesday, the 12th April 1961, near a small village in the flatlands of the Saratov region, Russia. A strange spherical object with a parachute had just landed, its surface burnt charred black from extreme re-entry temperatures. It had dropped from the sky and kissed the ground, bounced up, and fell again. A huge hole was created where it hit the first time. This was the Vostok 1 landing, the first human spacecraft to land successfully. Nearby, Yuri Gagarin lands ¹ using his parachute, which had opened ten minutes earlier and detached from Vostok 1, as illustrated in Fig. 1.1b.



(a) RTV-G4 Bumper



(b) Yuri Gagarin (left) and Vostok 1 (right)

Fig. 1.1 Historical photographs of (a) First hypersonic man-made object flight ([NASA, 2022](#)) and (b) First hypersonic person ([Energiya, 2022](#)).

¹A farmer and her daughter observed the scene of a man descending from space. Gagarin recalled walking up to them, clad in helmet and orange suit, just after landing: "When they saw me in my space suit and the parachute dragging alongside as I walked, they started to back away in fear. But, I told them, don't be afraid; I am a Soviet citizen like you, who has descended from space, and I must find a telephone to call Moscow!"

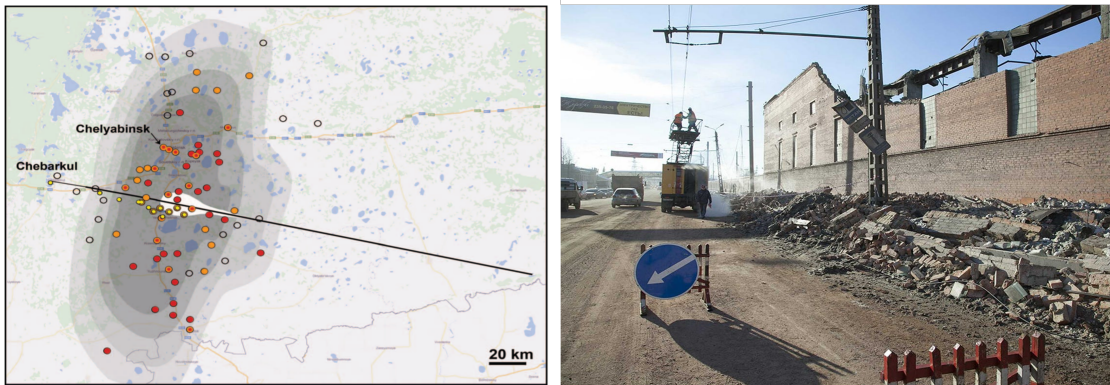
1.2 Applications

Hypersonic flows occur naturally and with man-made applications. Even before human existence, nature has been generating hypersonic flows with astrophysical jets and atmospheric entry of meteors. In contrast, it is only since the 1950s that man-made applications involving hypersonic flows have existed with *spacecraft atmospheric entry* and *sustained hypersonic flight*. Today's practical applications of hypersonic flows include:

- *Meteor entry assessment.* It is well known that large (>1 km in diameter) near-Earth asteroids threaten life on Earth. However, smaller meteors also pose a risk to life and can cause significant ground damage via an airburst shock wave from the detonation of the meteor above ground (Artemieva and Shuvalov, 2016). The mechanism behind airbursts is unknown and active research topic, but is known to be a function of the meteor's material properties and its aerothermal environment. An example of a recent, and significant, airburst was by the Chelyabinsk meteor (Brown et al., 2013). This 20 m diameter meteor entered the Earth's atmosphere at approximately 19 km/s and with 10^{15} J of kinetic energy at around Mach 70 at 100 km altitude. The kinetic energy of the meteor was equivalent to a blast from around 240 tonnes of TNT explosives. Directly below the meteor's path, the shock wave from the air burst was strong enough to blow people off their feet. The air burst caused permanent structural damage to buildings over a vast area, as illustrated by Fig. 1.2a. And the damage was reported to have cumulative financial implications of around \$33 M. Although, there were no human casualties, around 1500 people suffered from secondary blast effects like broken glass injuries from windows, etc. Also, the radiation emitted from the meteor was so powerful that the observers found it painful to look at the bright meteor, and in some cases it even induced mild sunburn. The Chelyabinsk example illustrates the potential impact of small meteor entries on people and infrastructure, whereas the catastrophic effects of large meteor entries are clear. Therefore, accurate predictions of meteor entries can help minimise the ground impact effects on people and infrastructure. And, accurate predictions of meteor entries demand understanding of meteor material properties, as well as accurate modelling of the hypersonic flow environment.
- *Disposed of space-debris atmospheric re-entry prediction and satellite design for atmospheric re-entry demise.* Increasing density of space debris in orbit can initiate Kessler syndrome (Kessler and Cour-Palais, 1978). It is a scenario where sequential collisions between space debris can cause a cascade of collisions, resulting in an exponential growth in the collision rate and the debris population. Without intervention, such a scenario can practically render space unusable for many generations. To avoid

a future Kessler scenario, various steps are being taken by the space community—a new standard practice is to dispose old and current space debris back towards Earth for demise during atmospheric re-entry. However, some debris may not be destroyed during the re-entry and may impact the ground, upon which they can cause human injuries or infrastructure damage. Moreover, the ground impact risk is not only from disposed satellites but also from discarded spacecraft components. Figure 1.2b shows examples of unburnt rocket debris found on the ground. Therefore, future satellites and spacecraft components' demisability during atmospheric re-entry must be predicted accurately to accurately assess the ground risk (Rees, 2020). Accurate predictions of demisability or the deliberate design of satellites and spacecraft components for demise requires an understanding and accurate modelling of the hypersonic flow environment.

- *Re-entry spacecraft and sustained hypersonic flight vehicle design.* Hypersonic vehicles have potentially revolutionary applications in national security, space industry and commercial travel. Two examples of hypersonic vehicles are shown in Fig. 1.2c. Hypersonic commercial travel may become a reality in the near future. Currently, various research prototypes exist, for example, (Hermeus, 2022). On the other hand, the recent development of low-cost launchers has enabled the space industry to grow enormously. The industry is projected to reach around a trillion dollars by 2040 (Morgan Stanley, 2022), with an increasing need for space vehicles. The design of hypersonic vehicles requires understanding and accurate modelling of the hypersonic flow environment.



(a) Left: Chelyabinsk airburst reported damage ([Popova et al., 2013](#)). Each point, irrespective of population density, represents one of many villages or city districts damaged. Solid red circles indicate most damage, solid orange circles indicate medium damage and open black circles for no damage. The black line shows the projected meteor trajectory. Right: building damage from the airburst ([National Post, 2022](#)).



(b) Ground impacting Delta II rocket debris ([Rees, 2020](#)). Left: small debris lightly impacting a person without causing serious injury. Right: Large debris, propellant tank landing on the ground.



(c) Left: SpaceX Dragon re-entry capsule. Right: Hermeus hypersonic passenger plane concept.

Fig. 1.2 Practical contexts involving hypersonic flows.

1.3 Phenomenology

Hypersonic flows are multiscale and multiphysics phenomena. For example, length scales in a hypersonic flow field range orders of magnitude, body length scale can be as large as $\sim O(10^2)$ m, whereas viscous length scales near boundaries can be as small as $\sim O(10^{-6})$ m. In addition, various physical processes occur, like chemical and thermal energy exchanges, plasma sheathing, radiative energy exchanges, ablation and transition to turbulence, and others. These processes often occur simultaneously, and understanding the coupled effects of these processes is still an active area of research (Candler, 2019; Renzo and Urzay, 2021). Moreover, these processes typically have a rate associated with them, which can vary by orders of magnitudes depending on the local and free-stream flow conditions. These rate processes introduce a range of timescales, with a similar breadth to the range of length scales, in hypersonic flow fields. Figure 1.3 summarises the flow phenomenology of around a hypersonic flight vehicle, more detailed discussions can be found in Anderson Jr (2006).

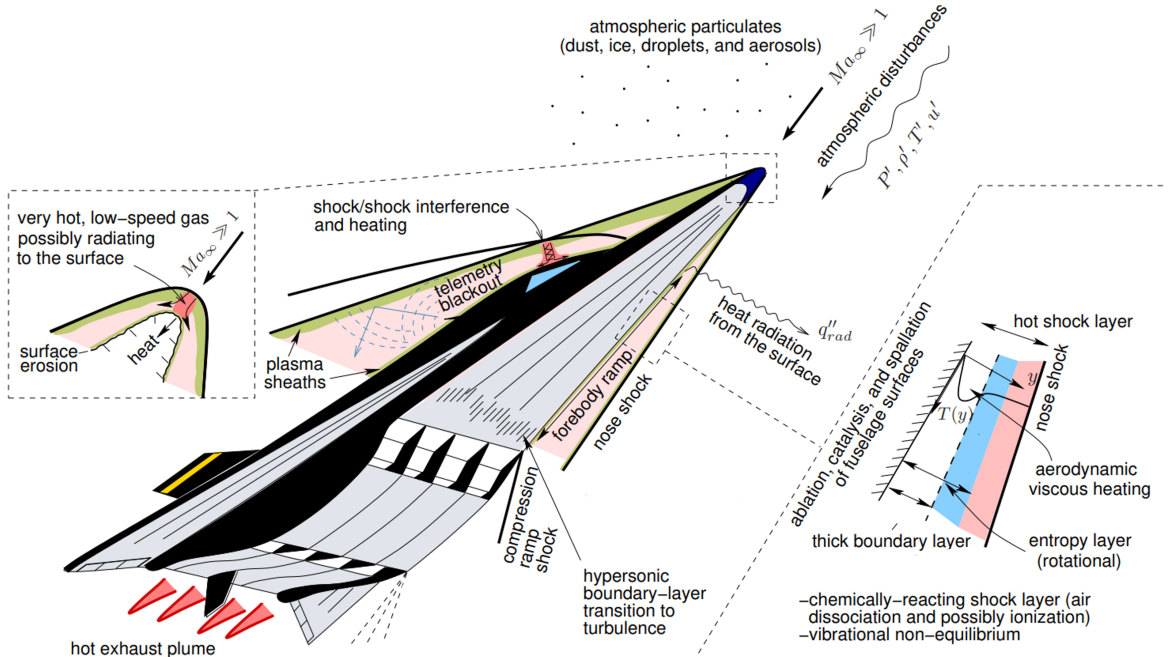


Fig. 1.3 Hypersonic flight vehicle phenomenology (Urzay, 2020).

Practical hypersonic flow space can be characterised by three non-dimensional numbers, free-stream Reynolds number (Re_∞), free-stream Mach number (M_∞) and free-stream stagnation enthalpy normalised by ionization energy ² ($h_{0,\infty}/e_I$). Range of these parameters for Earth entries are:

$$5 \lesssim M_\infty \lesssim 40; \quad 10 \lesssim Re_\infty/L \lesssim 10^7; \quad 0 \lesssim h_{0,\infty}/e_I \lesssim 2. \quad (1.1)$$

The range is graphically illustrated for various hypersonic vehicles in Fig. 1.4. The figure shows the "Heat barrier" region of the flow space where extreme aerothermal heating occurs. Typical entries in human contexts lie within this range, but meteor entries fall outside this range. Meteor entry Mach numbers can be $\sim 2\times$ larger than any engineered flight Mach number. An important dependent non-dimensional number governing the behaviour of a fluid is the Knudsen number (Kn_∞) which is a function of Re_∞ , M_∞ and specific heat capacities ratio (γ),

$$Kn_\infty = \frac{\lambda}{L} = \frac{M_\infty}{Re_\infty} \sqrt{\frac{\gamma\pi}{2}}. \quad (1.2)$$

Considering Eq. (1.2) ³ and Fig. 1.4, the range of Knudsen numbers throughout a trajectory is approximately

$$O(10^{-7}) \lesssim Kn_\infty/L \lesssim O(10). \quad (1.3)$$

The flow regime is considered continuum for $Kn_\infty \lesssim 10^{-2}$.

Difficulties in hypersonic testing. Hypersonic flows in the upper range of the non-dimensional numbers are difficult to re-create in laboratories due to the extreme power requirement. For example, the flow power at 10 km/s, 50 km altitude and through an area of 1 m² is around 500 MW. This power is roughly equivalent to the output of a small nuclear reactor (Locatelli et al., 2014). Furthermore, the gas temperatures in hypersonic flow fields are much higher than any known metal's melting point, making the design of load-bearing components complicated, especially at high stagnation pressures. A recent review by Gu and Olivier (2020) surveys the capabilities and limitations of existing hypersonic ground testing facilities. They categorise facilities by the flow total enthalpy they are able to generate—low, high (dissociating flow) and very high (ionising flow). Low enthalpy facilities allow the longest running times, detailed measurements and best knowledge of free-stream properties. But, can

²50 MJ/kg for air, as suggested by Fig. 1.4.

³This relationship can be derived using results from kinetic theory and is shown in Section A.1.

only cover a small part of the hypersonic flow space. On the other hand, high and very high enthalpy facilities can operate close to or at flight conditions, but suffer from short test times and a limited variety of measurement techniques. Furthermore, flight testing can allow testing in the whole flow space but is expensive and challenging from a data collection perspective. Alternatively, numerical simulations, with modern trends in increasing computational power, could offer an alternative approach to re-creating the hypersonic flow space for flow physics understanding and engineering design. Moreover, they can also complement experimental studies and flight studies.

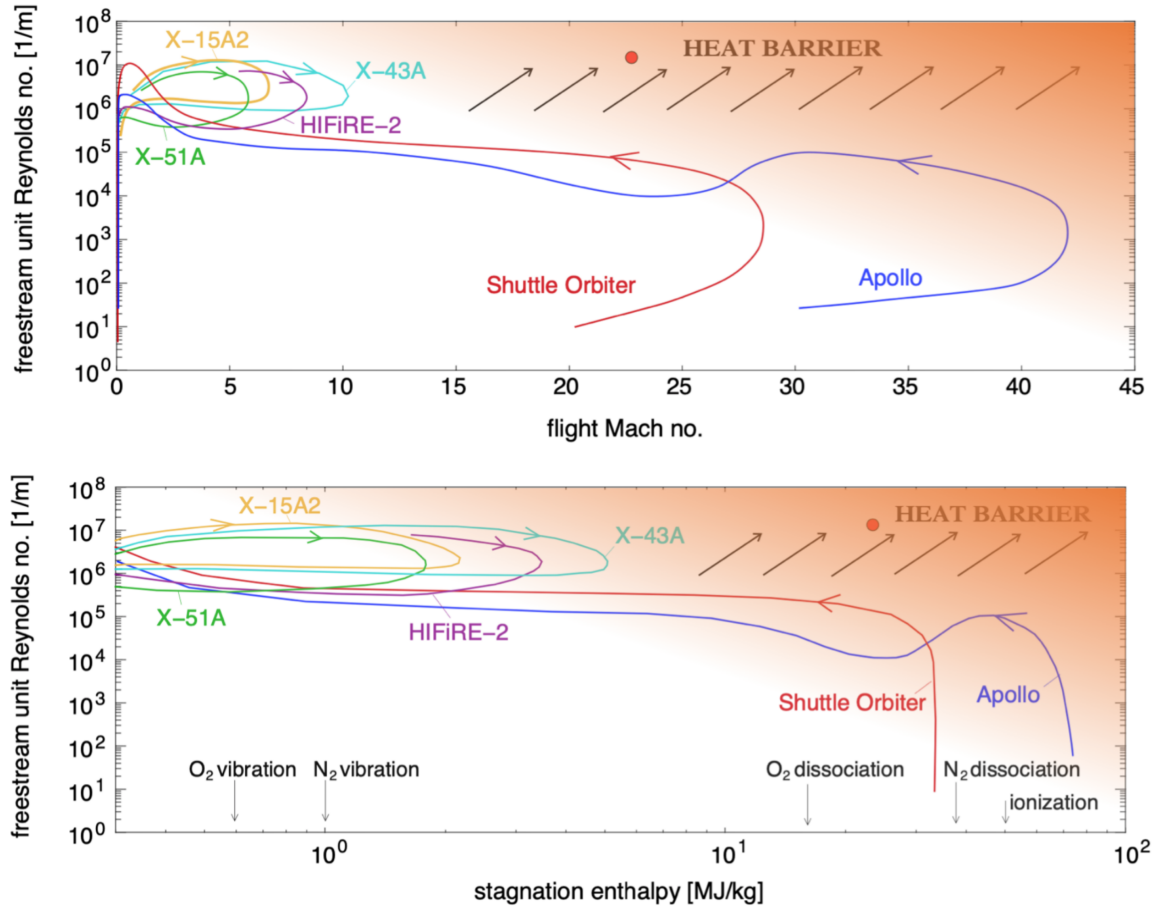


Fig. 1.4 Hypersonic flow space in Earth's atmosphere (Urzay and Di Renzo, 2021) for man-made applications with "heat barrier" regions shaded in orange, representing flow parameters leading to extreme aerothermal heating.

1.4 Existing numerical approaches

Numerical simulations of high-speed flows has been possible since the beginning of the computer era around 1960s (Courant et al., 1952; Godnov, 1969; VonNeumann and Richtmyer, 1950). Today, several computational fluid dynamics solvers exist specifically designed for hypersonic flows computations, motivated by applications discussed earlier, in Section 1.2. Continuum hypersonic flow solvers from literature in the last thirty years are listed in Table 1.1. The table shows that around one out of four of them have been developed in the last five years, most of these began development in parallel but independent to the current work. Several of the recent solvers remain in development at the time of writing.

Table 1.1 Continuum hypersonic computational fluid dynamics solvers as of 2022.

	Country ^a	TCNE ^b	Mesh ^c	Order ^d
LAURA (Cheatwood and Gnoffo, 1996)	US	Yes	SC	Low
DLR-TAU(Schwamborn et al., 2006)	DE	Yes	U	Low
US3D (Nompelis et al., 2006)	US	Yes	U	Low
LeMANS (Scalabrin and Boyd, 2006)	US	Yes	U	Low
DPLR (Wright et al., 2009)	US	Yes	SC	Low
JONATHAN (Matsuyama et al., 2013)	JP	Yes	SC	Low
Eilmer (Gollan and Jacobs, 2013)	AU	Yes	SC/U	Low
Hyfoam(Casseau et al., 2016)	UK	Yes	SC/U	Low
PHAROS(Hao et al., 2017)	CN	Yes	SC	Low
COOLFluid (Vandenhoeck and Lani, 2019)	BE	Yes	U	High
Vulcan (Baurle et al., 2020)	US	Yes	SC/U	Low
HTR (Di Renzo et al., 2020)	US	Yes	SC	High
AMROC (Atkins and Deiterding, 2020)	UK	Yes	SAH	High
CHAMPS (McQuaid et al., 2021a)	US	Yes	SAI	High

^a United Kingdom (UK), United States (US), Germany (DE), Japan (JP), China (CN), Belgium (BE).

^b Thermochemical non-equilibrium modelling (TCNE).

^c Structured conformal (SC), unstructured (U), structured adaptive immersed (SAI) or structured adaptive hybrid conformal-immersed (SAH).

^d Low is less than or equal to 3, otherwise high.

All existing solvers model thermochemical non-equilibrium, which is an important physical phenomenon ([Candler, 2019](#)). Another important physical phenomenon, especially for super-orbital atmospheric entries, is radiative heat transfer. Therefore, some solvers also include radiation transport models.

Most solvers, especially older ones, are unstructured or structured conformal, have a low-order of accuracy and high numerical dissipation, making them unsuitable for turbulent flows ([Ekaterinaris, 2005](#)). High-order spatial discretisation with unstructured meshes is extremely cumbersome, complex and computationally expensive, when compared to structured meshes. Yet, it is common amongst older solvers, which limits them to only laminar computations. The popularity of unstructured and conformal meshes can be attributed to their ability to model complex geometries. However, more recently non-conformal immersed boundaries have been developed and have become popular ([Mittal and Iaccarino, 2005](#)). These allow representation of complex geometries even on structured meshes. High-order discretisation is simple and efficient on a structured mesh than an unstructured mesh. Moreover, structured adaptive meshing with non-conformal immersed boundary methods allow automatic mesh generation when compared to unstructured and conformal methods. This also means that they are well suited for fluid-structure interactions.

Low-order and unstructured mesh solvers are generally based on finite volume methods, whereas high-order and structured solvers on finite difference methods. Higher-order methods with unstructured solvers are generally based on discontinuous Galerkin (finite element) methods, but these methods still remain in research and development ([Ben Ameer et al., 2021](#); [Ching et al., 2019](#)). The three methods, finite volume, finite difference and discontinuous Galerkin solve the Navier-stokes equations. Alternatively, a more fundamental approach involves solving the Boltzmann equation. This approach is taken by Direct Simulation Monte Carlo methods ([Boyd and Schwartzentruber, 2017](#)). These methods are only suitable for rarefied flows and are unsuitable for continuum flows due to their increasing computational expense with modelling many molecules. Moreover, Lattice Boltzmann methods also solve the Boltzmann equation, but they still remain in development for compressible flows ([Guo et al., 2020](#)) and for reacting mixtures ([Sawant et al., 2021](#)).

1.5 Thesis objectives and outline

The first objective of this thesis is to develop and test a high-order numerical method suitable for hypersonic flows around complex geometries. The motivation for this objective is to overcome the disadvantages of existing solvers in literature as discussed in Section 1.4. The second objective is to apply the developed method to study novel hypersonic flow problems.

The structure of the thesis is as follows. Chapter 2 describes the development and testing of finite difference solver with adaptive mesh refinement and thermochemical non-equilibrium. Chapter 3 describes the addition and testing of immersed boundaries. Chapter 4 describes the first application of the developed numerical method, where a novel investigation on heat transfer to proximal cylinders in hypersonic flows is performed. Chapter 5 describes the second application of the developed numerical method, where another novel study, investigates the fluid-structure interaction over ablating surfaces. Finally, Chapter 6 concludes the thesis by summarising key the findings and recommendations for future work.

2. Hypersonic flow modelling

This chapter develops a low dissipation adaptive mesh refinement computational fluid dynamics solver with thermochemical non-equilibrium. The code implementation details are kept brief, but instead the focus is on the physical models and numerical methods. With this in mind, this chapter is organised as follows. Section 2.1 describes conservation laws for gas in thermochemical non-equilibrium and reviews their closures. Section 2.2 describes the mathematical properties of the system of conservation equations and reviews discretisation methods from literature. Section 2.3 validates the developed numerical method.

2.1 Gas physical modelling

2.1.1 Energy partitioning

Hypersonic flows are commonly defined as flows with Mach number (M) greater than 5 (Anderson Jr, 2006). Mach number also represents the ratio of bulk kinetic energy (e_{kin}) to its internal energy (e_{int}) of the gas and is defined as

$$M^2 = \left(\frac{|\mathbf{u}|}{a} \right)^2 \propto \frac{e_{kin}}{e_{int}}, \quad (2.1)$$

where \mathbf{u} is the local fluid velocity and a is speed of sound. Hence, hypersonic flows are very energetic. For example, a Low Earth Orbit re-entry occurs around Mach 25 (7.5 km/s) where the kinetic energy of the flow ¹ is around 125 times that of the free-stream internal energy. The vast amounts of kinetic energy is transferred to the internal energy of the gas, by adiabatic compression and viscous dissipation, resulting high temperatures.

Other energy transfers also occur, but before describing them, total energy (e_t) of a dilute gas mixture must be defined. It is a linear combination of individual species (k) total energy (e_t) weighted by its mass fraction (Y) in that mixture,

$$e_t = \sum_k Y_k e_{t,k} = \sum_k Y_k (e_{0,k} + e_{kin,k} + e_{int,k}), \quad (2.2)$$

where e_0 is the enthalpy of formation.

¹In a body-fixed coordinate system.

Generally, when a gas' total energy is suddenly changed, its equilibrium is said to be disturbed from a thermodynamic point of view. Immediately after the change, various energy transfer processes begin and drive the gas back towards equilibrium. These are called non-equilibrium processes and complicate hypersonic gas modelling. In particular, internal energy and chemical energy exchanges are important. This is discussed next, in Section 2.1.2.

2.1.2 Molecular internal energy

In hypersonic flows, the detailed structure of atoms and molecules cannot be neglected entirely (Kruger and Vincenti, 1965; Park, 1990). A gas's complete description relies on knowing the energy states of all its molecules as a function of space and time. However, this level of detailed knowledge is computationally expensive and impractical for engineering calculations. Hence, a simplification of the problem is necessary. An ensemble view of the molecules via statistical thermodynamics offers a suitable approach for engineering calculations (Daily, 2018).

The molecular total energy (\mathcal{E}) is stored in multiple discrete energy modes, namely, translational (\mathcal{E}_t), rotational (\mathcal{E}_r), vibrational (\mathcal{E}_v) and electronic (\mathcal{E}_e). These discrete energy modes are described by quantum numbers l, v, J and n , respectively. For atoms, molecular energy is stored only in translational and electronic energy modes. Diatomic and polyatomic molecules store energy in translational, electronic, rotational and vibrational modes. The Born-Oppenheimer approximation allows energies stored in the different modes to be estimated via potential curves. It states that electrons reach steady-state motion much more rapidly than atoms under similar electrostatic forces. This is because atoms are more massive than electrons, as electron mass is $1/1830^{\text{th}}$ of a proton. So, the electrons accelerate much faster than atoms and are always in an equilibrium position with respect to the atoms. Figure 2.1 shows a schematic of molecular energy levels for a diatomic molecule. It suggests that electronic states have the largest energy difference, followed by vibrational and then rotational modes.

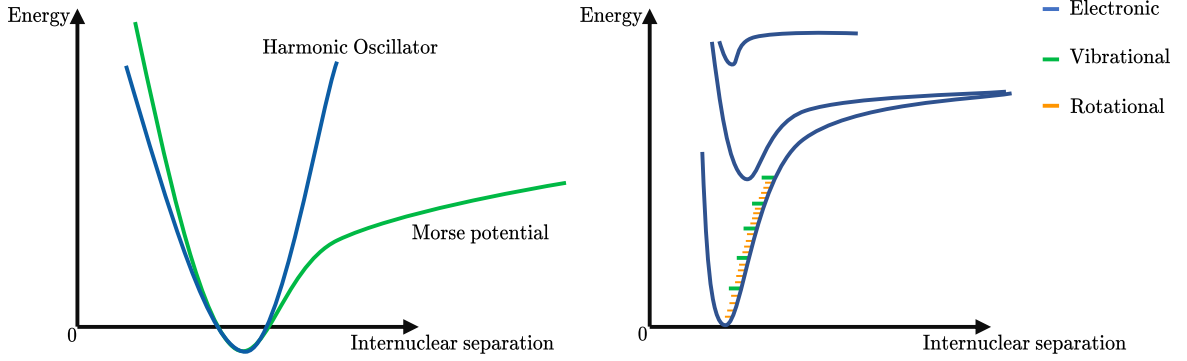


Fig. 2.1 Left: harmonic oscillator and Morse potentials. Right: rovibronic energy levels in diatomic harmonic oscillator model.

Generally, the molecular energy modes are coupled. A Rovibronic model accounts for this coupling and is often not used in engineering calculations due to its complexity:

$$\begin{aligned}\varepsilon(l, v, J, n) &= \varepsilon_t(l) + \varepsilon_e(n) + \varepsilon_v(n, v) + \varepsilon_r(n, v, J); \\ \varepsilon_v(n, v) &= \omega_n \left(\left(\frac{1}{2} + v \right) - x_n \left(\frac{1}{2} + v \right)^2 + y_n \left(\frac{1}{2} + v \right)^3 + z_n \left(\frac{1}{2} + v \right)^4 \right); \\ \varepsilon_r(n, v, J) &= BJ(J+1) - DJ^2(J+1)^2; \\ B &= B_n - \alpha_n \left(v + \frac{1}{2} \right); \quad D = D_n + \beta_n \left(v + \frac{1}{2} \right); \quad D_n = \frac{4B_n^3}{\omega_n^2}.\end{aligned}$$

Constants controlling rotational energy are B and D . Symbols with subscript n are molecular stereoscopic constants: $\omega_n, x_n, y_n, z_n, B_n, D_n$ and α_n , defined for each electronic state. They are given in (Park, 1990) and also available in other databases like National Institute of Standards and Technology (NIST) (Linstrom and Mallard, 2001).

All terms after the first term for vibrational energy are called anharmonic terms. For an air mixture, omission of these terms results in approximately 10% error in peak specific heat capacity of some vibrators around 15,000K in thermal equilibrium (Capitelli et al., 2005). However, the error diminishes when temperatures are much higher or lower than 15,000K. This is because diatomic species in equilibrium mixtures rarely exist at very high temperatures as they dissociate. Whereas, at very low temperatures, vibrational quantum numbers are small, and the anharmonic terms are insignificant.

The simplest model and commonly used for engineering calculations for internal molecular energy is the Rigid Rotor Harmonic Oscillator (RRHO) model. It assumes the internal energy

modes are fully separable. Hence, internal molecular energy is

$$\varepsilon(l, v, J, n) = \varepsilon_t(l) + \varepsilon_e(n) + \varepsilon_v(v) + \varepsilon_r(J). \quad (2.3)$$

The energy modes can be written as analytical functions of molecular properties and energy mode quantum numbers and can be found in standard texts like (Park, 1990). Figure 2.1a. shows potential energy models for RRHO and a more accurate Morse potential energy fit, which includes effects of energy modes coupling. Near the potential minima, both potential curves converge exactly. However, increasing potential energies decreases the accuracy of harmonic oscillator approximation. Despite this, it is often used in engineering calculations due to its simplicity (Panesi, 2009).

2.1.3 Partition function

For engineering calculations, average energy state of a population of molecules is required. Partition function for gas species (Q) represents how molecules are distributed across energy levels (l) for a given molecular energy model (δ). Considering a collection of dilute gas molecules of single species, the most probable population distribution of molecules at a given energy level follows a Boltzmann distribution (Daily, 2018):

$$\delta \in \{t, r, v, e\}; \quad \frac{n_{\delta l}}{N} = \frac{\exp\left(-\frac{\varepsilon_{\delta l}}{k_B T_\delta}\right)}{Q_\delta(T_\delta)}; \quad Q_\delta(T) = \sum_l a_{\delta l} \exp\left(-\frac{\varepsilon_{\delta l}}{k_B T_\delta}\right); \quad (2.4)$$

N is the total number of molecules; $n_{\delta l}$ is the number of molecules for a given energy mode and level; k_B is the Boltzmann constant; $a_{\delta l}$ represents the number of identical states also known as degeneracy; T_δ is the temperature of a given energy mode. More detailed models assume non-Boltzmann distributions; they are called state specific models (Scoggins, 2017) and are not commonly used in hypersonic flow engineering calculations.

RRHO model. The partition function for a given species is

$$Q_k = \sum_l Q_{rk}(T_t) \sum_r Q_{rk}(T_r) \sum_v Q_{vk}(T_v) \sum_e Q_{e,k}(T_e). \quad (2.5)$$

The partition functions for each mode (Scoggins, 2017) are:

$$\begin{aligned} Q_{tk}(T_t) &= \left(\frac{2\pi m_k k_B T_{tk}}{h^2} \right)^{3/2}, & Q_{rk}(T_r) &= \frac{1}{I_k} \left(\frac{T_r}{\theta_{rk}} \right)^{\frac{L_i}{2}}, \\ Q_{vk}(T_v) &= \prod_i \left(1 - \exp \left(-\frac{\theta_{vk,i}}{T_v} \right) \right)^{-1}, & Q_{ek}(T_e) &= \sum_i a_{ek,i} \exp \left(-\frac{\theta_{ek,i}}{T_e} \right); \end{aligned} \quad (2.6)$$

where m_k is the molecular mass, I_k is the moment of inertia, L_i is the linearity of the molecule², $a_{ek,i}$ is the degeneracy, θ_{rk} is the characteristic rotational temperature, $\theta_{vk,i}$ represents characteristic vibrational temperature for vibrational mode i ³, $\theta_{ek,i}$ is the electronic characteristic temperature of level i . All the molecular constants can be found in chemical databases such as NIST. Note, that all species have been assumed to be at the same modal temperature, this may not be valid in every case. However, this assumption greatly simplifies the calculations and is only important in non-equilibrium parts of a hypersonic flow-field. In practice, this is unlikely to result in significant inaccuracies, which can be inferred from (Panesi, 2009).

Knowledge of the partition function allows the calculation of thermodynamic properties and is described later in Section 2.1.6. The partition function is parameterized by temperature, which controls the energy distribution. When considering multiple energy modes, multiple temperatures also exist. In fact, thermal non-equilibrium phenomena is the need for multiple temperatures to accurately describe energy distribution in a gas.

2.1.4 Multi-temperature models

Thermal non-equilibrium phenomena can be modelled by multi-temperature (MT) models. MT models used in hypersonic flow calculations were initially developed by (Lee, 1984; Park, 1988, 1989). Maximum of four temperatures, one for each energy mode, are required to define a gas fully. Energy modes with the same temperature are said to be in equilibrium, whereas modes with different temperatures are said to be out of equilibrium. In this non-equilibrium state, energy exchange drives the system towards equilibrium. Such exchanges are especially important behind shockwaves and around strong expansions.

A four-temperature model is not usually necessary for accurate hypersonic computations, instead, a two-temperature model is sufficient and commonly used. It assumes translational and

² $L_i = 2$ for linear molecules and $L_i = 3$ for non-linear molecules.

³For simple diatomic molecules, there can be multiple vibrational modes which can be important. Whereas only one rotational mode is generally important, as the moment of inertia is only significant around one axis of rotation.

rotational modes (*tr*) have the same temperature, as do the vibrational and electronic modes (*ve*). Translational and rotational modes are reported to have post-shock non-equilibrium distances of around the mean free path (Park, 1990), whereas vibrational and electronic modes are slowest to reach equilibrium requiring orders of magnitude more time. Hence, a two-temperature model is usually accurate enough for engineering calculations. However, for strongly ionized flows, a two-temperature model may not be sufficient, and the electrons maybe need to be considered in more detail. This is because, electrons also equilibrate their energy slowly and may require a separate electron temperature—a three-temperature model maybe necessary for accurate electron density predictions (Ramjatan et al., 2020).

2.1.5 Conservation laws

Continuum conservation laws, neglecting radiative heat transfer are:

$$\frac{\partial}{\partial t} \begin{pmatrix} \rho Y_1 \\ \vdots \\ \rho Y_n \\ \rho \\ \rho \mathbf{u} \\ \rho e_t \\ \rho e_{ve} \end{pmatrix} + \nabla \cdot \begin{pmatrix} \rho Y_1 \mathbf{u} \\ \vdots \\ \rho Y_n \mathbf{u} \\ \rho \mathbf{u} \\ \rho \mathbf{u} \otimes \mathbf{u} + p \mathbf{I} \\ \rho \mathbf{u} h_t \\ \rho \mathbf{u} e_{ve} \end{pmatrix} + \nabla \cdot \begin{pmatrix} \mathbf{j}_1 \\ \vdots \\ \mathbf{j}_n \\ 0 \\ -\boldsymbol{\tau} \\ \mathbf{q} - \boldsymbol{\tau} \cdot \mathbf{u} \\ \mathbf{q}_{ve} \end{pmatrix} = \begin{pmatrix} \omega_1 \\ \vdots \\ \omega_n \\ 0 \\ 0 \\ 0 \\ \omega_{vt} + \omega_{vc} \end{pmatrix}; \quad (2.7)$$

where ρ is density, \mathbf{u} is the velocity vector, p is pressure, Y_k is the species mass fraction, e_t is the total energy, e_{ve} is the vibrational energy, n is the number of species, \mathbf{I} is the identity matrix, ∇ is the gradient operator, h_t is the total enthalpy, \mathbf{j}_k is species mass diffusion flux vector, $\boldsymbol{\tau}$ is the shear stress tensor, \mathbf{q} is the thermal diffusion flux vector, ω_k is the chemical source term, ω_{vt} is the translational-vibrational energy transfer term, and ω_{vc} is the vibrational-chemical energy transfer term.

On the right-hand side of Eq. (2.7) are highly non-linear source terms, exponential functions of primitive variables. On the left-hand side, the first divergence term represents the convective fluxes. It is a first-order derivative of triple products of field variables. It is a highly non-linear term. The second divergence term represents diffusive terms, second-order derivatives of field variables, and linear in the limit of constant transport properties. The

diffusive fluxes are

$$\begin{aligned} \mathbf{j}_k &= -\rho D_k \nabla Y_k, \quad \boldsymbol{\tau} = \mu \left(\nabla \mathbf{u} + (\nabla \mathbf{u})^T - \frac{2}{3} \nabla \cdot \mathbf{u} \mathbf{I} \right), \quad \mathbf{q}_{ve} = -\lambda_{ve} \nabla T_{ve}, \\ \mathbf{q} &= \rho \alpha \left(\nabla h + \sum_k \left[\left(1 - \frac{1}{Le_k} \right) h_k \cdot \nabla Y_k \right] + (1 - \Lambda) c_{ve} \nabla T_{ve} \right); \end{aligned} \quad (2.8)$$

where T_{ve} is the vibrational-electronic temperature, c_{ve} is the vibrational mode specific heat capacity, Λ is the ratio of thermal diffusivity of translational-rotational and vibrational-electronic modes⁴, α is the thermal diffusivity; h is the mixture enthalpy; Le_k is species Lewis number. If the thermal diffusivities of energy modes are approximately equal ($\Lambda \approx 1$) then thermal diffusion between energy modes can be neglected. Note, Ludwig-Soret effect which is species mass transfer driven by temperature gradients is neglected. Appendix A.3 shows the non-dimensional and the simplified forms of Eq. (2.7). Moreover, Appendix A.2 shows the derivation for the heat flux vector in Eq. (2.8).

2.1.6 Closures

Closures implemented in current work are through an open source library, Mutation++ (Scoggins et al., 2020). It provides thermodynamic, transport and chemical kinetics closures for solving Eq. (2.7). It is used to map a thermodynamic state to its properties, $(\rho, T_{tr}, T_{ve}, Y_1, Y_2, \dots, Y_n) \mapsto (\mu, D_{km}, \lambda_{tr}, \lambda_{ve}, \omega_k, \omega_{vt})$. Closures used in the current work from the library are summarised in this section.

Thermodynamics

Pure species. Partition functions defined in Eq. (2.5) can be used to calculate all thermodynamic properties:

$$e_{tk} = \frac{3}{2} R_k T_t, \quad h_{tk} = e_{tk} + R_k T_t, \quad s_{tk} = R_k \left(\frac{5}{2} + \ln(Q_{tk}/n_k) \right); \quad (2.9)$$

$$e_{\delta k} = R_k T_\delta^2 \frac{\partial Q_{\delta k}}{\partial T_\delta}, \quad h_{\delta k} = e_{\delta k}, \quad s_{\delta k} = R_k \left(T_\delta \frac{\partial \ln(Q_{\delta k})}{\partial T_\delta} + \ln(Q_{\delta k}) \right); \quad (2.10)$$

where n_k is the number density and R_k is specific gas constant, for species k . Internal energy (e), enthalpy (h) and entropy (s) for translational energy mode is different to other modes ($\delta \in \{r, v, e\}$). Other thermodynamic properties like the Gibbs free energy (g), specific heat

⁴ $\Lambda = \frac{\lambda_{ve}}{\lambda_{tr}} \frac{c_{p,tr}}{c_{ve}}$, and c_p is the specific heat capacity at constant pressure. With a three-temperature model, electrons are modelled separately, another ratio of energy mode thermal diffusivities will be introduced.

capacity at constant pressure (c_p) and specific heat capacity at constant volume (c_v) are defined as

$$g_{\delta k} = h_{\delta k} - T_{\delta} s_{\delta k}, \quad c_{p,\delta k} = \frac{\partial h_{\delta k}}{\partial T_{\delta}}, \quad c_{v,\delta k} = \frac{\partial e_{\delta k}}{\partial T_{\delta}}. \quad (2.11)$$

Thermodynamic properties used in the current work are under RRHO model assumption and can be calculated, using partition functions in Eq. (2.6) and Eqs. (2.9) and (2.10). For a two-temperature model and for any thermodynamic property (ϕ)

$$\phi_{tr,k} = \phi_{tk} + \phi_{rk}, \quad \phi_{ve,k} = \phi_{vk} + \phi_{ek}. \quad (2.12)$$

Mixture properties with two-temperature model are

$$\phi = \begin{cases} \sum_k Y_k \phi_k, & \text{if } \phi \in (e_{ve}, e_{tr}, c_{v,tr}, c_{p,tr}, c_{ve}, h_{tr}, g_{tr}, g_{ve}, s_{tr}, s_{ve}) \\ \sum_k Y_k (\phi_{tr,k} + \phi_{ve,k}), & \text{if } \phi \in (e, h, c_p, c_v) \\ \sum_k Y_k (\phi_{tr,k} + \phi_{ve,k} - R_k \ln(X_k)), & \text{if } \phi \in (s, g) \end{cases}, \quad (2.13)$$

X_k is the mole fraction and $-R_k \ln(X_k)$ term is due to the entropy of mixing. Furthermore, the equation of state for a dilute two-temperature gas is

$$P = \sum_k \rho_k R_k T_{tr}. \quad (2.14)$$

Speed of sound is defined as the speed of isentropic propagation of a perturbation through a media,

$$a^2 = \left(\frac{\partial p}{\partial \rho} \right)_s. \quad (2.15)$$

In thermochemical non-equilibrium the thermodynamic state is a function of more than two variables. This means that, entropy is $s(p, \rho, T_{ve}, Y_k)$ and inverting the relationship $p(s, \rho, T_{ve}, Y_k)$. Therefore, the derivative in Eq. (2.15) is not unique and is a function of the non-equilibrium state variables. However, its unique values can be computed with assumptions on T_{ve} and Y_k . By keeping *all* state variables constant apart from density, gives

the frozen speed of sound (a_f), which is valid when thermochemical source terms are small:

$$a_f^2 = \left(\frac{\partial p}{\partial \rho} \right)_{s, T_{ve}, Y_k} = - \frac{\left(\frac{\partial h}{\partial p} \right)_{T_{ve}, Y_k}}{\left(\frac{\partial h}{\partial p} \right)_{T_{ve}, Y_k} - \frac{1}{\rho}}. \quad (2.16)$$

Alternatively, local chemical and thermal equilibrium can be assumed—denoted by starred superscript (*). This assumption results in the equilibrium speed of sound (a_e), which is valid when thermochemical source terms are dominant. It is written as

$$a_e^2 = \left(\frac{\partial p}{\partial \rho} \right)_{s, T^*, Y_k^*} = - \frac{h_p}{h_p - \frac{1}{\rho}}, \quad h_p = \frac{\partial h}{\partial p} + \frac{\partial h}{\partial T^*} \frac{\partial T^*}{\partial p} + \sum_k \frac{\partial h}{\partial Y_k} \frac{\partial Y_k}{\partial p}, \quad h_p = \frac{\partial h}{\partial p} + \frac{\partial h}{\partial T^*} \frac{\partial T^*}{\partial p} + \sum_k \frac{\partial h}{\partial Y_k} \frac{\partial Y_k}{\partial p}. \quad (2.17)$$

More detailed discussions of speed of sound in non-equilibrium media can be found in [Kruger and Vincenti \(1965\)](#).

Transport

Pure species. Transport properties for pure gases are simple. Pure species viscosity (μ_k), thermal conductivity (λ_k) and binary diffusion coefficients (D_{kl}) are

$$\mu_k = \frac{5}{16} \frac{\sqrt{\pi m_k k_B T_t}}{\pi \bar{Q}_{kk}^{(2,2)}}, \quad \lambda_k = \frac{15}{4} R_k \mu_k \left(\frac{4}{15} \frac{c_{v,k}}{R_k} + \frac{3}{5} \right), \quad D_{kl} = \frac{3}{16} \frac{1}{\bar{Q}_{kl}^{(1,1)}} \sqrt{\frac{2\pi k_B T_t (m_k + m_l)}{m_k m_l}}, \quad (2.18)$$

where $\bar{Q}_{kk}^{(2,2)}$ and $\bar{Q}^{(1,1)}$ are collision integrals with standard definitions from standard transport texts like [Hirschfelder et al. \(1964\)](#). The collisional data for dominant interactions air species have been reported to have around 10% error compared to detailed quantum chemistry calculations ([Wright et al., 2005](#)). The thermal conductivity for a given energy mode can be calculated via Eucken relation ([Scoggins, 2017](#)). Equation (2.18) suggests $\lambda, \mu \propto \sqrt{T}$, and $D_k \propto T^{3/2}/P$.

Mixtures. Transport properties of mixtures are complex. They are most accurately derived from the kinetic theory of dilute gases and calculated by Chapman-Enskog expansion of the Boltzmann equation ([Hirschfelder et al., 1964](#)). Mutation++ is a computational library which includes transport models from kinetic theory models for partially ionized unmagnetised multicomponent non-equilibrium plasmas ([Magin and Degrez, 2004](#); [Scoggins, 2017](#)). The library's transport properties' computations are more accurate and computationally less expensive when compared to other commonly used transport models used in high-temperature

hypersonic flow computations. A relative difference of 10% in dissociating air and 70% in ionising air viscosity with Wilke's rule (Wilke, 1950), and up to 40% difference in viscosity for ionised air to Gupta-Yos viscosity model (Gupta et al., 1990) have been shown. Similar differences are reported for thermal conductivity. Moreover, other simpler methods like Sutherland's law and Bottnner's viscosity curves are limited to around 3000K in the air before they diverge by more than 10% when compared to Gupta-Yos models. Therefore, transport models from Mutation++ are preferred in the current work.

With Mutation++, the mixture viscosity (μ) and thermal conductivity (λ) are:

$$\mu = \sum_k \alpha_k X_k, \quad X_k = \sum_l G_{kl} \alpha_l; \quad (2.19)$$

$$\lambda = \sum_k \beta_k X_k, \quad X_k = \sum_l H_{kl} \beta_l; \quad (2.20)$$

where α_k and β_k are constants controlling contribution of species interaction pair, G_{kl} and H_{kl} represent the interaction between species k and l . The full expressions are given in (Scoggins, 2017). Considering Eqs. (2.19) and (2.20), the scaling of mixture properties is not trivial unlike pure species mixture, due to compositional changes.

Giovangigli (1991); Sutton and Gnoffo (1998) describe various modelling approaches for diffusion phenomena. The most rigorous approach is solving the full multi-component transport system, which is not common in CFD applications. A more practical approach is via solving the Stefan-Maxwell system (Hirschfelder et al., 1964), but it is computationally expensive. The simplest and most an accurate enough approach for the current study is the Fick's diffusion model. It is also known as the Hirschfelder-Curtis approximation (Hirschfelder et al., 1964; Poinso and Veynante, 2005),

$$D_k = \frac{1 - Y_k}{\sum_l \frac{X_l}{D_{kl}}}, \quad (2.21)$$

where D_k is the mixture diffusion coefficient, $M_{r,k}$ and M_r are species molar and mixture molar masses respectively. In practice, (Alkandry et al., 2013; Sutton and Gnoffo, 1998) find that Hirschfelder-Curtis approximation is accurate enough for heat transfer predictions even with ablating boundary layers. The approximation is equivalent to solving the full multicomponent system if the mixture contains only two species with only concentration driven diffusion. Neglecting other diffusion driving forces - body forces, temperature gradients, pressure gradients, etc. However, for more than two species, the approximation does not conserve overall mass. This can be seen by summing species mass transport for all species. To ensure

global mass conservation, a correction convective flux must be added to species convective flux (\mathbf{f}_k^c),

$$\mathbf{f}_k^c = \rho \sum_k D_k \frac{M_{r,k}}{M_r} \nabla X_k. \quad (2.22)$$

Internal energy exchanges

A multi-temperature model needs to account for energy exchanges between molecular energy modes. For a two-temperature model, as in Eq. (2.7), vibrational-translational mode changes and chemical-vibrational mode exchanges are important. Other exchanges like translational-electronic and rotational-vibrational are negligible (Park, 1990).

Vibrational-Translational(VT) energy exchanges. In binary interactions with the RRHO model, vibrational transitions can only be assumed to occur between neighbouring quantum states. Summating these interactions in a population of molecules results in a master equation describing the rate of change in vibrational energy in gas (Park, 1990). This yields an expression for vibrational-translational energy transfer source term (ω_{VT}). For a mixture with rigid rotors and harmonic oscillators, with a common vibrational temperature, the source term reads:

$$\omega_{VT,k} = \begin{cases} 0, & \text{if } k \text{ is monatomic} \\ \sum_k \rho_k \frac{e_{vk}(T_{tr}) - e_{vk}(T_{ve})}{t_k^{MW} + t_k^P}, & \text{if } k \text{ is diatomic} \end{cases}; \quad (2.23)$$

$$t_k^{MW} = \frac{p_{atm}}{p} \sum_j x_j \exp(a_{kj}(T_{tr}^{-\frac{1}{3}} - b_{kj}) - 18.42), \quad t_k^P = \left(n_k \sqrt{\frac{8k_B T_{tr}}{\pi m_k}} \sigma_{vk} \right)^{-1}; \quad (2.24)$$

where p_{atm} is atmospheric pressure, a_{kj} and b_{kj} are empirical constants, σ_{vk} is the effective cross-section for vibrational relaxation, t_k^{MW} are semi-empirical fits (Millikan and White, 1963), t_k^P is Park's 1st correction for increasing temperatures where the vibrational excitation becomes limited due to finiteness of elastic collision cross-sections (Park, 1984). For $T > 5000K$ Millikan and White fits predict a faster relaxation. Note, species k only includes oscillating species (diatomic harmonic oscillators).

Chemistry-Vibrational(CV) energy transfers. Molecules created or destroyed via chemical reactions also change the vibrational energy of the gas. There are two models characterising this phenomenon, either preferential or non-preferential. Preferential models like the Treanor-Marrone model (Macheret et al., 1994; Marrone and Treanor, 1963) are based on the premise that dissociation can occur more easily from the higher vibrational levels, whereas non-

preferential models assume the dissociation to be independent of the vibrational state of the molecule. Panesi (2009) compares preferential and non-preferential models behind a strong shock wave with $M \approx 25$, he finds up to 50% difference in composition of species in post-shock non-equilibrium region of $O(10^{-2})$ m. After which, the two models agree well and the choice of the model is not significant. Therefore, a simple and commonly used non-preferential model is deemed sufficient in this work,

$$\omega_{CV} = c_1 e_{vk} \omega_k. \quad (2.25)$$

The factor, c_1 controls the dissociation preference. When $c_1 = 1$, it represents a preferential model, and when $c_1 > 1$ a non-preferential model is obtained.

Chemical energy exchanges

A general reaction in a mixture reads

$$\sum_k v'_{rk} A_k \rightleftharpoons \sum_k v''_{rk} A_k, \quad r \in \mathcal{R}, \quad (2.26)$$

where r is a reaction from reaction set \mathcal{R} , v'_{rk} and v''_{rk} are forward and backward stoichiometric coefficients for species k in reaction r .

Law of mass action states that the rate of production of a reaction product (ω_k) is proportional to the product of the reactant densities raised to the power of their stoichiometric coefficients. In a general form, considering forward and backward reactions for each species,

$$\omega_k = \frac{\partial \rho_k}{\partial t} = M_k \sum_r \left[(v'_{kr} - v''_{kr}) \left(k_{br} \prod_{i=1}^{N_s} \left(\frac{\rho_i}{M_i} \right)^{v''_{i,r}} - k_{fr} \prod_{i=1}^{N_s} \left(\frac{\rho_i}{M_i} \right)^{v'_{i,r}} \right) \right] \quad (2.27)$$

where M_k is the molar mass of species, k_{fr} and k_{br} are forward and backward rates of reactions. The forward rate of reaction is in Arrhenius form and the backward reaction rate can be evaluated via the equilibrium constant (K_r^*),

$$k_{fr} = A T_{fr}^\beta \exp\left(\frac{-T_a}{T_{fr}}\right), \quad T_{fr} = \sqrt{T_{tr} T_{ve}}, \quad k_{br}(T_{br}) = \frac{k_{fr}(T_{br})}{K_r^*(T_{br})}, \quad (2.28)$$

where T_{fr} and T_{br} are the forward and backward reaction controlling temperatures, T_a is the activation temperature, β and A are constants. The rate-controlling temperature is dependent on the chemical mechanism driving the reaction. Generally, the chemical reactions are controlled by translational temperature only. However, in thermal non-equilibrium the rate-

controlling temperature is taken as the geometric mean of the translational-rotational and vibrational-electronic temperatures (Park, 1990). Moreover, electron impact reactions are controlled by the electron temperature instead. A more detailed discussion of the different reactions and mechanisms can be found in Scoggins (2017).

2.1.7 Thermochemistry trends

Mixture thermodynamic and transport properties strongly depend on the pure species properties. Common atmospheric mixtures, excluding trace species, include Air-11 (N_2 , O_2 , NO , N , O , N_2^+ , O_2^+ , NO^+ , N^+ , O^+ , e^-) for Earth's atmosphere and Carbon-dioxide-8 (CO_2 , O_2 , CO , C , O , C^+ , O^+ , e^-) for Mars and Venus atmospheres. All molecules in these mixtures are diatomic or monatomic, except CO_2 which behaves similar to a diatomic molecule.

Specie specific heat capacities for translational-rotational and vibrational-electronic energy modes are shown in Fig. 2.2, it suggests:

- Calorifically perfect gas assumption (c_p is constant) is only valid at low temperatures, for $T \lesssim 1,000 \text{ K}$.
- Diatomic neutral species like O_2 , N_2 , CO and NO , have $c_{ve} \approx 0.3c_{p,tr}$ around $T \approx 5,000 \text{ K}$. Whereas, CO_2 has significant vibrational energy storage capacity in vibrational-electronic mode with $c_{ve} \approx c_{p,tr}$.
- Considering neutral atoms, N can store significantly more energy in electronic modes than O and C . Ionised atomic and diatomic species at $T \gtrsim 10,000 \text{ K}$ can have $c_{ve} \approx 0.5c_{p,tr}$. A larger difference in c_{ve} and $c_{p,tr}$ can lead to stronger thermal non-equilibrium effects.

Mixture's equilibrium composition is a function of pressure⁵ and temperature only, and its variation is shown in Fig. 2.3. It suggests :

- Dissociation occurs at lower temperature with decreasing pressure. At low pressure, complete dissociation occurs around 6,000 K and 3,000 K for Air and Carbon-dioxide species sets respectively. However, at high pressures, approximately double temperatures are required for complete dissociation than at lower pressures.
- Mixture is fully ionized (assuming single ionization only, i.e. all molecules lose one electron only) when the electron mole fraction is 0.5. This occurs at a lower

⁵Pressure decreases exponentially with altitude in planetary atmospheres.

temperature at lower pressures. Both mixtures at $P = 100$ Pa reach a fully ionized state around 10,000K. Whereas, at $P = 10,000$ Pa the electron mole fraction just approaches 0.4 at 20,000 K.

In light of both Figs. 2.2 and 2.3, a chemically equilibrated mixture, the potential of thermal non-equilibrium increases as vibrational modes become activated, but decreases as molecules dissociate. In an intermediate temperature range of $2,500 \lesssim T(\text{K}) \lesssim 7,500$, the potential for thermal non-equilibrium is greatest. Contrary to a naive impression of thermal non-equilibrium effects becoming increasingly important with increasing temperatures. This is also discussed in depth by ?.

Equilibrium mixture's thermodynamic and transport properties depend on pressure and temperature only. Their variation is shown in Fig. 2.4. The following observations can be made:

- Ratio of frozen speed of sound for equilibrium⁶ to frozen mixture varies non-linearly but monotonically with temperature. The change in mixture specific heats ratio and mixture specific gas constant cause this behaviour. The composition can affect the frozen speed of sound by a factor of $\sim 2 - 3$.
- Viscosity increases with temperature until dissociation, after which it reduces drastically as the mixture is ionized. The viscosity at very low pressure tends towards zero at very high temperatures and low pressures, indicating a collisionless plasma.
- Thermal conductivity is highly non-linear with respect to temperature. It increases rapidly until ionization, after which it reduces drastically.

The diffusion coefficient also shows a similar magnitude of variation to viscosity and thermal conductivity but is not shown here for brevity. In summary, composition affects the thermodynamic and transport properties non-linearly and up to a factor of ~ 3 for up to 20,000 K temperature range. Under 5,000 K equilibrium temperatures, the composition may affect the thermodynamic and transport properties by maximum factor of ~ 1.5 .

⁶Note, in current figure a_e is not defined as Eq. (2.17), but instead it is just the frozen speed of sound of the equilibrium mixture.

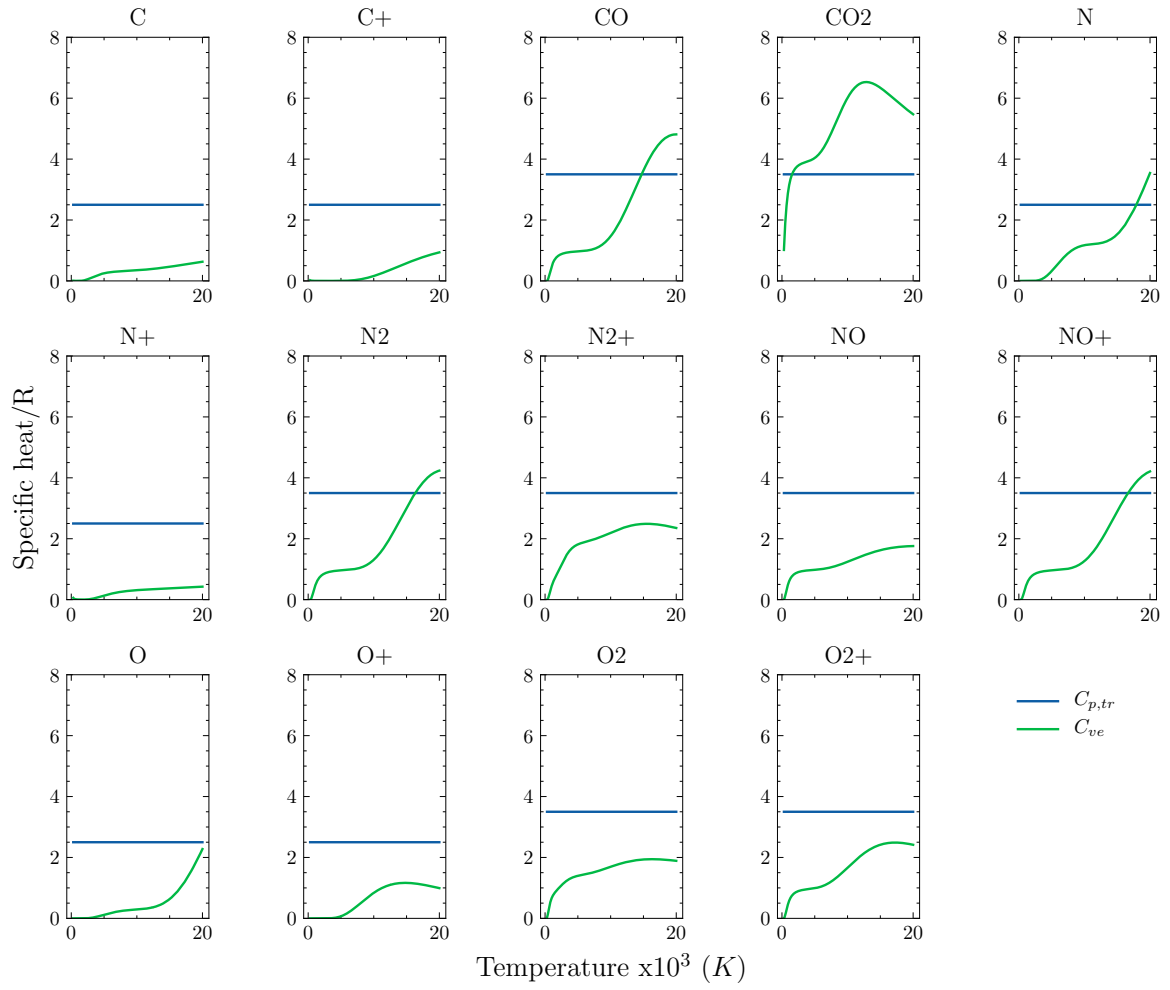
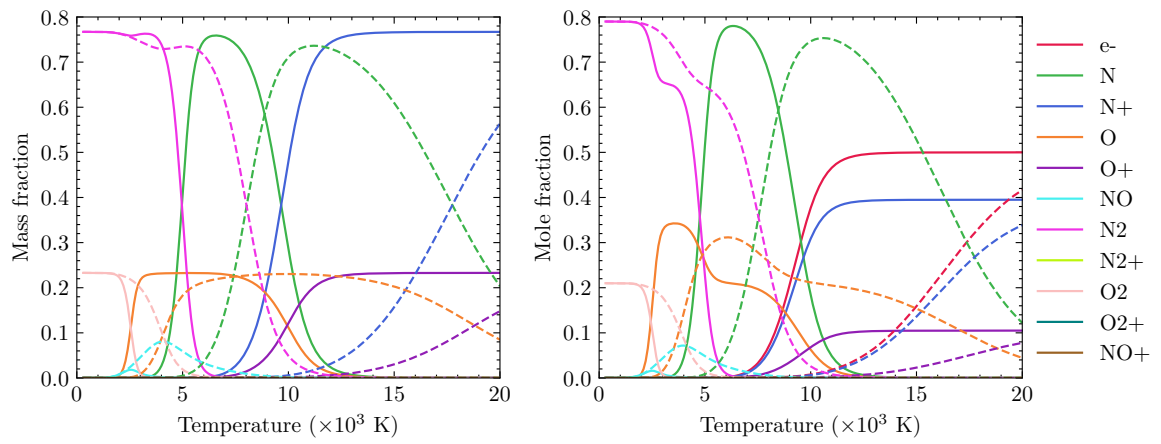
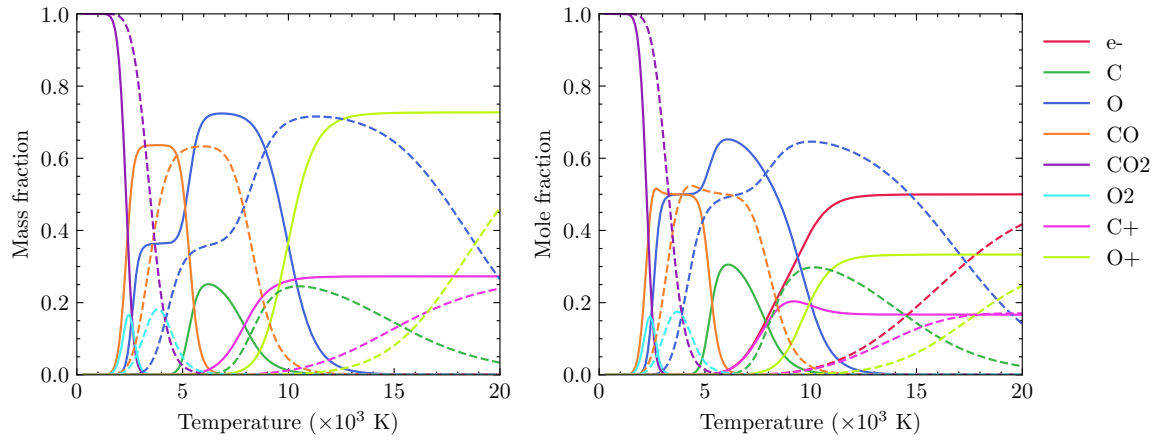


Fig. 2.2 Air-11 and carbon-dioxide-8 species translational-rotational ($c_{p,tr}$) and vibrational electronic (c_{ve}) specific heats normalised with universal gas constant (R) varying with temperatures up to 20,000 K.



(a) Air-11 Earth entry mixture.



(b) Carbon-dioxide-8 mixture.

Fig. 2.3 Equilibrium mass and mole fractions of mixtures with varying temperatures and pressures. Low pressure at 10^2 Pa (—) and high pressure at 10^5 Pa (---).

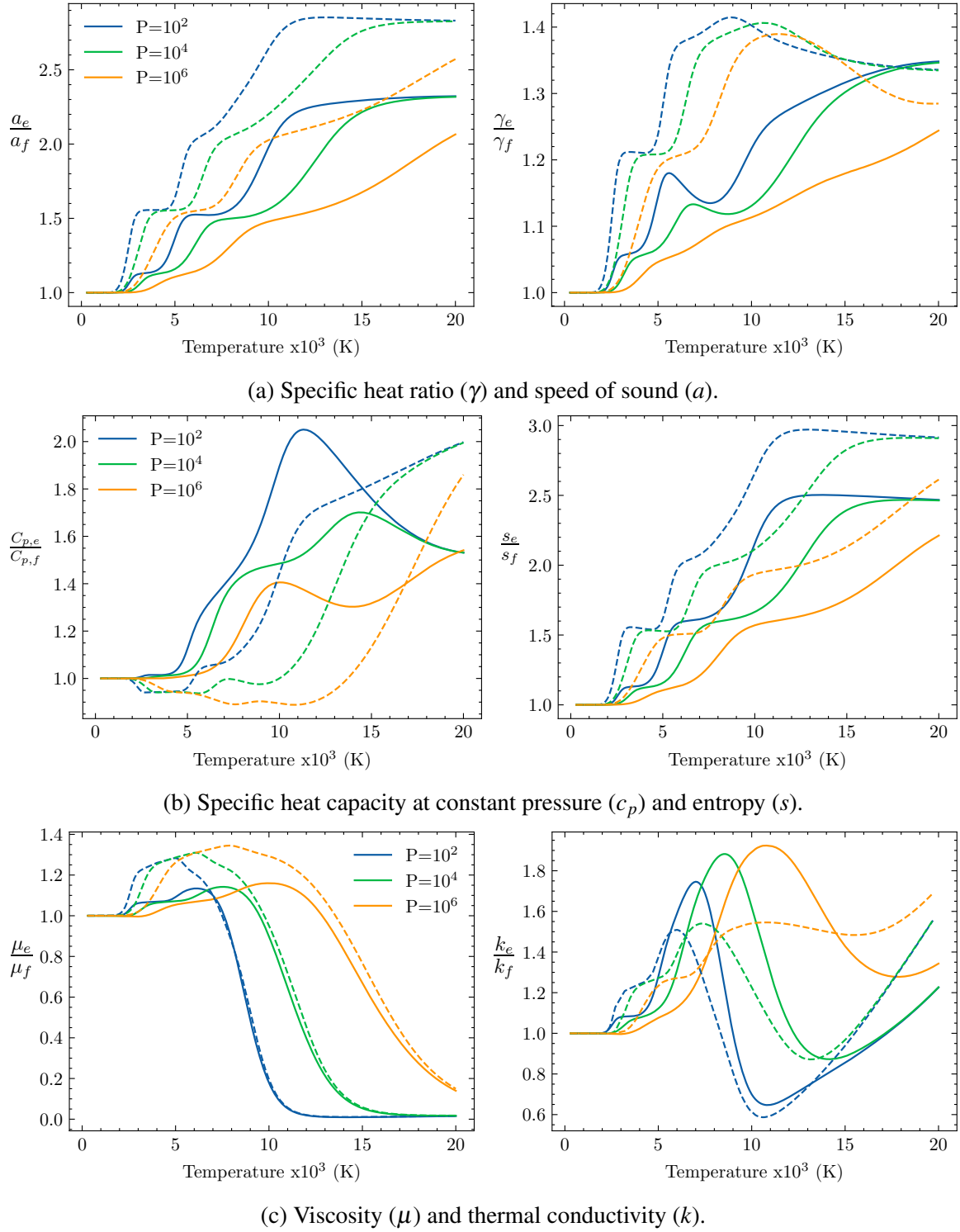


Fig. 2.4 Mixture equilibrium (e) to frozen (f) thermodynamic and transport properties ratio, varying with temperature and pressure (P) for Air-11 (—) and Carbon-dioxide-8 (---) mixtures.

2.2 Gas numerical modelling

In this section, the key mathematical concepts useful for solving conservation laws, described in Section 2.1.5, are highlighted. Then, numerical methods for computing Euler fluxes are surveyed, diffusive terms discretisation, source terms and time integration approaches used in the current work are described. Finally, structured adaptive meshing methodologies are surveyed, and high-level AMR algorithms used in the current work are described.

2.2.1 Mathematical theory for conservation laws

The system of conservation laws in Eq. (2.7) in compact form are:

$$x_n, t \in \mathbb{R}_{\geq 0}, \quad \mathbf{q}(\mathbf{x}, t) : \mathbb{R}^{n_d} \times \mathbb{R}_{\geq 0} \rightarrow \mathbb{R}^{n_q}, \quad \mathbf{f}_n(\mathbf{q}), \mathbf{f}_n^v(\mathbf{q}), \mathbf{s}(\mathbf{q}) : \mathbb{R}^{n_q} \rightarrow \mathbb{R}^{n_q};$$

$$\int_V \left(\frac{\partial \mathbf{q}}{\partial t} \right) dV + \sum_{n=1}^{n_d} \int_S \left(\mathbf{f}_n + \mathbf{f}_n^v \right) \cdot \hat{\mathbf{n}}_n dS = \int_V \mathbf{s} dV; \quad (2.29)$$

$$\frac{\partial \mathbf{q}}{\partial t} + \sum_{n=1}^{n_d} \frac{\partial}{\partial x_n} \left(\mathbf{f}_n + \mathbf{f}_n^v \right) = \mathbf{s}; \quad (2.30)$$

where n_q represents the number of conserved variables, n_d is the number of dimensions, x_n represents a coordinate in an orthogonal coordinate system, \mathbf{q} is conserved variables vector, \mathbf{f}_n is the Euler flux function, \mathbf{f}_n^v is the diffusive flux function which is inversely proportional to Reynolds number (Re) and \mathbf{s} is the source vector which scales with Damköhler number (Da). Non-dimensional form of the conservation laws are shown in Appendix A.3. Equations (2.29) and (2.30) are control volume and differential forms of the conservation laws, also known as the weak and strong forms respectively. They are equivalent as $dV \rightarrow 0$ and when shock waves are not present. In other words, an algorithm solving either equation on a sufficiently refined grid and away from shock waves, is solving the same problem.

Finite difference methods aim to solve Eq. (2.30) which is a highly coupled non-linear system. Coupled meaning that a given conservation law is dependent on another. The non-linearity is mainly from the flux functions and source terms, making the system complex such that general analytical solutions are impossible. Therefore, numerical solutions are often sought. In search of a numerical solution, taking limits of the non-dimensional numbers reveals sub-problems. Beginning from Eq. (2.7) and taking limits as $Re \rightarrow \infty$ and $Da \rightarrow 0$ reveals relevant sub-problems. One dimensional (x_1) forms of these sub-problems are shown in Table 2.1. On the other hand, $Re \rightarrow 0$ and $Da \rightarrow \infty$ lead to elliptic and parabolic type problems, which are of secondary importance in the context of hypersonic flows and are not considered here.

Table 2.1 Sub-problems of the system of conservation laws in Eq. (2.30).

	$0 \ll Re \ll \infty$	$Re \rightarrow \infty$
$Da \gg 0$	Reacting viscous $\frac{\partial \mathbf{q}}{\partial t} + \frac{\partial \mathbf{f}_1}{\partial x_1} + \frac{\partial \mathbf{f}_1^v}{\partial x_1} = \mathbf{s}$	Reacting inviscid $\frac{\partial \mathbf{q}}{\partial t} + \frac{\partial \mathbf{f}_1}{\partial x_1} = \mathbf{s}$
$Da \rightarrow 0$	Frozen viscous $\frac{\partial \mathbf{q}}{\partial t} + \frac{\partial \mathbf{f}_1}{\partial x_1} + \frac{\partial \mathbf{f}_1^v}{\partial x_1} = \mathbf{0}$	Frozen inviscid $\frac{\partial \mathbf{q}}{\partial t} + \frac{\partial \mathbf{f}_1}{\partial x_1} = \mathbf{0}$

Hyperbolicity. Frozen inviscid and reacting inviscid sub-problems are systems of hyperbolic equations. Chain rule introduces the flux Jacobian (\mathbf{A}), taking the inviscid problem as an example,

$$\frac{\partial \mathbf{q}}{\partial t} + \mathbf{A} \frac{\partial \mathbf{q}}{\partial x_1} = \mathbf{0}, \quad \mathbf{A} = \frac{\partial \mathbf{f}_1}{\partial \mathbf{q}}. \quad (2.31)$$

Diagonalisation of \mathbf{A} reveals the eigenvalues $\{u, u + c, u - c\}$, where u is the velocity in x_1 direction and c is the local speed of sound. A system is hyperbolic when the flux Jacobian has eigenvalues which are all real. With thermally and chemically relaxing flows, with vibrational energy and species density conservation laws, Eq. (2.30) is indeed a hyperbolic problem, which are convected at flow bulk velocity (\mathbf{u}).

Strong and weak solutions. Solutions to inviscid problems do not remain continuous. In fact, solutions to Eq. (2.30) are called *strong solutions*. They are only valid until the solution remains smooth. This is because the flux derivatives are not well undefined in presence of discontinuities. To allow discontinuous solutions, the inviscid problem needs to be represented in a more general manner, as in Eq. (2.29)—solutions to which are called *weak solutions*. However, these weak solutions are not unique. Vanishing viscosity method can be used to highlight the physical solution, entropy satisfying solution; alternatively, entropy conditions from thermodynamics can be used to select the physical solution (LeVeque, 1992).

Effect of viscosity. Frozen viscous and reacting viscous solutions are mathematically simpler as the viscous fluxes prevent discontinuities and wave breaking. The solutions are smooth for all time, even with a discontinuous initial field.

2.2.2 Numerical methods

The most challenging part of solving a nonlinear hyperbolic system is the need to allow discontinuous solutions even when the initial fields are smooth. Hence, numerical methods are developed specifically for these types of systems, also known as shock-stable methods. Consolidated theory on these methods can be found in standard texts of [Laney \(1998\)](#); [LeVeque \(1992\)](#); [Toro \(2013\)](#). Important recent developments in low dissipation finite difference shock-capturing methods are summarised by [Ekaterinaris \(2005\)](#); [Pirozzoli \(2011\)](#). Furthermore, performance comparisons between the methods are shown by [Brehm et al. \(2015\)](#); [Johnsen et al. \(2010\)](#); [Zhao et al. \(2019, 2020\)](#). This section aims to summarise finite difference shock-capturing methods from these sources.

Properties

Important properties of numerical methods, namely conservation, consistency, stability, convergence, numerical errors and upwinding are discussed below.

- *Conservation and consistency.* Conservation is not directly enforced in finite difference methods, it demands direct attention. Conservative form of frozen Euler from Eq. (2.29) in 1D, semi-discrete form and considering a discrete one-dimensional uniform grid is,

$$\frac{d\bar{\mathbf{q}}_i}{dt} + (\mathbf{f}_{i+1/2} - \mathbf{f}_{i-1/2}) = 0, \quad \bar{\mathbf{q}}_i = \frac{1}{\Delta x_1} \int_{x_{i-1/2}}^{x_{i+1/2}} \mathbf{q}(x_1, t) dx_1. \quad (2.32)$$

The space averaged conserved vector ($\bar{\mathbf{q}}$) in higher dimensions the integral is over a surface and volume. Numerical fluxes ($\mathbf{f}_{i+1/2}, \mathbf{f}_{i+1/2}$) in higher dimensions are line and surface integrals. Equation (2.32) is still exact in semi-discrete form, no approximations have been introduced yet. Summing the expression $\forall i$ results in the cancellation of the internal fluxes and the sum reduces to only the boundary fluxes. This is called “telescoping flux property”, inspired by telescoping series in calculus where, all terms cancel except the first and the last. In higher dimensions, Eq. (2.32) is not exact as conservation errors are introduced by approximating the integrals. Nevertheless, numerical methods still strive for the telescoping flux property by ensuring interface fluxes cancel on summation. Considering a uniform Cartesian grid (G) in three

dimensions— $G = \{(x_{1,i}, x_{2,j}, x_{3,k}), i = 1, \dots, N_1, j = 1, \dots, N_2, k = 1, \dots, N_3\}$,

$$\begin{aligned} \frac{dq}{dt} \Big|_{\mathbf{x}=(x_1, x_2, x_3)} + \frac{1}{\Delta x_1} (\mathbf{f}_{1,i+1/2} - \mathbf{f}_{1,i-1/2}) + \frac{1}{\Delta x_2} (\mathbf{f}_{2,j+1/2} - \mathbf{f}_{2,j-1/2}) \\ + \frac{1}{\Delta x_3} (\mathbf{f}_{3,k+1/2} - \mathbf{f}_{3,k-1/2}) \approx 0. \end{aligned} \quad (2.33)$$

The number of grid points in each coordinate direction are N_1, N_2 and N_3 . In the limit of infinitely small discretisation, the errors tend to zero, and Eq. (2.33) becomes exact. Such a method is called *conservative*. A *consistent* numerical method is one which, has its numerical fluxes approach the true (physical) fluxes in the limit of infinitely small discretisation. Lax-Wendroff theorem (Lax, 1959) states that a numerical method converges to a weak solution, given it is consistent and conservative. See LeVeque (1992) for a mathematically rigorous statement. This property of converging to the weak solution is inherited by the conservative finite differences (Pirozzoli, 2011), as they are forced to follow the form in Eq. (2.33).

- *Stability and convergence* are important properties of a numerical method. Considering the frozen Euler problem, a necessary but not sufficient condition for stability is that the numerical domain of dependence must be inside the physical domain of dependence (Courant et al., 1967). In other words, maximum wave speed ($\text{maxeigen}(\mathbf{A})$) must be smaller or equal to numerical speed $(\Delta t / \Delta x_1)^{-1}$ of information propagation is

$$CFL = \text{maxeigen}(\mathbf{A}) \frac{\Delta t}{\Delta x_1} \leq 1. \quad (2.34)$$

LeVeque (1992) show how convergence is related to stability. For smooth solutions in linear and non-linear problems, stability is equivalent to convergence, in other words, stability is sufficient for convergence. However, for non-smooth solutions in non-linear problems, stability is equivalent to convergence given monotonicity. A monotone method is exclusively decreasing or increasing at all times, and does not even allow benign small oscillations. These are very numerically dissipative and limited to first-order accuracy, as suggested by Godunov's theorem (LeVeque, 1992). To avoid the order-of-accuracy sacrifice, total variation diminishing (TVD) methods are preferred, which have a more relaxed policy towards minor oscillations than monotone methods. A TVD scheme is defined as

$$TV(\mathbf{q}^{n+1}) \leq TV(\mathbf{q}^n), \quad TV(\mathbf{q}^n) = \sum_i (\mathbf{q}_{i+1}^n - \mathbf{q}_i^n). \quad (2.35)$$

- *Numerical errors* can be from two sources, *truncation errors* or *aliasing errors*. Aliasing errors become important for derivatives of products of non-linear functions. The Euler flux function is a highly non-linear term where the flux functions are triple products. General form of the Euler flux in one dimension is, conserved quantity ($g = \rho\phi$) multiplied by velocity (u_1), also written as $f_1 \rightarrow \rho\phi u_1 = gu_1$ and $\phi \in \{1, u_1, u_2, h_t, Y_k, e_{ve}\}$.

$$\left. \frac{df_1}{dx} \right|_{x=x_{1,i}} = \mathcal{D}_i\{f_1\} + \text{truncation error}, \quad (gu)|_{x=x_{1,i}} = \mathcal{D}_i^*\{gu\} + \text{aliasing error}. \quad (2.36)$$

Where, \mathcal{D}_i and \mathcal{D}_i^* are discrete approximation operators evaluated at $x = x_{1,i}$. Truncation errors are introduced through discrete approximation of derivatives via truncation of Taylor series, while aliasing errors are introduced by discretising non-linear terms. Aliasing errors are known to be important for modelling turbulent flows and minimising them improves stability. Errors from discretisation of non-linear derivatives are dependent on the expression's form in continuous space. Mathematically, this can be seen easily in Fourier space as shown in [Kravchenko and Moin \(1997\)](#). They show aliasing error of conservative and non-conservative forms of derivatives have opposite signs. A combination of these two forms—called the skew-symmetric form can result in *aliasing error cancellation*. The different forms of Euler flux derivative can be written as,

$$\text{Conservative: } \left. \frac{\partial gu}{\partial x} \right|_{x=x_{1,i}} = \mathcal{D}_i\{gu\} + \text{error}_1. \quad (2.37)$$

$$\text{Non-conservative: } u_{1,i} \left. \frac{\partial g}{\partial x} \right|_{x=x_{1,i}} + g_{1,i} \left. \frac{\partial u}{\partial x} \right|_{x=x_{1,i}} = u_i \mathcal{D}_i\{g\} + g_i \mathcal{D}_i\{u\} + \text{error}_2. \quad (2.38)$$

$$\begin{aligned} \text{Skew-symmetric: } \frac{1}{2} \left(\left. \frac{\partial gu}{\partial x} \right|_{x=x_{1,i}} + u_{1,i} \left. \frac{\partial g}{\partial x} \right|_{x=x_{1,i}} + g_{1,i} \left. \frac{\partial u}{\partial x} \right|_{x=x_{1,i}} \right) = \\ \frac{1}{2} \left(\mathcal{D}_i\{gu\} + u_i \mathcal{D}_i\{g\} + g_i \mathcal{D}_i\{u\} \right) + \text{error}_3. \end{aligned} \quad (2.39)$$

Although the skew-symmetric discretisation will reduce aliasing errors, the resulting discrete approximations are generally not in locally conservative form, as in Eq. (2.33) ([Coppola et al., 2019](#)).

- *Upwinding*. There are three types of stencils to calculate fluxes: downwind, upwind and central. Downwind stencils violate the *CFL* condition and are not useful. Central

stencils are preferred in smooth parts of the flow as they can be of high order of accuracy. However, they are not preferred near large gradients as they generate spurious oscillations. Upwind stencils discretise in the direction of information propagation and avoid discontinuities. This minimises spurious oscillations, but are of lower order of accuracy than central stencils. They are also the most stable class of methods. A simple example of a first order accurate upwind method is

$$\mathbf{f}_{i+1/2} = \begin{cases} \mathbf{f}_i, & \text{if } \lambda_{i+1/2} > 0 \\ \mathbf{f}_{i+1}, & \text{if } \lambda_{i+1/2} < 0 \end{cases}, \quad (2.40)$$

where $\lambda_{i+1/2}$ is the largest eigenvalue at the interface $i + 1/2$. Following [Yee et al. \(1999\)](#), let S be the set of numerical methods, then $S_{\text{monotonic}} \subset S_{\text{TVD}} \subset S_{\text{ENO}} \subset S_{\text{upwind}}$.

Euler fluxes

Methods to calculate Euler fluxes⁷ are based on properties discussed in previously. They must be shock stable, as non-linear Euler equations lead to discontinuous solutions, as seen in Section 2.2.1. The methods can be categorised by their formal order of accuracy, namely, low and high order methods. *Low order methods* have order of accuracy less than or equal to 3. They were primarily developed in the 1970s to 1980s and are primarily wave based. Wave based methods are upwinded and leverage the hyperbolicity of the system to calculate $\mathbf{f}_{i-1/2}$ and $\mathbf{f}_{i+1/2}$. There are two approaches for identifying upwind directions, Godunov/Flux difference splitting/Riemann or Flux vector/Boltzmann approach. Herein referred as Riemann approach and Flux vector splitting, respectively. For both of approaches, the interface flux to first order accuracy can be written as

$$\mathbf{f}_{i+1/2} = \mathcal{R}\{\mathbf{q}_i, \mathbf{q}_{i+1}\}. \quad (2.41)$$

The exact numerical procedure of operator \mathcal{R} is not shown here for brevity but can easily be found in Chapters 10 and 11 in [Toro \(2013\)](#). In summary:

- *Riemann approach* involves solving a Riemann problem (\mathcal{R}) between two adjacent points to calculate the interface fluxes. Solving the Riemann problem exactly requires an iterative method and is computationally expensive. To reduce the computational expense, approximate Riemann solvers are used. A popular approximate Riemann solver is ‘‘Harten-Lax-Van-Leer’’ (HLL) solver ([Einfeldt, 1988](#)), modelling only two waves from the hyperbolic system. A more accurate method is ‘‘Harten-Lax-Van-Leer-

⁷Euler fluxes in x_1 direction are simply referred to without directional subscript - \mathbf{f} .

Contact” (HLLC) (Toro et al., 1994), which includes an additional contact wave, three waves in total from the hyperbolic system. Lastly, Roe solver (Roe, 1981) is also common and is usually even more accurate than HLL and HLLC solvers.

- *Flux vector splitting* schemes were initially developed by Steger and Warming (1981) and van Leer (1982). They leverage homogeneity property of the Euler flux function,

$$\mathbf{f}(\mathbf{q}) = \frac{\partial \mathbf{f}(\mathbf{q})}{\partial \mathbf{q}} \mathbf{q} = \mathbf{A} \mathbf{q}, \quad \mathbf{A} = \frac{\partial \mathbf{f}}{\partial \mathbf{q}}. \quad (2.42)$$

Since \mathbf{A} is diagonalisable, this allows $\mathbf{f}_{i+1/2}$ to be written as sum of individual waves (splitting of flux):

$$\mathbf{f}_{i+1/2} = \mathbf{K} \mathbf{\Lambda} \mathbf{K}^{-1} \mathbf{q}_{i+1/2} = \mathbf{K} (\mathbf{\Lambda}^+ + \mathbf{\Lambda}^-) \mathbf{K}^{-1} \mathbf{q}_{i+1/2} = \mathbf{f}_{i+1/2}^+ + \mathbf{f}_{i+1/2}^-. \quad (2.43)$$

Different splitting methods lead to variation in flux vector splitting methods (Toro, 2013). Advection upstream splitting method (AUSUM) family schemes use Mach number to split the flux and are commonly used in hypersonic computations (Liou, 2006).

2nd/3rd order methods also known as high resolution, corrected or limited methods. They are not naturally monotone, so their stability is enforced via flux limiters/correctors. More details on these methods can be found in Laney (1998); Yee (1989).

High order methods are defined as greater than or equal to 3rd order accurate. They were primarily developed around the 1990s and are still an active area of research, see Eka-terinaris (2005); Pirozzoli (2011) for developmental reviews. High order methods rely on re-constructing the interface flux to a higher order of accuracy than low order methods. They can be classified into two families, weighted non-oscillatory (WENO) or artificial dissipation (AD):

- *Weighted essentially non-oscillatory (WENO)* methods were developed by Liu et al. (1994). The key idea behind these methods is a non-linear adaptive procedure to choose the locally smoothest stencil automatically. This procedure tries to avoid stencils crossing discontinuities when interpolating the interface flux. There are many variations within the WENO family, and the family can be classified further. However, in all WENO methods, the interface flux ($\mathbf{f}_{i+1/2}$) remains a linear combination of fluxes from stencils. Here, only the two methods from the family are briefly discussed.

WENO-JS is one of the earliest methods developed by [Jiang and Shu \(1996\)](#):

$$\mathbf{f}_{1,i+1/2} = \sum_{s \in \mathbb{S}} w_s \mathbf{f}_{1,i+1/2}^s, \quad w_s = \frac{\alpha_s}{\sum_s \alpha_s}, \quad \alpha_s = \frac{d_s}{(\beta_s + \varepsilon)^B}; \quad (2.44)$$

where \mathbb{S} is the set of candidate stencils, illustrated graphically in Fig. 2.5, the set is larger for increasing the order of accuracy of the scheme. The interface flux ($\mathbf{f}_{1,i+1/2}$) can be calculated with wave-based methods in Eq. (2.41) which gives improved performance ([Wong and Lele, 2019](#)). Alternatively, the flux can be calculated as just a simple product of variables and is preferred in the current work. Moreover, d_s are optimal weights of the stencils, which are modified by local smoothness indicator β_s to give stencil coefficient (α_s). The weights are also controlled by parameters B , often more than 2, and ε is a small number to avoid a zero denominator. Also, w_s is the stencil weight and is generally the most expensive part of the numerical scheme because of the large number of floating-point operations required to evaluate β_s . It is well known that reconstruction in characteristic variables gives improved performance, as the post-shock oscillations are reduced ([Brehm et al., 2015](#)). WENO-JS is known to be excessively dissipative in smooth parts of the flow. To solve this issue, a notable development, amongst others, is weighted essentially non-oscillatory central-upwind (WENO-CU) ([Borges et al., 2008](#)). It uses an improved weighting strategy and an additional candidate stencil which ensures the method reverts to a central scheme in smooth parts. This makes them more suitable for direct numerical simulation of interactions between turbulent flows and shock waves because of low numerical dissipation and good shock-capturing properties. WENO-CU methods are not mathematically described here as they are not used in the present work.

Targeted essentially non-oscillatory (TENØ) methods ([Fu et al., 2017](#)) are designed to reduce numerical dissipation further than WENO-CU. This method is different in three ways: first, candidate stencils are different as shown in Fig. 2.5; second, complete removal of candidate stencils if not smooth enough; and third, modified stencil weights to further reduce dissipation. These differences in mathematical form are:

$$w_s = \frac{\delta_s \alpha_s}{\sum_{s \in \mathbb{S}} \delta_s \alpha_s}; \quad \delta_s = \begin{cases} 0, & \text{if } \chi_s < C, \\ 1, & \text{otherwise} \end{cases} \quad ; \quad \chi_s = \frac{\gamma_s}{\sum_{s \in \mathbb{S}} \gamma_s}; \quad \gamma_s = \left(A + \frac{d_s}{\beta_s + \varepsilon} \right)^B \quad (2.45)$$

where β_s is the same as WENO formulation, ξ_s is the stencil mesh smoothness parameter of different form when compared to α_s from WENO-JS. Moreover, δ_s is

stencil cut-off binary indicator, dependent on a constant cut-off value C . The method is parameterised by two constants, commonly $A = 1$, $B = 6$ and $C = 10^{-7} - 10^{-5}$. TENO methods in the form above cost around 10-15 % more than WENO-JS (Fu et al., 2018). Many variations exist within TENO family exist, they are not surveyed here. A notable variation is the adaptive TENO (TENO-A) in which C is no longer a constant but a function of the shock sensor. This adjusts the cut-off parameter such that shocks are captured more robustly and the smooth parts of the flow are dissipated less, however, this adds computational cost.

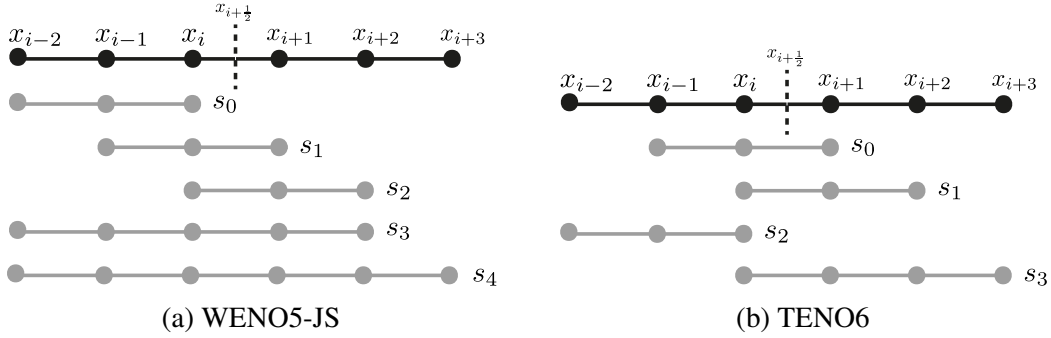


Fig. 2.5 WENO family methods' stencils.

- Artificial dissipation (AD) methods, unlike WENO methods, aim to manage large gradients in stencils by modifying local fluxes. These methods are distinguished by how they add the local dissipation flux and can be classified as artificial viscosity (AV) or artificial flux (AF) methods.

Artificial viscosity (AV) method (Cook and Cabot, 2004, 2005) adds dissipation flux via artificial transport properties. The transport properties adjust depending on the local gradients in the solution and can be made to dampen high frequency noise around Nyquist wave numbers (twice the wave number based on mesh size). For example, artificial viscous stress tensor can be written as

$$\boldsymbol{\tau}^* = \mu^* (\nabla \mathbf{u} + (\nabla \mathbf{u})^T) + (\beta^* - 2/3 \mu^*) (\nabla \cdot \mathbf{u}) \mathbf{I}, \quad (2.46)$$

where $\boldsymbol{\tau}^*$ is the artificial stress tensor controlled by the artificial shear viscosity μ^* and bulk viscosity β^* . These parameters are proportional to local gradients and mesh size and are not mathematically described here for brevity but can be found in Kawai et al. (2010). The same idea applies to thermal conductivity and mass diffusivity.

Artificial flux (AF) methods add a dissipation flux directly instead of adding a flux via artificial transport properties. These methods are also known as non-linear filtering methods (Yee et al., 1999). Considering a scalar conservation equation form for simplicity:

$$f_{i+1/2} = f_{i+1/2}^c + f_{i+1/2}^d; \quad (2.47)$$

where $f_{i+1/2}^d$ is the dissipative, also called shock-capturing flux and $f_{i+1/2}^c$ is a low dissipation flux, usually from central schemes. The dissipative flux has various forms, discussing and comparing all in detail is beyond the scope of the current work. Yee and Sjögreen (2018) summarise and compare various non-linear filtering methods.

Another category of methods is known as hybrid methods (Lusher, 2020; Zhao et al., 2020). These methods combine shock-stable ($f_{i+1/2}^{su}$) methods from AD or WENO family with shock-unstable ($f_{i+1/2}^{ss}$) methods like standard central-difference. These flux contributions from the two different methods are weighted by a shock sensor ($\psi_{i+1/2}$):

$$f_{i+1/2} = (1 - \psi_{i+1/2})f_{i+1/2}^{su} + \psi_{i+1/2}f_{i+1/2}^{ss}; \quad (2.48)$$

where the shock sensor tends towards 1 near shocks and 0 in smooth parts. These methods are highly sensitive to shock sensors and are not reviewed in detail here as they are not used in the current study.

Diffusive fluxes

Generally, the computation of diffusive fluxes is trivial compared to Euler fluxes. Often standard finite differences are used to compute the divergence of the diffusive fluxes in conservative form. Alternatively, the divergence of diffusive terms can be fully expanded in terms of the primitive field variables and then discretised. This form has improved accuracy and robustness (Pirozzoli, 2011).

Temporal discretisation and source term

Time discretisation. After an appropriate spacial discretisation (\mathcal{D}_i) the original problem from Eq. (2.30) is a semi-discrete ordinary differential equation,

$$\frac{d\mathbf{q}_i}{dt} = \mathcal{D}_i\{\mathbf{q}\}. \quad (2.49)$$

With high-order space discretisation, strong-stability preserving (SSP) time discretisation methods are preferred (Shu, 1988; Shu and Osher, 1988). They are total variation diminishing (TVD) with time. Explicit, less than third-order TVD Runge-Kutta (RK) scheme can be written in Shu-Osher form as:

$$\mathbf{q}_i^{(j)} = \sum_{k=0}^{n-1} \alpha_{jk} \mathbf{q}^{(k)} + \beta_{jk} \Delta t \mathcal{D}_i[\mathbf{q}^{(k)}] \quad , j = 1, \dots, n; \quad n \leq 3. \quad (2.50)$$

Where the j^{th} sub-step is a weighted linear combination of operator \mathcal{D}_i on previous $\{0, \dots, j-1\}$ solution field. Sub-steps and operator \mathcal{L} with the coefficients α_{jk} and β_{jk} . A general RK method is only TVD if the *CFL* condition is satisfied.

Source term. RK methods are usually stable and accurate for moderately stiff problems. Stiff problems occur with large Damköhler numbers, where explicit RK is not stable —unless very small time-steps are used. To avoid this, a common approach for stiff terms is called Operator splitting/Fractional stepping and when applied to derivatives in spacial directions it is also called directional splitting (LeVeque et al., 2002). Splitting schemes integrate partial differential equation terms separately. Considering the differential conservation law in Eq. (2.30):

$$\frac{\partial \mathbf{q}}{\partial t} + \sum_{n=1}^{n_d} \frac{\partial \mathbf{f}(\mathbf{q})_n}{\partial x} = 0, \quad \mathbf{q}^{t_0+\Delta t} = \mathcal{S}^{\Delta t} \{\mathbf{q}^{t_0}\}; \quad (2.51)$$

and

$$\frac{\partial \mathbf{q}}{\partial t} = \mathbf{s}(\mathbf{q}), \quad \mathbf{q}^{t_0+\Delta t} = \mathcal{F}^{\Delta t} \{\mathbf{q}^{t_0}\}. \quad (2.52)$$

Denoting the discrete solution operators of as $\mathcal{S}^{\Delta t}$ and $\mathcal{F}^{\Delta t}$ over time Δt of the two partial differential equations respectively. The two simplest splitting approaches are:

$$\text{Godunov splitting, } \mathbf{q}^{t_0+\Delta t} = \mathcal{S}^{\Delta t} \{\mathcal{F}^{\Delta t} \{\mathbf{q}^{t_0}\}\} = \mathcal{F}^{\Delta t} \{\mathcal{S}^{\Delta t} \{\mathbf{q}^{t_0}\}\} \quad (2.53)$$

$$\text{Strang splitting, } \mathbf{q}^{t_0+\Delta t} = \mathcal{S}^{\Delta t/2} \{\mathcal{F}^{\Delta t} \{\mathcal{S}^{\Delta t/2} \{\mathbf{q}^{t_0}\}\}\} \quad (2.54)$$

Godunov splitting is a first-order accurate method, whereas Strang is second-order accurate. From a practical perspective, the coefficient of error from Δt in the Godunov splitting term may be much smaller than the coefficient of $(\Delta t)^2$ term (LeVeque et al., 2002). Hence, both methods can be considered of similar accuracy. Godunov splitting has a simple physical meaning; it suggests the decoupling of chemical reactions to flow over Δt . Since the physical processes are decoupled, the operators are commutative.

If the source term is solved separately, it can be solved implicitly, whilst the hyperbolic part of the partial differential equation is solved explicitly. This further adds stability with a stiff source term. Current work solves Eq. (2.52) implicitly, with an iterative procedure.

Implementation

In this work, diffusive fluxes are discretised with second-order accurate standard central finite differences. A third-order accurate TVD-RK and first-order accurate implicit source term Godunov splitting are implemented. High-order Euler flux calculation method is selected based on the following:

- *Comparison of AV (artificial viscosity) with WENO.* AV methods dissipate high-frequency solutions less than WENO methods and were originally designed with shock-turbulence interactions application. The added bulk viscosity is important in capturing shocks without affecting the vorticity field, unlike AF methods, which pollute the vorticity field. However, AV methods can be more expensive than WENO schemes for inviscid computations and less expensive than WENO for viscous computations. They are less robust than WENO schemes with strong discontinuities (Brehm et al., 2015). AV methods also require a Gaussian filter for long-time stability with a higher-order accuracy than the numerical scheme itself, and their stencils are larger than WENO. These large stencils can be particularly inefficient for structured adaptive meshing, described further in Section 2.2.3. Hence, they are not favoured in the current work.
- *Comparison of AF (artificial flux) with WENO.* AF methods pollute the vorticity field more than WENO methods; therefore, they are generally not preferred for shock-turbulence interactions. However, without strong shock-turbulence interactions, they can be attractive (Sciacovelli et al., 2021) as central schemes are generally computationally cheaper than WENO and AV methods.

However, it is difficult to conclude the "best" numerical method family, so representative methods from both families are implemented.

Implementations from WENO family include WENO-JS (WENO5), a fifth-order accurate method. Also, TENO (TENO6), a sixth-order accurate method. The re-construction of interface flux is with global Lax-Friedrichs flux splitting, and in characteristic variables, as outlined by Lusher (2020); Shu (1997). The variable change Jacobians with chemical species are given in Di Renzo et al. (2020); Grossman and Cinnella (1990) and are not repeated here.

From the AF family. A central skew-symmetric (CS) split with Jameson-Schmidt-Turkel (JST) (Jameson, 2017) artificial dissipation is implemented. This method was first introduced by (Ducros et al., 2000). The splitting of convective derivative in skew-symmetric conservative form reduces aliasing errors as explained in Section 2.2.2. CS methods have been shown to have improved stability and kinetic energy preservation in the inviscid limit (Coppola et al., 2019), when compared to simple unsplit central differences. Though, recently, central unsplit schemes with artificial dissipative fluxes have also been shown to be robust with hypersonic turbulent and thermochemically reacting flows (Sciacovelli et al., 2021). CS fluxes in compact notation of Pirozzoli (2010):

$$f_{i+1/2}^c = \sum_{l=1}^{p/2} a_l \sum_{m=0}^{l-1} F_{i-m,l}; \quad F_{i-m,l} = 1/4(q_{i-m} + q_{i-m+l})(u_{i-m}u_{i-m+l}); \quad (2.55)$$

where a_l are standard central difference coefficients. In current work $p \in \{2, 3\}$, corresponding to 4th and 6th order schemes are implemented. The dissipation flux is a combination of second-order dissipative flux activated only near shocks and a fourth-order dissipation which filters high-frequency oscillations:

$$\begin{aligned} f_{i+1/2}^d &= -\varepsilon_{i+1/2}^{(2)} |\lambda_{i+1/2}| \Delta q_{i+1/2} - \varepsilon_{i+1/2}^{(4)} |\lambda_{i+1/2}| (\Delta q_{i+3/2} - 2\Delta q_{i+1/2} + \Delta q_{i-1/2}); \\ \varepsilon_{i+1/2}^{(2)} &= \max(0, C_2 \psi_{i+1/2}), \quad \varepsilon_{i+1/2}^{(4)} = \max(0, C_4 |\lambda_{i+1/2}| - \varepsilon_{i+1/2}^{(2)}); \\ \Delta q_{i+1/2} &= (q_{i+1} - q_i); \end{aligned} \quad (2.56)$$

where $|\lambda_{i+1/2}|$ is the characteristic speed and spectral radius of the Jacobian matrix for multi-wave systems. The dissipative coefficients $\varepsilon_{i+1/2}^{(2)}$ and $\varepsilon_{i+1/2}^{(4)}$ are controlled by a pressure sensor ($\psi_{i+1/2}$):

$$\begin{aligned} \psi_{i+1/2} &= \max(\psi_i, \psi_{i+1}), \quad \psi_i = \frac{|p_{i+1} - 2p_i + p_{i-1}|}{(1 - \omega)\mathcal{P}_{TVD} + \omega\mathcal{P}_{JST} + \varepsilon}; \\ \mathcal{P}_{TVD} &= |p_{i+1} - p_i| + |p_i - p_{i-1}|, \quad \mathcal{P}_{JST} = p_{i+1} + 2p_i + p_{i-1}. \end{aligned} \quad (2.57)$$

The sensor at the interface is the maximum of the pressure sensors evaluated at points i and $i + 1$. Typical constants are $C_2 \approx 0.5 - 1.5$, $C_4 \approx 0.016 - 0.032$, $\omega \approx 0.0 - 1.0$ (Lodato, 2008). Moreover, the sensor can be on multiple field variables, such as pressure and mass fraction. In such cases, an averaged sensor ($\bar{\psi}$) is substituted for ψ in Eq. (2.56):

$$\bar{\psi}_{i+1/2} = \sum_k \psi_{i+1/2,k}^2 / \sum_k \psi_{i+1/2,k}, \quad k \in \{p, \rho, Y_1, \dots, Y_n\}. \quad (2.58)$$

2.2.3 Structured adaptive mesh refinement (SAMR)

Structured adaptive mesh refinement (SAMR) algorithms are more complex than structured non-adaptive algorithms, especially for parallel computations. Consequently, SAMR algorithms are often found as AMR frameworks created with significant software developmental efforts. Commonly available frameworks are reviewed by [Dubey et al. \(2014, 2021\)](#). SAMR methods can be patch-based or tree-based, as illustrated in Fig. 2.6. In patch-based SAMR, individual meshes are organised in an overlapping hierarchy. Whereas tree-based SAMR, the meshes are organised in a tree-like structure with parent-child relationships without any overlapping meshes. Examples of patch-based SAMR frameworks include BoxLib ([Zhang et al., 2016](#)), AMREX ([Zhang et al., 2021](#)), SAMRAI ([Zhang et al., 2021](#)), waLBerla ([Bauer et al., 2021](#)), AMRClaw ([Mandli et al., 2016](#)), AMROC ([Deiterding, 2003](#)). Examples of tree-based SAMR frameworks include P4est ([Burstedde et al., 2011](#)), Forestclaw ([Calhoun and Burstedde, 2017](#)), Paramesh ([MacNeice et al., 2000](#)), ENZO-P ([Bordner and Norman, 2018](#)), Deandro ([Fernando et al., 2018](#)), Afivo ([Teunissen and Ebert, 2018](#)). These frameworks are highly scalable up to $O(10^5)$ cores with 70-90% weak scaling efficiencies. Historically these frameworks have been designed to operate on central processing units (CPUs) only. The latest developments involve hybrid CPU-GPU⁸ architectures, which have shown up to 4× speed-ups ([Zhang et al., 2021](#)).

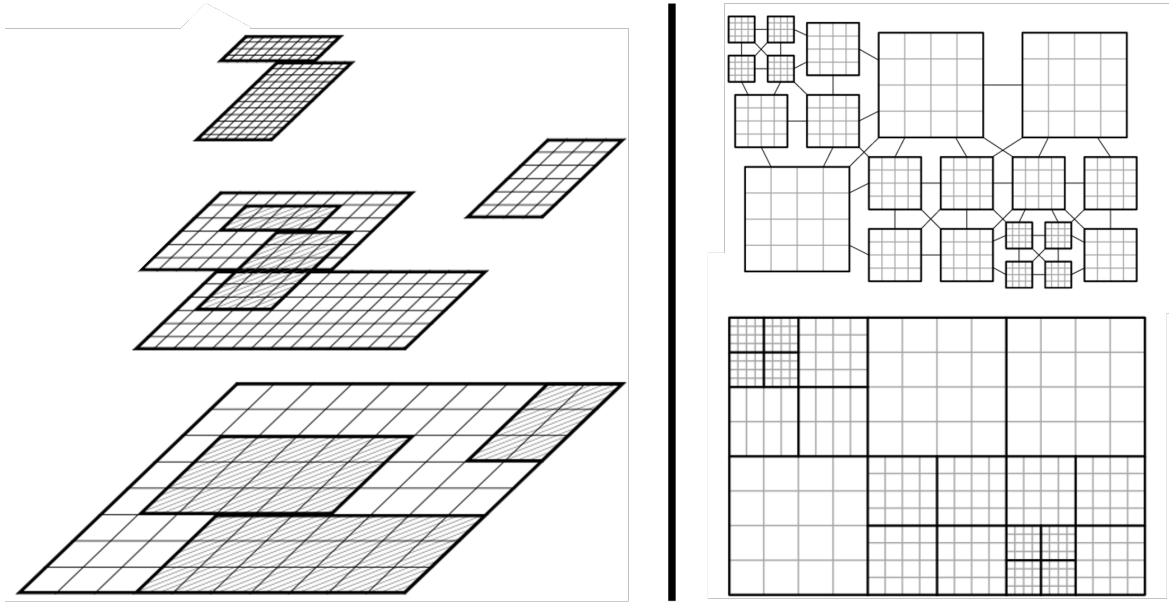


Fig. 2.6 Two-dimensional SAMR meshes. Left: patch-based, adapted from [Deiterding \(2003\)](#). Right: tree-based, adapted from [Bauer et al. \(2021\)](#).

⁸Graphics processing units (GPUs).

Both tree-based AMR and patch-based AMR methods have advantages and disadvantages (Deiterding, 2011). Tree-based AMR methods generally produce more efficient grids with fewer number computational of points. However, without complicated re-numbering and re-arrangement of the vector of cells based on the mesh topology, memory access during computation is highly irregular and as a result the performance on vector computers can be poor. On the other hand, patch-based AMR methods can leverage vectorisation speed-ups as information structure of patches can be directly translated to information storage in memory. This enables efficient data access for stencil operations, as neighbouring elements in computational (and real) space are also neighbours in memory. Moreover, the connectivity of mesh points does not need to be explicitly stored or computed unlike tree-based AMR methods. Additionally, refinement in time to maintain constant CFL number at different mesh resolutions is not possible with tree-based AMR, whereas this (also known as local time-stepping or sub-cycling) remains common practice with patch-based AMR. This further negates any computational benefits from reduced number of computational points with tree-based AMR, as the existing computational points need to be advanced more times.

Though, newer approaches (Bauer et al., 2021; Burstedde et al., 2011) have addressed the vectorisation issues with tree-based methods by essentially hybridising the two approaches. These methods are at cost of added complexity in algorithms, and their benefits compared to modern patch-based AMR methods are not clear as no direct comparisons are available in the literature. In summary, generally, patch-based AMR methods are simpler and computationally more efficient despite their suboptimal meshing when compared to tree-based methods. Therefore, patch-based AMR is preferred in this work. Current work uses patch-based SAMR via the BoxLib framework (Zhang et al., 2016). BoxLib has been used in various fields, including astrophysics, turbulent combustion, etc. It contains all the functionality to write a massively parallel AMR solver in two or three dimensions. Key concepts of patch-based SAMR approach and high level algorithms are discussed next.

Patches and boundary conditions

Patches. A cell-centred approach is chosen, and the whole computational mesh is composed of overlapping nested rectangle (2D) or cuboid (3D) meshes at different resolutions:

$$G = \bigcup_l G_l; \quad l = 0, \dots, L; \quad G_l = \bigcup_k G_{l,k}; \quad G_l \subseteq G_{l-1}. \quad (2.59)$$

The whole mesh (G) is a union of mesh patches at different levels of refinement. The mesh at a given level of refinement G_l is a union of multiple patches. Each mesh patch ($G_{l,k}$) can be referred to by its level (l) and its index at a given level (k). All meshes on a given level are properly nested, meaning that G_{l+1} is fully contained within meshes at level G_l . In parallel computations each core computes a subset of G , and the patches, $G_{l,k}$, are distributed and computed by a single processor. Mesh distribution amongst the processors is determined by load balancing algorithms, which are based on space-filling curves ([Luitjens et al., 2007](#)). For a given mesh, in two-dimensions, the mapping between real space (x, y) and computational space (i, j) is as follows

$$C_l = [0, rN_x] \times [0, rN_y]; \quad (x, y) = ((i + 1/2)\Delta x_l, (j + 1/2)\Delta x_l); \quad (i, j) \in C_l; \quad (2.60)$$

where C^l are all the possible coordinates in the computational mesh on level l , N_x and N_y are the number of points in two dimensions on level l , and r is the refinement ratio. Although $r = 2$ for all levels in current work, $r = 4$ is also possible with BoxLib. The mesh size Δx_l is the same in all directions, strictly Cartesian.

Boundary conditions. Patch boundaries are defined as: physical, coarse-fine or same level. Physical patch boundaries are also computational domain boundaries. Coarse-fine boundaries are between two levels of refinement. Same level boundaries are between two patches at the same level. All patches have halo points which are used to enforce boundary conditions. In parallel computations, halo point states must be communicated from other cores. Furthermore, with coarse-fine boundaries, halo points on the fine mesh are interpolated from the coarse mesh. BoxLib allows second-order and fourth-order accurate interpolations. Alternative and more detailed descriptions of AMR boundary conditions and implementation can be found in [Deiterding \(2003\)](#).

Time-stepping and conservation

Refinement in space with SAMR can be followed with refinement in time, where different refinement levels are advanced with different time steps. This strategy is called local time-stepping (LTS) and is required to maintain $CFL \leq 1$ in higher levels with decreasing mesh size. Alternatively, all meshes can be advanced at the same time step. This strategy is called global time-stepping (GTS). Intuitively, LTS is more computationally efficient than GTS as meshes are advanced with larger time steps. More formally, the advantage of LTS over GTS is demonstrated as follows. Consider a grid G with the workload on each level as α_l and the work fraction of each level β_l , the time-stepping work ratio between LTS (W_{LTS}) and GTS (W_{GTS}):

$$W_{LTS} = \sum_{l=0}^L r^l \alpha_l; \quad W_{GTS} = r^L \sum_{l=0}^L \alpha_l; \quad \frac{W_{LTS}}{W_{GTS}} = \sum_{l=0}^L r^{l-L} \beta_l; \quad \beta_l = \alpha_l / \sum_{l=0}^L \alpha_l. \quad (2.61)$$

Since $\beta_l \geq 0$, $W_{LTS} \leq W_{GTS}$, LTS is always computationally cheaper than GTS. Also, higher levels contribute more to the work load and adding a level of refinement becomes increasingly expensive with increasing number of levels. The work increases exponentially with the number of refinement levels. Furthermore, time stepping efficiency can be improved with an automatic LTS (Domingues et al., 2009; Kaiser et al., 2019), where Δt_l varies each computational step, and its size is chosen dynamically in runtime.

Figure 2.7 shows the LTS time-stepping strategy with three levels of refinement and two sub-steps. The numbers indicate the order of computation for patches on a given level. In between sub-steps, halo points are updated. Current work uses linear interpolation in time.

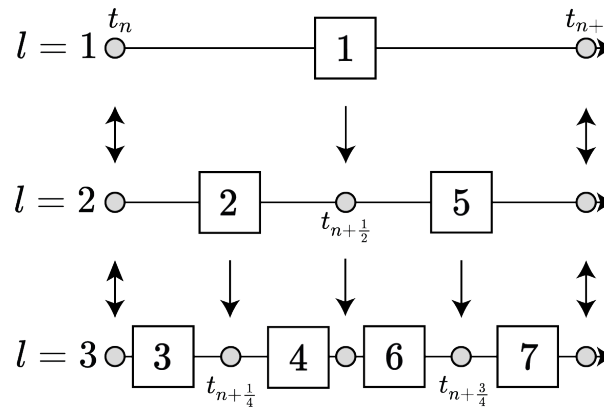


Fig. 2.7 Local time stepping with two sub-steps. Single arrows indicate prolongation procedures, whereas double arrows indicate restriction and prolongation procedures.

Conservation. To ensure solution consistency and minimise conservation errors in a hierarchical grid, a couple of extra procedures are required when compared to uniform meshes. Detailed mathematical descriptions of these procedures are given in most AMR literature, for example, [Berger et al. \(1989\)](#); [Deiterding \(2003\)](#). However, they are briefly described here:

- *Coarse to fine interface flux correction*, which corrects the coarse grid flux at coarse-fine interfaces to match the fine grid fluxes. This is particularly important when there are large gradients, like shock waves, across coarse-fine interfaces.
- *Restriction* procedure replaces the coarse grid solution with a fine grid solution where grids overlap. In current work, it is simply an average of 4 (2D) or 8 (3D) of the closest fine points to a given coarse point.

Both of these procedures assume that the fine mesh solution is more accurate than the coarse mesh solution. Note that coarse-fine interface correction is not used in current work, as the procedure contained a coding error in BoxLib. However, this is not likely to be significant as, the intersection of large gradients and the coarse-fine interfaces can be avoided by refining around the large gradients frequently enough.

Mesh refinement

Mesh refinement is composed of three main sub-steps:

- *Tagging*, which involves marking each computational point for refinement. The heuristics for this can be classified into physics-based or error-based methods. This work uses physics-based tagging criteria based on shock sensor in Eq. (2.57), distance to boundary, field variables and their gradients.
- *Clustering*, which uses the tagged field, to decide areas where refinement patches are to be added. Berger-Rigoutsos ([Berger and Rigoutsos, 1991](#)) algorithm is a common clustering algorithm used by many AMR frameworks. This algorithm can be run locally or globally, with global clustering scaling poorly ([Luitjens and Berzins, 2011](#)).
- *Generating the refined mesh* involves a prolongation (interpolation) operation on the newly created patches and evenly distributing the mesh to processors in parallel computations. All AMR frameworks use space-filling curves to distribute patches across processors. These curves are locality preserving mappings, $\mathbb{N}^n \rightarrow \mathbb{N}^1, n \in \mathbb{N}$. In particular, BoxLib uses the Morton space-filling curve.

Alternative and more detailed descriptions of these steps can be found in [Deiterding \(2003\)](#).

The hierarchical AMR mesh in BoxLib is controlled by five parameters (Bell et al., 2014): the maximum patch size in any direction is controlled by `max_grid_size`; the radius (in computational space) of additional tagged points around those already tagged by the tagging criteria is controlled by `amr_buf_width`; the minimum patch size in any direction is controlled by `cluster_minwidth`; `cluster_blocking_factor` is the integer multiple of cells in all directions; lastly, `cluster_min_eff` which is a number between 0 and 1 that controls how tightly the newly created grids match the tagged cells. The default parameter values used in the current work are:

```
max_grid_size = 32; amr_buf_width = 2; cluster_minwidth = 8;  
cluster_blocking_factor = 2; cluster_min_eff = 0.7.
```

Note, the regrid frequency is not included here, as it is deemed to be a case specific parameter and is irrelevant for statically refined meshes. When different values to above are used, these will be stated explicitly.

Algorithms

The SAMR BoxLib framework adopted in the current work can be described by high-level Algorithms 1, 2 and 3. Algorithm 1 shows the main algorithm with the inputs, number computational steps (n_f) and the number of refinement levels (L). Initialisation and grid refinement procedures is also not described as they are taken directly from BoxLib. Algorithm 2 with `ADVANCEGTS(G)` procedure shows the global time-stepping approach, where all levels are advanced with same time-step. Algorithm 3 shows the recursive `ADVANCELTS(G)` procedure, which advances solution with smaller time-steps on finer meshes.

Algorithm 1

```

1: procedure MAIN( $n_f, L$ )
2:   initialise AMR grid with  $L$  levels  $\rightarrow G$ 
3:    $n=1$ 
4:   while  $n < n_f$  do
5:     if LTS then
6:        $l = 0; i_s = 1$ 
7:       call ADVANCELTS( $G, l, i_s$ )
8:     else
9:       call ADVANCEGTS( $G$ )
10:    end if
11:    if time to refine then
12:      call function to adapt grid
13:    end if
14:     $n = n + 1$ 
15:  end while
16: end procedure

```

Algorithm 2

```

1: procedure ADVANCEGTS( $G$ )
2:   for  $i = 1, n_{rk}$  do
3:     set halo points on  $G$ 
4:     for  $l = 1, L$  do
5:       advance solution
6:       ( $G^l$ )
7:       restriction  $G^l$  to
8:        $G^{l-1}$ 
9:       coarse-fine flux
10:      correction
11:    end for
12:  end for
13: end procedure

```

Algorithm 3

```

1: procedure ADVANCELTS( $G, l, i_s$ )
2:   set halo points on  $G^l$  at
3:   sub-step  $i_s$ 
4:   advance solution ( $G^l$ )
5:   if  $l < L$  then
6:     for  $i = 1, r$  do
7:       call ADVANCELTS( $G, l+1, i$ )
8:     end for
9:     restriction  $G^l$  to  $G^{l-1}$ 
10:    coarse-fine flux correction
11:  end if
12: end procedure

```

2.3 Numerical validations

Physical models from Section 2.1 and numerical methods implemented from Section 2.2 are compared, validated and tested. For this section, the shock-capturing parameters are selected based on previous works: CS6-JST from Lodato (2008), $C_2 = 1.5$ and $C_4 = 0.016$; WENO5 from Jiang and Shu (1996), $B = 2.0$; TENO6 from Fu et al. (2017), $A = 1.0$, $B = 6.0$ and $C = 10^{-7}$.

2.3.1 Weak Riemann problem

Weak Riemann problem, also known as Sod's test (Toro, 2013) involves a left running rarefaction wave, contact wave and right running weak shock wave. The aim of this case is to validate the Euler flux methods' implementations and the time-stepping approaches in the AMR framework.

The base mesh has 100 points in the x direction, with CFL around 1. The initial conditions are

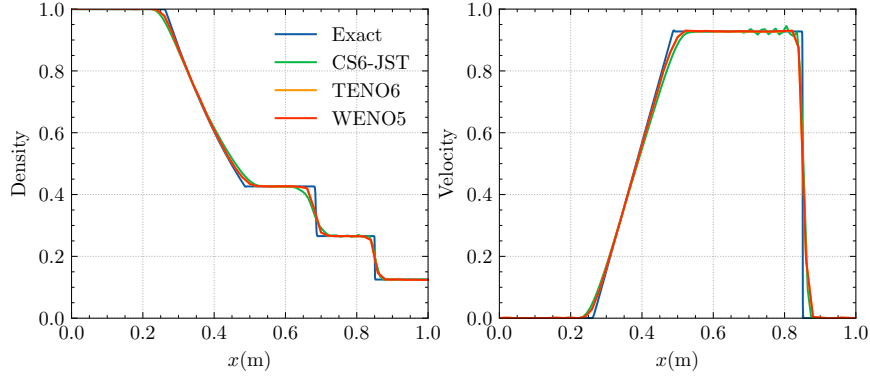
$$(\rho, u, p) = \begin{cases} (1, 0, 1), & \text{if } 0 < x < 0.5 \\ (0.1, 0.0, 0.125), & \text{if } 0.5 \leq x \leq 1 \end{cases}.$$

Comparison of numerical methods without AMR. Figure 2.8a shows CS6-JST produces high-frequency oscillations in the post-shock region, unlike WENO5 and TENO6 which produce a non-oscillatory solution. This is expected as CS6-JST is only TVD near shocks, whereas WENO5 and TENO6 are designed to be essentially non-oscillatory. Moreover, the differences between TENO6 and WENO5 are visually indistinguishable. And overall, CS6-JST is less accurate than the WENO methods.

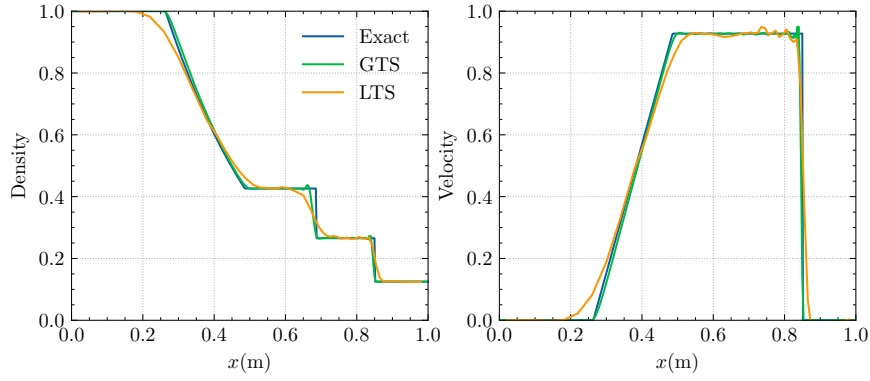
Validation of CS6-JST with AMR. Mesh refinement is around shock only and occurs every 10 time-steps, where JST shock sensor from Eq. (2.57) is used for refinement criteria. Figure 2.9 shows the moving mesh with the shock front. Figure 2.8b shows that GTS is more accurate than LTS. This is expected as LTS introduces halo point interpolations for patches on levels 1-2.

Strong Riemann problems. For example, Test 3 from Toro (2013), is found to be unstable with all current implemented high order Euler flux methods (CS6-JST, WENO5 and TENO6). With test initial conditions, the case generates a shock wave travelling at $M \approx 60$. Systematically reducing the initial pressure ratio between left and right states, the methods are found to be stable around $M \approx 30$. From the literature however, TENO6 is known to be stable

with a flux limiter up to $M = 2000$ (Fu, 2019). It is also likely that an artificial dissipation flux limiter for the CS6-JST method can add stability around strong shock waves. However, these potential modifications are not explored in the current study.



(a) Comparison of WENO5, TENO6 and CS6-JST methods without AMR.



(b) Comparison of GTS and LTS with 2 levels of AMR, with CS6-JST.

Fig. 2.8 Weak Riemann problem comparisons with WENO5, TENO6 and CS6-JST Euler flux computation methods; and AMR GTS and LTS time-stepping strategies.

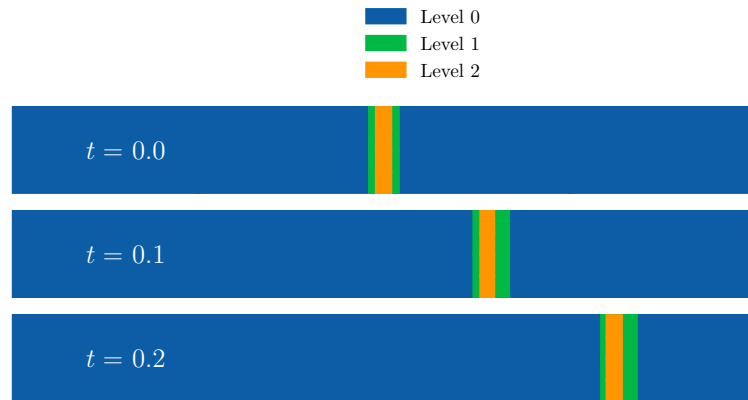


Fig. 2.9 Weak Riemann problem with 2 levels of AMR around the shock wave.

2.3.2 High temperature Riemann problem

A Riemann problem where the left state is high pressure and temperature, and the right state is low pressure and temperature. This results in a thermochemical non-equilibrium fluid in the rarefaction and post-shock regions. The aim of this case is to validate the chemical non-equilibrium modelling (CNE) and verify the thermal non-equilibrium (TNE) and thermochemical non-equilibrium (TCNE) implementations.

The fluid is five species air and is initially in local thermodynamic equilibrium. The initial conditions are,

$$(u, P, T) = \begin{cases} (0, 9525, 300), & \text{if } x \leq 0.5 \\ (0, 19526, 9000), & \text{otherwise} \end{cases};$$

$$(X_{N_2}, X_{O_2}, X_{NO}, X_N, X_O) = \begin{cases} (0.02, 0, 0, 0.77, 0.21), & \text{if } x \leq 0.5 \\ (0.79, 0.21, 0, 0, 0), & \text{otherwise} \end{cases}.$$

The simulation time is $90 \mu\text{s}$ and the time-step is $0.3 \mu\text{s}$ and the CFL is around 0.6. The domain length (L) is 1 m with 600 grid points in the x direction. The shock propagates to $x = 0.61$ during the simulation time. The reference solution is the equilibrium solution from the computational study by [Grossman and Cinnella \(1990\)](#).

Comparison of numerical methods. The thermodynamic reference state (subscript r) is the right initial state, and the reference velocity is the right state's initial frozen speed of sound. CS-JST6 was found to be unstable without an artificial dissipation sensor on the mass fraction field and pressure field, and Equation (2.58) was used to compute the average sensor. Figure 2.10 shows CS6-JST performs poorly when compared to TENO6, the artificial dissipation sensor is likely have caused these large errors. A different dissipation sensor for each conservation law may improve performance, but this potential solution is not explored in the current study.

Verification of thermochemical model implementation. Figures 2.11a and 2.11b shows that rarefaction and shock waves induce regions of non-equilibrium, where TNE, CNE and TCNE models have small discrepancies. In TCNE, the source term and thermodynamic properties calculations dominate the computational cost, 50% (5 species) and 75% (11 species) of the total run time. On the other hand, the computation of the Euler fluxes takes around 5-10 % of the total run time. Therefore, thermochemistry is the bottleneck for computational speed with thermochemical non-equilibrium.

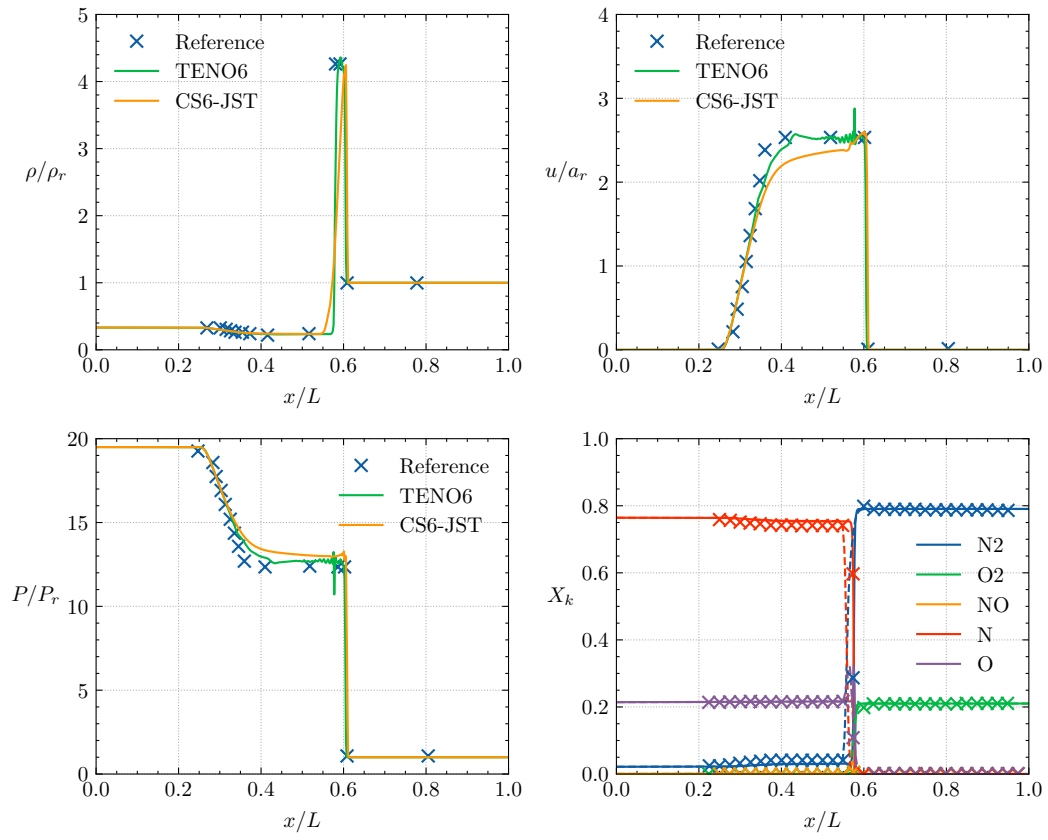


Fig. 2.10 CS6-JST and TENO6 comparison with high temperature Riemann problem with chemical reactions.

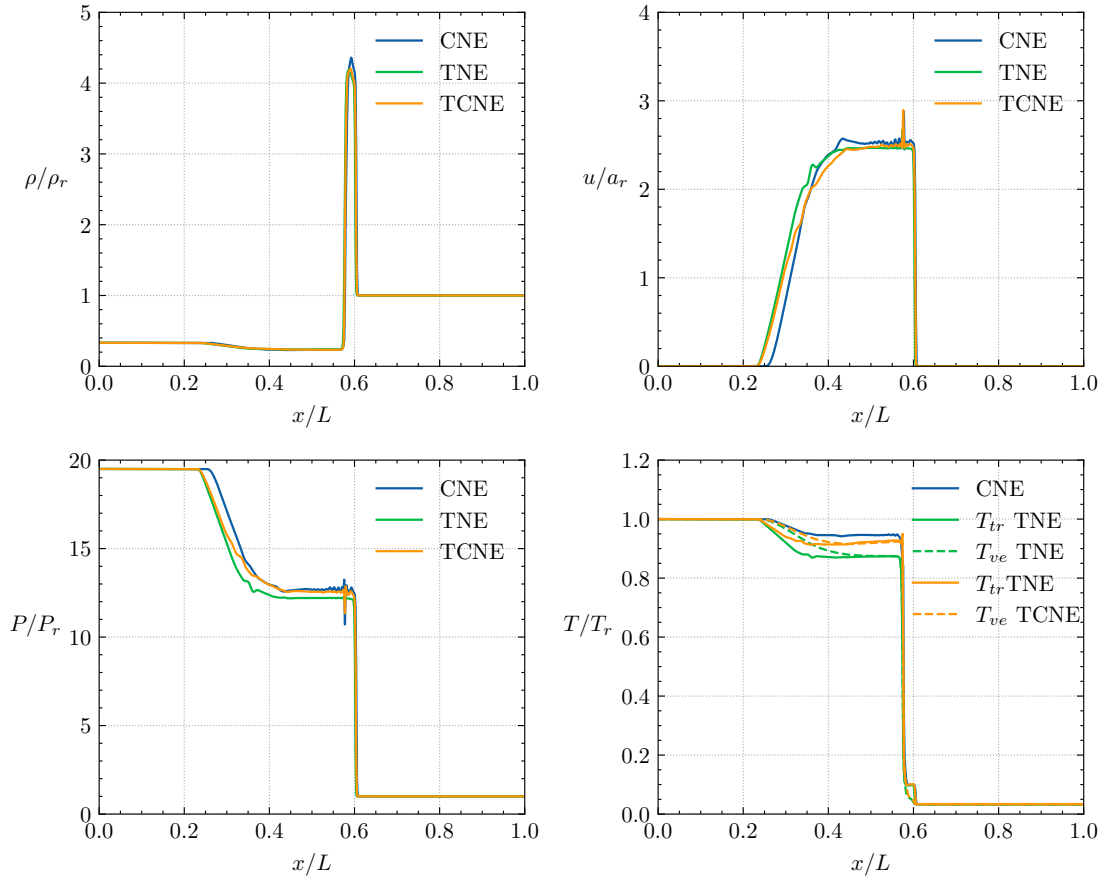
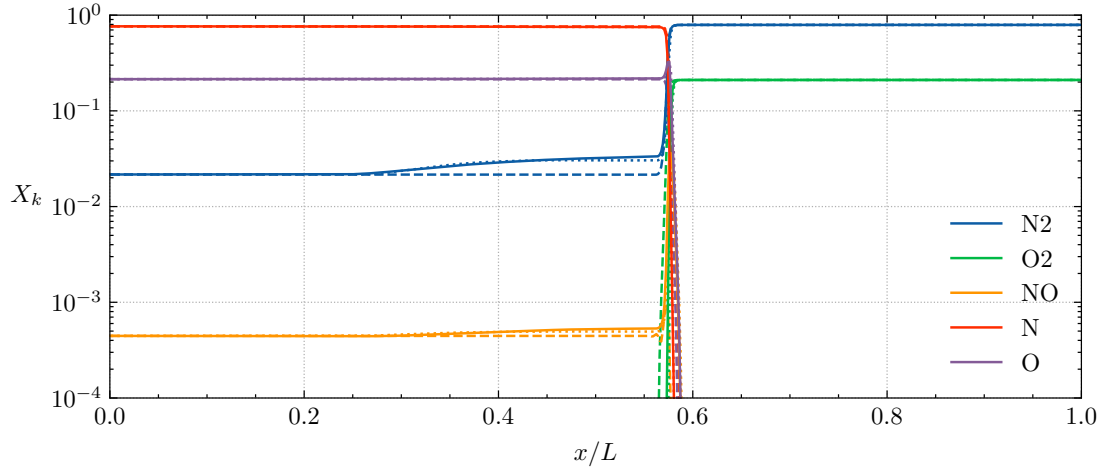

 (a) Comparison of primitive variables at $90\mu\text{s}$ in TNE, CNE and TCNE.

 (b) Mole fraction (X_k) comparison with TNE (---), CNE (.....) and TCNE (—).

Fig. 2.11 Verification of the thermochemical models' implementation—chemical non-equilibrium (CNE), thermal non-equilibrium (TNE) and thermochemical non-equilibrium (TCNE)—with the high temperature Riemann problem and WENO5.

2.3.3 Shu-Osher problem

The Shu-Osher problem involves a normal shock wave at $M \approx 3$, interacting with a fluctuating entropy wave. The aim of this case is to test the Euler flux computation methods' numerical dissipation.

The computational domain length is 1 m with 200 uniformly distributed mesh points. The simulation time is 1.8 s with CFL around 1 and the initial conditions are:

$$(\rho, u, P) = \begin{cases} (3.857143, 2.629369, 10.3333), & \text{if } x \leq 1 \\ (1 + 0.2\sin(50x), 0, 1), & \text{otherwise} \end{cases}.$$

Figure 2.12 shows that TENO6 and WENO5 are less dissipative than CS6-JST. The JST artificial flux is the culprit for the high dissipation. Simple attempts to solve this by replacing the JST shock sensor in Eq. (2.57) by Ren's sensor (Ren et al., 2003), which is reported to be sharper (Zhao et al., 2020) and less dissipative sensor, were unsuccessful. Another observation from the figure is that TENO6 is the least dissipative, as expected. Moreover, WENO5 disperses the high-frequency post-shock solution the most. Computational cost wise, TENO6 and WENO5 are $\sim 3\times$ and $\sim 2.5\times$ more expensive than CS6-JST. Despite the fact that current implementation of the CS-JST6 scheme is not optimal in terms the computational efficiency. Pirozzoli (2010) has suggested an improved implementation which can almost half the computational cost for sixth-order skew-symmetric flux. So, overall CS6-JST seems to be more attractive from a computational cost to accuracy ratio perspective than the WENO methods.

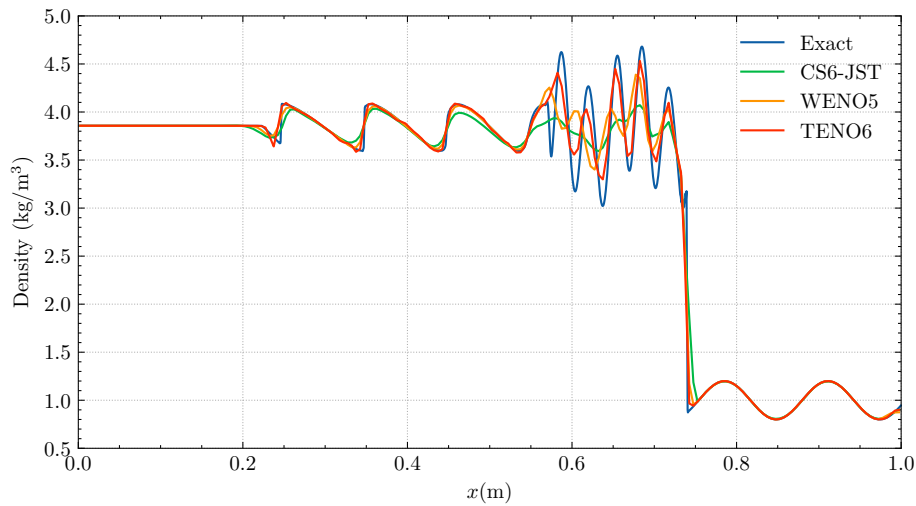


Fig. 2.12 Shu-Osher problem comparison with CS6-JST, WENO5 and TENO6 at $t = 1.8$ s.

2.3.4 Isentropic vortex propagation

Isentropic vortex propagation case involves an isolated incompressible vortex pair advecting continuously. It is popular in literature (Brehm et al., 2015; Doru, 2016; Spiegel et al., 2015) because of its simplicity and availability of exact analytical solutions at all times. It tests a numerical method's ability to sustain vortical flow structures, which is important for accurate simulation of turbulent flows. This ability is tested: first, with a uniform grid; and then, with the vortex passing through a coarse-fine interface with a 1 level static AMR mesh. The latter case is a simplification of turbulent flow simulations, where mesh is refined near walls and vortical structures often pass through the coarse-fine interface.

The initial flow is a uniform mean flow with superimposed perturbations in velocity and temperature:

$$\begin{aligned} r &= \frac{\sqrt{(x-x_0)^2 + (y-y_0)^2}}{l_v}, \quad \bar{y} = \frac{y-y_0}{l_v}, \quad \bar{x} = \frac{x-x_0}{l_v}; \\ u &= u_0(1 - \beta \bar{y} \exp(-r^2/2)), \quad v = -u_0 \beta \bar{x} \exp(-r^2/2); \\ T &= T_0 - \frac{u_0^2 \beta^2}{2c_p} e^{-r^2}, \quad \rho = \rho_0 \left(\frac{T}{T_0} \right)^{\frac{1}{\gamma-1}}, \quad M_0 = \frac{u_0}{\sqrt{\gamma R T_0}}. \end{aligned}$$

With parameters

$$p_0 = 10^5 \text{ Pa}, \quad T_0 = 300 \text{ K}, \quad l_v/L = 1/20, \quad (M_0, \beta) = \begin{cases} (0.05, 0.02), & \text{if slow vortex} \\ (0.5, 0.2), & \text{if fast vortex} \end{cases},$$

where subscript 0 denotes the initial state, (x_0, y_0) are the initial vortex centre coordinates, l_v is the vortex length scale (radius), (x, y) are the Cartesian coordinates, and (\bar{x}, \bar{y}) are the normalised coordinates by the vortex position. The thermodynamic variables are T , p , ρ , c_p and γ ; lastly, velocities in x and y directions are u and v respectively.

For the accuracy assessment, L_2 error norm (root-mean-squared error) is computed as follows

$$\left(\frac{\sum_{i=1}^N (\phi_i - \phi_i^*)^2}{N} \right)^{1/2}, \quad (2.62)$$

where ϕ is the computed solution value, ϕ^* is the exact solution value and N is the number of computational points (number of samples).

Spatial discretisation order of accuracy

The spatial discretisation schemes' (CS6-JST and TENO6) order of accuracy approach their formal 6th order of accuracy as shown in Fig. 2.13, with CFL around 0.02 and 5 computational time steps. The small CFL number and the number of time steps ensure error accumulation due to time integration is small. Uniform meshes without AMR of 40×40 , 80×80 and 160×160 are used to evaluate the order of accuracy.

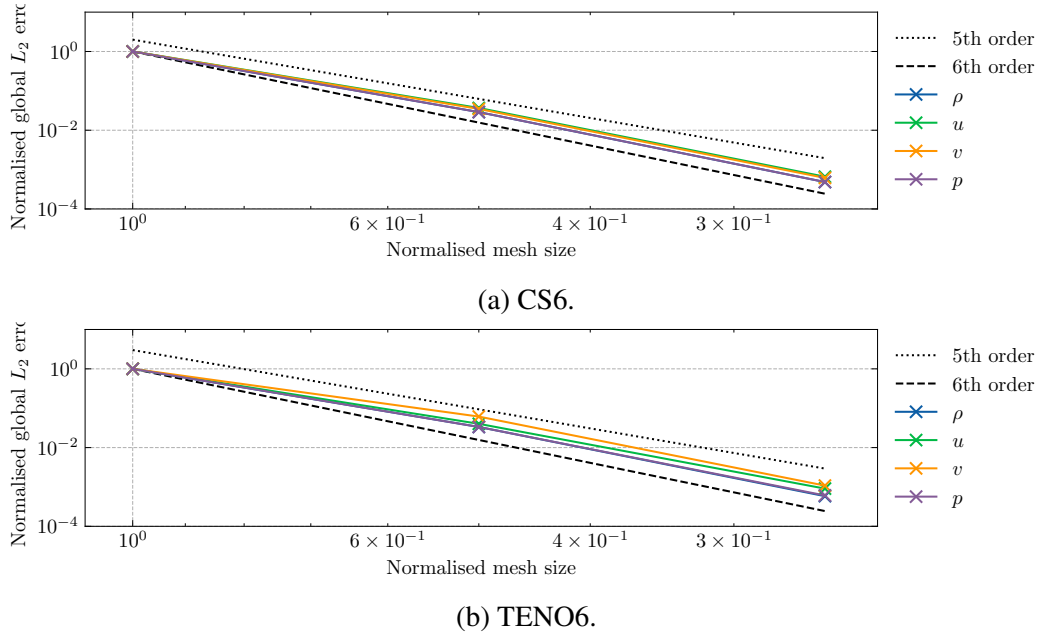


Fig. 2.13 Spatial discretisation order of accuracy assessment for CS6 and TENO6.

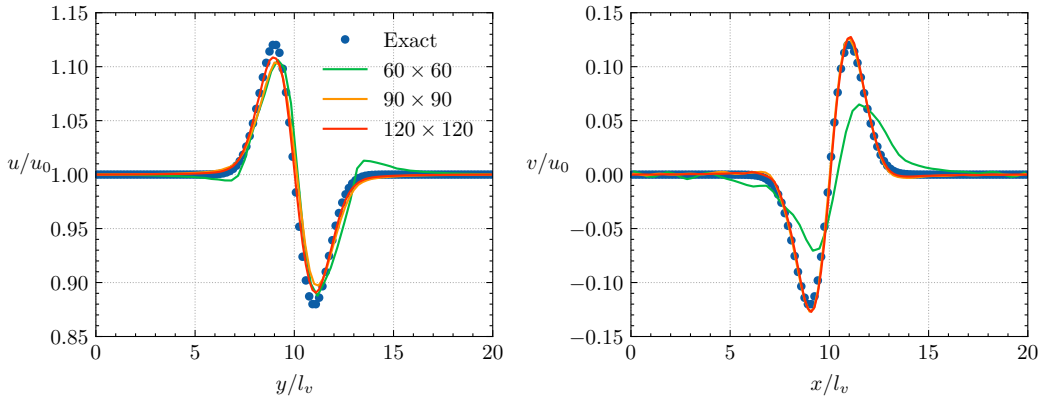
Overall discretisation order of accuracy

To verify and benchmark the implementation, an order of accuracy study is performed. The fast vortex case is preferred as its larger gradients are likely to be more numerically challenging than the slow vortex, especially with AMR and a coarse-fine interface. The CFL number is kept around 0.75 for all meshes and the vortex is convected for 50 times exactly. All domain physical boundaries are periodic and do not introduce any errors in the solution.

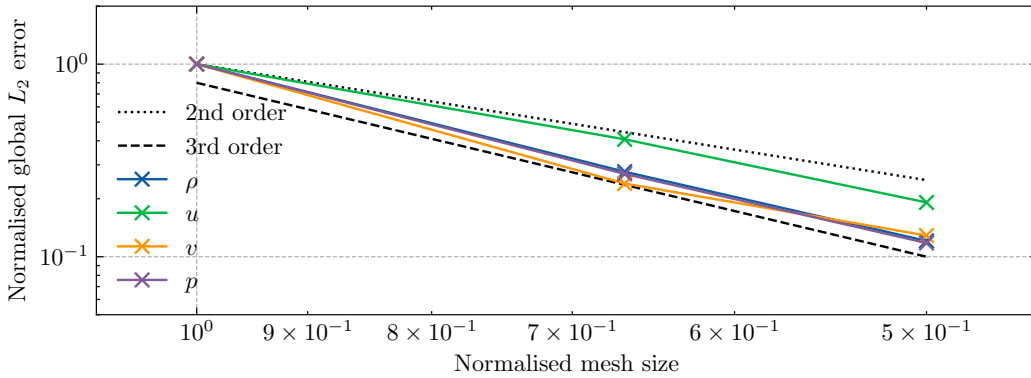
Without AMR. Figure 2.14a shows the velocity profiles across the vortex with different meshes, compared against the exact solution. Slight attenuation in the vortex velocity even with the finest mesh (120×120) is observed over 50 flow-through times with TENO6 with $C = 10^{-9}$. Figure 2.14b shows that the method is second to third-order accurate in different primitive variables. Overall however, the method is third-order accurate as suggested by Table 2.2. This is expected for long simulation times with large CFL numbers (closer to 1.0

than 0.0) as the errors introduced are likely to be dominated by time integration, which is third-order accurate.

With AMR. Figure 2.15a shows the mesh with one level of static refinement. This setup allows effect of restriction, prolongation for halo point filling and coarse-fine flux correction to be investigated. The vortex is initialised on the coarse mesh and propagates through the coarse-fine interface 50 times. Figure 2.15b shows visually perfect conservation of vortex with GTS and TENO6. Note, since coarse-fine interface flux correction is not used in current work. The results suggest that it is not important in this case, and reaffirms that flux correction is not important in smooth flows and is likely only important near large gradients like shock waves. Moreover, Fig. 2.15c and Table 2.2 show that the method is third-order accurate even with a hierarchical AMR grid. This is expected as the prolongation operation is fourth-order accurate, and the overall solution accuracy is limited by the third-order time integration, as in the case without AMR.

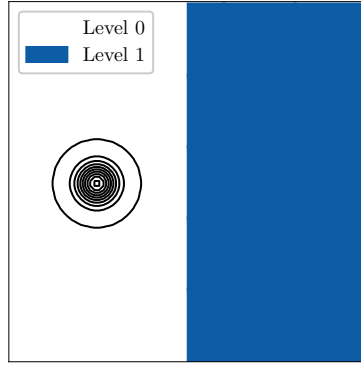


(a) Velocity profiles across the fast vortex with 60×60 , 90×90 and 120×120 uniform meshes, and TENO6 ($C = 10^{-9}$).

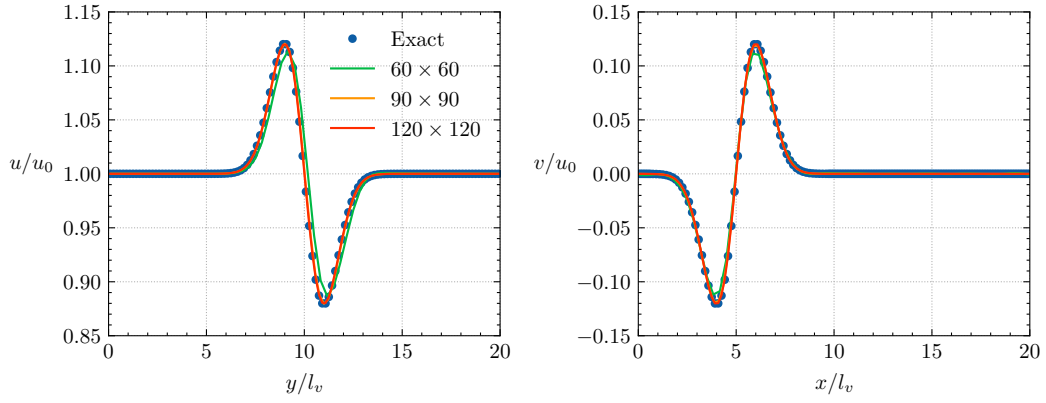


(b) Order of accuracy using L_2 norm of the global error in primitive variables.

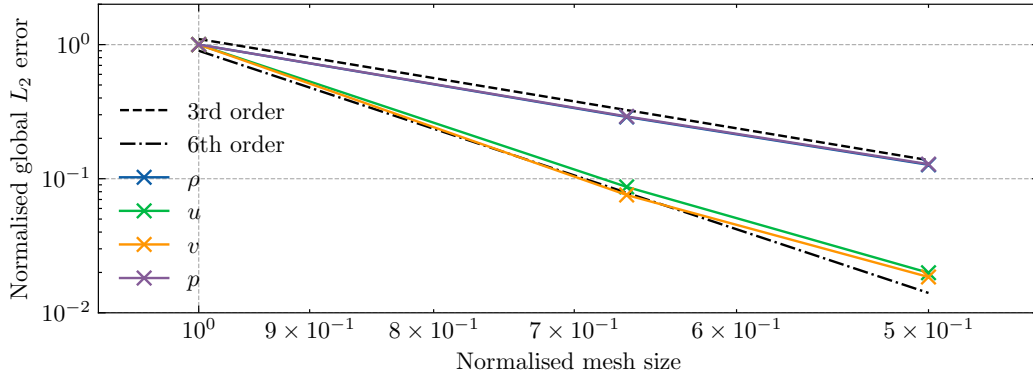
Fig. 2.14 Fast vortex propagation without AMR order of accuracy over 50 vortex flow-through times.



(a) AMR mesh with a single level of refinement in right half of the domain and initial vortex on the left.



(b) 1 level of refinement and with GTS and TENO6 ($C = 10^{-9}$).



(c) Order of accuracy with AMR (GTS)

Fig. 2.15 Fast vortex propagation with AMR (1 level) order of accuracy over 50 vortex flow-through times.

Table 2.2 Observed order of accuracy with and without AMR.

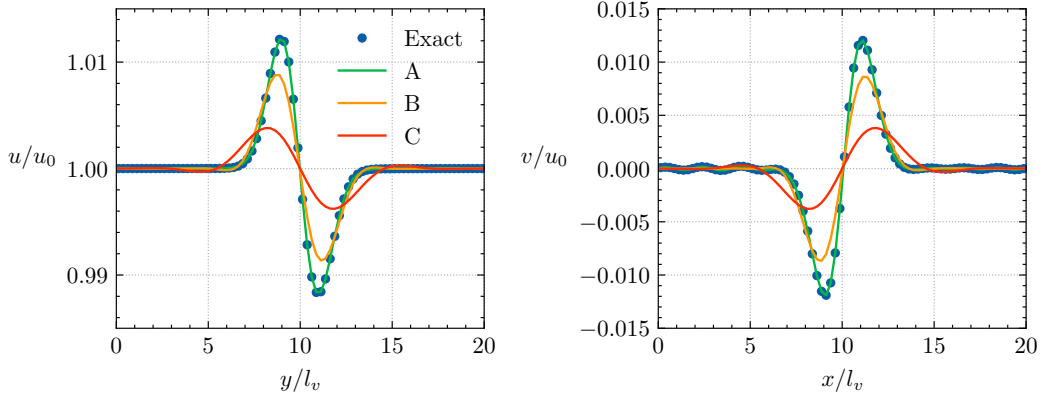
Base Mesh	Global L_2 error		Observed Order	
	Without AMR	With AMR	Without AMR	With AMR
60×60	30.9	11.1	-	-
90×90	8.32	3.23	3.23	3.04
120×120	3.64	1.42	2.87	2.85

Comparison of numerical methods

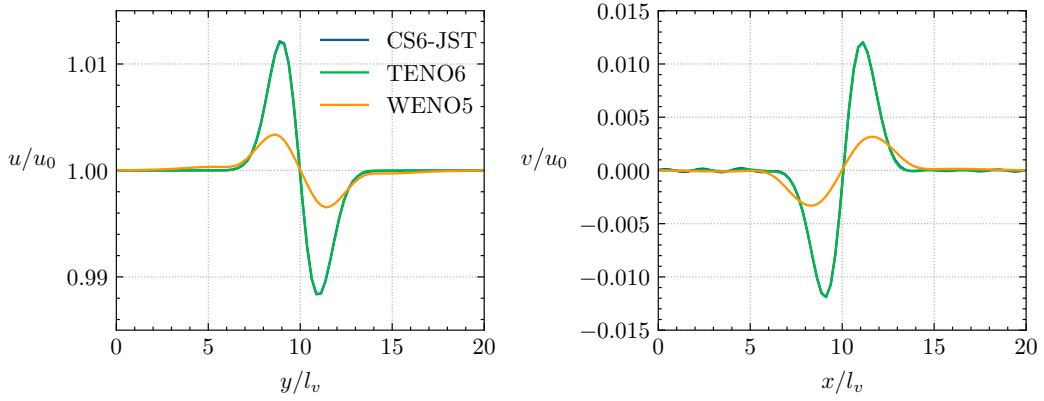
With any numerical method, the vortex accumulates errors over time. A lower dissipation method maintains the vortex integrity for longer times. In literature, the mesh resolution for this test case with different numerical methods is not absolute and varies. For example, [Brehm et al. \(2015\)](#) use 32×32 to 257×257 meshes, whereas [Spiegel et al. \(2015\)](#) use 40×40 to 200×200 meshes. Here, 80×80 is chosen to compare the numerical dissipation of the different numerical methods, namely CS6-JST, TENO6 and WENO6. Computationally, a weaker vortex is more difficult to sustain than a stronger vortex as it is more sensitive to numerical errors. Therefore, the slow vortex case is selected. The simulation time is 50 vortex rotations exactly (0.28323125676 s). The CFL number is kept the same over all cases, the CFL number is approximately 0.7. All domain physical boundaries are periodic, so the boundaries do not introduce any errors in the solution.

Effect of artificial dissipation with CS-JST6. Figure 2.16a Case A shows that shock-capturing does not affect the vortex propagation as expected, because the pressure sensor avoids the activation of artificial diffusion flux away from shock waves. However, damping dissipates the vortex. Even in Case B with $C_4 = 0.00016$, the vortex dissipates over 50 flow times. This suggests that C_4 values much smaller than default must be used when modelling turbulent flows. Also, erroneous oscillations of unknown origin appear in velocity perpendicular to the direction of vortex propagation.

Comparison of CS6-JST, WENO5 and TENO6. Figure 2.16b shows CS6-JST and TENO6 almost perfectly preserve the vortex after 50 flow times and are visually identical in accuracy. In contrast to WENO5, which dissipates the vortex, as expected from its high dissipation reporting from the literature. The cut-off parameter (C) from Eq. (2.45) for TENO6 needed to be at least $100\times$ lower than default ($C = 10^{-9}$) for the vortex to be preserved. With CS6-JST, artificial damping is turned off with $C_4 = 0$. Hence, CS6-JST and TENO6 are deemed suitable for accurate turbulent flow modelling, unlike WENO5.



(a) CS6-JST with cases: A - shock-capturing only ($C_2 = 0.5, C_4 = 0.0$); B - damping only, $100\times$ smaller than default ($C_4 = 0.00016$); C - damping only, $10\times$ smaller than default ($C_4 = 0.0016$).



(b) Comparisons between CS6-JST ($C_2 = 0.5, C_4 = 0.0$), WENO5 ($B = 2.0$) and TENO6 ($A = 1.0, B = 6.0$ and $C = 10^{-9}$).

Fig. 2.16 Slow vortex propagation case velocity profile comparisons with different numerical methods over 50 vortex flow-through times.

2.3.5 Supersonic turbulent channel flow

Channel flow configuration is one of the simplest turbulent flow cases. This case aims to validate the current method's three-dimensional implementation and the suitability of chosen numerical methods for modelling turbulent flows. TENO6 is known to perform well with this test case (Hamzehloo et al., 2021), whereas WENO5 is well known to be unsuitable for accurate turbulent flows calculations due to its high dissipation in smooth parts of the flow. Hence, both of these methods are not tested here, and instead CS6-JST is tested. A large volume of literature exists on turbulent channel flows, and no attempt has been made to survey it. Pope (2000) summarises key theoretical aspects of the turbulent channel flows.

Setup

Current test case was originally studied by Coleman et al. (1995), and has been used extensively as a validation case for direct numerical simulation codes, for example Di Renzo et al. (2020); Piquet (2017). In this case, the fluid is an ideal gas with constant specific heats, constant Prandtl number ($Pr = 0.7$), and power-law temperature-dependent viscosity. Isothermal-wall boundary conditions give a statistically stationary state, and the flow is driven by a uniform body force rather than a mean pressure gradient to preserve streamwise homogeneity. The case parameters are:

$$\begin{aligned}
 h &= 0.006845 \text{ m}, \quad L_x = 4h, \quad L_y = 2h, \quad L_z = 12h; \\
 Re_b &= \frac{\rho_b u_b h}{\mu_w} = 3000, \quad Re_\tau = \frac{\rho_w u_\tau h}{\mu_w} = 220, \quad M_b = \frac{u_b}{\sqrt{\gamma R T_w}} = 1.5, \quad f_x = -\frac{\partial \bar{P}}{\partial x} = \frac{\tau_w}{2h\rho_b}; \\
 T_w &= 500 \text{ K}, \quad \rho_b = \frac{1}{2h} \int_0^{2h} \rho dy, \quad u_\tau = \sqrt{\frac{\tau_w}{\rho_w}} = 35 \text{ m/s}, \quad u_b = \frac{1}{\rho_b h} \int_0^{2h} \rho u dy.
 \end{aligned}$$

Subscript b represents bulk flow quantities, subscript w represents wall quantities, h is the half channel height, (L_x, L_y, L_z) are the domain lengths, Re_b is the bulk Reynolds number based on bulk velocity u_b , Re_τ is the friction Reynolds number based on friction velocity u_τ , M_b is the Mach number based on the fluid bulk velocity and f_x is the body force in streamwise direction. A flow time is $L_z/u_b \approx 120 \mu\text{s}$, a time-step of $0.12 \mu\text{s}$ is used, CFL number is around 0.8 and around 1000 steps are equivalent to one flow time. The flow is computed for 150 flow times with CS6-JST, where $C_2 = 0$ and $C_4 = 0.0016$ ($C_4 = 0.00016$ was found to be unstable over long times).

Initialisation of turbulent flows is not trivial. An accurate initialisation is statistically close to the turbulent equilibrium solution. The more accurate the initial solution, the fewer the number of computational steps required for the turbulent channel flow to reach equilibrium.

A simple and inaccurate initialisation is via laminar velocity profiles with sine wave perturbations, the approach taken in [Hamzehloo et al. \(2021\)](#). On the other hand, an accurate method to initialise a turbulent flow-field is the digital filtering method ([Klein et al., 2003](#)). This method gives a kinetic energy spectrum with a decay slope of -2 instead of equilibrium -5/3 ([Xie and Castro, 2008](#)). However, it is deemed good enough for a first approximation, as the spectrum will reach equilibrium over time. This approach is preferred in the current work. The original digital filtering initialisation involves spatially correlating velocity perturbations in all directions. As a first approximation, the velocity field perturbations are not correlated in the current work. It is expected that the perturbations will correlate themselves over time. The initial field requires computation of u', v', w', p', T' and ρ' . The velocity fluctuations (u', v', w') are calculated using the digital filter method:

$$\tilde{\mathcal{R}}(x, y, z) = \sum_{i=-N_{f,x}}^{N_{f,x}} \sum_{j=-N_{f,y}}^{N_{f,y}} \sum_{k=-N_{f,z}}^{N_{f,z}} b_{ijk} \mathcal{R}(x + \Delta x, y + j\Delta y, z + k\Delta z),$$

$$b_{ijk} = b_i b_j b_k, \quad b_k = \frac{\exp(-\frac{\pi}{2}(\frac{k\Delta z}{L_I})^2)}{\sqrt{\sum_{k=-N_{f,z}}^{N_{f,z}} \exp(-\frac{\pi}{2}(\frac{k\Delta z}{L_I})^2)^2}};$$

where $\mathcal{R}(x, y, z)$ is the random Gaussian field, $\tilde{\mathcal{R}}$ is the filtered (smoothed) Gaussian field; $N_{f,x} = \frac{2\Delta x}{\Delta x}$ is the filter stencil size in x direction, $N_{f,y}$ and $N_{f,z}$ take similar form in y and z directions; L_I is the integral length scale; b_k is smoothing coefficient in k^{th} direction, b_i and b_j in the other orthogonal directions are calculated similarly. The thermodynamic fluctuations p', T' and ρ' are calculated using the strong Reynolds analogy ([Guarini et al., 2000](#)), which relates the velocity fluctuations to the temperature fluctuations

$$\frac{T'}{\bar{T}} = (\gamma - 1) M^2 \frac{u'}{\bar{u}}.$$

Assuming the mean pressure gradient is constant across the channel and P'/\bar{P} is negligible, and using the equation of state, ρ' can be calculated. Note, the digital filter method requires the whole grid to be on a single patch. In theory, this is possible by a two-step process of initialising the flow-field with only one patch on a single processor and then restarting parallel simulation with smaller patches. However, this approach is not taken here; instead, the initial field is a collection of smoothed patches.

Results

A mesh refinement study is performed with the different cases shown in Table 2.3, Case A mesh is low resolution without AMR, Case B is high resolution mesh without AMR and Case C mesh is with static AMR.

Table 2.3 Mesh refinement study

Case	y_w^+	Base mesh ($N_x \times N_y \times N_z$)	Points ($\times 10^6$)		
			Level 0	Level 1	Total
A	6.8	$384 \times 64 \times 128$	3.1	-	3.1
B	3.4	$768 \times 128 \times 256$	25.2	-	25.2
C	3.4	$384 \times 64 \times 128$	3.1	3.1	6.2

From literature, a typical resolved stretched mesh for the current case has a computational domain of $256 \times 128 \times 128 = 4.2 \times 10^6$ points with wall $\Delta y^+ = 0.8$. The isotropic AMR mesh adds significant unnecessary computation to this problem, as the current implementation with BoxLib does not allow the anisotropic mesh. Hence, further refined meshes in search of more accurate solutions are not explored in the current work. However, anisotropic AMR mesh will likely be computationally competitive with stretched meshes in turbulent channel flow and other grid aligned boundary layer flows.

Figure 2.18a shows the mean flow channel profiles over 150 flow times. The mean flow profile errors are less than 4% even with $\sim 8 \times$ lower Δy_w^+ than the reference solution. Secondly, Fig. 2.18b shows the Van Driest transformed velocity (u_{VD}^+) profile. The transformation is as follows

$$y^+ = \frac{\rho_w u_\tau y}{\mu_w}, \quad u^+ = \frac{u}{u_\tau}, \quad u_{VD}^+ = \int_0^{u^+} \left(\frac{\rho}{\rho_w} \right) du^+,$$

where u^+ is non-dimensional velocity by friction velocity. In cases without wall normal variation of density and transport properties, such as in everyday incompressible flows, the mean velocity is nearly a universal function of the distance from the wall when appropriately transformed. However, in cases with wall-normal variations of density and transport properties, often found in high-speed compressible flows, there is no transformation which maps all flows to onto a universal profile. These ideas are discussed in more detail by Griffin et al. (2021). Since the current case includes an isothermal wall with heat transfer, density variations in the boundary layer are expected. Moreover, for direct comparison of the velocity profile with previous works (Foyisi et al., 2004), Van Driest transformed velocity profile is

computed. The first point in the viscous sublayer, and the maximum error is around 20% error. Close to the wall, all three cases result in similar profiles. However, away from the wall, Case B is the most accurate whereas Case A is the least accurate.

Lastly, Fig. 2.18c shows Case B with $\sim \times 4$ lower Δy_w^+ leads to around 15% error in velocity fluctuations kinetic energy and Case C results in even larger errors. Overall, the error accumulation with Case C (with adapted mesh) is higher than in case B (high resolution mesh) because of grid adaptation errors. The discrepancy in Cases B and C with the reference solution are likely due to the lack of resolution in the wall normal direction.

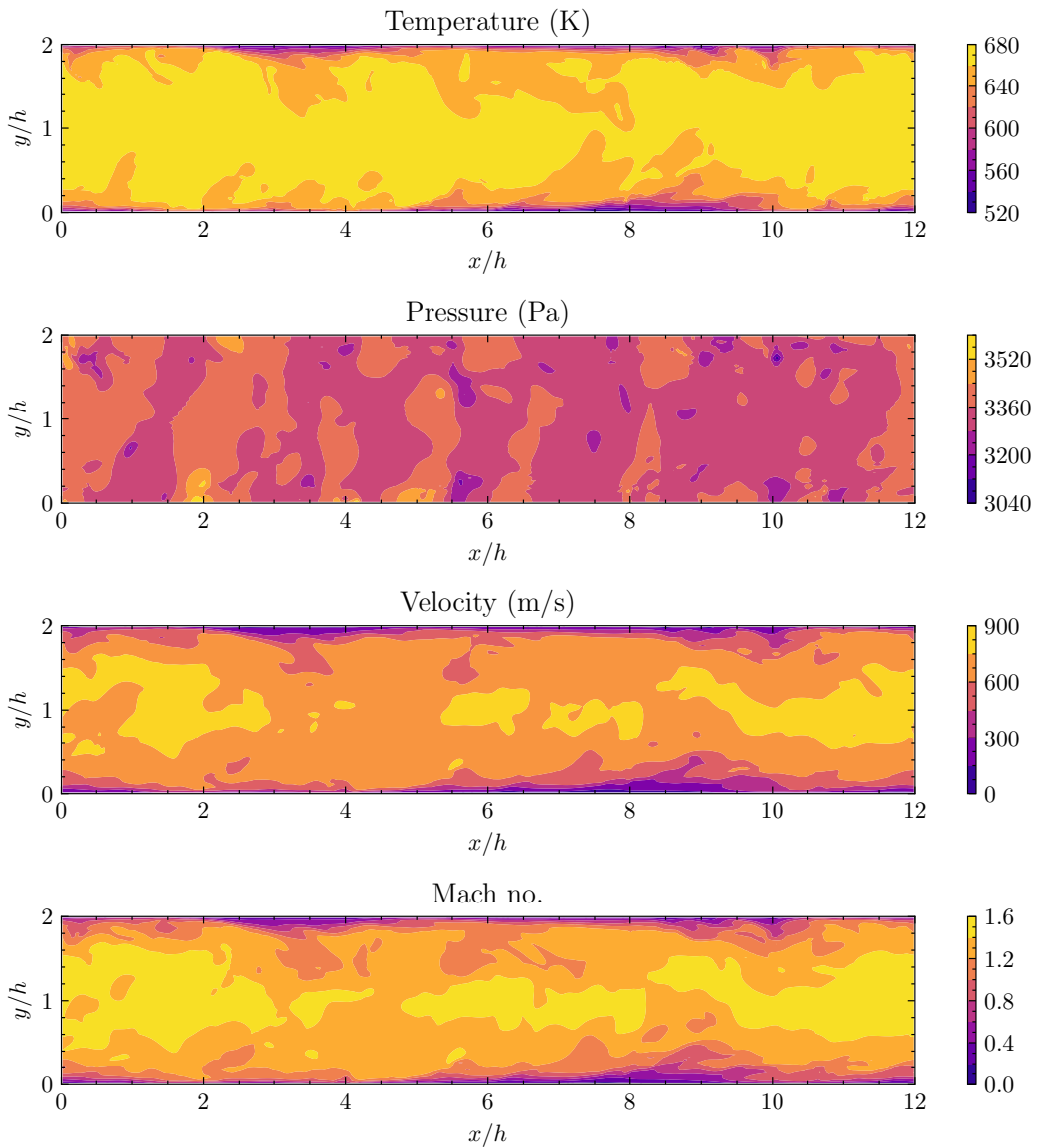
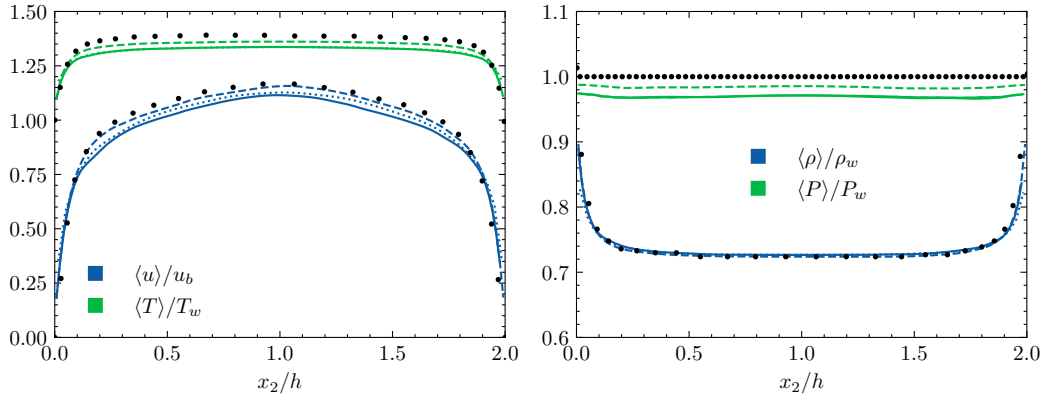
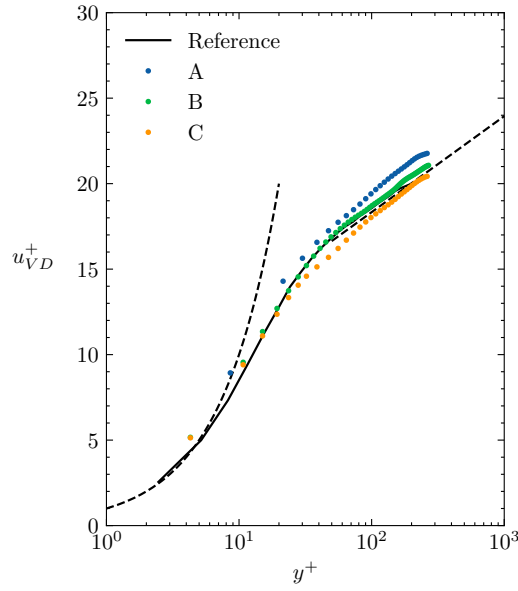


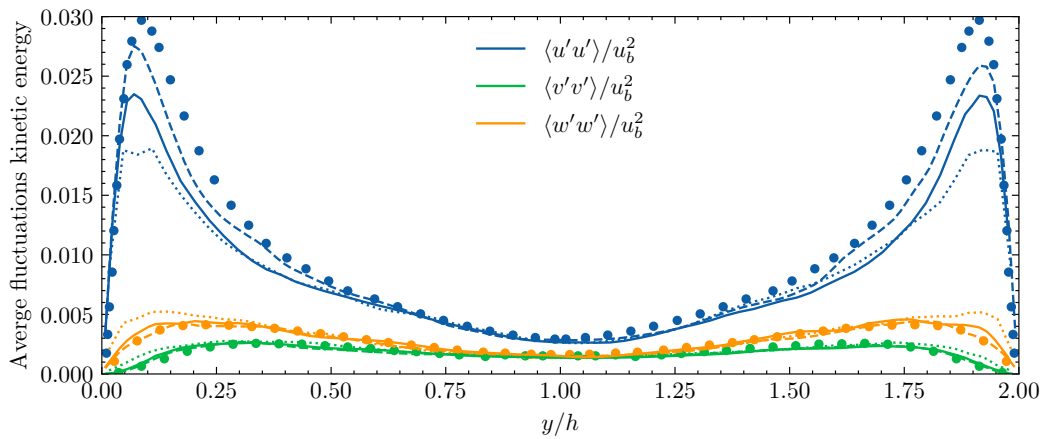
Fig. 2.17 Supersonic turbulent channel flow scalar field variables instantaneous slices from case C.



(a) Mean flow velocity, temperature, density and pressure profiles.



(b) Van Driest transformed velocity profile.



(c) Velocity fluctuations kinetic energy.

Fig. 2.18 Supersonic turbulent channel flow mean flow and fluctuations profiles for Case A (.....), Case B (- - -) and Case C (—) compared against reference solution by Foysi et al. (2004) (•).

2.4 Summary

This chapter developed and validated a finite-difference low dissipation computational fluid dynamics solver for hypersonic flows with adaptive mesh refinement (AMR).

Firstly, physical models for accurate hypersonic computations in literature are reviewed. Then, a two-temperature thermochemical non-equilibrium model with its thermodynamic and transport closures are implemented via the Mutation++ library. Trends in these properties are discussed.

Secondly, the mathematical theory of conservation laws is reviewed. It suggests that shock-capturing without introducing significant dissipation is the most challenging part of the numerical method. Along with computing across a range of time scales, especially with stiff source terms. Then, high-order and low dissipation shock-stable numerical methods are reviewed and implemented. Particular attention is given to Euler flux calculation methods, namely methods from the weighted essentially non-oscillatory (WENO) and artificial flux (AF) families. Representative methods from each family are implemented, namely WENO5 and TENO6; and CS6-JST.

Thirdly, simple numerical tests are used to validate and compare performance of the implemented methods:

- The weak Riemann problem showed that CS6-JST generates an oscillatory solution in the post-shock regions, unlike WENO methods.
- The high-temperature Riemann problem validated the source term integration method and implementation of thermodynamic closures for thermochemical non-equilibrium flows. It also suggested that with 5 and 11 species air mixtures and mechanisms, the source term and the thermodynamic properties accounted for 50% and 75% of the total computational cost respectively.
- The Shu-Osher problem suggested that the JST sensor causes excessive dissipation compared to TENO6. It showed that CS6-JST is around $\times 2.5$ to $\times 3$ less computationally less expensive than WENO5 and TENO6.
- The vortex propagation case suggested that both TENO6 and CS6-JST methods' dissipation is very sensitive to shock-capturing parameters. Therefore, great care must be taken in selecting values for these parameters.
- The supersonic turbulent channel case validated the implementation in three dimensions. It showed that isotropic AMR mesh results in an excessive number of computa-

tional points when compared to body-fitted methods. However, an AMR framework with anisotropic mesh could be competitive with body-fitted methods due to the efficiency of the local time-stepping strategy, compared with global time-stepping.

3. Hypersonic flow around complex geometries

Previously, Chapter 2 developed a numerical method for modelling hypersonic flows with simple computational domain enforced boundary conditions. This chapter aims to build on previous work to develop a numerical method for modelling hypersonic flows with complex geometries.

3.1 SAMR-GPIBM Coupling

Embedded boundary methods, also known as Immersed Boundary Methods (IBM) (Mittal and Iaccarino, 2005), allow representation of complex geometries on structured grids. These methods require minimal changes to the flux derivative calculation unlike body-fitted approaches which require complex coordinate transformations. Furthermore, these methods are well suited to fluid-structure interactions when compared to body-fitted methods. Embedded boundary methods can be classified into two main categories: cut-cell methods or ghost-point methods. The latter is the focus for this study.

Cut-cell methods (Berger, 2017; Colella et al., 2006) originate from finite volume discretisation and are designed to satisfy discrete conservation at the embedded boundary. They involve representing a boundary via a piecewise reconstruction in a Cartesian mesh, resulting in a sharp representation of the interface. Some cut cells can have arbitrarily small volume fraction which imposes severe constraints on the time step for explicit numerical schemes. Historically, this has been a major problem with the method, but solutions to this problem have been proposed recently by Berger and Giuliani (2021); Gokhale et al. (2018). These methods are considered more complex as the method depends on the cut-cell topology, meaning the area of each cut-face and edge lengths of cut-faces need to be computed. Performing this task automatically and generally, for arbitrary geometries, is not a trivial task.

Ghost-point methods, hereon referred to as ghost-point immersed boundary methods (GPIBM), originate from finite difference discretisation and are not designed to satisfy discrete conservation at the embedded boundary. Despite this, these methods give accurate results have been widely adopted (Ghias et al., 2007; Tseng and Ferziger, 2003). They rely on approximating the closest point to the embedded boundary, called the ghost point, in such a manner that it

implies the correct boundary flux. These methods are simpler as there is no need to define cut-cell topology.

GPIBM studies in context of compressible flows include [Boukharfane et al. \(2018\)](#); [Chaudhuri et al. \(2011\)](#); [Ghias et al. \(2007\)](#); [Tseng and Ferziger \(2003\)](#); [Wang et al. \(2022\)](#). These studies focus on flows up to supersonic Mach numbers. Hypersonic flow studies with GPIBM are rare, partial studies include [McQuaid et al. \(2021b\)](#); [Sekhar and Ruffin \(2013\)](#). A full study by [Bridel-Bertomeu \(2021\)](#) uses an essentially non-oscillatory like reconstruction method for robustness. Additionally, IBMs are well suited to fluid-structure interactions. Studies focusing on fluid-structure interactions in the context of compressible flows include [De Vanna et al. \(2020\)](#); [Khalili et al. \(2018\)](#).

The main novelties of the current study are describing the coupling of structured adaptive mesh refinement with ghost-point immersed boundary method (SAMR-GPIBM); applying computationally less expensive artificial dissipation shock capturing Euler flux scheme instead of commonly used WENO based methods and the selected numerical method validation cases.

3.1.1 Algorithms

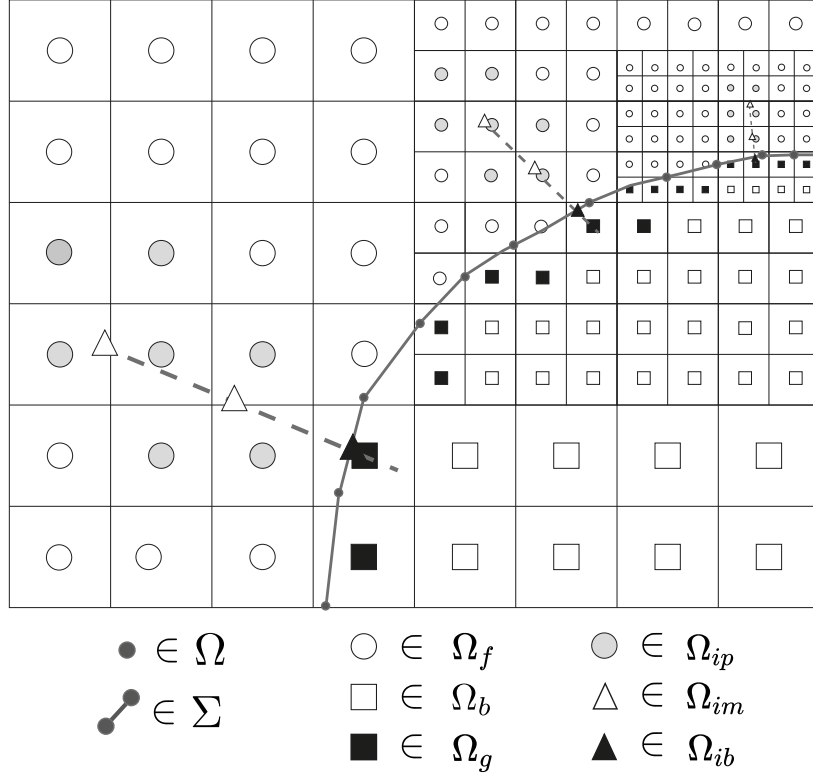


Fig. 3.1 Ghost point immersed boundary with patch-based adaptive mesh refinement

Figure 3.1 illustrates the current SAMR-GPIBM approach in two dimensions, and the grey curve represents the immersed boundary drawn on a hierarchical Cartesian grid. Immersed boundaries can be represented by a closed polygon (2D or 3D). In discrete space, it is represented by a set of elements (Σ_n) with vertices (Ω_n), where n is the body index. In 3D, the body is handled by a computational geometry library, GTS (Popinet, 2006), for efficient element search and access operations. The library stores and organises the geometry data in a tree structure allowing efficient element operations. The geometry handling in 3D is verified in Appendix Chapter B.

Set of points on i^{th} patch on level l is represented by P_i^l . On a given patch, each body separates a set of fluid points (Ω_f) and a set of body points (Ω_b). A body point directly adjacent to a fluid point is also part of a set of ghost points (Ω_g). The following relations hold between the sets of grid points:

$$\Omega_b \subseteq P_i^l; \quad \Omega_f \subseteq P_i^l; \quad \Omega_s \cap \Omega_f = \emptyset. \quad (3.1)$$

A ghost point's state is re-constructed using interpolation points (Ω_{ip}), image points (Ω_{im}) and immersed boundary points (Ω_{ib}). The current IBM approach is similar to Ghias et al. (2007), they offer an alternative basic explanation of the method but without AMR.

A generic patch-based AMR algorithm, as shown in Algorithm 1 in Section 2.2.3, can be coupled with IBM resulting in Algorithm 4. The new algorithm includes enforcing boundary conditions, computing immersed boundary aware fluxes, computing surface state from the flow-field and moving the immersed boundary. All of these features can be implemented in six steps:

1. INITIALISEIB procedure is added at the start of the computation and after re-gridding in Algorithm 4. Given a discretised body and an AMR grid, the grid points need to be classified and additional immersed boundary sub-grid points need be interpolated as shown in Fig. 3.1 in two dimensions. Same idea applies in three dimensions but with triangular elements. Type of grid point (P_{ijk}) is stored in solid maker field as

$$S_{ijk} = \begin{cases} 1, & \text{if } P_{ijk} \in \Omega_s, \\ 0, & \text{otherwise.} \end{cases} \quad (3.2)$$

Then, sub-grid points are calculated. A ghost point is

$$G_{ijk} = \begin{cases} 1, & \text{if any } (x_l, y_m, z_n) \in \Omega_f \text{ for } l = i - n_g, \dots, i + n_g, \\ & m = j - n_g, \dots, j + n_g, n = k - n_g, \dots, k + n_g \\ 0, & \text{otherwise.} \end{cases} \quad (3.3)$$

$D_{\perp}(P, \sigma)$ is the orthogonal distance between a grid point and an element. The closest element to a given ghost point is:

$$\sigma_c = \min\{D_{\perp}(P_g, \sigma)\}, \quad \forall \sigma. \quad (3.4)$$

This is a computationally expensive procedure, especially with many elements. However, the cost can be significantly reduced if the search is limited to the body element within the patch. An immersed boundary point is

$$\mathbf{x}_{ib} = d_{ib} \cdot \hat{\mathbf{n}}_c + \mathbf{x}_g, \quad d_{ib} = D_{\perp}(P_g, \sigma_c). \quad (3.5)$$

The two image points are

$$\mathbf{x}_{im}^1 = \alpha_{im}\Delta \cdot \hat{\mathbf{n}}_c + \mathbf{x}_{ib}, \quad \mathbf{x}_{im}^2 = 2\alpha_{im}\Delta \cdot \hat{\mathbf{n}}_c + \mathbf{x}_{ib}, \quad (3.6)$$

where Δ is the local mesh size and α_{im} is a constant factor (typically $0.6 - 1.2$). IBM methods with increasing order of formal accuracies require more image points and can also use image points in element tangent direction. However, image points in the normal direction only are deemed acceptable for a first study. All IBM data are local, stored per patch on each processor, and do not need to be communicated.

2. CALCULATEGP procedure is added before computing the fluxes to represent the immersed boundary, as shown by Algorithms 5 and 6. Firstly the image point state (ϕ_{im}) is interpolated via inverse distance interpolation,

$$\phi_{im} = \frac{\sum_{i \in \mathcal{S}} w_i \phi_i}{\sum_{i \in \mathcal{S}} w_i}, \quad w_i = \|\mathbf{x}_{im} - \mathbf{x}_{ip,i}\|_2; \quad (3.7)$$

where \mathcal{S} is the set of interpolation points—four closest grid points in 2D and eight closest grid points in 3D to the image point, w_i is the weighting of each interpolation point, and \mathbf{x}_{ip} is the position vector of the interpolation points.

Then, the image point velocity is transformed from global to the local coordinate system to match the coordinate system of the boundary conditions. The transformation matrix is determined by the normals and tangent vectors of the closest element to the ghost point. Note, the closest element is found and stored per ghost point in INITIALISEIB. Immersed boundary state (ϕ_{ib}) for Neumann boundary conditions to computed to second order accuracy using Taylor expansion,

$$\left. \frac{d\phi}{d\eta} \right|_{\eta=0} = \frac{-1/2\phi_{im}^2 + 2\phi_{im}^1 - 3/2\phi_{ib}}{\alpha_{im}\Delta} + O(\alpha_{im}\Delta)^2; \quad (3.8)$$

where η is the wall normal coordinate (zero on the immersed surface), ϕ_{im}^2 and ϕ_{im}^1 are the interpolated values at the image points, Δ is the local mesh size, α_{im} is a constant factor. The factor ranges from 0.6 to 1.2 typically, smaller values lead to a more accurate interpolation of ϕ_{ib} but tend to be less stable compared to larger values which are less accurate but more stable. In the present work, $d_{im} = 1$ is generally used. On the other hand, for Dirichlet conditions the boundary value is known.

Lastly, the ghost point state (ϕ_g) is extrapolated along the local surface normal, as shown by dotted grey lines in Fig. 3.1. Linear extrapolation is used

$$\left. \frac{d\phi}{d\eta} \right|_{\eta=0} = \frac{\phi_{ib} - \phi_g}{d_{ib}} + O(d_{ib}). \quad (3.9)$$

An important observation is that extrapolation of thermodynamic quantities (typically T, P) can result in unphysical values. This problem is exaggerated with low density plus strong shocks and cold wall plus hot flow cases. This problem often indicates insufficient resolution, but even with sufficient steady state resolution, it can occur during transients. Moreover, it is typically a problem near perfectly sharp leading edges as the required theoretical resolution is infinite. In this work, the extrapolated state is forced to remain physical by clipping the thermodynamic quantities, $T_g \geq 50$ K and $p_g \geq 1$ Pa. After clipping the primitive variables, the conserved variables are recomputed to ensure consistency. The unphysical ghost point problem could be avoided if the ghost point's state is extrapolated in conservative (or flux) variables, which are not required to be only positive. However, such a solution's implementation is cumbersome as the wall fluxes require irregular treatment and cannot be calculated with the regular numerical method. So, this solution is not preferred.

3. SURFACEPROPS procedure is added at the end of each time-step, as shown by Algorithm 4. Usually, the immersed boundary is represented on the finest level on a given level. Elements' states residing in each patch are calculated in the same manner as CALCULATEGP, at the element centre instead of the IB point. Then the surface state can be written in parallel or communicated to a single processor. The former is more efficient for frequent writing. However, the current work communicates to a single input-output processor.
4. *Order reduction near IB* is necessary as only one ghost point is extrapolated. Though, with the current method, more ghost points can be extrapolated such that the full numerical flux stencil is valid near IB. However, in practice, this led to stability issues and worsened the unphysical extrapolated ghost point problem. After calculating fluxes using the full numerical flux stencil on a patch, fluxes near IB points are recomputed with a reduced order stencil. Fluid points requiring recomputation are identified using solid and ghost marker fields.
5. *Modification of prolongation and restriction operators.* Prolongation and restriction operators described in Section 2.2.3 also need to be considered. Current work uses linear prolongation and restriction operators, such that the interpolations only use the

closest 4 (in 2D) and 8 (in 3D) points. The restriction operator is inaccurate near the immersed boundary. On the other hand, prolongation operation is inaccurate when the immersed boundary intersects a coarse-fine interface. The prolongation operator is always inaccurate when the grid interface intersects with field variable discontinuity. In Section 2.2.3 conservative flux correction was described, considering a shock wave instead of IB intersecting a coarse-fine interface. Fig. 3.2 illustrates the inaccurate operations in presence of an immersed boundary.

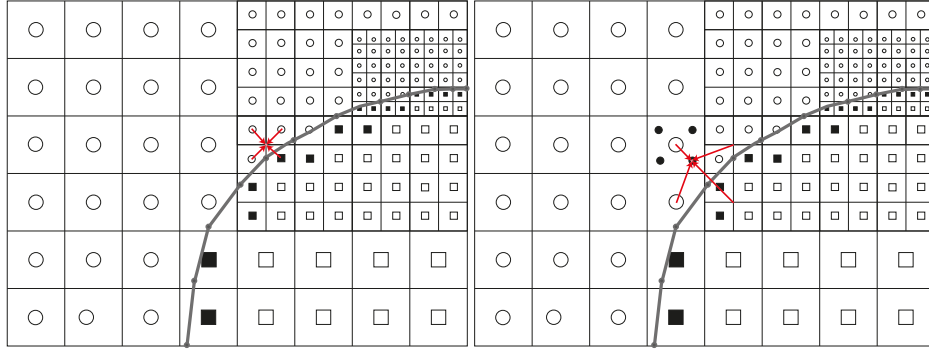


Fig. 3.2 Restriction and prolongation around immersed boundary with AMR mesh.

In practice, modification of restriction and prolongation operators is not deemed necessary. There are a couple of reasons for this: first, the ghost point's contribution is only wrong by Δt^l , even smaller for multi-stage methods like Runge-Kutta used in the current work; second, there are very few points which suffer from this condition, so the overall errors introduced without this correction are no significant.

However, in the case where the errors become significant, a simple and efficient way to enforce consistent interpolations close and far from IB is using the solid marker field to "block out" solid points in prolongation and restriction stencils. Considering a linear prolongation or restriction operator:

$$\phi_{ijk}^l = \frac{1}{\sum_{\alpha_{mnp}} \sum_{(m,n,p) \in I_{ijk}} \alpha_{mnp} \phi_{mnp}^{l \pm 1}}, \quad \alpha_{mnp} = w_{mnp}(1 - S_{mnp}). \quad (3.10)$$

I_{ijk} is the interpolation stencil of point $(i, j, k) \in C_l$, w_{mnp} is the original interpolation weight and α_{mnp} are corrected interpolation weights, S_{mnp} is a solid marker field with value 1 if point is solid and 0 otherwise.

6. MOVEIB procedure in Algorithm 10 is added to Algorithm 4. The procedure manages the immersed boundary topology for moving boundary problems; it displaces the

geometry vertices, in 2D this is done directly, and in 3D it is done via GTS library (Popinet, 2006); and it re-calculates S_{ijk} and G_{ijk} marker fields, Ω_{ib} and Ω_{im} . With fluid-structure interaction problems, especially with large displacements, geometry fairing may also be required to ensure discrete geometry curvature is larger than the local mesh size. However, the current work does not implement geometry fairing.

Algorithm 4

```

procedure MAIN( $n_f, L$ )
  initialise AMR grid with  $L$  levels  $\rightarrow G$ 
  call INITIALISEIB( $G, \Sigma$ )
  n=1
  while  $n < n_f$  do
    if time to move IB then
      call MOVEIB( $\Sigma$ )
    end if
    if LTS then
      call ADVANCELTS( $G$ )
    else
      call ADVANCEGTS( $G$ )
    end if
    if time to refine then
      refine grid ( $G$ )
      call INITIALISEIB( $G$ )
    end if
    if time to calculate surface properties then
      call SURFACEPROPS( $G$ )
    end if
    n = n + 1
  end while
end procedure

```

Algorithm 5

```

1: procedure ADVANCEGTS( $G$ )
2:   for  $i = 1, n_{rk}$  do
3:     set halo points on  $G$ 
4:     for  $l = 1, L$  do
5:       call CALCULATEGP( $G^l$ )
6:       advance solution on  $G^l$ 
7:       restriction  $G^l$  to  $G^{l-1}$ 
8:       coarse-fine flux
       correction
9:     end for
10:  end for
11: end procedure
    
```

Algorithm 6

```

1: procedure ADVANCELTS( $G, l, i$ )
2:   set halo points on  $G^l$  at  $i$ 
3:   call CALCULATEGP( $G^l$ )
4:   advance solution on  $G^l$ 
5:   if  $l < L$  then
6:     for  $i = 1, r$  do
7:       call ADVANCELTS( $G, l + 1, i$ )
8:     end for
9:     restriction  $G^l$  to  $G^{l-1}$ 
10:    coarse-fine flux
    correction
11:  end if
12: end procedure
    
```

Algorithm 7

```

1: procedure CALCULATEGP( $G$ )
2:   For each  $P_g \in \Omega_g$  do
3:     interpolate  $\phi_{im}$ 
4:     transform  $\mathbf{u}_{im}|_{local} \rightarrow \mathbf{u}_{im}|_{global}$ 
5:     apply bc  $\rightarrow \phi_{ib}$ 
6:     transform  $(\mathbf{u}_{im}, \mathbf{u}_{ib})|_{local} \rightarrow \mathbf{u}_{im}|_{global}$ 
7:     extrapolate  $\phi_g(\phi_{ib}, \phi_{im})$ 
8:   end for
9: end procedure
    
```

Algorithm 8

```

1: procedure INITIALISEIB( $G$ )
2:   For each  $l = 1, \dots, L$  do
3:     For each patch do
4:       calculate  $S_{ijk}$  and  $G_{ijk}$ 
5:       calculate  $\Omega_{ib}$  and  $\Omega_{im}$ 
6:     end for
7:   end for
8: end procedure
    
```

Algorithm 9

```
procedure SURFACEPROPS(lev)
  For each  $l = \text{lev}$  do
    For each patch do
      For each  $\sigma \in \Sigma$  do
        if  $\sigma$  in patch then
          calculate element state
        end if
      end for
    end for
  end for
  write elements
end procedure
```

Algorithm 10

```
procedure MOVEIB( $\Sigma$ )
  for each body do
    move verticies
    if body needs faring then
      refine elements
    end if
  end for
  for  $l = 1, L$  do
    for each patch do
      update  $S_{ijk}$  and  $G_{ijk}$ 
      re-calculate  $\Omega_{ib}$  and  $\Omega_{im}$ 
    end for
  end for
end procedure
```

3.2 Numerical tests

This section aims to test the numerical methods developed and implemented, as described by algorithms in Section 3.1.1. The performance of the numerical method is compared with theory and experiments. For tests where numerical dissipation is not important, CS4-JST is used; otherwise, CS6-JST is preferred. The default shock-capturing parameters are used $C_2 = 1.5$ and $C_4 = 0.016$, unless otherwise stated. The default AMR meshing parameters and their values are as in Section 2.2.3, deviations from these default values are reported where they occur.

3.2.1 Euler sphere

Hypersonic flow over a sphere is a common test case. The surface pressure distribution in frozen flow and shock stand-off distance in frozen, equilibrium non-equilibrium flow are described by simple theories. The aim of this test is to test the stability of the numerical method with strong shocks, up to sub-orbital Mach numbers in Euler reacting flow.

Theory

Local pressure coefficient (C_p) is defined as

$$C_p = \frac{P - P_\infty}{\frac{1}{2}\rho_\infty u_\infty^2}, \quad (3.11)$$

where subscript ∞ represents the free-stream quantities. For frozen flow, using simple force balance and normal shock relations, the modified Newtonian theory (Anderson Jr, 2006) gives an analytical approximation for the surface pressure coefficient

$$C_p = C_{p,max} \sin^2(\theta), \quad C_{p,max} = \frac{2}{\gamma M^2} \left(\left(\frac{(\gamma+1)^2 M^2}{4\gamma M^2 - 2(\gamma-1)} \right)^{(\gamma/(\gamma-1))} \left(\frac{1-\gamma+2\gamma M^2}{\gamma+1} \right) - 1 \right); \quad (3.12)$$

where γ is the specific heats' ratio, θ is the local angle of inclination relative to the free-stream velocity vector. This result becomes more accurate as $M \rightarrow \infty$ and $\gamma \rightarrow 1$. The result also becomes independent of Mach number as $M \rightarrow \infty$. In thermochemically relaxing flows, the stagnation point C_p does not change. However, the C_p is different to frozen flows and without a simple predictive theory. Park (1990) presents a case study of thermochemically relaxing flow effects on space shuttle during re-entry; they find that thermochemical relaxation can alter the centre of pressure by around 0.7% of the body length.

Stagnation line shock stand-off distance, herein referred simply as stand-off distance, in a reacting gas was initially studied by [Freeman \(1958\)](#); [Lighthill \(1957\)](#). Building upon these studies, an original theory for predicting stand-off distance in frozen, equilibrium and non-equilibrium flows for an arbitrary set of post-shock chemical reactions was developed by [Wen and Hornung \(1995\)](#). Most recently, [Belouaggadia et al. \(2008\)](#) marginally improved the original theory by approximately 3% with some added complexity in calculations. Their results remain within the reference experiments' ([Nonaka et al., 2000](#)) uncertainties of around 5%. Their marginal improvement is deemed unimportant for current work, and for simplicity, the stand-off distance between the original theory of Wen and Hornung is preferred instead. The non-dimensional stand-off distance ($\tilde{\Delta}$) is defined as

$$\tilde{\Delta} = \frac{\rho_s}{\rho_\infty} \frac{\Delta}{d}, \quad (3.13)$$

where d is the sphere diameter and Δ is the dimensional stand-off distance and ρ_s is the post-shock density on the stagnation line—computed from normal shock relations.

For reacting flows, considering mass balance on the stagnation line, the following expressions can be found ([Wen and Hornung, 1995](#)):

$$\tilde{\Delta} = \begin{cases} \frac{1}{\tilde{\Omega}} \left[-1 + (1 + 2L\tilde{\Omega})^{1/2} \right], & \text{if } \rho_b < \rho_e \\ \frac{\rho_s}{\rho_e} \left[L + \frac{\tilde{\Omega}}{2} \left(\frac{\rho_e}{\rho_s} - 1 \right)^2 \right], & \text{if } \rho_b = \rho_e \end{cases}. \quad (3.14)$$

The constant (L), where $L = 0.41$ for a sphere and $L = 1.16$ for a cylinder. The equilibrium density on stagnation line is represented by ρ_e , and ρ_b is the density at the stagnation point on the body. The equilibrium density can be calculated from equation of state at equilibrium stagnation point, $\rho_e = P_s/R_e T_e$. The reaction rate parameter ($\tilde{\Omega}$) is defined as

$$\tilde{\Omega} = \frac{-d}{\rho_s u_\infty} \left(\frac{\partial h}{\partial \rho} \sum_k h_k \frac{dY_k}{dt} \right)_s \sim \rho_s d \sum_k h_k \left(\frac{dY_k}{dt} \right) / \rho_\infty u_\infty^3. \quad (3.15)$$

The scaling suggests that the parameter is the ratio between the rate of energy removal by chemical reactions and kinetic energy addition rate. The case $\rho_b < \rho_e$ refers to non-equilibrium flow on stagnation line for small values of $\tilde{\Omega}$. Whereas, the case $\rho_b = \rho_e$ refers to equilibrium mixture at the body for large values of $\tilde{\Omega}$. These two regimes can be clearly seen in Fig. 3.3 plotted using Eq. (3.14). Note, the non-equilibrium solution is parameterised

by ρ_s/ρ_e . For frozen flow ($\tilde{\Omega} = 0$) considering the case $\rho_b = \rho_e$, Eq. (3.14) is simply

$$\tilde{\Delta} = L \frac{\rho_s}{\rho_b}. \quad (3.16)$$

Furthermore, $\rho_e \approx \rho_s$, the stagnation point density is approximately the post shock density. In other words, the density gradient on stagnation line is negligible. Therefore, $\tilde{\Delta} \approx L$, as suggested by Fig. 3.3 when $\tilde{\Omega} \ll 1$.

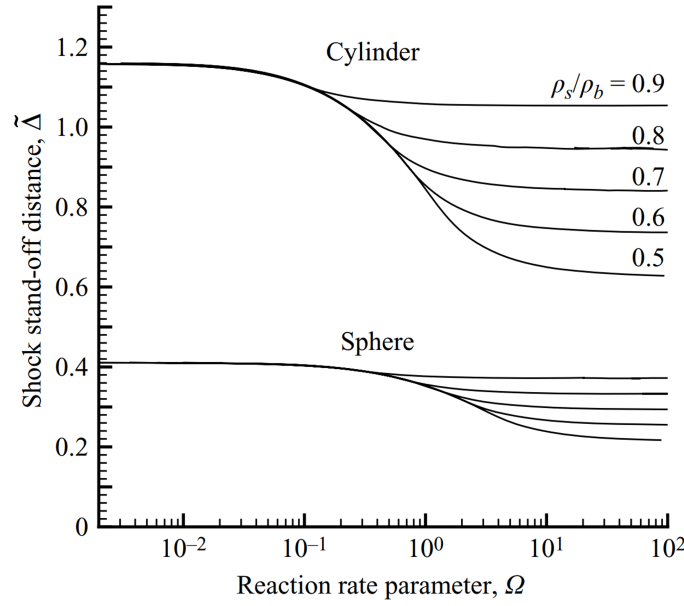


Fig. 3.3 Stagnation line shock stand-off distance in reacting flow, adapted from Belouaggadia et al. (2008).

Frozen

Firstly, axisymmetric frozen flow is considered. The sphere diameter (d) is 1 m, the domain size is $[0.7 \times 1.05]d$ with a uniform mesh and without AMR, free-stream temperature is 300 K, free-stream pressure is 10^5 Pa and the Mach number is varied from 4 to 32, and the stagnation enthalpy varies from around 1 to 60 MJ/kg.

A mesh refinement study is performed at Mach 4 without AMR with 20, 40, and 80 mesh points in the shock layer on the stagnation line, results from which are summarised in Table 3.1. The stand-off distance¹ converges with increasing resolution. The relative error is $\epsilon_{\Delta} = (\Delta - \Delta^*)/\Delta^*$, where Δ^* is the theoretical stand-off prediction from Eq. (3.13). This suggests that around 80 points on the stagnation line are sufficient for accurate stand-off predictions.

¹The shock is detected using JST shock sensor from Eq. (2.57) with $\psi > 0.1$.

Table 3.1 Mesh refinement study with frozen flow over sphere at $M = 4$.

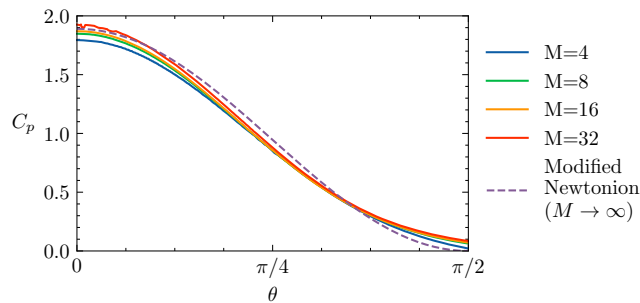
N_s	$N_x \times N_y$	$\Delta^*/d (\times 10^{-2})$	$\Delta/d (\times 10^{-2})$	$\epsilon_\Delta(\%)$
20	150×225	8.40	7.56	-10%
40	300×450	8.40	7.97	-5.1%
80	600×900	8.40	8.37	-0.4%

Table 3.2 shows the stand-off predictions over the Mach number range, compared with theoretical predictions from Eq. (3.13). The stand-off is predicted within 2% compared to theory. With increasing Mach numbers the number of mesh points ($N_x \times N_y$) increases to keep the number of mesh points in the shock layer on the stagnation line approximately constant (around 80 points). Moreover, with increasing Mach number C_2 and C_4 both are increased to maintain stability. In the current Mach range, $C_2 = 1.0 - 1.5$ and $C_4 = 0.016 - 0.032$.

Table 3.2 Stand-off predictions in frozen flow over a sphere at $M = [4, 8, 16, 32]$

M	$h_0(\text{MJ/kg})$	$N_x \times N_y$	ρ_s/ρ_∞	$\Delta^*/d (\times 10^{-2})$	$\Delta/d (\times 10^{-2})$	$\epsilon_\Delta(\%)$
4	1.27	600×900	4.88	8.40	8.37	-0.4
8	4.18	900×1350	6.74	6.08	6.20	1.9
16	15.8	1000×1500	7.96	5.03	5.14	2.1
32	62.4	1100×1650	8.71	4.71	4.82	2.4

Figure 3.4 shows the surface pressure coefficient distribution is within 5% of the modified Newtonian theory (in the limit as $M \rightarrow \infty$). Figure 3.5 shows smooth flow-fields of primitive variables across the Mach number range and visible reduction in the shock stand-off distance at $M = 32$ when compared to $M = 4$.

Fig. 3.4 Surface pressure coefficient (C_p) predictions in frozen flow over a sphere at $M = [4, 8, 16, 32]$ compared with modified Newtonian result in the limit $M \rightarrow \infty$.

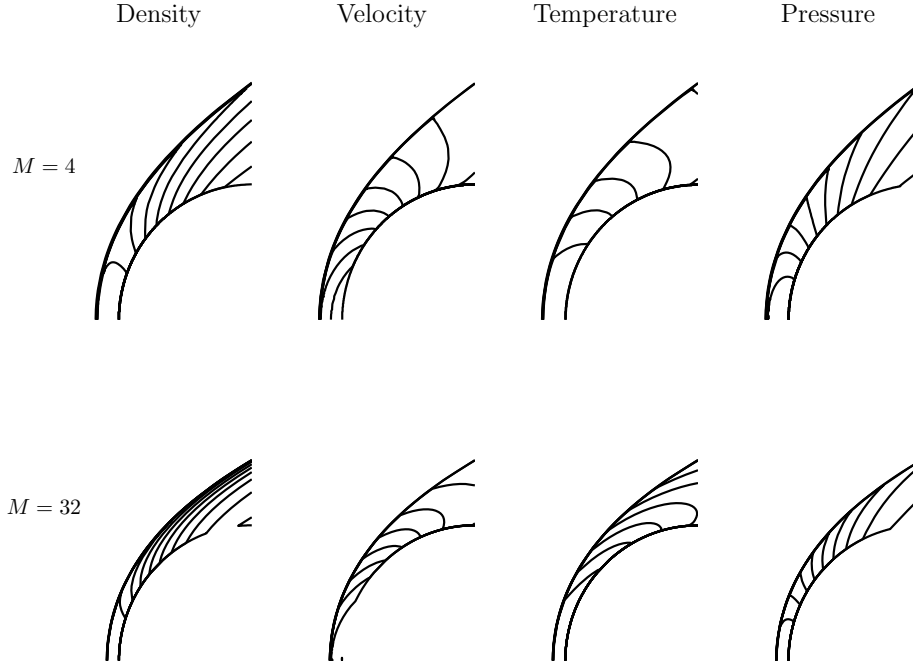


Fig. 3.5 Contour plots of primitive variables of frozen flow around a sphere at $M = 4$ and $M = 32$.

Reacting

Small values of $\tilde{\Omega}$ mean chemical timescales are larger than the flow timescales, whereas large values suggest the opposite. Based on this, two contrasting cases are selected to test the numerical method over the possible range of $\tilde{\Omega}$:

$$\begin{aligned} \text{slow with } M = 10, \quad p_\infty = 10^3, \quad \tilde{\Omega} = 0.3, \quad \rho_s/\rho_e = 0.71; \\ \text{fast with } M = 10, \quad p_\infty = 10^4, \quad \tilde{\Omega} = 30, \quad \rho_s/\rho_e = 0.77. \end{aligned}$$

The free-stream temperature is $T_\infty = 300\text{K}$ and the fluid is five species air (N_2, O_2, N, O, NO) with Park's mechanism (Park, 1990). Note, this numerical test is independent of the specific chemical mechanism, as the analytical stand-off predictions account for the rate of reactions. Moreover, this is a rare method of validation. In the author's knowledge, only Wen et al. (2018) have taken this approach before. The domain is $[1, 5/3]d$ with the sphere diameter (d) equal to 0.24 m. The base mesh is $[288 \times 580]$ with 2 levels of refinement around shock and boundary, as shown in Fig. 3.6. Once the shock is fully developed the AMR mesh has around 300×10^3 grid points, solid and fluid combined. The AMR parameter's values are same as in Section 2.2.3; the CS4-JST shock capturing parameters are $C_2 = 1.0$, $C_4 = 0.064$, where a higher value of C_4 is used to maintain stability at high Mach numbers; the IBM image

point distance parameter takes its default value, $\alpha_{im} = 1.0$. The flow is initialised with $M = 5$ everywhere with the inflow at $M = 10$, and free-stream temperature and pressure everywhere. The CFL number is kept around 0.3, the simulation is computed for 10 flow times and the computational cost is around 160 CPU hours with 16 processors (10 hours total runtime). The domain boundary conditions, considering the schematic in Fig. 3.6: free-stream inflow on the left boundary, and zero-gradient in primitive variables for all other boundaries. For the immersed boundary, no-slip, constant wall temperature and zero pressure gradient conditions are imposed.

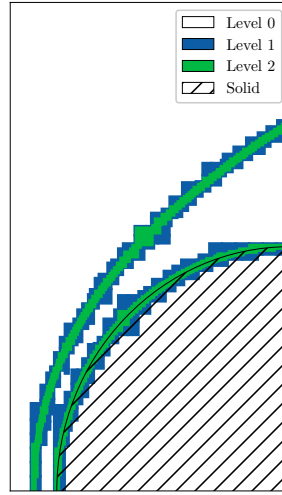


Fig. 3.6 Refined mesh around the bow shock and sphere immersed boundary.

Figure 3.7 shows the stand-off predictions from the numerical method have around 5% discrepancy compared to theory, where Equations (3.14) and (3.15) are used to calculate the theoretical stand-off. Wen et al. (2018) also observed errors of 6% between their numerical method and the theory. Note, their results are with a different numerical method to the current work, but its details are not important and therefore not described here. Figure 3.8 shows the contours for field variables. The contours are smooth and have more turning points than frozen cases, as in Fig. 3.5 due to chemical reactions. Furthermore, the reduction in stand-off observed with the fast case compared to slow case. More clearly, Fig. 3.9a shows the reduction in stand-off distance of around 0.15 mm (15% reduction from slow case). It also shows, for a fast reaction rate, the temperature profile shows a non-equilibrium region where all the chemical reactions occur before the mixture reaches equilibrium. The flow is in chemical equilibrium close to the stagnation point. In contrast, the flow is still reacting close to the stagnation point with the slow case. This is shown more clearly by Figure 3.9b, where the differences in species mass fractions between the two cases can be around an order of

magnitude at a given point in space. In summary, this case verifies the stability and accuracy of the numerical method with reacting flows.

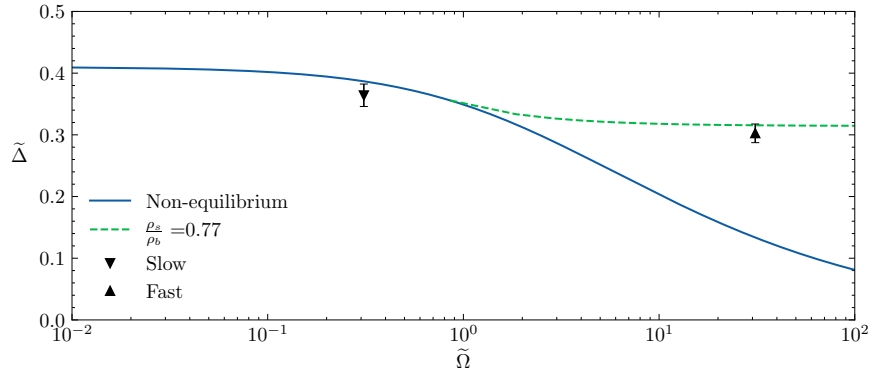


Fig. 3.7 Sphere's shock stand-off distance for slow and fast cases with 5% error bars.

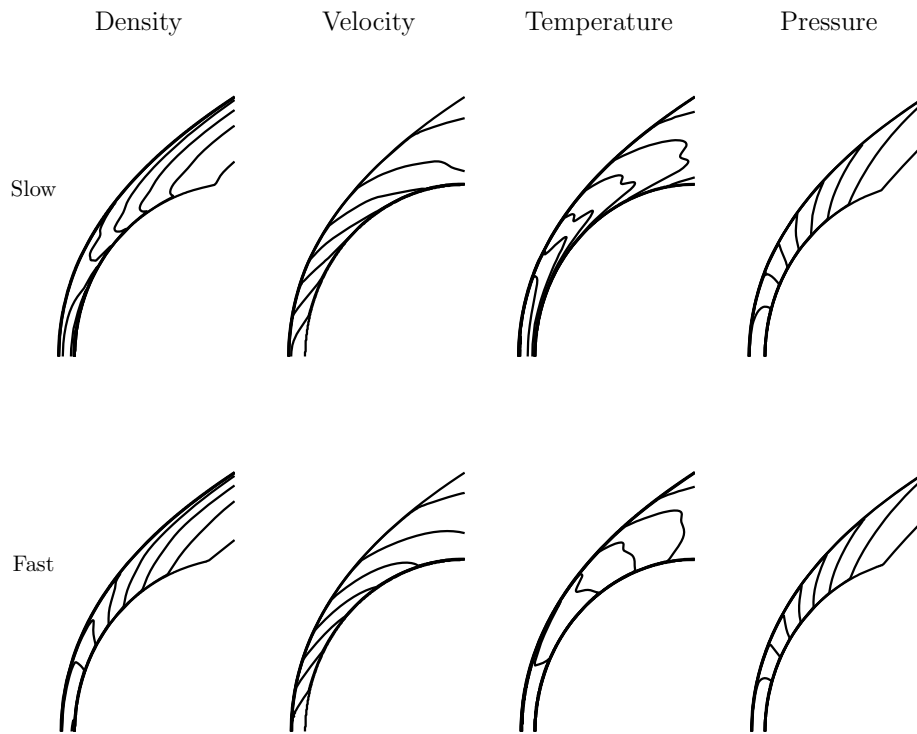
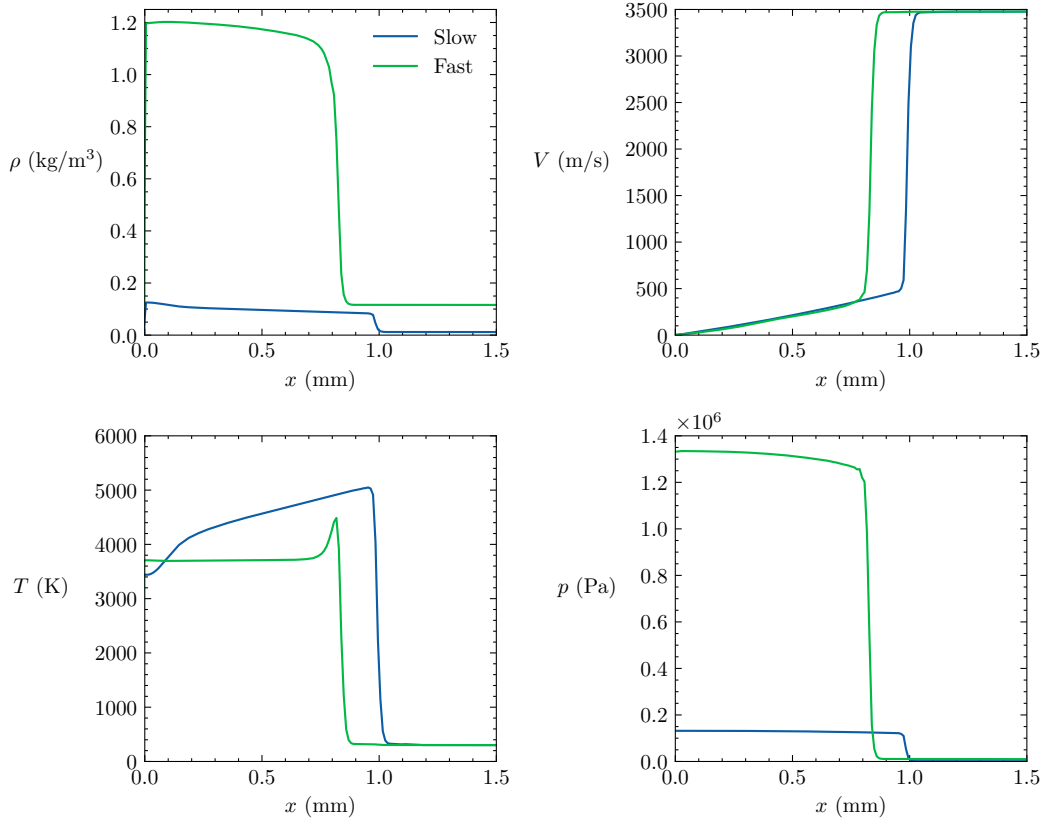
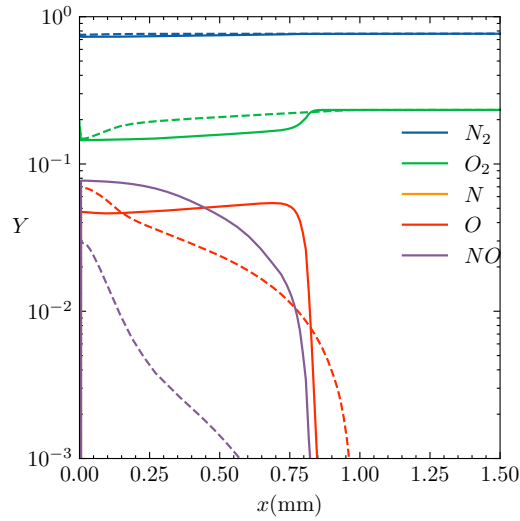


Fig. 3.8 Reacting flow contours around sphere for slow and fast cases.



(a) Primitive variables' density (ρ), velocity (v), pressure (p) and temperature (T).



(b) Composition for slow (---) and fast (—) reacting cases with Air-5 species set and Park's mechanism (Park, 1990).

Fig. 3.9 Sphere stagnation centreline profiles (from the stagnation point at $x = 0$) for slow and fast reacting flow cases.

3.2.2 Flat plate

The primary aim of this case is to test the stability and accuracy of the method with viscous boundary layers. Two subcases are considered: first, grid aligned immersed boundary with horizontal flat plate; second, grid misaligned immersed boundary with inclined flat plate. The second case is a more numerically challenging configuration of the same physical problem. A secondary aim is to observe the mesh resolution required for accurate surface predictions. The free-stream parameters are $T_\infty = 57.8K$, $M_\infty = 6.85$, $Re_L = 5 \times 10^5$, plate length $L = 0.205m$ and wall temperature $T_w = 300K$. The numerical setup matches physical experiments performed by [Smith \(1993\)](#).

Theory

The reference temperature method is a semi-empirical method for engineering accuracy predictions of surface properties in laminar and turbulent hypersonic boundary layers ([Anderson Jr, 2006](#)). The method essentially modifies the incompressible boundary layer results with the help of a reference state denoted by (*), for laminar boundary layers:

$$C_f^* = \frac{\tau_w}{\frac{1}{2}\rho^*u_e^2} = \frac{0.664}{\sqrt{Re_x}}, \quad C_h^* = \frac{q_w}{\rho^*u_e(h_{aw} - h_w)} = \frac{C_f^*}{2}Pr^{*-2/3}, \quad (3.17)$$

$$Re_x^* = \frac{\rho^*u_ex}{\mu^*}, \quad Pr^* = \frac{\mu^*C_p^*}{k^*}, \quad (3.18)$$

$$T^* = T_e \left(1 + 0.032M_e^2 + 0.58 \left(\frac{T_w}{T_\infty} - 1 \right) \right). \quad (3.19)$$

Subscript e represents boundary layer edge conditions, for a flat plate, they can be assumed be the same as free stream (∞) because the oblique shock is weak. Subscript w represents the wall state. T is the temperature, u is the velocity, ρ is the density, M is the Mach number, μ is the viscosity, C_p is the specific heat capacity, k is the thermal conductivity, h is the enthalpy and h_{aw} is the adiabatic wall temperature, C_f^* is the skin friction coefficient, C_h^* is the heat transfer coefficient, Re_x is the Reynolds number based on plate coordinates (tangent to the plate surface and $x = 0$ at the leading edge), and Pr is the Prandtl number.

Presence of the boundary layer introduces a length scale in the computational domain. Parameters exist which indicate the resolvedness of the boundary layer with a given mesh. There are two commonly used parameters: a global parameter, Reynolds number based on mesh size (Re_h); a local parameter, non-dimensional wall normal coordinate (y_h^+). They are

defined as

$$Re_h = \frac{\rho_\infty U_\infty h_w}{\mu_\infty}; \quad y_w^+ = \frac{h_w}{l_v}, \quad l_v = \frac{\mu}{\sqrt{\rho} \tau_w}; \quad (3.20)$$

where h is the local mesh size. Typically, $Re_h \sim O(1)$ is required for converged aerothermal predictions (Ren et al., 2019). Whereas $y_w^+ \lesssim 5$ is required to resolve near-wall flows, which has a physical meaning of having at least one computational point in the viscous sub-layer. If $Pr > 1$, the thermal boundary layer is smaller than the momentum boundary layer, and the thermal boundary layer-based criteria should be considered. Furthermore, with catalytic walls or ablating boundaries, the chemical boundary layer may be of a limiting size (small Schmidt numbers).

Results

Surface properties for the horizontal flat plate: the pressure coefficient (C_p) is defined as in Eq. (3.11); the skin friction coefficient (C_f) and the skin heat transfer coefficient (C_h) are defined as in Eq. (3.17) but with free-stream density and velocity instead of the reference state density and boundary layer edge velocity;

$$C_f = \frac{\tau_w}{1/2 \rho_\infty u_\infty^2}, \quad C_h = \frac{q_w}{1/2 \rho_\infty u_\infty (h_{aw} - h_w)}. \quad (3.21)$$

The wall normal coordinate (y_w^+) is defined as in Eq. (3.20). These properties vary along the length of the plate, where $x = 0$ is the leading edge, as shown in Fig. 3.11a. The figure shows $Re_h = 100$ mesh is clearly not sufficiently refined, but the other meshes produce essentially converged solution. Moreover, the y_w^+ suggests that the leading edge is not adequately resolved. An infinitely sharp edge is enforced by changing the boundary conditions from slip to no-slip on the flat part of the ramp. Such a leading edge needs infinitely small mesh size. Hence, errors in the form of disturbances in C_p , C_f and C_h can be observed. Despite these errors, the agreement with Eqs. (3.18) and (3.19), and Smith (1993)'s experiments is within 1% on average for C_h for the finest mesh. Importantly, the order of convergence of the surface properties are shown to be second-order in Fig. 3.10c, where the error is measured relative to the finest mesh solution.

For the inclined case, 30° to the horizontal, the flow conditions are identical to the horizontal flat plate. The physical domain and the base mesh have the same resolution as the horizontal flat plate, but the domain size is larger. This case is numerically more challenging when compared to the horizontal flat plate test. Because, inclining the immersed boundary results in ghost point re-construction which is not grid aligned and is susceptible to larger errors.

Mesh is refined around the boundary, as shown in Fig. 3.10b. Figure 3.11b shows interesting difference when compared to horizontal flat plate, $Re_h = 100$ gives much better agreement in the inclined flat plate case. This is most likely to be a coincidence due to the sensitivity of the infinitely sharp leading edge. The accuracy is comparable to the horizontal case.

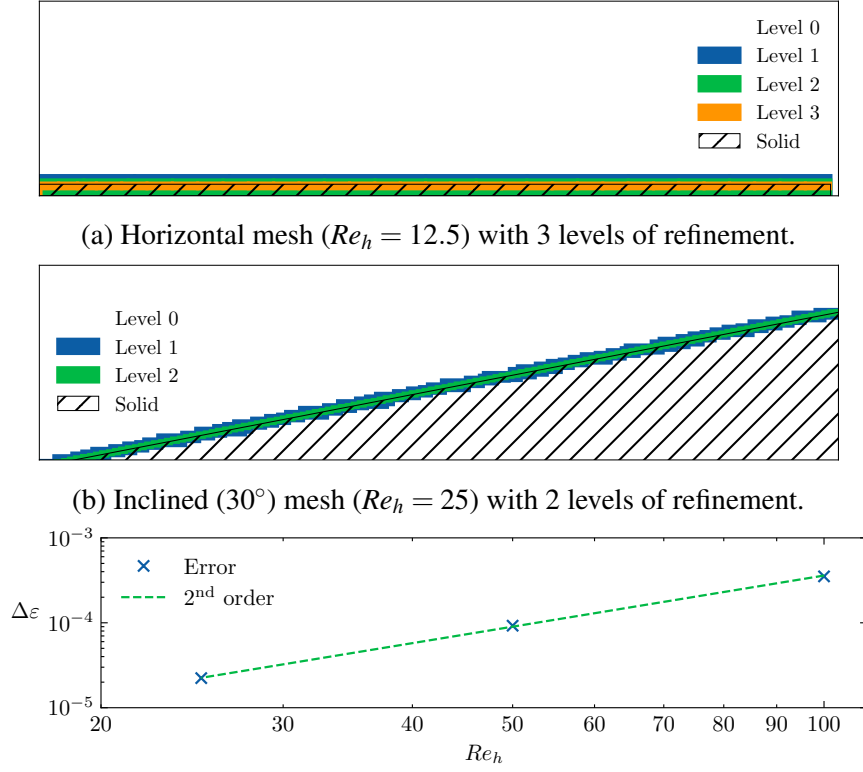
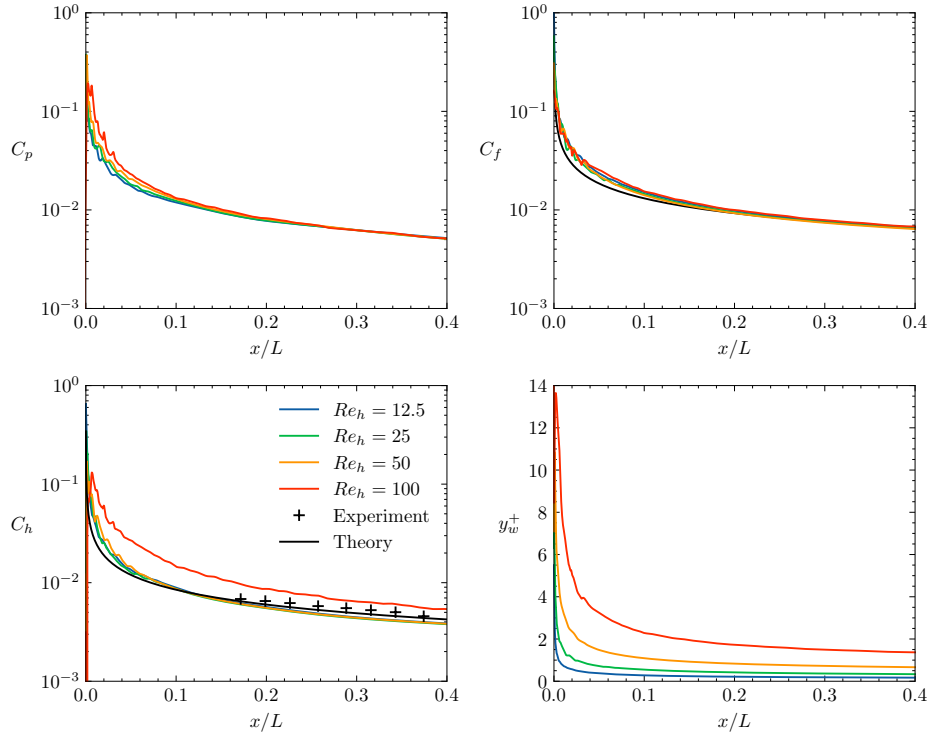
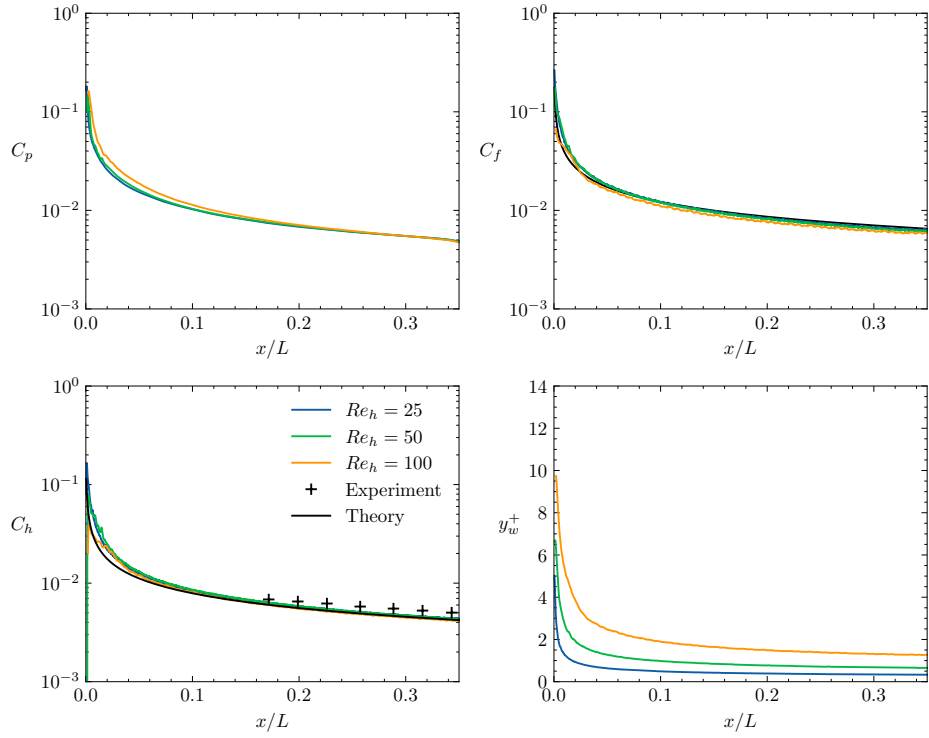


Fig. 3.10 Flat plate case mesh and order of convergence results.



(a) Horizontal.



(b) Inclined (30°).

Fig. 3.11 Flat plate surface properties: coefficient of pressure C_p , coefficient of heat transfer C_h , coefficient of skin friction C_f and non-dimensional wall normal coordinate based on the local mesh size y_w^+ .

3.2.3 Single compression ramp

Aim of this test is to assess the performance of the numerical method with simple steady-state shock-boundary layer interaction in two-dimensions. This test case is a 24° compression ramp from the experiments of (Holden, 1970) and is widely used for numerical method validations (Damm et al., 2020; Grasso and Marini, 1996; Navarro-Martinez, 2003; Rudy et al., 1991). The numerical setup is illustrated in Fig. 3.12. The case parameters are $l = 0.4389\text{m}$, $Re_l = 1.04 \times 10^5$, $M_\infty = 14.1$, $p_\infty = 28.8\text{Pa}$, $T_\infty = 88\text{K}$, $T_w = 297\text{K}$. As in the flat plate cases, the leading edge does not have geometric thickness as it is imposed by switching from slip to no-slip boundary condition. The flow is chemically frozen, as the stagnation temperature is around 3600K which is lower than the dissociation onset temperature of N_2 of 4000K .

A refinement study is conducted in which cases with $Re_h = [40, 20, 10]$. The base mesh is selected arbitrarily with 672×224 points, and the number of refinement levels is selected by ensuring $y_w^+ \sim 1$ at the impingement point. Table 3.3 shows the computational point's distribution and the computational cost for each refinement case. For all meshes, around half of the total grid points are solid points, however they do not contribute to the computational cost and are not reported explicitly. The total number of grid points for the coarsest to the finest mesh are $[400, 742, 1445] \times 10^3$. For the highest resolution mesh, $Re_h = 10$, the finest level mesh size is $32\times$ smaller than the base level mesh size. Moreover, its higher levels contain the half of the total fluid points. Figure 3.13 illustrates the finest mesh. The computational cost increases with a larger factor than the increase in the computational points. For example, $Re_h = 40$ and $Re_h = 20$ have a factor of 1.6 increase in the number of computational points, whereas the cost increases by a factor of 3. This is expected as the time advancement cost of points on level l is 2^l times more than points on level 0. All the simulations are computed for 10 flow times, where a flow time is equal to $2l/u_\infty$, approximately $300\mu\text{s}$.

The AMR parameter values are: `max_grid_size` = 64; `cluster_minwidth` = 16; `cluster_min_eff` = 0.95; and the other parameters keep the same value as in Section 2.2.3. The maximum grid size is increased to ensure that there are not too many patches, reducing the number of patches reduces the number of halo points which need to be communicated. But, the maximum grid size is small enough to ensure even load distribution across processors. The simulations are initialised at the free-stream temperature and pressure everywhere and $M = 10$, with inflow at the free-stream Mach number. To maintain stability with this impulsive initialisation and CS4-JST, $C_2 = 1.0$ is required. After transients (two flow times) it is reduced to its default value, $C_2 = 0.5$, while $C_4 = 0.032$ throughout the computation.

The IBM image point distance parameter takes its default value, $\alpha_{im} = 1.0$. The domain boundary conditions, considering the schematic in Fig. 3.12: free-stream inflow on the left boundary, and zero-gradient for all other boundaries. For the immersed boundary, no-slip, constant wall temperature and zero pressure gradient conditions are imposed.

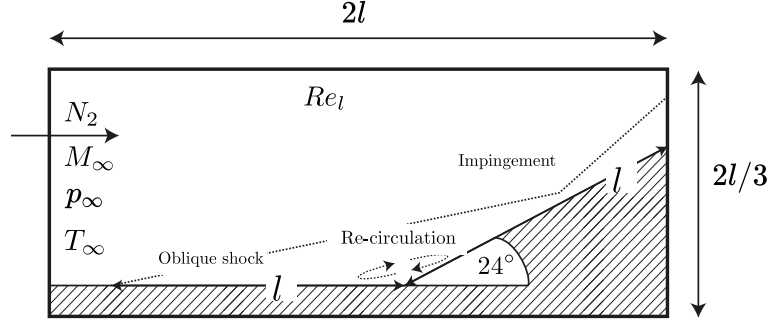


Fig. 3.12 Single compression ramp numerical setup.

Table 3.3 Compression ramp refinement cases ($Re_h = [40, 20, 10]$) computational fluid points distribution and cost.

Re_h	Fluid points per refinement level ($\times 10^3$)							Cost (CPU hours)
	0	1	2	3	4	5	Total	
40	123	16	30	70	-	-	239	450
20	123	18	28	58	162	-	389	1350
10	123	19	45	49	125	461	822	3360

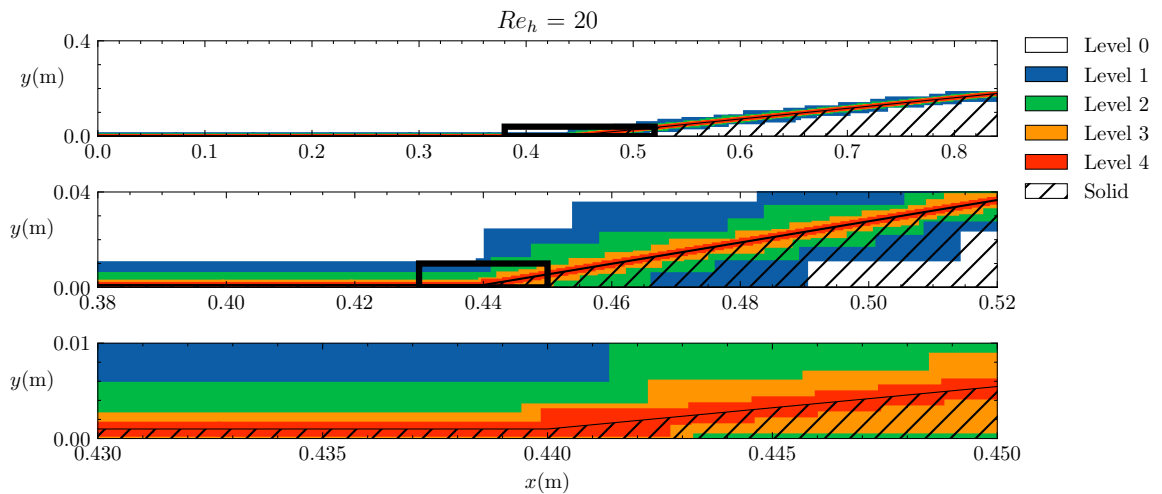


Fig. 3.13 AMR $Re_h = 20$ mesh with successively zoomed views of the near wall mesh around the compression corner.

The surface properties are defined as in Section 3.2.2, except C_h which is defined as $C_h = q/\rho_\infty u_\infty (h_0 - h_w)$, (consistent with literature (Holden, 1970)) where h_0 is the flow stagnation enthalpy. Figure 3.14 shows the surface properties where there are 25×10^3 to 100×10^3 surface elements and the surface properties are smoothed with moving average of 100 adjacent elements. The figure shows that the profiles qualitatively agree well with experiments, the flat plate region, the separation point, re-circulation region and impingement point are clearly visible. The minimum and maximum values of C_p , C_f and C_h converge with increasing mesh resolution. However, the profiles are shifted in space as the separation point moves forwards with lower mesh resolution.

The C_p profiles are smooth and almost identical for the highest two mesh resolutions, and excellent quantitative agreement with the experiment is observed. The location of the separation point and the impingement point is accurately predicted with $Re_h = 10$ and 20.

The C_f profiles are smooth generally, except around the impingement area. The $Re_h = 10$ mesh peak is slightly shifted towards the leading edge and is smaller in magnitude when compared to $Re_h = 20$. This could be due to lack of refinement around shockwave and shock layer with large gradients. The minimum value of C_f at the re-attachment point converges and its magnitude agrees excellently with the experiment.

The C_h profiles suggest that $Re_h = 40$ mesh under-predict the peak heat transfer. $Re_h = 20$ and 10 predict the peak heat transfer very accurately, however, the re-circulation region and post-peak region heat transfer is under-predicted.

A body-fitted mesh with the same test case requires 310×10^3 points with $Re_h = 1$ (Navarro-Martinez, 2003) and gives similar accuracy when compared to the experiments. SAMR-GPIBM approach here has a larger near-wall mesh size but around $\times 2$ the number of computational points. Considering the y_w^+ profiles, the mesh requirement over the surface is not uniform, as expected. The impingement point has more than $\times 10$ the y_w^+ than the flat part of the compression ramp away from the leading edge. This suggests that a more efficient mesh could be generated with refinement criteria based on local y_w^+ . This could lead to an AMR mesh with similar number of computational points as body-fitted methods. However, the overall computational cost between the AMR-IBM approach and body-fitted meshes is not clear by simply comparing the computational points. As the global time-stepping used in body-fitted meshes is less efficient than local time-stepping. Therefore, direct comparisons are required to definitely assess the cost-accuracy benefits of AMR-IBM and body-fitted approaches

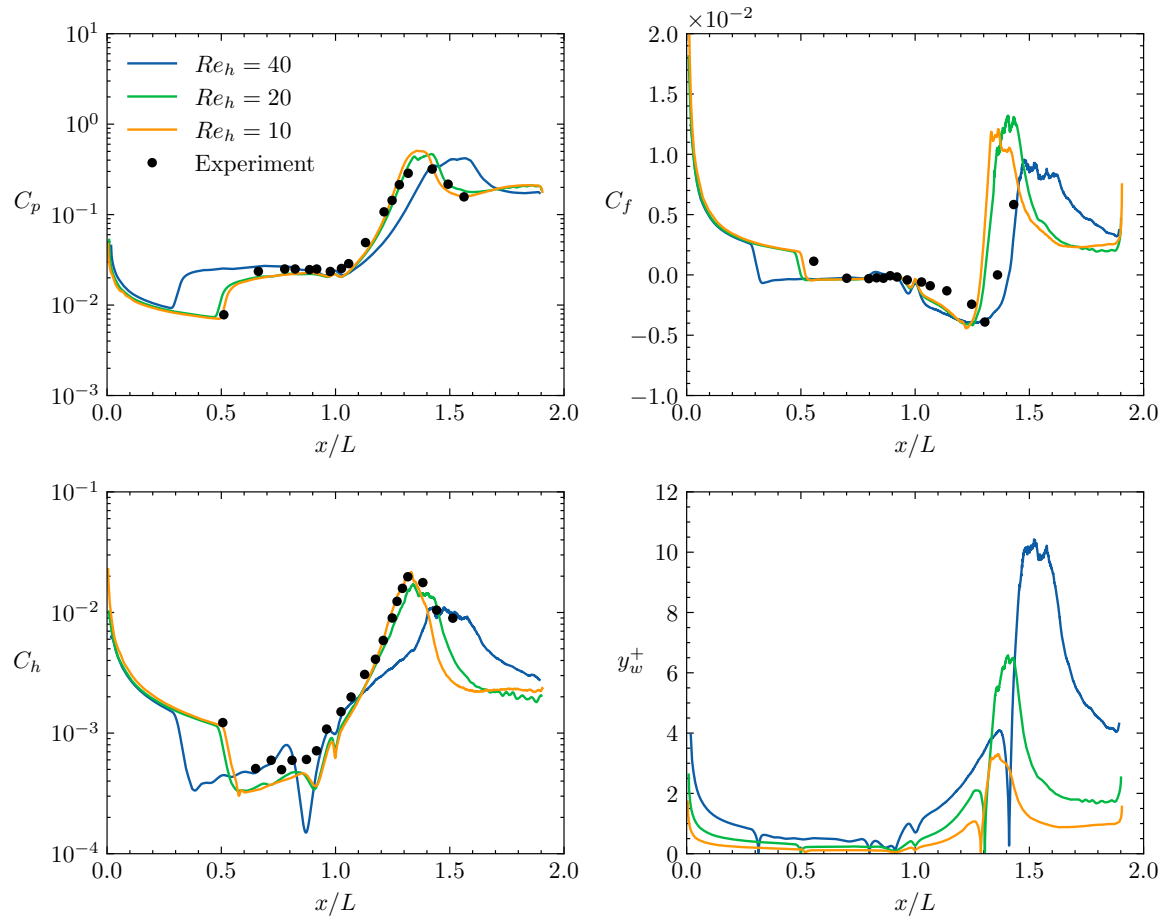


Fig. 3.14 Single compression ramp surface properties: coefficient of pressure C_p , coefficient of heat transfer C_h , coefficient of skin friction C_f and non-dimensional wall normal coordinate based on the local mesh size y_w^+ .

3.2.4 Double compression ramp

This case aims to test the numerical method with a challenging numerical problem involving unsteady shock-shock and shock-boundary layer interactions in two-dimensions, it was originally created to assess the CFD capability for predicting shock-boundary layer interactions (Knight et al., 2017; Swantek, 2012). While this case has been simulated by various different authors, the numerical investigation of the case with SAMR-GPIBM method is novel.

Figure 3.15 illustrates the numerical setup. It shows that the forward 30° ramp generates a forward oblique shock, and the rear 55° ramp angle generates a detached bow shock. The interaction of the bow shock with the oblique shock results in a separating boundary layer on the forward ramp. The separation forms a separation shock and a re-circulation region. The reattachment of the boundary layer on the rear ramp causes a local peak in surface heat transfer. The separation shock intersects with bow shock and forms a triple point above the separation region. A second triple point is formed by the intersection of the shock emanating from the first triple point and the bow shock. This generates a strong shear layer with a subsonic flow and a shock expansion beneath. Moreover, the flow is chemically frozen as the stagnation temperature is around 2000 K—much lower than dissociation temperature of N_2 of around 4000K, so thermochemical non-equilibrium modelling is not required. The case parameters are:

$$\begin{aligned} M_\infty &= 7.11, h_0 = 2.1 \text{ MJ/kg}, T_\infty = 191 \text{ K}, T_w = 298 \text{ K} \\ P_\infty &= 391 \text{ Pa}, l = 0.0254 \text{ m}, L = 0.06 \text{ m}, \tau_{test} = 270 \mu\text{s}, Re_L = 6.6 \times 10^4; \end{aligned} \quad (3.22)$$

where h_0 is the stagnation enthalpy, l is the geometry length parameter, L is the characteristic length scale and Re_L is the Reynolds number based on the characteristic length, is the test time (τ_{test}) from experiments and the working fluid is N_2 gas.

A mesh refinement study is performed with $Re_h = [12, 6, 3]$. The base mesh is 768×1024 and additional refinement levels are added near the immersed boundary. Figure 3.16 shows the finest AMR mesh ($Re_h = 3$) with 5 levels of refinement near walls, the smallest mesh size is $3.05 \mu\text{m}$ and $32\times$ smaller than the largest mesh size. Table 3.4 shows the fluid computational points distribution across refinement levels. The finest mesh has around 70% more points in total than the coarsest mesh, and the finest level has about half the number of points than the base mesh. All cases are computed for $300 \mu\text{s}$ to match the test time of the experiments and the computational cost for each case is also reported.

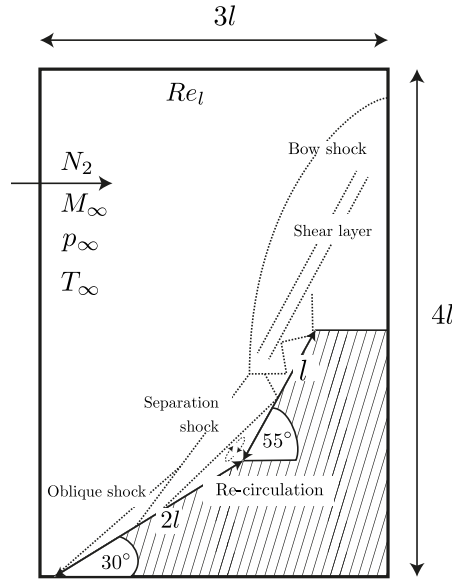


Fig. 3.15 Double ramp numerical setup.

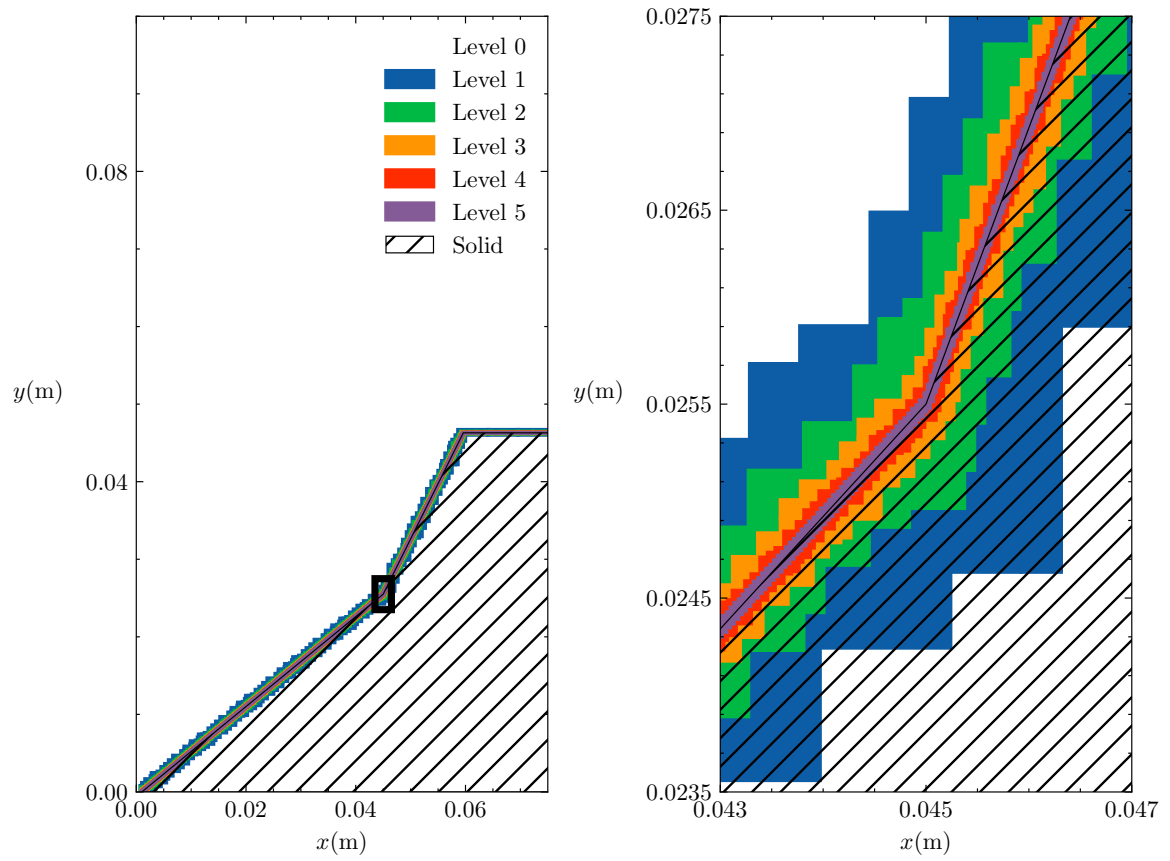


Fig. 3.16 Double ramp AMR mesh with uniform 5 levels of refinement around walls.

Table 3.4 Double compression ramp case AMR mesh points count.

Re_h	Fluid points at each refinement level ($\times 10^3$)							Cost (CPU hours)
	0	1	2	3	4	5	Total	
12	598	27	47	76	-	-	747	590
6	598	29	56	92	153	-	926	1010
3	598	30	60	106	187	307	1288	2430

The AMR parameter values are: $\text{max_grid_size} = 128$; $\text{cluster_minwidth} = 8$; $\text{cluster_min_eff} = 0.95$; and the other parameters keep the same value as in Section 2.2.3. The maximum grid size is increased to ensure that there are not too many patches, reducing the number of patches reduces the number of halo points which need to be communicated. But, the maximum grid size is small enough to ensure even load distribution across processors. The simulations are initialised at the free-stream conditions everywhere, uniform in space. To maintain stability with this impulsive initialisation and CS4-JST, $C_2 = 1.0$ is required. After transients (two flow times) it is reduced to its default value, $C_2 = 0.5$, while $C_4 = 0.016$ throughout the computation. The IBM image point distance parameter takes its default value, $\alpha_{im} = 1.0$. The domain boundary conditions, considering the schematic in Fig. 3.12: free-stream inflow on the left boundary, and zero-gradient for all other boundaries. For the immersed boundary, no-slip, constant wall temperature and zero pressure gradient conditions are imposed.

Figure 3.17 shows numerical schlieren over slightly longer time (up to $300\mu\text{s}$) than experimental test time ($270\mu\text{s}$). It shows flow field features like oblique shock, bow shock, separation shock, triple points and shear layer—as illustrated in Fig. 3.15. The numerical schlieren agrees well with experimental schlieren in Fig. 3.18 for up to $210\mu\text{s}$. The fine details of the flow field are very faint in the experimental schlieren, but larger features like oblique shock and triple point can be located more clearly. For later times, the numerical simulation's re-circulation zone grows rapidly, becoming larger than the one observed in experimental schlieren. However, the growth of the re-circulation zone is likely to be inaccurate in two-dimensional planar simulations as separation and attachment are fundamentally three-dimensional phenomena (Détery, 2001). Moreover, this particular case has been observed to show three-dimensional effects (Reinert et al., 2020) caused by the shock interactions, separated region or both, which results in asymmetry about the mid-plane in the spanwise-direction. In the current simulations, the discrepancy in numerical schlieren is only a problem towards the end of the simulation time, after $210\mu\text{s}$. Hence, accurate surface results maybe achieved despite the erroneous behaviour of the separation region growth.

In Fig. 3.17, as the separation zone increases ($150\mu\text{s}$ onwards), the primary re-circulation zone divides into secondary and tertiary regions. This physical behaviour, the fragmentation of the primary re-circulation zone forming nested persisting smaller re-circulations has been reported by Gai and Khraibut (2019).

The surface properties are defined as in Section 3.2.2, except the heat transfer coefficient $C_h = q_w / \rho_\infty u_\infty h_0$, where h_0 is the stagnation enthalpy. Figure 3.19 shows time averaged surface properties over the test period with sampling frequency of $10\mu\text{s}$. The C_p is mostly independent of the mesh, apart from the separation region which is to be sensitive to the mesh. The C_f and y_w^+ peak on the rear ramp close to the triple points and at the leading edge. The y_w^+ is around $\times 4$ larger on close to the wall near the triple point when compared to the front ramp away from the leading edge.

The C_h in Fig. 3.19 follows a laminar ramp profile initially and then becomes oscillatory in the re-circulation region. The agreement is mostly within experimental results. Since the flow is unsteady and current simulations are in two-dimensions instead of three, it is not expected to match exactly. The peak heat transfer is well predicted, especially when compared to the reference results by Durna and Celik (2019) with body-fitted mesh. Their finest mesh contains around 300×10^3 points, which is around 1/4 of the current mesh. An AMR mesh with refinement ratio of 4 instead of 2 (used currently due to implementation) can half the number of refinement levels required and the computational points. With the extra computational points, the current method predicts the peak heat transfer more accurately. However, the discrepancy in wall heat flux on the rear ramp is around 50%, this is likely due to three-dimensional effects. Such effects in this case have been shown by Reinert et al. (2020), where they suggest the time-averaged heat transfer can vary in the spanwise-direction by $O(10\%)$ and the instantaneous heat transfer by as much as $\times 2$. Hence, the two-dimensional simulations are not expected to match exactly with experiments. A three-dimensional simulation would require $O(100\text{M})$ computational points, especially with isotropic mesh—a constraint in the current implementation.

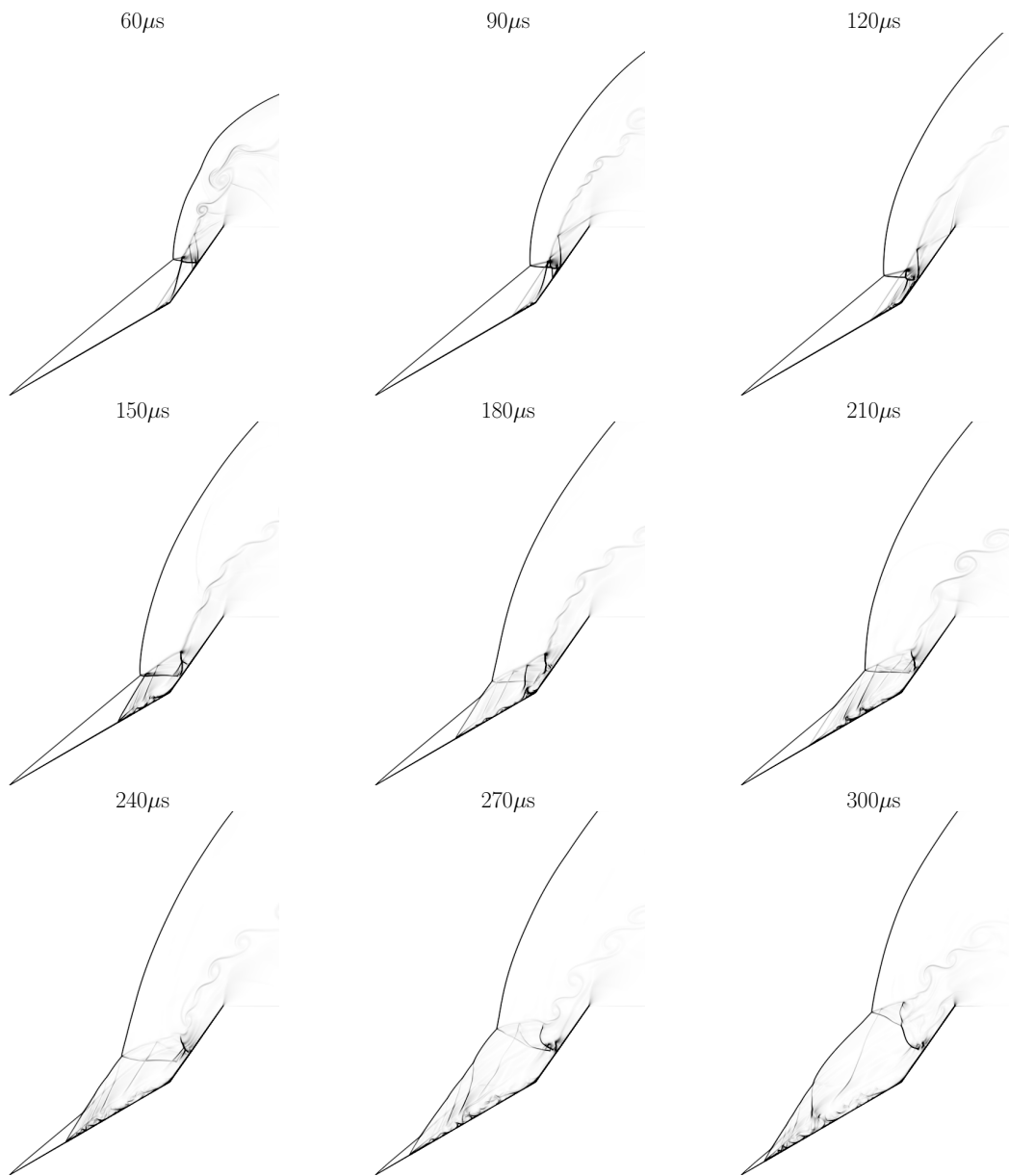


Fig. 3.17 Double ramp schlieren images from two-dimensional numerical simulation with the finest mesh ($Re_h = 3$).

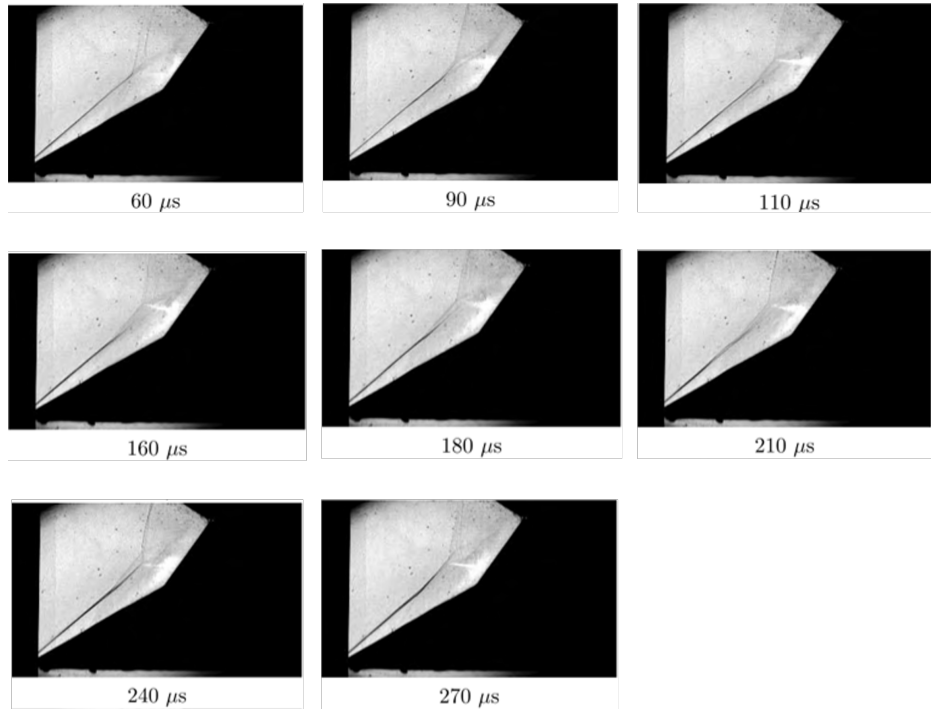


Fig. 3.18 Double ramp schlieren images from experiments (Swantek, 2012).

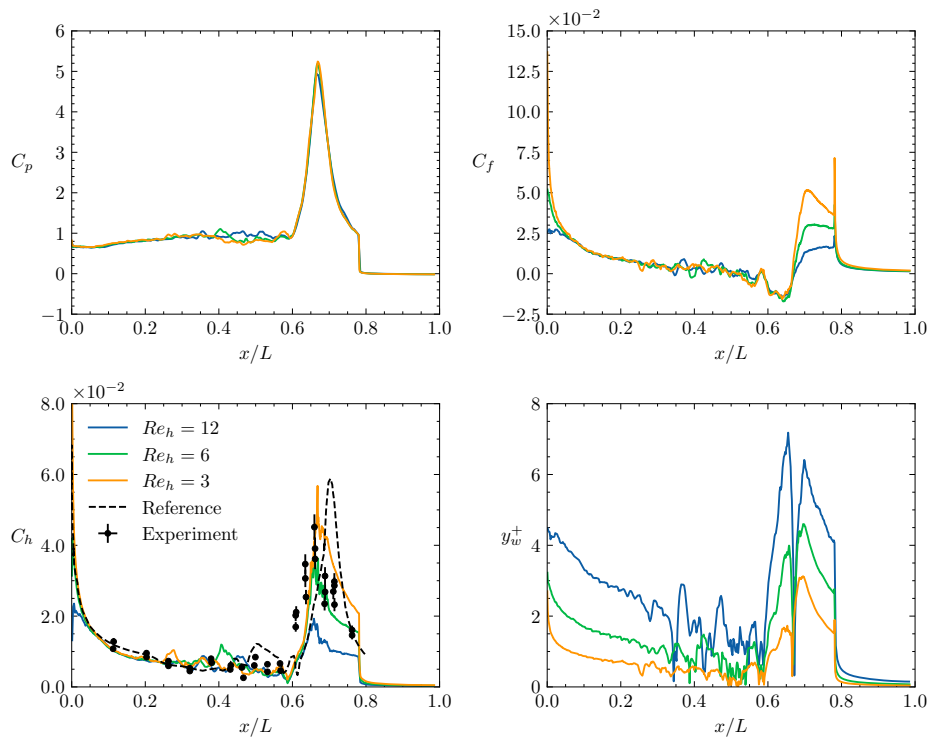


Fig. 3.19 Double ramp case time averaged surface properties.

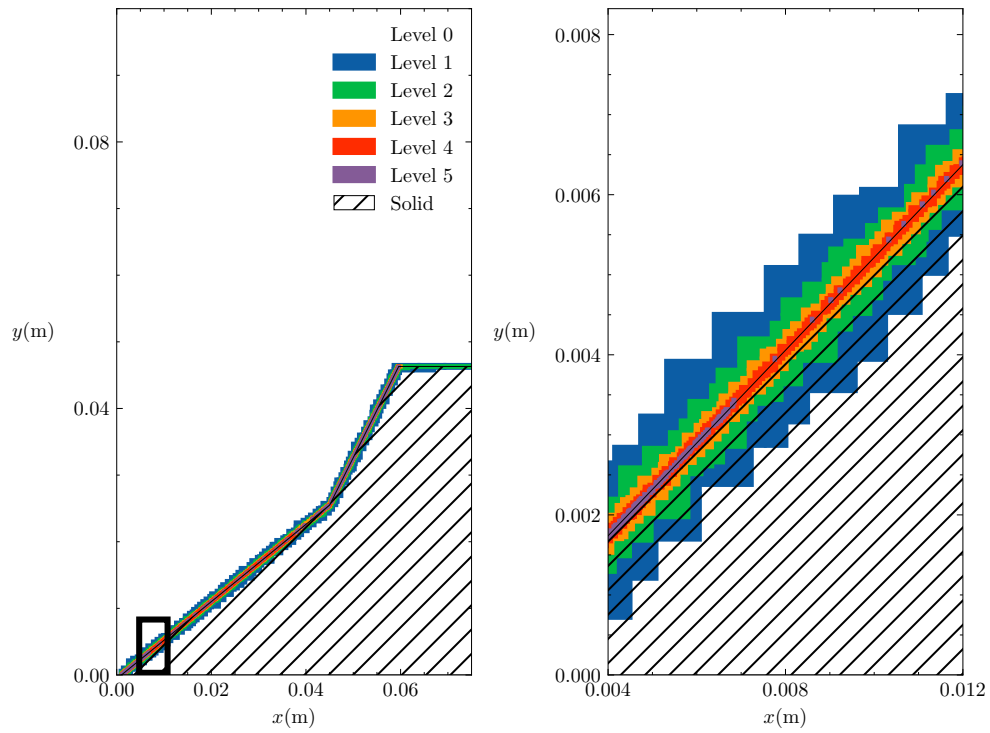
Effect of adaptive mesh refinement

All previous tests use simple refinement criteria based on the proximity to the wall. Surface properties in Figs. 3.11a, 3.14 and 3.19 suggest that y_w^+ varies significantly with location on the body. Considering this, how much can a refining strategy based on local y_w^+ improve the computational cost to accuracy ratio? Also, previously no additional resolution was added around shock interactions. Does adding resolution around shock interactions improve the accuracy of results in this case? To answer these questions, the following cases are considered: case A with refinement where $y_w^+ > 2$; case B with refinement where $y_w^+ > 2$ and two levels of refinement around shock waves; and Base case with a fixed mesh around wall only (from Fig. 3.19). Figure 3.20a shows case A mesh with a higher resolution near the leading edge and on the rear ramp compared to central parts of the forward ramp. Figure 3.20b shows Case B mesh, essentially with case A mesh with two levels of refinement around shock waves. Figure 3.22 shows the number of computational points varying with time. It shows that there are around 25% more computational points with case B compared to the base case, whereas case B has around 25% fewer computational points.

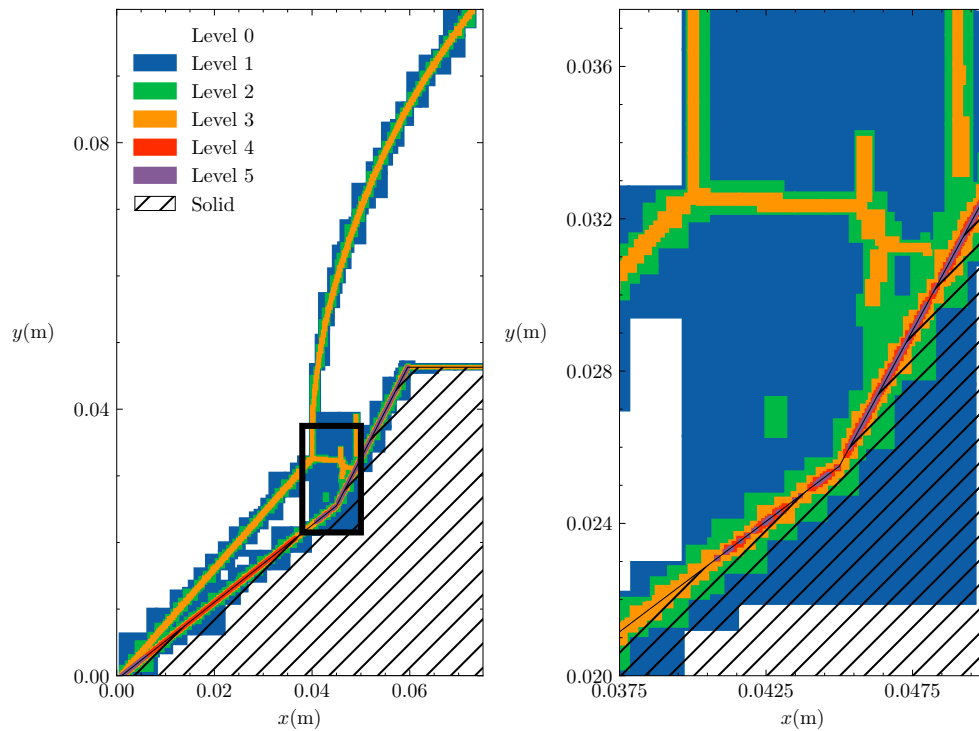
Figure 3.21a shows numerical schlieren comparison between case A, with wall y -plus based refinement, and the base case with a fixed mesh. The figure shows that the flow structures are visually identical at the beginning, after which case A's re-circulation zone grows slower and discrepancy between the two cases in the shock positions appear around $240 \mu s$. Figure 3.21b shows numerical schlieren comparison between case B and fixed mesh case. It shows that case B, similar to case A, also starts deviating from the base case around $240 \mu s$. However, at later times case B agrees better with the base case than case A. Clearly, the meshing strategy can significantly affect the flow features' development.

Lastly, Fig. 3.23 shows the time averaged surface properties for the three cases. The surface pressure peak variation is around 15% between case A and B compared to the base case. A taller and sharper peak is observed with case B and an attenuated peak with case A. This suggests that refining around the shock (with case B) results in higher surface peak pressure. Moreover, the rear ramp shear stress and heat transfer differ significantly, as much as around 50%; and surprisingly, the both the quantities are lower when shock interactions are better resolved in case B.

Overall, these cases suggest that the surface properties are very sensitive to mesh resolution around shock-shock and shock-boundary layer interactions. In such cases, body-fitted methods are disadvantaged and plagued with complex meshes, whereas AMR methods are much better suited in such cases. However, AMR meshing strategy needs to be carefully selected for accurate results.

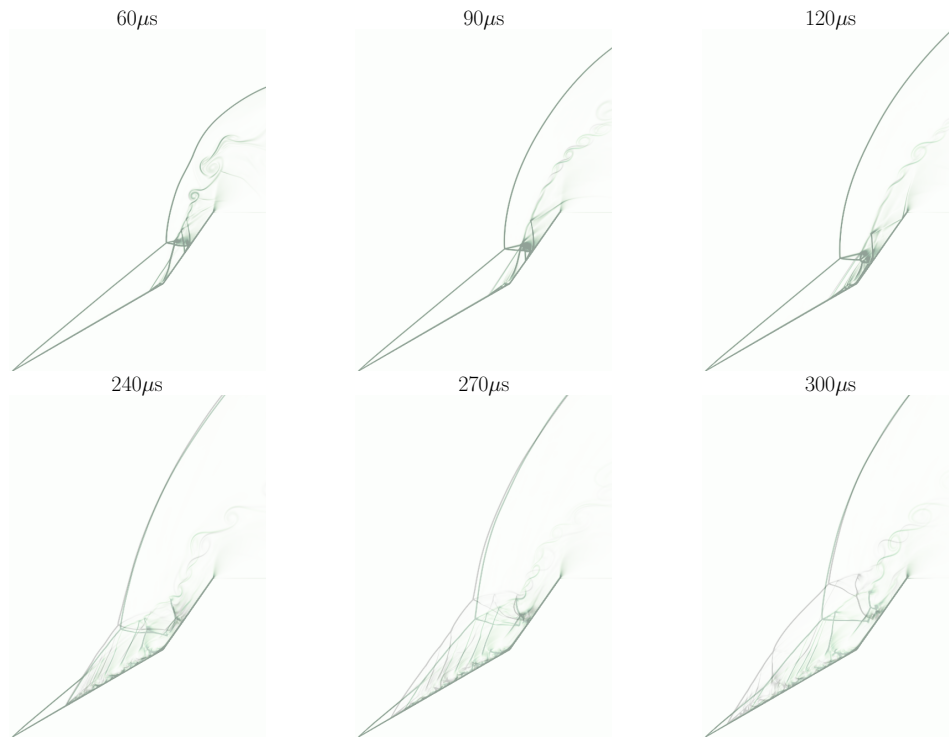


(a) Case A whole mesh (left) and zoomed-in view just after the leading edge (right).

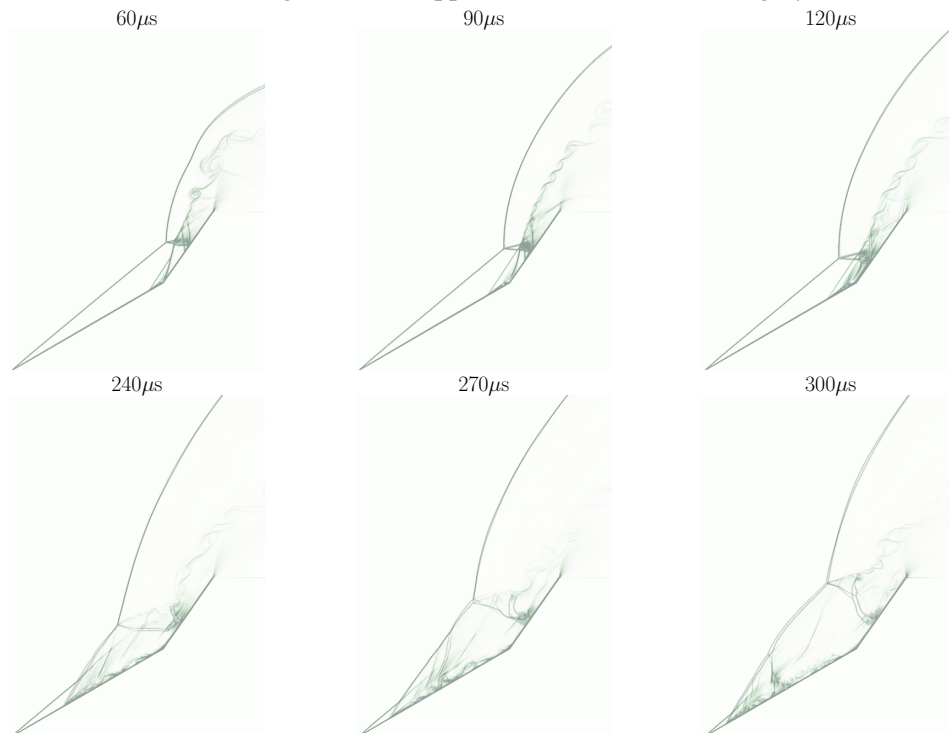


(b) Case B whole mesh (left) and zoomed-in view close to the two ramp surfaces' intersection (right).

Fig. 3.20 Double ramp instantaneous AMR meshes at $120\mu s$ for Case A and Case B.



(a) Case A (green) overlapped with fixed mesh case (grey).



(b) Case B (green) overlapped with fixed mesh case (grey).

Fig. 3.21 Double ramp numerical schlieren image comparison over time.

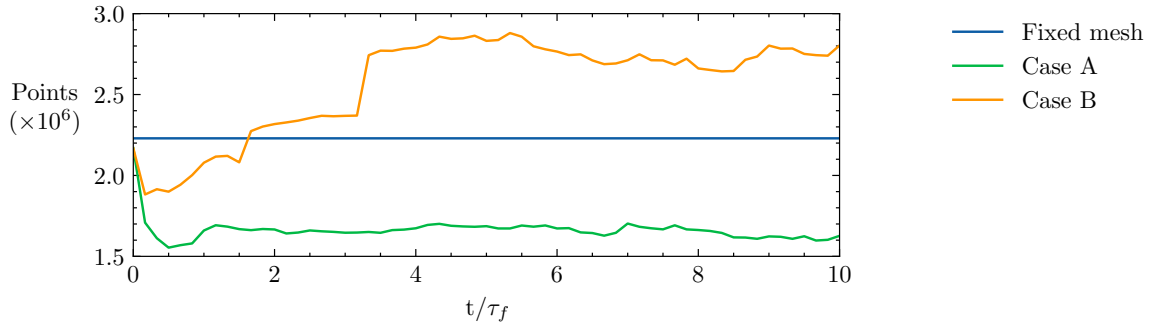


Fig. 3.22 Double ramp case number of AMR mesh points varying over time with different meshing strategies.

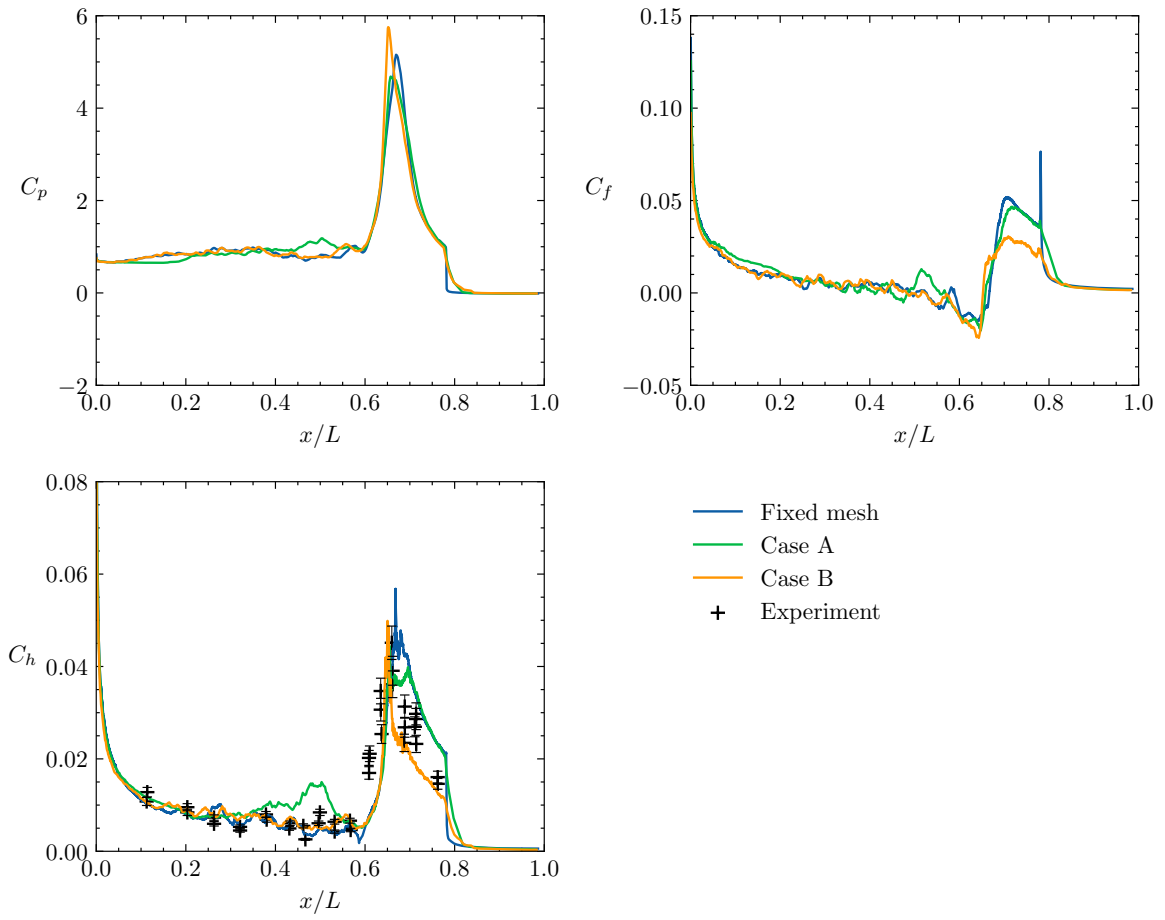


Fig. 3.23 Time averaged surface properties with 5 level AMR mesh but different meshing criteria.

3.2.5 Supersonic turbulent channel flow

This case aims to test the numerical method's performance by modelling turbulent supersonic flows. The numerical setup is almost identical to case C from Section 2.3.5 and is not repeated here. The only difference is that the channel walls are represented by IBM, and shock-capturing is used with $C_2 = 0.5$. The shock-capturing ensures stability during initialisation, where the fluctuations are less correlated and more violent.

Figure 3.24a shows that the channel mean flow profiles with IBM and without IBM (conformal boundary) are similar. The mean pressure is 3% higher with the IBM case, likely due to shock-capturing. Fig. 3.24b shows that the average velocity fluctuation kinetic energy is also similar, and the shock-capturing reduces the dissipation of velocity fluctuations. Turbulent channel flow is very sensitive to errors, as they accumulate over time in the closed system. However, open systems like external boundary layers are expected to be less sensitive to the accumulation of errors. For these, the current method is expected to be even more accurate than in the current case.

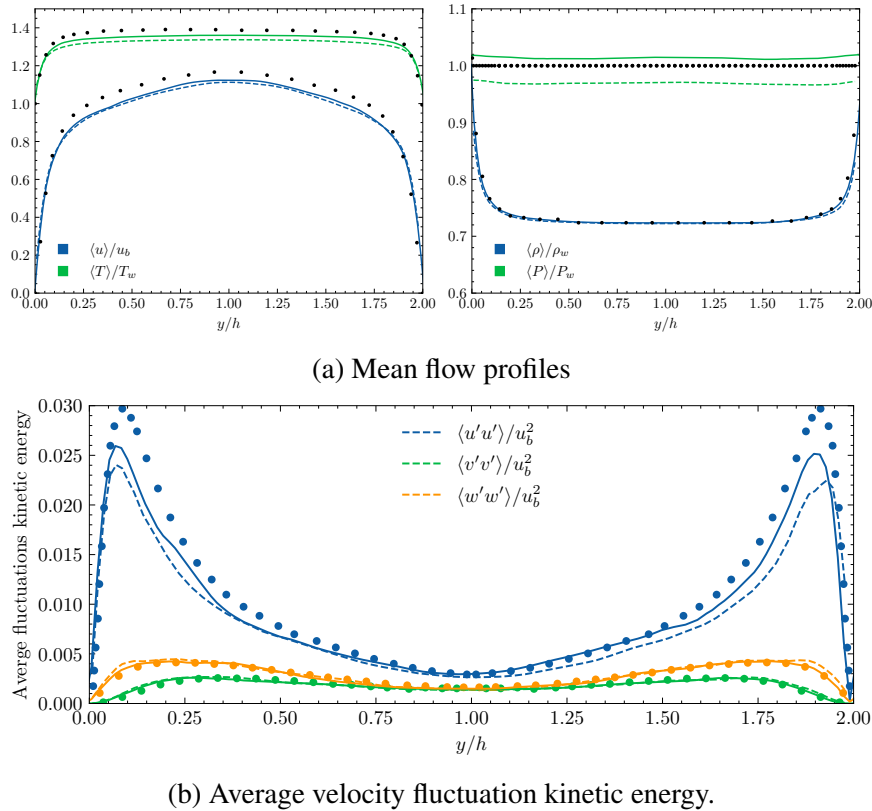


Fig. 3.24 Supersonic turbulent channel flow profiles with IBM walls (—) compared with conformal boundary (---), and with reference results (·) from (Foyi et al., 2004).

3.2.6 Transversely oscillating cylinder

The aim of this case is to test the numerical method's ability to model moving boundaries. Although the current work focuses on hypersonic flows, near-wall flow is always subsonic, which justifies the selected test case. This test case has been studied extensively, both numerically (De Vanna et al., 2020; Khalili et al., 2018; Schneiders et al., 2013) and experimentally. All studies are not listed here, only the most relevant ones - studies with IBM. It involves vortex shedding from the cylinder reaching a periodic steady-state, synchronising with its forced periodic motion.

Setup

The Reynolds number based on the cylinder diameter and the free-stream density and velocity is $Re_L = 185$, where L is the cylinder diameter. The vertical oscillatory motion is imposed by $y_c = -A \cos(2\pi f_c t)$; where the amplitude of motion is $A = 0.02L$ and frequency $f_c = 0.8f_0$. The motion is selected to be slower than the flow for simplicity. The vortex shedding frequency (f_0) can be characterised by the Strouhal number (S_0), which follows Williamson's universal law (Williamson, 1988), $S_0 = f_0 L / u_\infty = 0.195$. A subsonic free-stream is chosen at $M_\infty = 0.1$. Zero gradient and inflow boundary conditions are used, and characteristic boundary conditions are not used. Instead, a large computational domain is selected to minimise the boundary's effect on the flow field. Efficient computations on such a large domain with highly localised resolution requirements are ideal for AMR. In 2D, the domain size is $60L \times 30L$ with the finest mesh size² of $0.01L$ and the body is represented by 628 elements (half of the mesh size). In 3D, the domain size is $32L \times 16L \times 2L$ with the finest mesh size of around $0.08L$, and 140^3 elements. The mesh size is larger in 3D to minimise computational cost. Both cases use three levels with refining around the body only. Mesh from 2D simulation is shown in Fig. 3.25. The cylinder's position is $(x_c, y_c, 0)$. The acoustic CFL is kept around 0.5, with total simulation time of $700\tau_f$, where a flow time is $\tau_f = L / \sqrt{\gamma RT_\infty}$. Re-gridding occurs every $2\tau_f$, and surface properties are calculated every time-step.

²Mesh refinement study is not repeated here, as it can be found in previous works same resolution as (De Vanna et al., 2020) is used.



Fig. 3.25 Transversely oscillating cylinder with 2D AMR mesh.

Results

Figure 3.26 shows the vorticity field and Von Kármán vortex street behind the oscillating cylinder in 2D. Figure 3.27 shows the Q-criterion³ in 3D. Small discontinuities in the Q-criterion surfaces are from spurious oscillations (SFOs), which are common to IBM (Mittal and Iaccarino, 2005). The Oscillations have a larger magnitude in the current 3D than 2D case due to the larger mesh size. It was observed that high frequency filter, 4th order dissipation term from Eq. (2.56) with CS6–JST is critical to the stability and smoothness of solution, without it the simulation is not stable and errors blow up. Effect of different of C_2 and C_4 are not examined here.

Figure 3.28 shows C_D and C_L for up to 700 non-dimensional times from the 2D simulation, both quantities reach steady state. C_L oscillates around zero, and C_D oscillates around a non-zero positive value, as expected. High frequency low amplitude SFOs can be observed clearly.

Table 3.5 compares the mean drag (\bar{C}_D), root-mean-squared drag fluctuations ($C'_{rms,D}$) and root-mean-squared lift ($C'_{rms,L}$) with literature. The lift and drag quantities are defined as:

$$\mathbf{F} = \oint_{Cyl} (\boldsymbol{\tau}\hat{\mathbf{t}} - p\hat{\mathbf{n}})dS; \quad (3.23)$$

$$C_L = \frac{\mathbf{F} \cdot \hat{\mathbf{j}}}{1/2\rho_\infty u_\infty^2 D}; \quad C_D = \frac{\mathbf{F} \cdot \hat{\mathbf{i}}}{1/2\rho_\infty u_\infty^2 D}; \quad (3.24)$$

$$\bar{C}_L = \frac{1}{t} \int_0^t C_L(\tau) d\tau; \quad \bar{C}_D = \frac{1}{t} \int_0^t C_D(\tau) d\tau; \quad (3.25)$$

$$C'_L = C_L - \bar{C}_L; \quad C'_D = C_D - \bar{C}_D; \quad (3.26)$$

$$C'_{rms,L} = \sqrt{\int_0^t C'_L(\tau)^2 d\tau}; \quad C'_{rms,D} = \sqrt{\int_0^t C'_D(\tau)^2 d\tau}. \quad (3.27)$$

³ $1/2(|\boldsymbol{\Omega}|^2 - |\boldsymbol{S}|^2)$. Where $\boldsymbol{\Omega}$ and \boldsymbol{S} are the symmetric and antisymmetric part of the velocity gradient tensor ($\nabla \mathbf{u}$)

Note, the root-mean-squared does not indicate the magnitude of SFOs, but rather the peak to peak magnitude of the signal. They are computed using outputs of Algorithm 9.

For $M = 0.1$, current 2D simulation's \bar{C}_D is within 1.5% of previous studies and $C'_{D,rms}$ discrepancy is even lower. However, $C'_{L,rms}$ has error of 90% and is likely to be due to the method used to calculate the body forces. The systematic error in calculating forces by summation on each element, using Algorithm 9 is likely to be larger than a control volume balance used by previous studies. For $M = 0.25$ CS6-JST results in around maximum of 3% difference to literature in \bar{C}_D and $C'_{D,rms}$. $C'_{L,rms}$ has significantly larger errors, and again, it is likely to exist because of Algorithm 9.

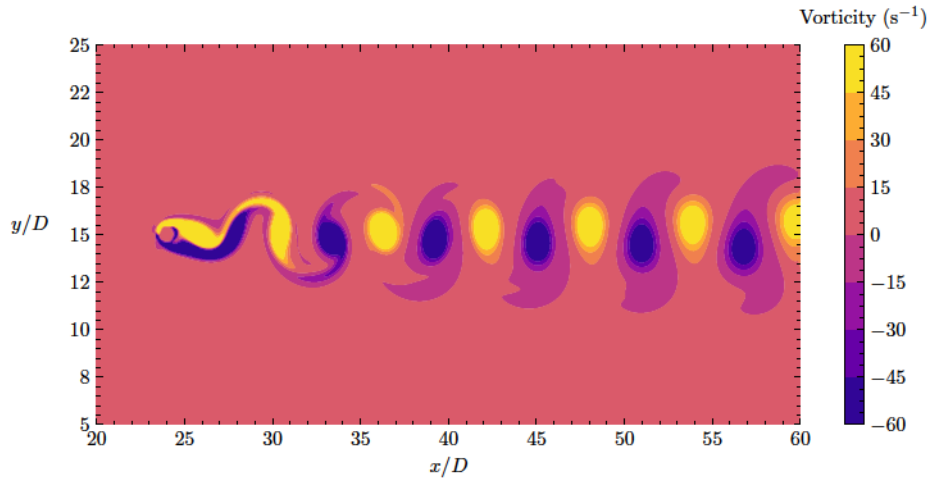


Fig. 3.26 Transversely oscillating cylinder vorticity field from 2D computations.

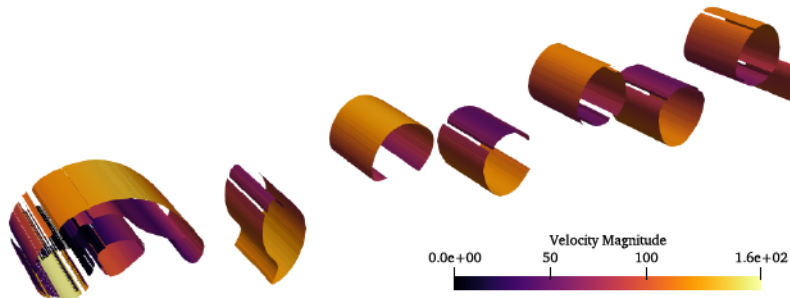


Fig. 3.27 Transversely oscillating cylinder Q-criterion surfaces from 3D computations.

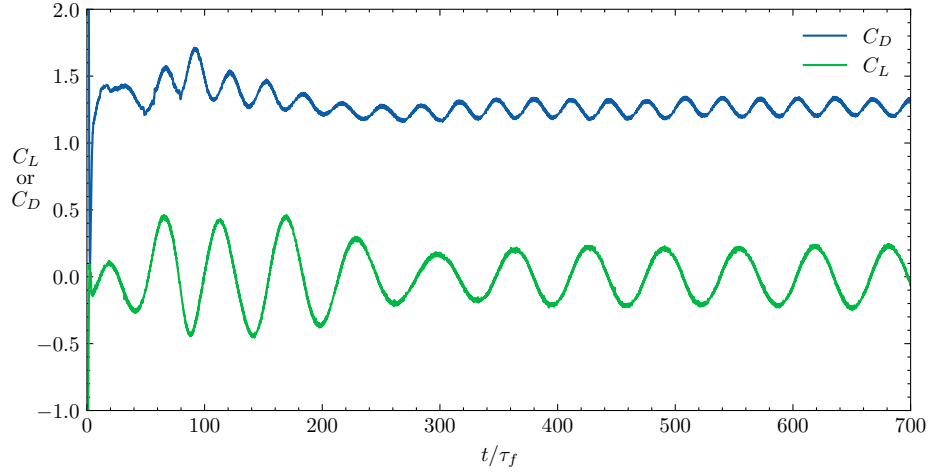


Fig. 3.28 Transversely oscillating cylinder C_D and C_L varying with non-dimensional time.

Table 3.5 Transversely oscillating cylinder mean drag (\bar{C}_D), root-mean-squared drag fluctuations ($C'_{rms,D}$) and root-mean-squared lift ($C'_{rms,L}$) comparisons with literature.

Study	\bar{C}_D	$C'_{rms,D}$	$C'_{rms,L}$
Schneiders et al. (2013) (2D), $M_\infty = 0.1$	1.279	0.042	0.082
Khalili et al. (2018) (2D), $M_\infty = 0.25$	1.287	0.045	0.079
De Vanna et al. (2020) (2D), $M_\infty = 0.25$	1.272	0.043	0.065
Present CS6–JST (2D), $M_\infty = 0.1$	1.268	0.045	0.153
Present CS6–JST (2D), $M_\infty = 0.25$	1.307	0.047	0.336
Present WENO-JS (2D), $M_\infty = 0.25$	1.289	0.049	0.121
Present CS6–JST (3D), $M_\infty = 0.25$	1.362	0.103	0.242

Profiling

Profiling with moving boundary IBM was conducted with a single processor, using Intel Vtune. The closest element search in Eq. (3.4) becomes expensive with increasing number of grids. For increased efficiency, the search is limited to the elements in the current patch only. The only variable is the number of triangular elements in the cylindrical body, which affects the runtimes as shown in Table 3.6.

Table 3.6 Percentage (%) of run time for each code function

Number of elements	0.9×10^3	2×10^4	1.4×10^5
Element area/mesh face area	40	4	0.6
ADVANCELTS	97	97	97
MOVEIB	3	5	18
Total run time	100	102	113

Increasing the number of elements increases the computation time modestly, MOVEIB's time complexity is approximately $O(\log(n_e))$ as $\times 155$ increase in the number of elements only increases the runtime $\times 6$.

3.3 Summary

This chapter developed a structured adaptive mesh refinement ghost-point immersed boundary (SAMR-GPIBM) solver suitable for modelling stationary and moving complex boundaries with hypersonic flows. GPIBM can be coupled to a SAMR framework in six steps. The artificial flux dissipation method is chosen for Euler fluxes, as it is computationally less expensive than WENO methods. This method with SAMR-GPIBM framework is one of the novelties of the current work. A challenge with IBM with hypersonic flows is maintaining stable and accurate solutions in the presence of large boundary layer gradients, especially with shock-boundary layer interactions.

Secondly, the developed numerical method is tested with a range of cases:

- Euler sphere test case showed the method is stable for up to sub-orbital Mach numbers ($M \lesssim 30$), resulting in smooth and accurate flow fields and surface properties with frozen and reacting flow, with both fast and slow reactions.
- The flat plate case suggests that the order of accuracy of the surface properties is second-order, as expected.
- Single and double compression ramp cases show that the method is stable and accurate with shock-boundary layer interactions. Moreover, the cases also highlighted the advantages of AMR-IBM over body-fitted meshes when complex shock interactions are present. As refinement around shocks resulted in around 50% lower heat flux on the upper ramp.
- The supersonic turbulent channel flow test case showed the low numerical dissipation and stability of the numerical method with turbulent flows.
- Transversely oscillating cylinder validated the implementation of the moving algorithm, accuracy and stability of the numerical method.

Many computations of hypersonic boundary layers exist in literature with body conformal meshes, which typically require $y_w^+ \sim 1$ for accurate surface properties predictions even in laminar hypersonic flows. However, with SAMR solvers, this criteria's validity is unclear. Current work over the three viscous cases shows this criterion is also valid. The viscous cases also suggest that the resolution requirement over a boundary layer is not uniform, and adaptively refining based on local y_w^+ can be computationally more efficient. This is shown by the double compression ramp case, where around 25% reduction in the number of computational points is observed with similar accuracy results. In the author's opinion, efficiently adapted grids could be competitive in computational cost with conformal meshes,

especially considering adaptive time-stepping. However, direct comparison with a body-conformal mesh solver is required for quantified cost benefits.

4. Heat transfer to proximal circular cylinders in hypersonic flow

Previously, Chapters 2 and 3 developed a numerical method for modelling hypersonic flows around complex geometries. This chapter applies the method to investigate the heat transfer to proximal circular cylinders in hypersonic flow.

4.1 Introduction

Uncontrolled atmospheric entry often results in fragmentation and partial or complete ablation of the entry body. The fragments formed during the entry can interact, altering each other's aerothermal environment. Such interactions occur in meteor entries ([Register et al., 2020](#)), and are known to affect their trajectories and ground dispersion ([Passey and Melosh, 1980](#)). Moreover, discarded spacecraft components and whole satellites ([Lips and Fritsche, 2005](#)) also fragment during re-entry, and their demise is also likely to be affected by the fragment interactions.

Only in the last 15 years, the problem of proximal body interactions in hypersonic flow has received attention. So far though, all studies have focused on aerodynamic forces, and aerothermal heating has not been investigated, despite its importance in re-entry body demise.

One of the first studies by [Laurence et al. \(2007\)](#) experimentally and computationally investigated the forces on binary proximal cylinders and spheres in fixed positions, specifically when the secondary body is entirely within the primary body's shock layer. First, they developed an analytical theory based on the blast wave analogy and validated it experimentally and numerically. They found that the secondary body experiences not only a drag force, but also a lift force. This lift force is exclusively attractive towards the second body, if its diameter is larger than one-sixth of the primary body. This follows the intuition of the secondary body being pulled behind the primary body and becoming trapped in the wake. More recently, [Marwege et al. \(2018\)](#) developed a data-driven method for calculating the forces in binary proximal body interactions, which achieves accuracies within a few percent of numerical simulations.

Another early study by [Laurence et al. \(2012\)](#) investigated the dynamic separation of two spheres, which are initially attached. They classified three main behaviours dependent on the sphere radii and the position of the detaching body. First, expulsion from bow shock layer, which occurs with increasing radii ratios and detachment position towards the front stagnation-point. It results in the secondary body being permanently excluded from the primary body's bow shock. Second is shock surfing ([Laurence and Deiterding, 2011](#)), at a critical angle for a given radii ratio, the detached body follows the primary body's bow shock downstream. Third is entrapment in bow shock, decreasing radii ratios and moving the detachment position towards the rear centreline increases the probability of the secondary body being entrained within the primary body's bow shock.

There are several recent studies which expand on the initial studies. For example, [Park et al. \(2021\)](#) experimentally investigated the separation behaviour of cubes and rough spheres. They note that the body shape, surface roughness, and rotational motion affect the separation velocity. Furthermore, [Park and Park \(2020\)](#); [Whalen and Laurence \(2021\)](#) experimentally studied sphere clusters as large as 36 spheres and found that larger clusters separate faster than smaller ones. Moreover, [Butler et al. \(2021\)](#); [Sousa et al. \(2021\)](#) experimentally and computationally investigated the dynamics of a spherical body shedding from a hypersonic ramp.

In summary, the literature suggests the possibility of persisting proximal body interactions, as the fragmented bodies could be trapped in the parent body's bow shock during entry. Despite this, aerothermal heating in proximal bodies during atmospheric entry has not been investigated. Previously, studies focusing on proximal body separation ([Laurence et al., 2007, 2012](#)) have used computational methods similar to the current work, SAMR with moving embedded boundaries for modelling Euler flows in three dimensions. Here however, viscous flow is computed and boundary layers resolved. As a first study focusing on heat transfer, this work aims to investigate the heat transfer to proximal circular cylinders in two dimensions.

4.2 Flow physics

4.2.1 Wake and shock shape

Hypersonic wakes consist of a rotational inviscid shock layer, a viscous inner wake and various shock and expansion waves. Many studies have investigated hypersonic near wakes and are comprehensively summarised in [Hinman and Johansen \(2018\)](#), whereas less is known about far hypersonic wakes ([Behrens, 1967](#); [Lees, 1964](#); [Wilson, 1967](#)). The key features and length scales in hypersonic wakes reported in the literature are illustrated in Fig. 4.1. It shows a bow shock around the blunt body drastically slowing the flow to subsonic speeds around the front of the cylinder. A boundary layer starts from the front stagnation-point and remains attached for larger turn angles around the cylinder shoulder when compared to subsonic flows due to the favourable pressure gradient created by the expansion fan. However, adverse pressure gradients eventually form and separate the boundary layer, resulting in a separation shock—also known as a lip shock ([Hama, 1968](#)). The separated flow converges towards the wake centreline at the reattachment point, where some flow is directed back to create a counter-rotating vortex pair near the base. With increasing Reynolds number, the re-circulation may have more than one vortex pair. The flow that continues away from the body along the centreline creates a reattachment shock and forms a viscous inner wake. This may transition to turbulence and mix with the inviscid shock layer downstream. The flow field is symmetrical along the centreline for symmetric blunt bodies, but the symmetry breaks as the wake transitions to turbulence.

Wake Reynolds number (Re_w) governs the wake topology,

$$Re_w = \frac{\rho_d u_d h}{\mu_d}; \quad (4.1)$$

where h is the wake base height, the shortest distance between the separation point and the centreline. Semi-analytical expressions for calculating the dividing streamline density (ρ_d), temperature (T_d) and viscosity (μ_d) can be found in equations 3.1-3.7 from [Hinman and Johansen \(2018\)](#). A more convenient scaling parameter is free-stream Reynolds number (Re_∞), which is based on free-stream flow properties and body length scale. However, it is not useful in describing the wake behaviour as it does not account for the flow features that occur upstream of the wake. Figure 4.2 shows the relationship between the two Reynolds numbers and free-stream Mach number (M_∞) without thermochemical effects. It shows that Re_w is generally orders of magnitude smaller than Re_∞ . It also suggests that increasing the free-stream Mach number for a given Re_∞ reduces Re_w , due to increasing temperature and

viscosity. Finally, it outlines four flow regimes: A is diffusion dominated, essentially Stokes flow; in B, the recirculation region changes from diffusion to convection dominated; C is convection dominated, where the wake maybe unsteady; and D is convection dominated, where $Re_w \gg 1000$ will lead to transition and a turbulent wake.

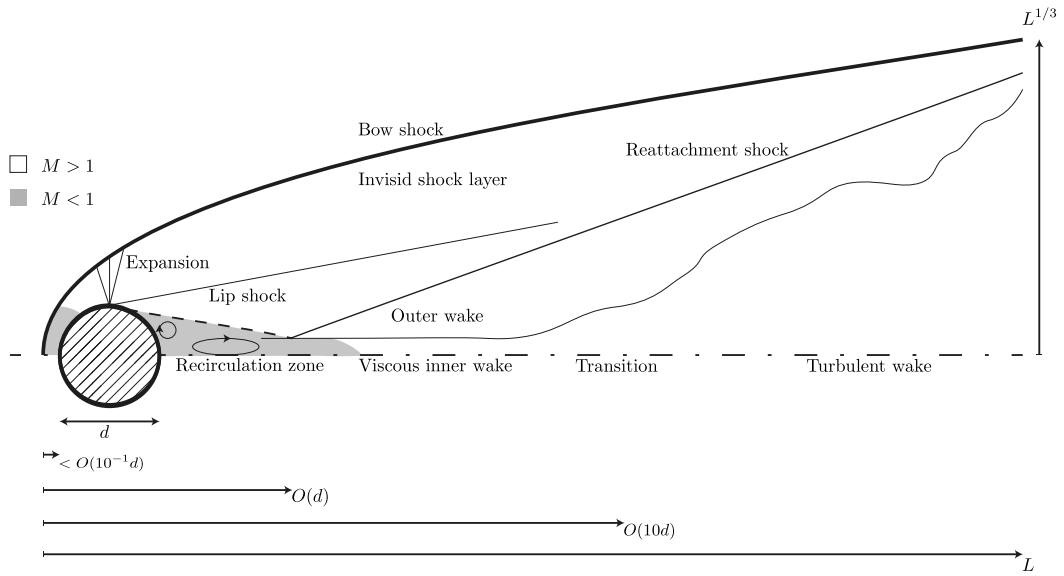


Fig. 4.1 Hypersonic blunt body wake features with approximate length scales.

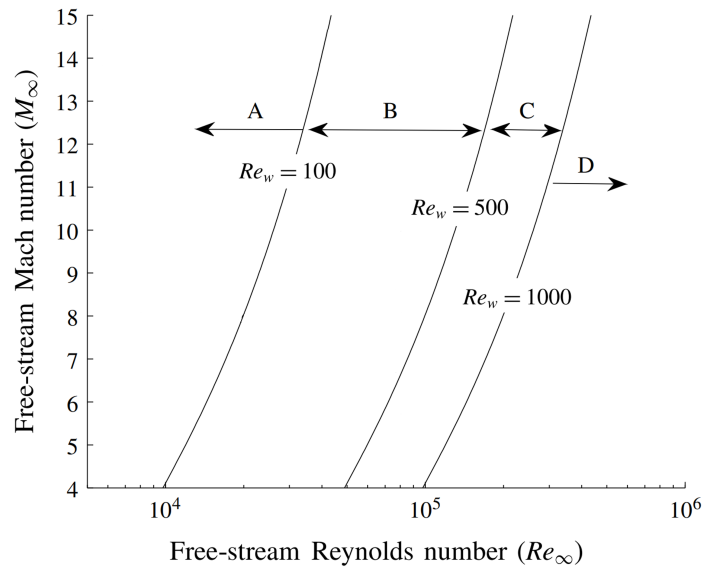


Fig. 4.2 Relationship between wake Reynolds number (Re_w), free-stream Reynolds number (Re_∞) and free-stream Mach number (M_∞). Adapted from [Hinman and Johansen \(2018\)](#).

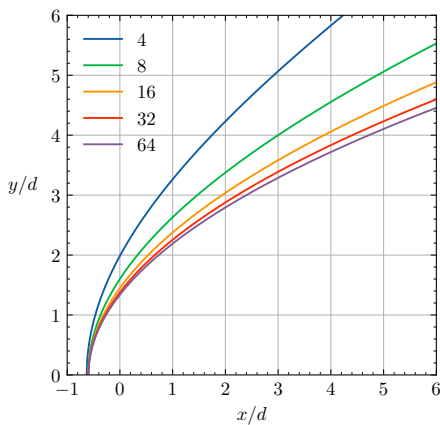
Shock shape. The bow shock around a blunt body is a hyperbola and empirical functions approximate its shape to engineering accuracy (Billig, 1967),

$$\hat{x} = \frac{1}{2} \left[\hat{r}_c \cot(\beta) \left(1 + \left(\frac{\hat{y} \tan(\beta)}{\hat{r}_c} \right)^2 \right)^{1/2} - \hat{\delta} - 1 \right],$$

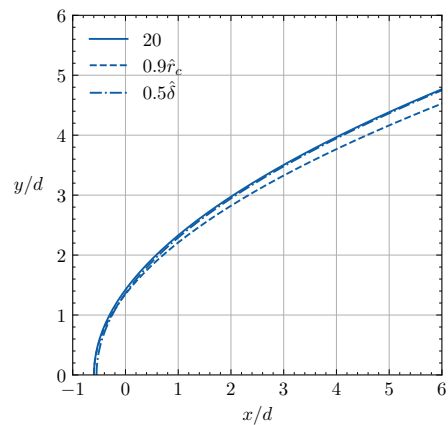
$$\hat{\delta} = 0.193 \exp(4.67/M_\infty^2), \quad \hat{r}_c = 0.693 \exp(1.8/(M_\infty - 1)^{0.75}); \quad (4.2)$$

where quantities with the hat symbol ($\hat{\cdot}$) are non-dimensionalised by the body radius ($D/2$, where D is the diameter), $\hat{\delta}$ is the shock stand-off distance on stagnation line, \hat{x} and \hat{y} are Cartesian coordinates, β is the shock wave angle in the limit of infinite distance away from the nose, \hat{r}_c is the shock radius of curvature on the stagnation line. Equation (4.2) suggests that the shock shape becomes independent of Mach number as $M_\infty \rightarrow \infty$, this is the Mach number independence principle in hypersonic flow (Anderson Jr, 2006). Figure 4.3a shows the shock shape variation with Mach number for a near body flow field ($D \leq 5$).

Thermochemical relaxation effects are not included in Eq. (4.2) and Fig. 4.3a. Thermochemical non-equilibrium effects are important for $M \gtrsim 8$ and can change $\hat{\delta}$ or \hat{r}_c . Shock stand-off theory (Belouaggadia et al., 2008) suggests in equilibrium flow, $\hat{\delta}$ can be $\lesssim 50\%$ smaller than in frozen flow. Despite the dramatic reduction in the stand-off distance, the shock shape in the near field is insensitive to it, as shown in Fig. 4.3b. Shock shape is much more sensitive to changes in \hat{r}_c , Billig (1967) suggests a 10% change in \hat{r}_c at $M=20$. The effect of this change on shock shape is illustrated in Fig. 4.3b. It suggests the shock position can be altered around $O(10^{-1})d$ in the near wake. Therefore, as a first approximation, the effect of thermochemical relaxation on the near-field shock shape is not significant and can be neglected.



(a) Effect of Mach number.



(b) Effect of thermochemical relaxation at $M = 20$.

Fig. 4.3 Cylinder bow shock shape.

4.2.2 Stagnation-point and shock-interaction heat transfer

Stagnation-point heat transfer is governed by the exact solution of compressible boundary layer equations (Fay and Riddell, 1958). The boundary layer equations are not shown here and can be found in standard texts (Anderson Jr, 2006). For frozen flow around a cylinder, the stagnation heat flux is

$$q_0 = 0.57 Pr^{-0.6} (\rho_e \mu_e)^{1/2} \sqrt{\frac{du_e}{d\xi}} (h_{aw} - h_w); \quad (4.3)$$

$$\frac{du_e}{d\xi} \approx \frac{1}{R} \sqrt{\frac{2(P_e - P_\infty)}{\rho_e}}. \quad (4.4)$$

Where q_0 is the stagnation-point heat flux, Pr is the Prandtl number, ρ_e is the boundary layer edge density, μ_e is the boundary layer edge viscosity, h_{aw} is adiabatic wall enthalpy, h_w wall enthalpy and $du_e/d\xi$ is the velocity gradient in the wall tangent direction (ξ) at the boundary layer edge. Similar expression with chemically reacting flows is not shown here as current work assumes frozen flow. The velocity gradient can be approximated using Newtonian theory (Anderson Jr, 2006), as in Eq. (4.4). Where R is the nose radius, P_∞ is the free-stream pressure, and P_e and ρ_e are boundary layer edge pressure and density.

There are many simplified forms of Eq. (4.3) and are reviewed by Tauber (1989), where they state a simple expression valid for cylinders:

$$q_0 = 1.29 \times 10^{-4} \left(\frac{\rho_\infty}{R} \right)^{0.5} V_\infty^3 \left(1 - \frac{h_w}{h_{aw}} \right), \quad (4.5)$$

where h_{aw} is the adiabatic wall enthalpy and h_w is the actual wall enthalpy. They also state that the distribution of surface heat transfer is approximately

$$q_w = q_0 \cos(\theta) (1 - 0.18 \sin^2(\theta)), \quad h_{aw} = h_\infty + 1/2 V_\infty^2 (1 - 0.18 \sin^2(\theta)), \quad (4.6)$$

where θ is the position angle on the cylinder surface. Assuming $h_{aw} \gg h_w$. Eq. (4.5) can also be written in terms of non-dimensional flow parameters, free-stream temperature and length scale,

$$q_0 \propto R^{-1} Re_\infty^{1/2} M_\infty^{5/2} T_\infty^{5/4}; \quad (4.7)$$

where C is a constant which includes free-stream fluid properties, namely, specific heats' ratio, gas constant and viscosity. This expression suggests stagnation heat flux scales with $Re_\infty^{1/2}$ and $M_\infty^{5/2}$ assuming the wall temperature is much colder than the stagnation temperature.

Shock interaction heating occurs when an impinging shock interacts with the body's back shock near its surface. These interactions can be decomposed into six canonical flow patterns, as initially described by [Edney \(1968\)](#) and summarised in Fig. 4.4. Types I, II, and V are associated with a shock-boundary-layer interaction; type III is characterized by an attaching free shear layer; type IV is characterized by an impinging or grazing supersonic jet; and type VI by an expansion-fan-boundary-layer interaction. Only type VI results in a reduction of surface gradients and pressure, all other types result in an increased in local pressure and surface gradients. Most severe heating generally occurs when shock or shear layer impinges on the body surface and can lead to $10\times$ nominal heating or even higher. This increase in heating also usually correlates with an increase in surface pressure of a similar magnitude.

Semi-empirical heat transfer correlations have been developed for each type of interaction by [Keyes and Hains \(1973\)](#). Although the exact equations are not shown here for brevity, the correlations suggest that the all types of interactions strongly depend on the impinging and bow shock angles at the intersection. As well as the local surface inclination and interaction type specific flow feature length scales.

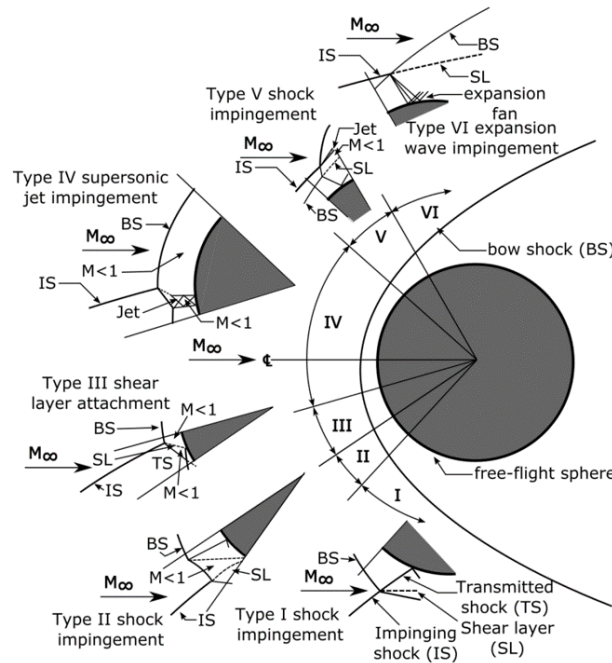


Fig. 4.4 Blunt body Edney shock interactions, from [Fisher \(2019\)](#).

4.3 Binary bodies

An expression for the transverse velocity (V_t) of fragmented spherical bodies was first presented by [Passey and Melosh \(1980\)](#). Later, dynamical separation studies by [Laurence et al. \(2012\)](#); [Park et al. \(2021\)](#) have verified it further. The expression reads,

$$\frac{V_t}{V_\infty} = \sqrt{Cn \frac{r_1 \rho_\infty}{r_b \rho_b}}; \quad r_2 \leq r_1. \quad (4.8)$$

Where C is a constant, r_1 and r_2 are radii of two spherical bodies, ρ_∞ is free-stream density, V_∞ is free-stream velocity, ρ_b is density of the detached body. The order of magnitudes for each variable considering Earth entries are as follows. The magnitude of the constant C is discussed by [Laurence et al. \(2012\)](#) and is $10^{-2} < O(C) < 1$. The number of fragments are assumed to be small, so $O(n) = 1$. The fragmented bodies are assumed to be smaller than primary body but not too small, which means $10^{-1} < (r_1/r_2) < 1$. Finally, the ratio of the free-stream density to body density is not trivial. Spacecraft components and satellites are usually metallic, and common meteorites ([Britt and Consolmagno, 2003](#)) are stony, stony-iron or iron. A reasonable assumption is to consider a metallic body, so $O(\rho_b) = 10^3$. [Passey and Melosh \(1980\)](#) suggest that breakup altitudes can be as low as 6 km and as high as the mesosphere (approximated at 80 km here), so $10^{-5} < O(\rho_\infty) < 1$. Therefore, $10^{-6} < O(V_t/V_\infty) < 10^{-1}$, this suggests the separation velocity varies over orders of magnitude and is much slower than free-stream velocity. Therefore, the flow adjusts very quickly around the body and so neglecting dynamics is justified as a first study.

In this work, two identical bodies with 0.1 m diameter are considered a first study. Non-dimensionalisation of the body position using flow length scales is preferred over the body length scale, as it allows a meaningful comparison of positions across different Mach numbers. The positions in real space (x, y) and non-dimensional space (\hat{x}, \hat{y}) are illustrated in Fig. 4.5. It also shows a hatched region representing a collision area where the second body cannot be placed. In the current study, the second body's position is systematically varied in primary body's near wake, $0 \leq \hat{x} \leq 2$ and $0 \leq \hat{y} \leq 2$. The reference length scale in the y direction is the shock radius (y_s) and in the x direction is the rear stagnation-point distance (L_s) from the body centre. Different positions are investigated at Mach numbers 2, 4 and 8. The free-stream Reynolds number is fixed at 10^4 , and the free-stream temperature is 300 K. The wall temperature is 300K for $M = 2$ and 500 K for other the Mach numbers. The following assumptions are made: N_2 gas free-stream, frozen flow, Sutherland's law viscosity, constant specific heat capacity ($C_p = 1040$ kJ/kg K) and constant Prandtl number ($Pr = 0.7$).

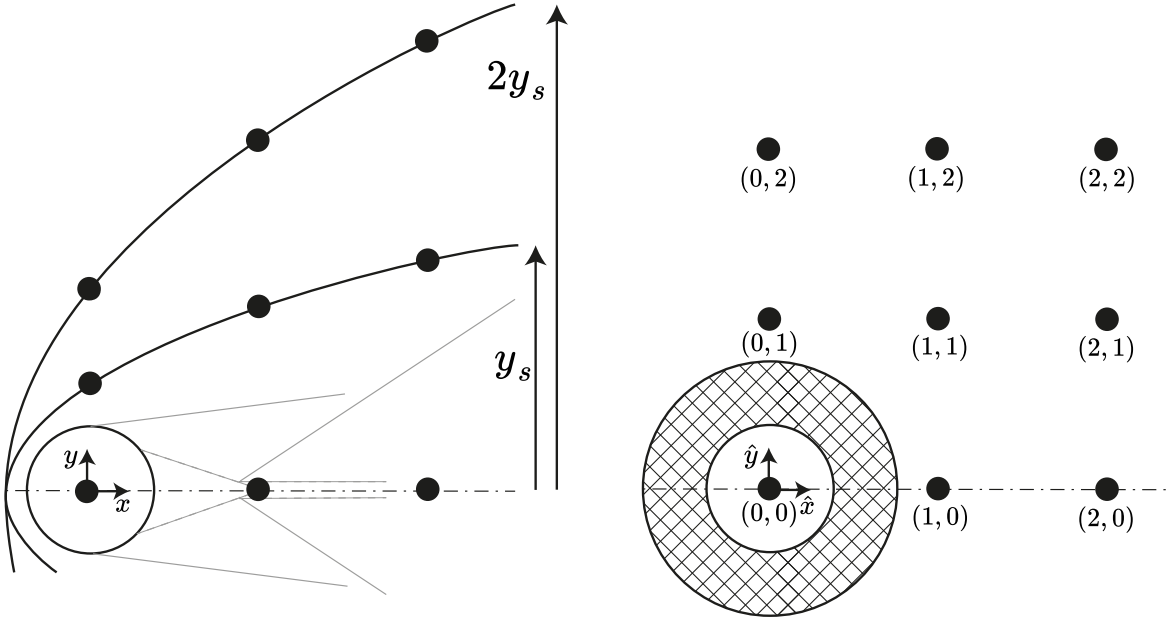


Fig. 4.5 Binary bodies arrangements in real (left) and non-dimensional space (right).

4.3.1 Mesh refinement

A mesh refinement study is conducted at the three Mach numbers, where the meshes are summarised in Table 4.1. The $M = 2$ mesh is larger, in terms of the number of computational points, than $M = 4$ mesh. This is because a larger domain is required at $M = 2$ due to the larger shock layer than at higher Mach numbers. The mesh requirement for accurate stagnation-point heat transfer prediction can be estimated using Eq. (4.5). The boundary layer thickness (δ_0) on the stagnation line is

$$q_0 = k_w \left. \frac{dT}{dn} \right|_{wall} \approx k_w \frac{T_0 - T_w}{\delta_0} \rightarrow \delta_0 \approx k_w (T_0 - T_w) / q_0, \quad (4.9)$$

$\delta_0 \approx [1330, 882, 482] \mu\text{m}$ with $M = [2, 4, 8]$ respectively. The boundary layer thicknesses are used to select the Base mesh size and number of refinement levels.

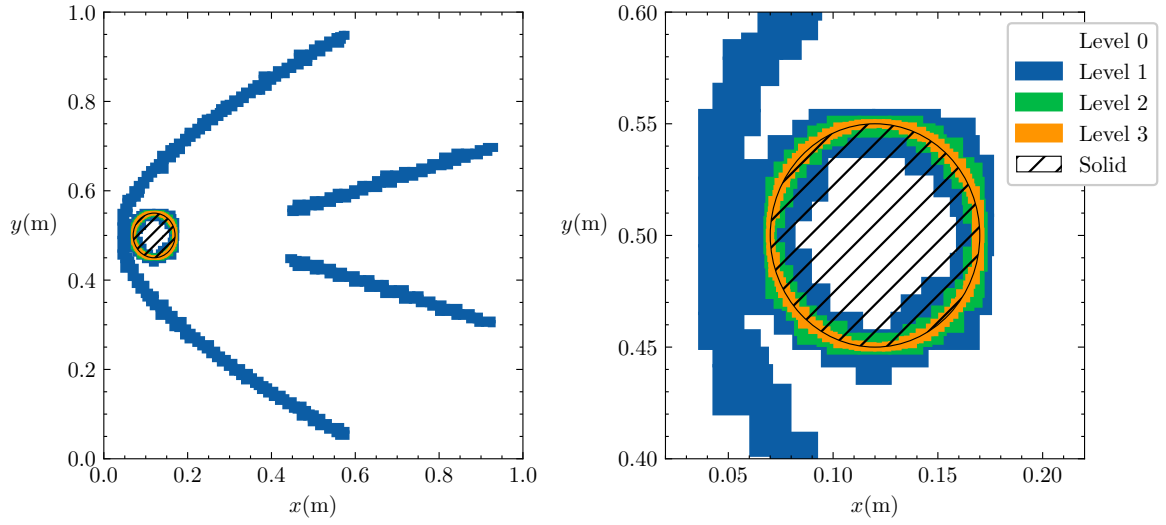
Figures 4.6a and 4.6b show the mesh in a fully developed flow field, with refinement around shock and cylinder boundary at $M = 4$, with refinement around the cylinder boundary only at $M = 8$. The mesh for $M = 2$ is similar and not shown for brevity. For the $M = 8$ case, the higher levels of refinement are only added around stagnation region using criteria are based on the wall pressure coefficient. Re-gridding occurs every 0.5 flow times.

The AMR parameter values are: $\text{max_grid_size} = 64$; $\text{cluster_minwidth} = 16$; $\text{cluster_min_eff} = 0.95$; and the other parameters keep the same value as in Section 2.2.3. The maximum grid size is increased to ensure that there are not too many patches, reducing the number of patches reduces the number of halo points which need to be communicated. But, the maximum grid size is small enough to ensure even load distribution across processors. The simulations are initialised at the free-stream temperature and pressure free-stream Mach number everywhere except for a small annulus around the cylinder where the Mach number is zero. Euler fluxes are computed with CS4-JST, where $C_2 = 1.0$ and $C_4 = 0.016$ throughout the computation. The IBM image point distance parameter is $\alpha_{im} = 0.6$, it is reduced to ensure the first image point is close to the surface. The domain boundary conditions, considering Fig. 4.6, are free-stream inflow on the left boundary and zero-gradient for all other boundaries. For the immersed boundary, no-slip, constant wall temperature and zero pressure gradient conditions are imposed.

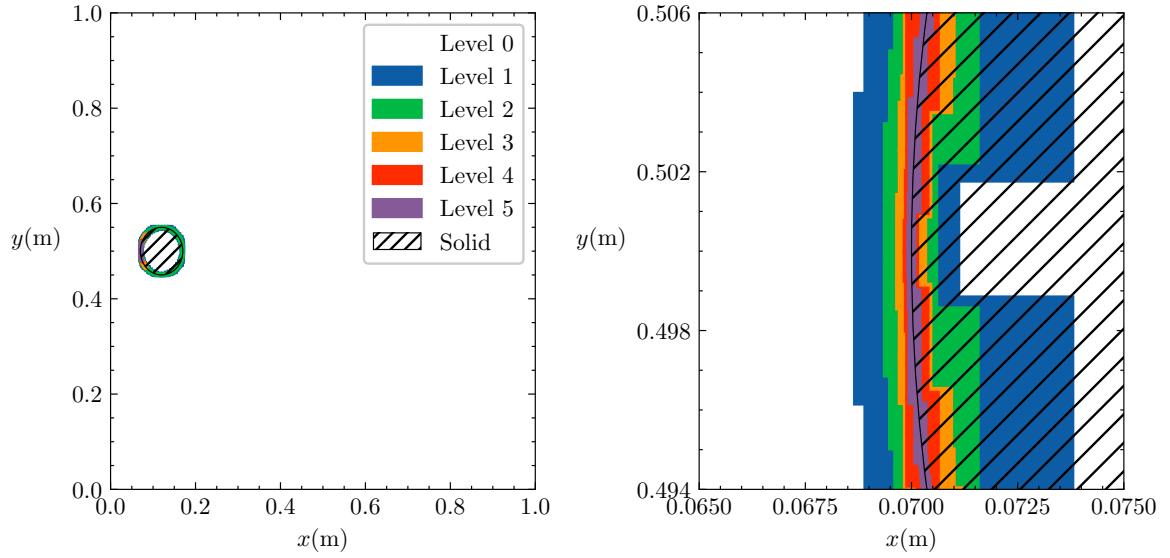
The simulations are computed for 30 flow times, where a flow time is defined as the domain length divided by the free-stream velocity. Such a long duration is required for the back pressure to change less than 1%, and the rear stagnation-point to move by less than 1% over a single flow time. The maximum CFL number is around 0.5. The medium meshes have around $[11, 7, 31]$ mesh points in the boundary layer at stagnation-point for $M = [2, 4, 8]$. Significant computational efficiency is gained by allowing the flow to develop for 20 flow times at low resolution. Then, only for the last 10 flow times full resolution is added.

Table 4.1 Mesh refinement cases low, medium and high resolutions for each Mach number. Number of computational points ($\times 10^6$) and number of refinement levels in brackets.

M	Size	Base	Low	Medium	High
2	$20D \times 20D$	2048×2048	4.60 (2)	4.88 (3)	5.12 (4)
4	$10D \times 10D$	1024×1024	1.34 (2)	1.45 (3)	1.66 (4)
8	$10D \times 10D$	2048×2048	5.31 (4)	6.18 (5)	7.50 (6)



(a) At $M = 4$, left is the entire mesh and right is the zoomed mesh around the body.



(b) At $M = 8$, left is the entire mesh and right is zoomed mesh around stagnation-point.

Fig. 4.6 Medium resolution mesh with coloured AMR patches at different Mach numbers.

Surface properties

The non-dimensional surface properties, pressure (C_p), skin friction (C_f) and heat transfer (C_h) coefficients are defined as:

$$C_p = \frac{P_w}{1/2\rho_\infty u_\infty^2}; \quad C_f = \frac{\tau_w}{1/2\rho_\infty u_\infty^2}; \quad C_h = \frac{q_w}{1/2\rho_\infty u_\infty^3}. \quad (4.10)$$

Figure 4.7 shows surface properties down-sampled to 100 surface elements and a 3-point moving average. The pressure field does not vary significantly with increasing resolution at all Mach numbers. The reference (Ref) heat transfer profile is from Eq. (4.6), which are known to include around 25% error when compared to ground shock-tube and ballistic range experiments (Tauber, 1989). The stagnation point heat transfer predictions from all meshes are within this error. Table 4.2 suggests that at $M = 2$, the stagnation heat transfer is overpredicted by 10%. At $M = 4$ and 8, the stagnation heat transfer is underpredicted by around 10%. Another observation is that the heat transfer profile qualitatively agrees but is offset around factor of the stagnation point heat transfer error, and it does not agree well beyond $3\pi/8$ as expected. For all Mach numbers, the medium mesh resolution gives results within 3% of the fine mesh results, therefore it is deemed acceptable for binary bodies computations.

Table 4.2 Stagnation point heat transfer convergence (C_h) with increasing Mesh resolution at different Mach numbers and comparison with semi-empirical correlations of Tauber (1989).

M	$ C_h \times 10^{-2}$						
	Low	Change (%)	Medium	Change (%)	High	Difference (%)	Reference
2	1.36	8.1	1.47	2.7	1.51	10.2	1.37
4	1.47	14.2	1.68	3.0	1.73	-5.4	1.83
8	2.91	20.0	3.49	2.0	3.56	-9.2	3.92

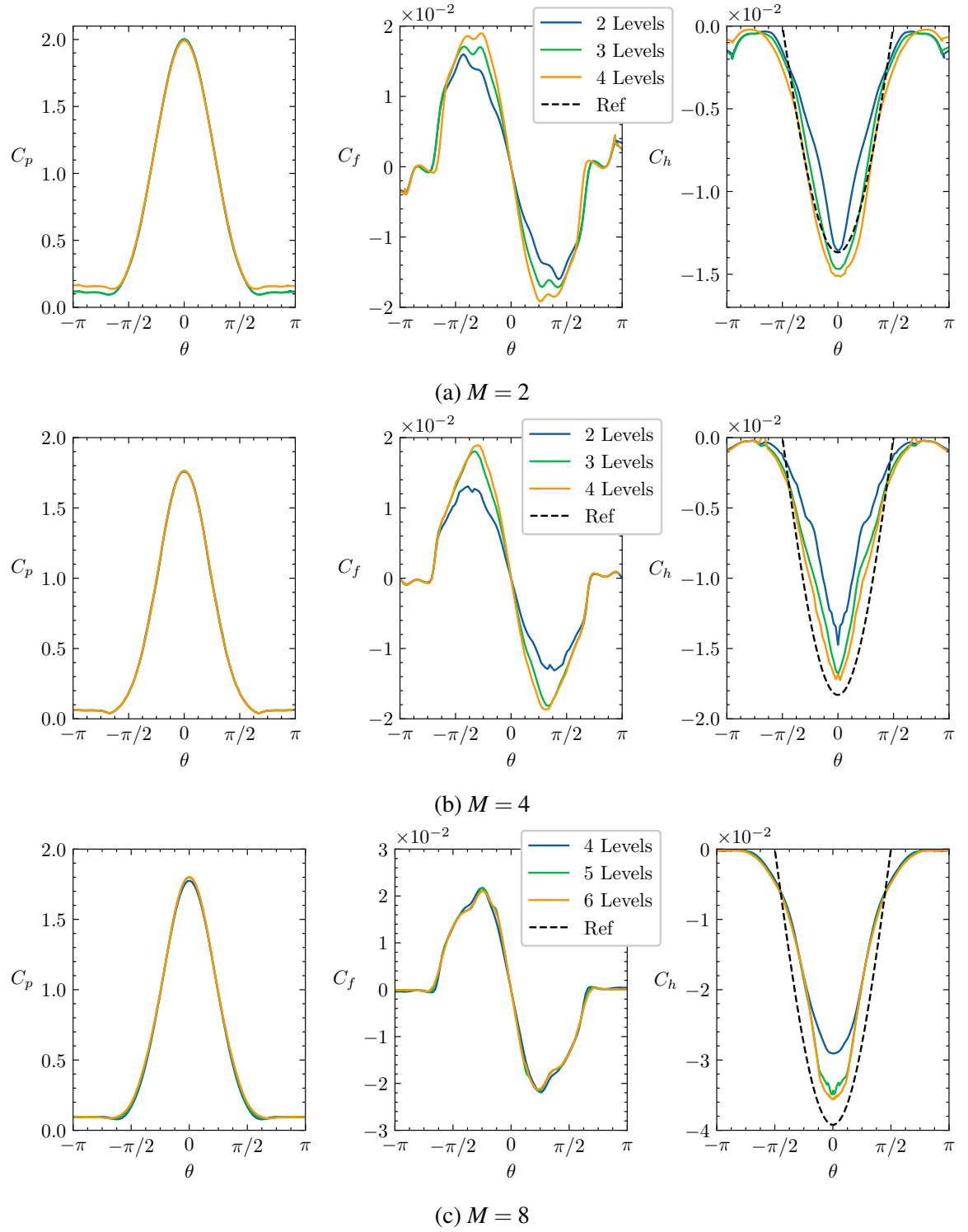


Fig. 4.7 Surface properties from mesh refinement study at different Mach numbers.

Flow length scales

Figure 4.8 shows the hypersonic wakes at different Mach numbers. Flow length scales, namely the rear stagnation-point distance (l_s) and bow shock transverse distance (y_s) are estimated from the mesh refinement study and summarised in Table 4.3. These values are used calculate positions of the secondary cylinder, according to non-dimensionalisation in Fig. 4.5.

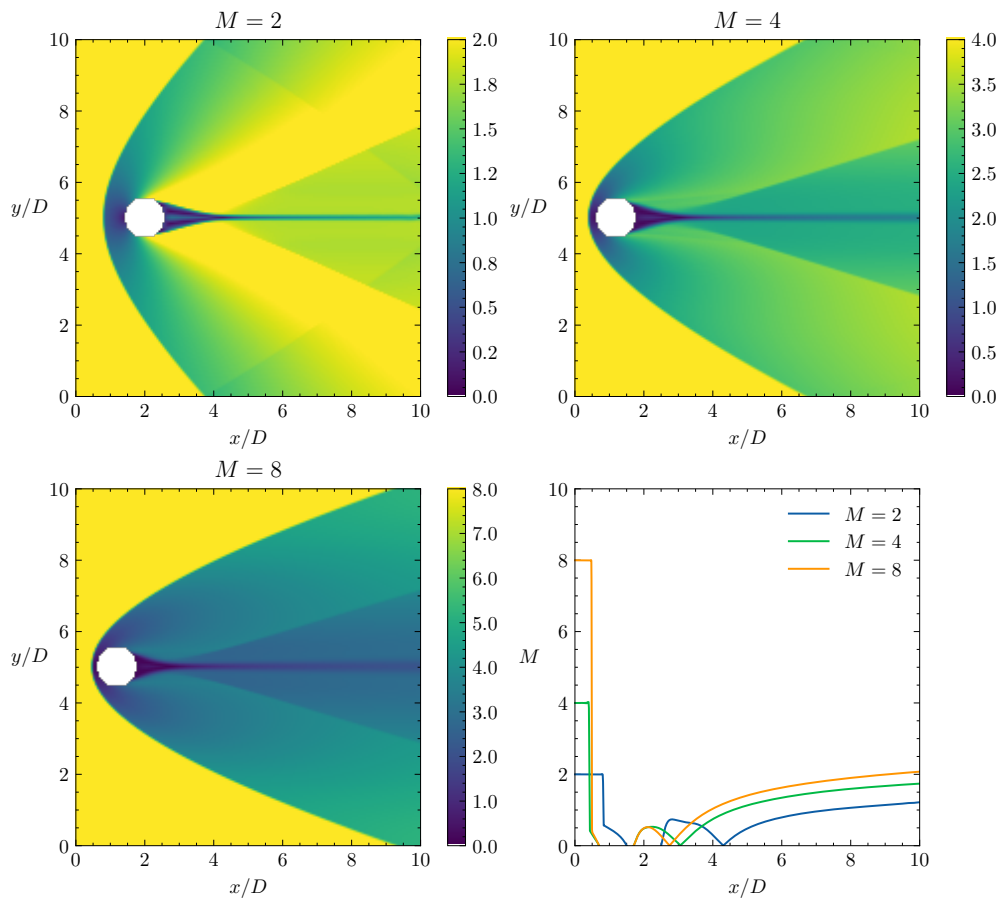


Fig. 4.8 Mach number field and centreline profile.

Table 4.3 Flow length scales at different Mach numbers.

M	l_s (m)	$y_s(\hat{x} = 0)$	$y_s(\hat{x} = 0.5)$	$y_s(\hat{x} = 1)$	$y_s(\hat{x} = 2)$
2	0.222	0.288	0.430	0.550	1.250
4	0.186	0.148	0.228	0.292	0.404
8	0.155	0.128	0.180	0.232	0.311

4.3.2 Results

Initial studies suggested secondary body arrangements with $\hat{y} = 2$ were too far to observe any effect on each other. So, despite the illustration in Fig. 4.5 the study is limited to $\hat{y} \leq 1$. Eight arrangements of the bodies are considered, in (\hat{x}, \hat{y}) coordinates and in order from 1 to 8 are: $\{(1,0), (2,0), (0,0.5), (1,0.5), (2,0.5), (0,1), (0.5,1), (1,1)\}$. Simulations are conducted using these arrangements and the medium mesh from Section 4.3.1. The numerical setup for these simulations is identical to medium mesh from refinement study in Section 4.3.1, but with two immersed boundaries. The meshing criteria around both bodies is the same. The simulations are advanced for 10 flow through times, this duration is sufficient for the surface gradients to be developed close to steady state, as shown in Fig. 4.9. The figure shows heat load variation of primary and secondary bodies over non-dimensional time. The heat load is more unsteady at lower Mach numbers but only for a couple of arrangements. Specifically, at $M = 2$ in arrangements 2 and 4, and at $M = 4$ in arrangements 2 and 5. Therefore, the surface properties for these cases are time-averaged over 6-10 flow times, but for all other cases surface properties are taken at their steady state.

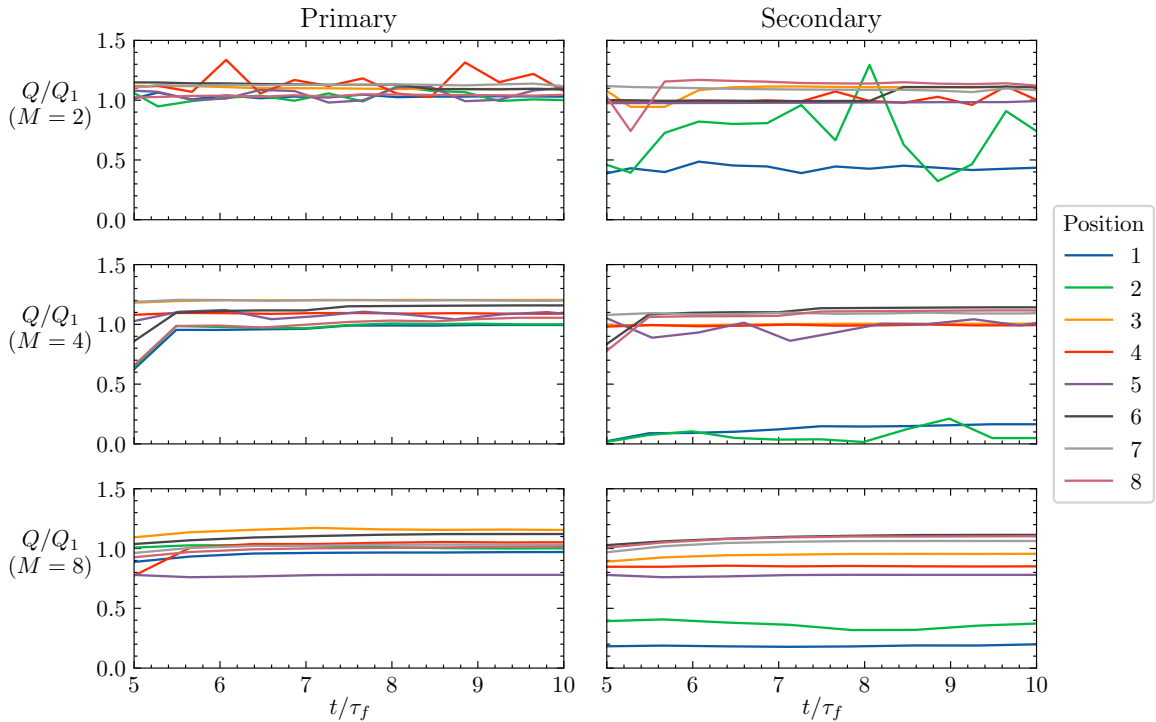


Fig. 4.9 Heat load convergence for all positions and Mach numbers over non-dimensional time.

The average mesh size for Mach numbers [2, 4, 8] is around $[4.6, 1.5, 5.6] \times 10^6$ points. In all meshes, more than 80% of computational points are on the base level. Each binary arrangement costs around [980, 170, 1590] CPU hours to compute. The $M = 2$ mesh is almost the same size as the $M = 8$ mesh as the lower Mach number domain is twice as big, and the base mesh resolution is the same for both Mach numbers. A smaller mesh is possible at $M = 2$ with base mesh 1024×1024 and four refinement levels. However, meshes have not been optimised for efficient computations in the current work.

On the other hand, the current numerical approach becomes computationally inefficient with higher Mach numbers. For example, with the same free-stream conditions but $M = 16$, 9-10 refinement levels are needed for the stagnation point heat transfer to converge. With an increasing number of refinement levels, communication costs and load balancing become more challenging with a hierarchical grid. The computational efficiency can be improved if the refinement ratio between each level is more than two, maybe four or even eight. However, the current implementation does not allow this, as stated in Section 2.2.3.

Numerical schlieren

Figures 4.10, 4.11 and 4.12 show similar flow features to Fig. 4.1, namely bow shock, lip shock and reattachment shocks. They show that the secondary body does not have a bow shock when directly behind the primary body, as in arrangements 1 and 2 for all Mach numbers. The figures also show that both bodies have interacting bow shocks in arrangements 3 to 8. The bow shocks combine and form a single smooth bow shock in arrangements 3, 6 and 7 at $M = 2$, 3 and 6 for $M = 4$ and only in arrangement 6 at $M = 8$; or they result in interactions which can lead to unsteady wakes with oscillating reattachment shocks and shocklet shedding. Counter-intuitively, the wake becomes more steady at increasing Mach numbers since the wake behaviour is governed by the wake Reynolds number which decreases with increasing free-stream Mach number for a fixed free-stream Reynolds number, as shown in Fig. 4.2.

An observation from the numerical schlieren is that the zero-gradient boundary conditions on the top and bottom edges of the computational domain partly reflect the bow shock back into the computational domain. This reflection maybe avoided by using more sophisticated characteristic boundary conditions. However, this reflection has negligible impact on the current study, and more accurate boundary conditions are deemed unnecessary. Moreover, the reflection seems to become less polluting with increasing Mach number.

Another observation is that Edney-type shock interactions do not manifest. They are known to occur with near body shock interactions, as discussed in Section 4.2.2. However, most

binary body arrangements are such that the secondary body is positioned fully inside the shock layer of the primary body. This is the case for $M = 2$ and $M = 4$ with all arrangements; and for $M = 8$ with arrangements 1, 2, 6 and 7. Thus, these cases do not include impinging shock and bow shock interactions. However, arrangements 3, 4, 5 and 8 at $M=8$ are close to producing Edney type interactions. But, the secondary body positions are such that shock interactions occur far from the body. In arrangement 8, if the secondary body is positioned slightly higher, then Edney type VI interaction would occur. On the other hand, if the secondary body is positioned slightly lower, then Edney type I interaction would manifest.

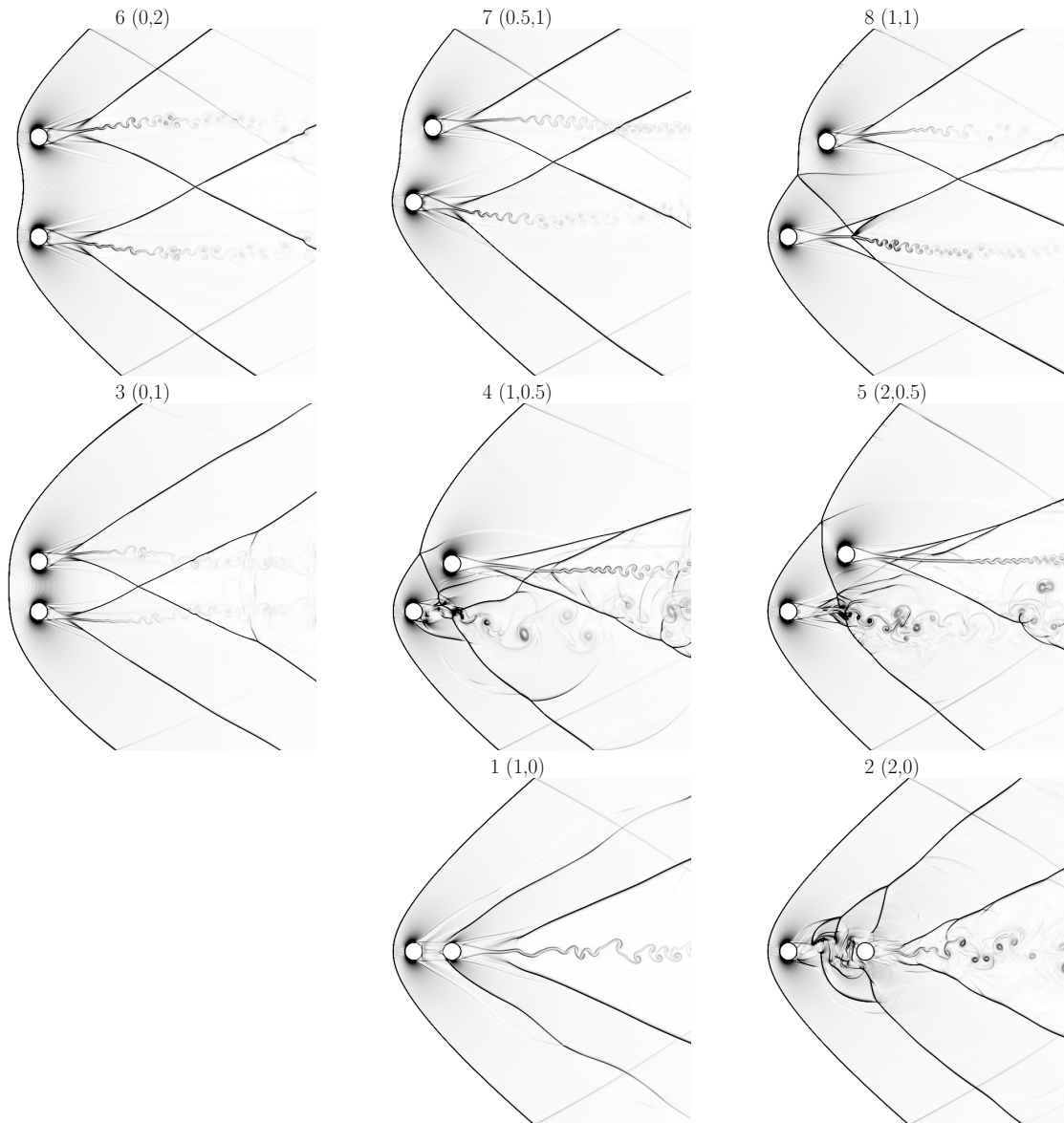


Fig. 4.10 Numerical schlieren for binary body arrangements at $M = 2$.

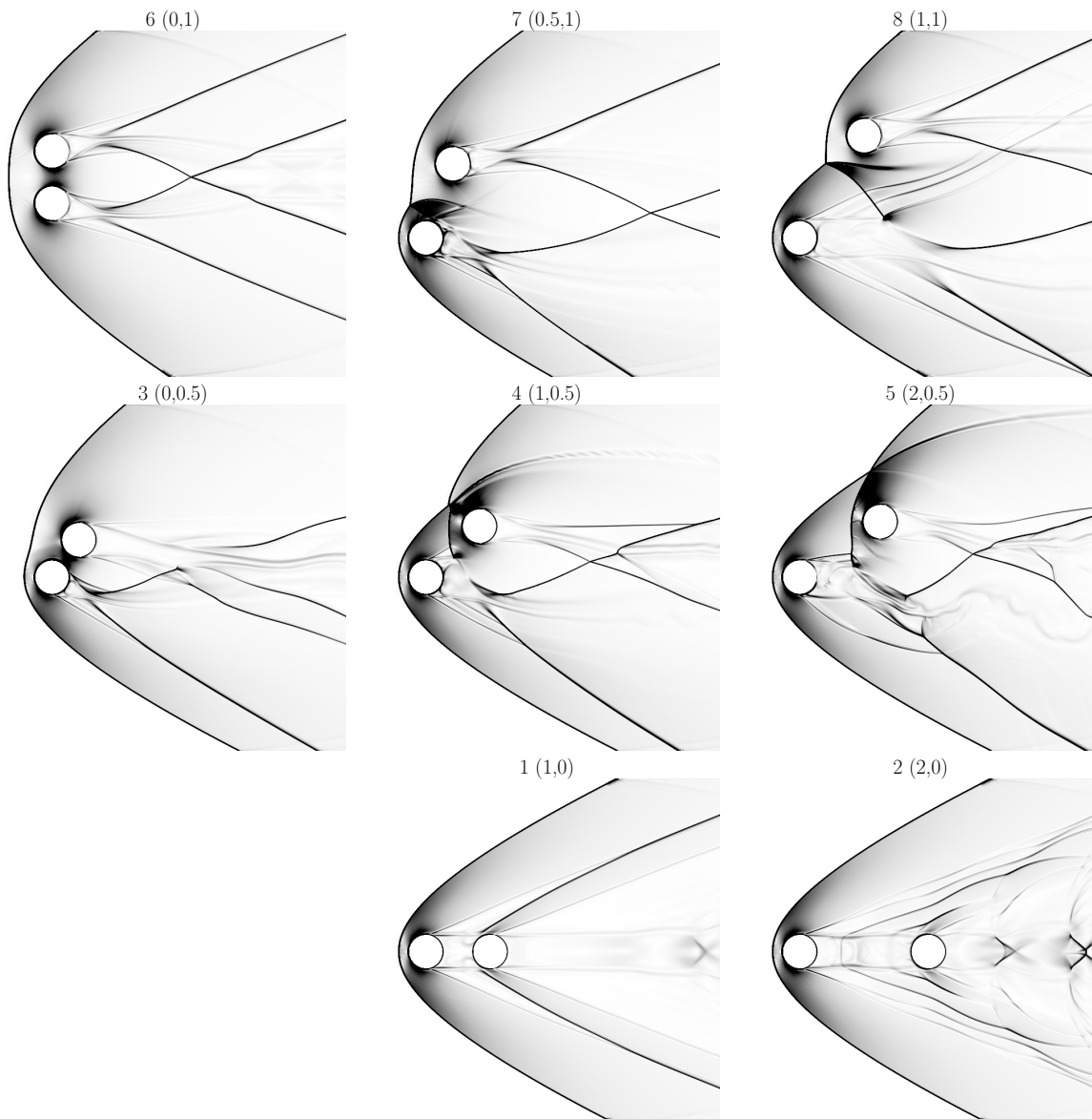


Fig. 4.11 Numerical schlieren for binary body arrangements at $M = 4$.

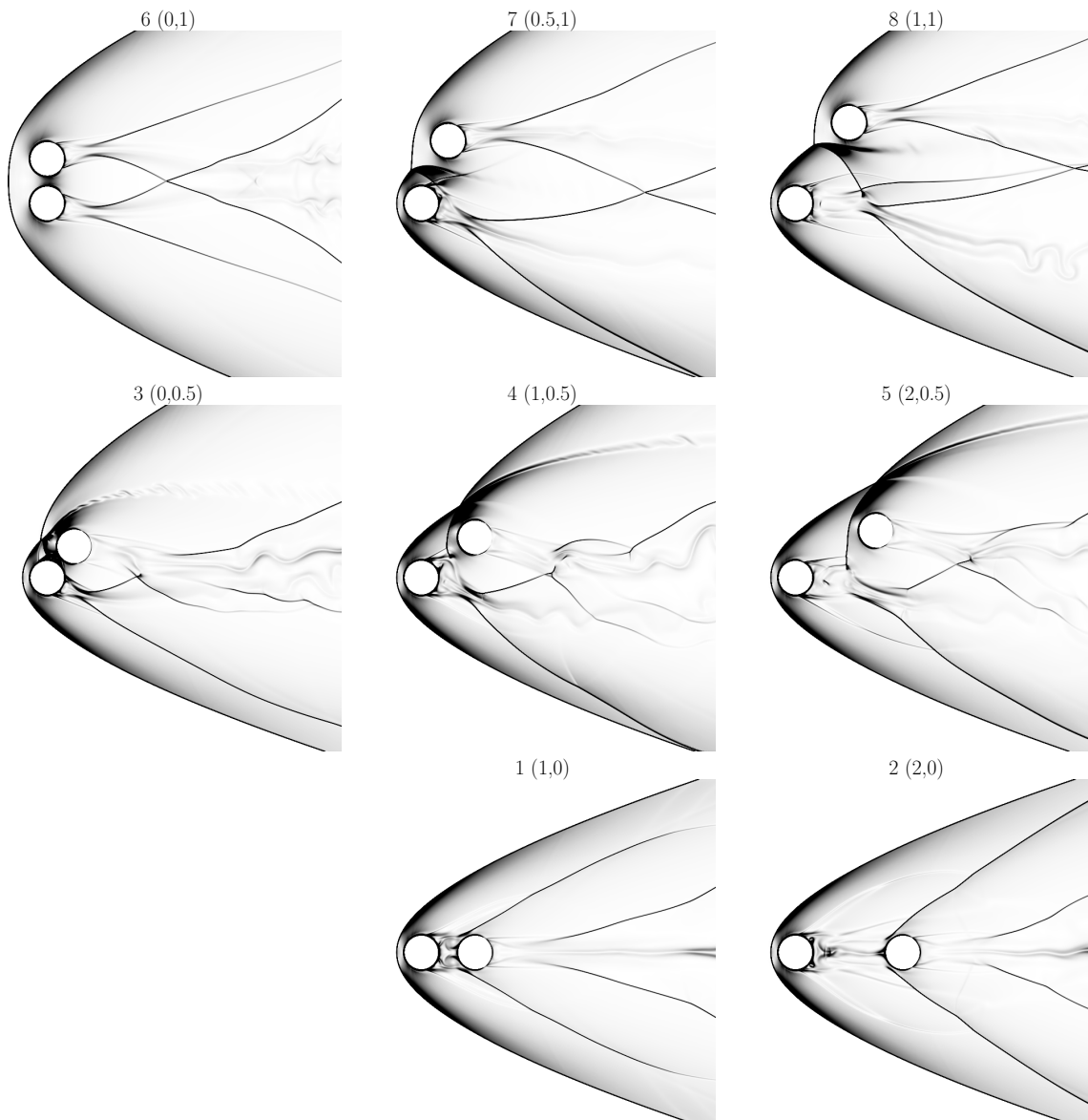


Fig. 4.12 Numerical schlieren for binary body arrangements at $M = 8$.

Surface properties

Figures 4.13, 4.14 and 4.15 show surface pressure coefficient (C_p), skin friction coefficient (C_f) and heat transfer coefficient (C_h). Both C_p and C_f profiles imply the forces acting on the bodies, and C_h implies the total heat load. Observations from these profiles include:

- Often C_p is symmetrical around body centreline aligned with free-stream velocity vector ($\theta = 0$). This means there is no net lift ¹ force and only a drag force is acting on the body due to pressure. Whereas an asymmetrical C_p profile suggests the presence of a lift force and drag force. C_p profile peaks at the stagnation-point and is close to zero behind the cylinder.
- Often C_f is antisymmetric around body centreline aligned with free-stream velocity vector ($\theta = 0$). This suggests zero net torque acting on the body and only drag force due to viscosity. Note, C_f magnitude is around $100\times$ smaller than C_p , so its contribution to drag is negligible. Whereas an asymmetrical profile suggests a net torque acting on the body. C_f tends to zero at the stagnation-point and peaks when surface tangents are aligned with the free-stream. Local maxima and minima are due to boundary layer separations and attachments.
- A symmetrical C_h around the body centreline aligned with the free-stream velocity vector ($\theta = 0$) suggests even heating on both sides of the cylinder. Whereas an asymmetrical profile suggests that one side is heated more than the other. C_h peaks at the stagnation-point and is negligible on a surface with zero projected area (shadow surfaces) in the flow direction. Profile's asymmetry increases with increasing Mach number. The peak heat transfer and the heat load are also visibly different with Mach number and arrangements. As with C_f , local maxima and minima are due to boundary layer separation and re-attachment, clearly visible in arrangements 6, 7 and 8. Moreover, as expected

Generally, surface properties are symmetrical or anti-symmetrical if the body is isolated as it does not feel the other body's presence, for example, the primary body in arrangements 1 and 2. However, a body is feels another's presence, then its surface properties are generally in asymmetrical as in arrangements 3 to 8.

¹The lift force is defined as perpendicular to the free-stream velocity vector.

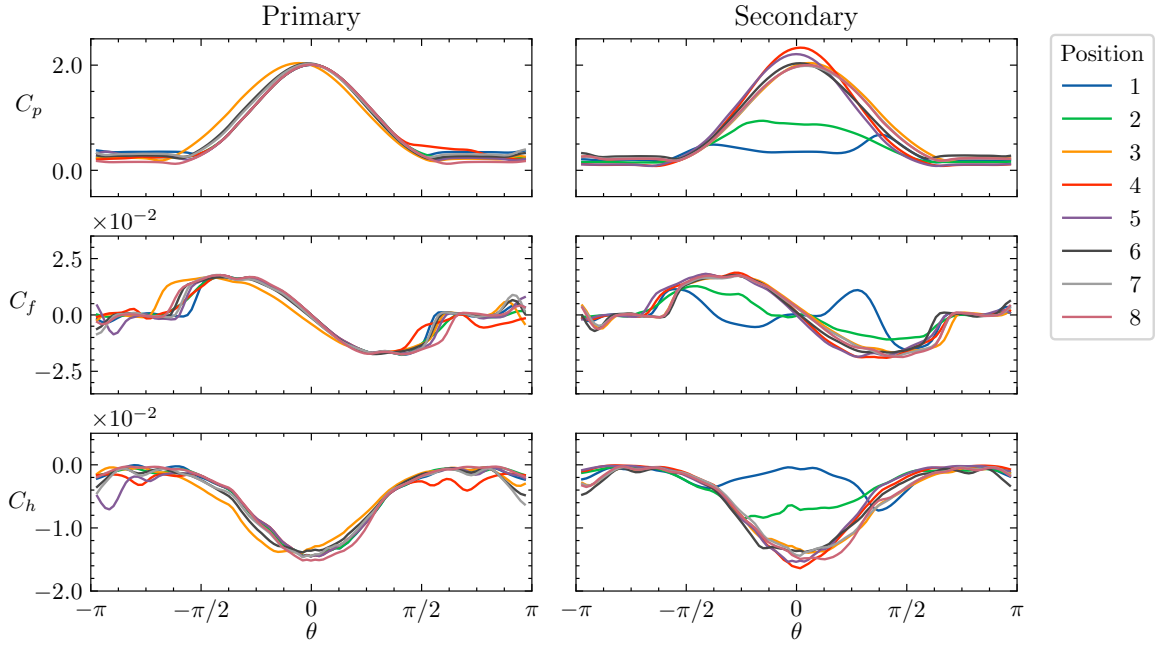


Fig. 4.13 Surface properties for binary body arrangements at $M = 2$. Where θ is positive in anti-clockwise direction and negative in clockwise direction.

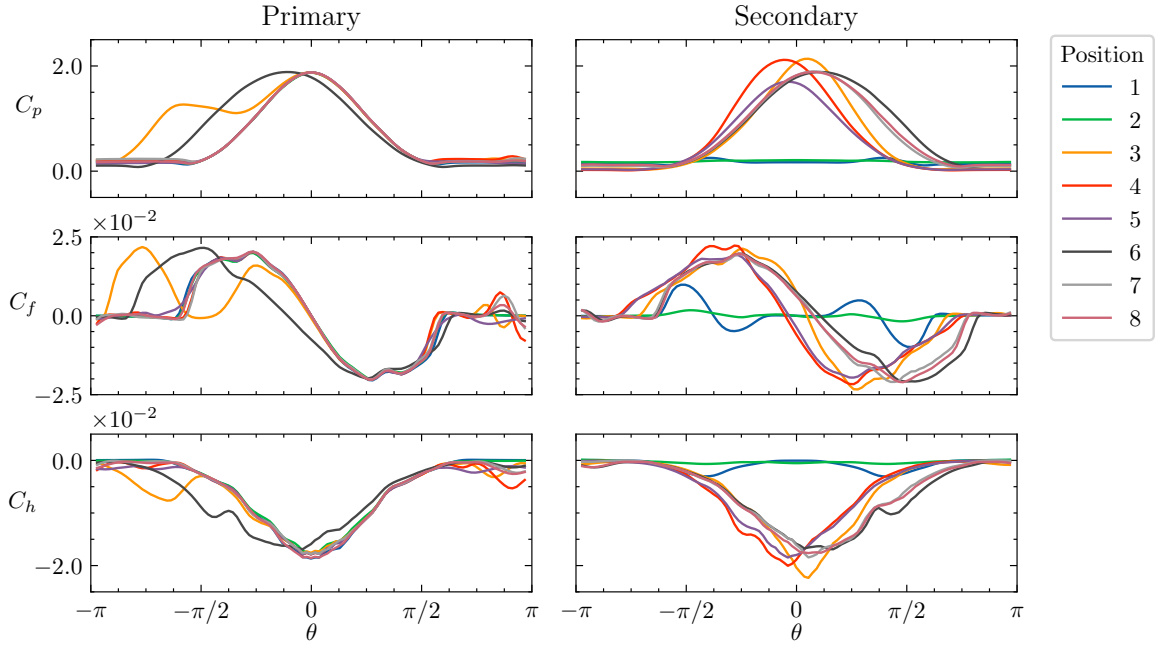


Fig. 4.14 Surface properties for binary body arrangements at $M = 4$. Where θ is positive in anti-clockwise direction and negative in clockwise direction.

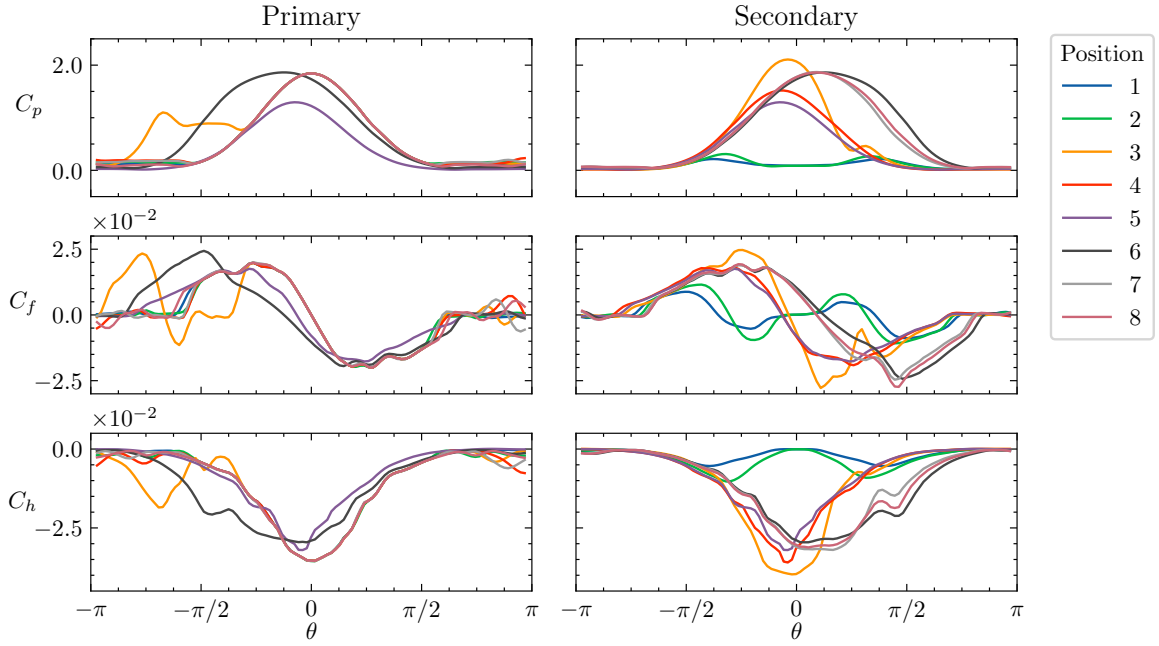


Fig. 4.15 Surface properties for binary body arrangements at $M = 8$. Where θ is positive in anti-clockwise direction and negative in clockwise direction.

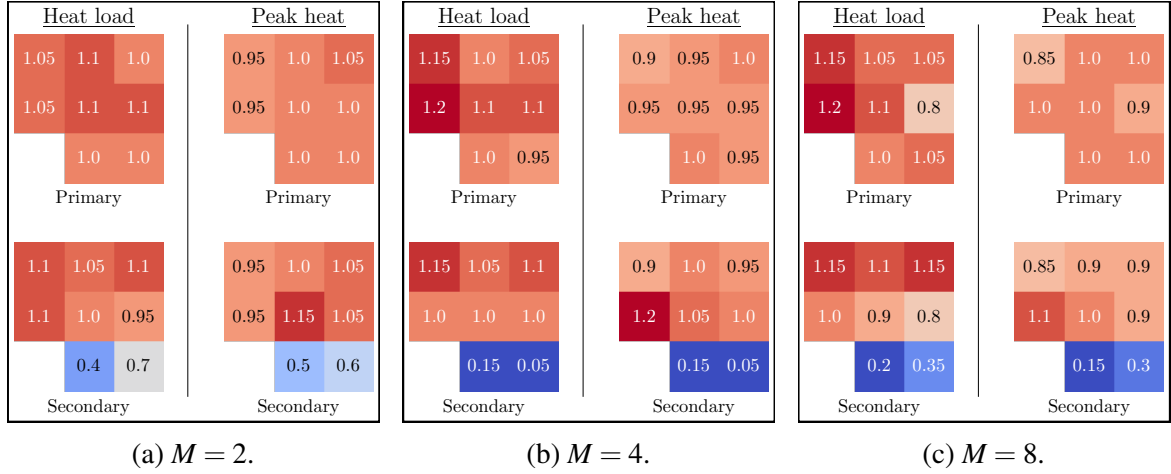


Fig. 4.16 Normalised heat load and peak heat for binary body arrangements.

Figures 4.16a, 4.16b and 4.16c show the heat load and the peak heat flux on each body in all arrangements, normalised by the heat load and stagnation point heat flux for an isolated body. Conservatively given to two significant figures considering mesh convergence in Section 4.3.1. The different binary body arrangements in the figures are in the same order as in Figs. 4.10, 4.11 and 4.12.

Overall, around 20% increase and 90% decrease in heat load and peak heat flux are observed. Generally, the magnitude of variation in heat load and peak heat augmentation is observed to be insensitive to the Mach number. Similar magnitude of variation is also likely to be the case for even higher Mach numbers, and thermochemically frozen flow, as the wake topology remains similar.

When the secondary body is directly behind the primary body, it is thermally shielded significantly. The thermal shielding is due to reduction in heat transfer on the front half of the cylinder ($-\pi/2 < \theta < \pi/2$). This occurs in arrangements 1 and 2 for all Mach numbers, but can also be seen in arrangements 4 and 5 at $M = 8$. The heat transfer is reduced on the front half of the cylinder due to a weaker flow impingement around the stagnation region because of shielding from the leading body, this can also be observed in arrangement 5 at $M = 8$. This behaviour is likely to continue at higher Mach numbers.

On the other hand, the increase in heat load is due to increase to heat transfer on the top ($-\pi/2 < \theta < 0$) or bottom ($0 < \theta < \pi/2$) half. This occurs as the hot shock layer flow is forced between the two bodies. As the secondary body moves towards the primary body's bow shock, as in arrangements 3 and 6, the heat transfer to both bodies increases.

Another observation is that at $M = 2$, arrangements 1 and 2 generate larger heat loads and peak heating than at $M = 4$ and $M = 8$. This is because of mixing of shock layer and cooler inner viscous wake due to wake unsteadiness, which only occurs at $M = 2$, as noted and explained in Section [4.3.2 Numerical Schlieren](#).

Sensitivity to numerical method

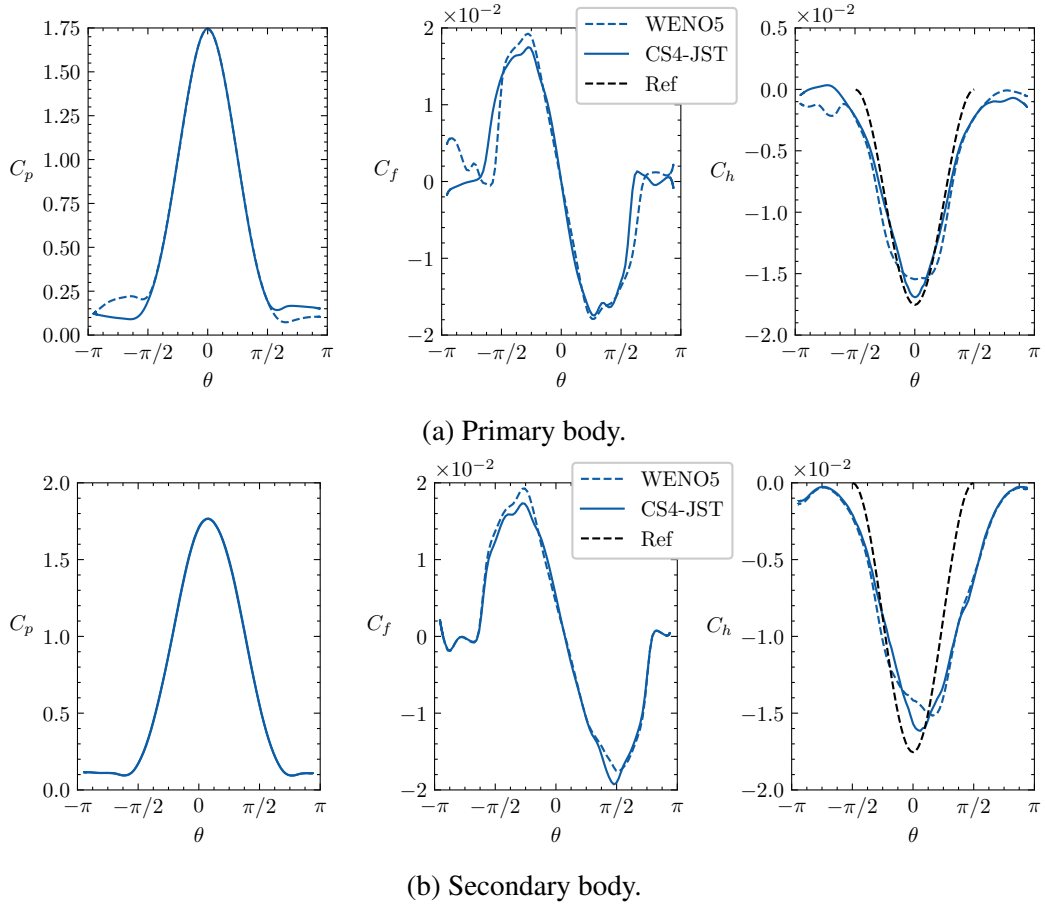


Fig. 4.17 Effect of Euler flux calculation method with WENO5 and CS4-JST in arrangement 4 at $M = 4$.

Surface properties sensitivity to Euler flux calculation method is evaluated with WENO5 and CS4-JST from Section 2.2. Arrangement 4 at $M = 4$ is selected with identical numerical setup as before. The results in Fig. 4.17 suggests that the surface pressure profile is visually identical for the secondary body, whereas the separation point around the cylinder is different between the two methods and differs less than 18° . The peak skin friction coefficient differs less than 10%, the peak heat transfer coefficient is around 6% smaller with WENO5, the head load also has similar magnitude difference. The numerical schlieren images are visually identical and not shown here.

4.4 Multiple bodies

Following the study on heat transfer in binary proximal bodies, a natural first step is to consider multiple bodies, also referred to as a cluster. As before, a static study is justified as the flow timescales are expected to be orders of magnitudes smaller than the relative movement timescales of the bodies.

The heat transfer problem in proximal body clusters has more independent parameters than with binary bodies. Many parameters which affect the body's surface properties are the same as before, namely the flow Mach number and Reynolds number. However, the number of bodies in a cluster, size, and position of the bodies give a larger parameter space than in the binary bodies problem. As a first study, the focus is on the effect of body positions on the cluster averaged body surface properties. Only one flow condition with free-stream $M = 4$ and $Re = 10^4$, and clusters with 5 equal-sized bodies are considered.

The cases are generated by randomly placing cylinder centres whilst ensuring no collisions with each other, and that the bodies are located within the computational domain. Several cases are generated, but eight cases are deemed enough for a first investigation. In this group of eight cases, variety in spacial arrangement of the bodies in the cluster is ensured: cases 7 and 8 are closely arranged; 1 and 2 are medium distance apart; 5 and 6 are loosely arranged; finally, 3 and 4 are more or less arranged linearly—horizontally and vertically. The body positions for each case are listed in Table 4.4.

Table 4.4 Cylinder centre coordinates (x, y) (m) for each case.

Case	A	B	C	D	E
1	(0.150,0.413)	(0.463,0.570)	(0.260,0.335)	(0.171,0.551)	(0.303,0.629)
2	(0.303,0.532)	(0.477,0.310)	(0.562,0.463)	(0.375,0.400)	(0.790,0.485)
3	(0.171,0.576)	(0.537,0.636)	(0.664,0.675)	(0.380,0.684)	(0.874,0.585)
4	(0.254,0.179)	(0.333,0.314)	(0.353,0.675)	(0.327,0.478)	(0.278,0.796)
5	(0.171,0.179)	(0.537,0.478)	(0.664,0.675)	(0.380,0.720)	(0.691,0.192)
6	(0.223,0.671)	(0.335,0.204)	(0.654,0.705)	(0.887,0.577)	(0.312,0.512)
7	(0.306,0.439)	(0.416,0.528)	(0.517,0.452)	(0.342,0.624)	(0.505,0.623)
8	(0.259,0.583)	(0.340,0.672)	(0.388,0.566)	(0.283,0.451)	(0.398,0.453)

The numerical setup is identical to $M = 4$ binary body study in Section 4.3.2 with medium mesh from Section 4.3.1. The only difference is the number of bodies in the computational domain. Fig. 4.18 shows the instantaneous mesh for cases 2 and 5.

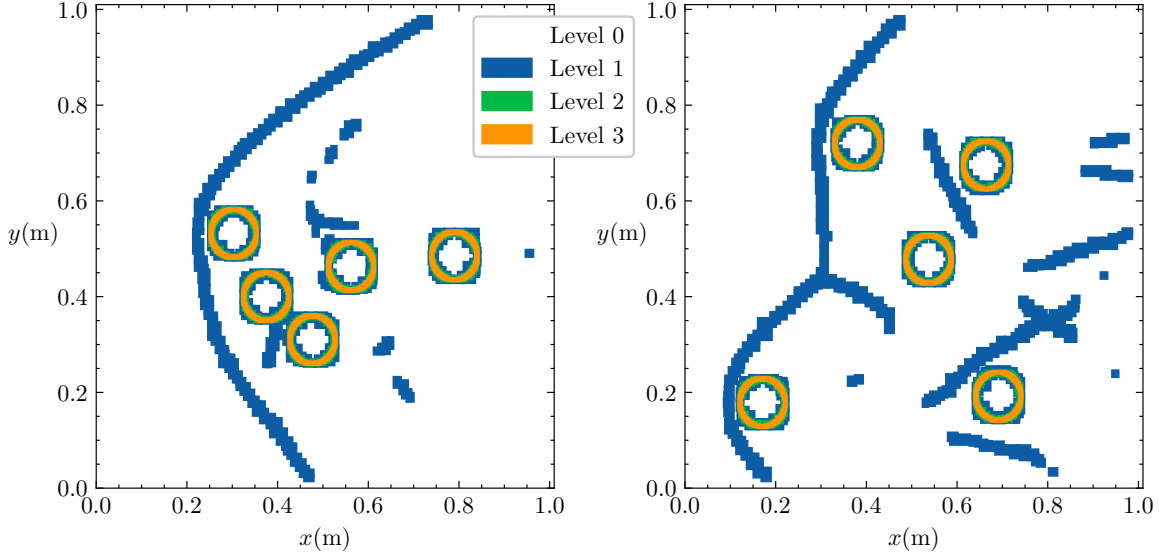


Fig. 4.18 Cases 2 (left) and 5 (right) instantaneous AMR mesh with 3 levels of refinement around body and 1 level of refinement around shocks.

4.4.1 Results

In this work, as a first study, the focus is on cluster average properties and not on a single body from a given cluster. Let $h_{ij}(\theta)$ be the local time varying heat transfer for body i in a given cluster at time j ,

$$Q_{ij} = \int_0^{2\pi} h_{ij}(\theta) d\theta, \quad \bar{Q}_i = \frac{\sum_j Q_{ij}}{N_t}, \quad \langle \bar{Q} \rangle = \sum_i \frac{\bar{Q}_i}{N_b}, \quad \sigma\{\bar{Q}\} = \left(\sum_j \frac{(\bar{Q}_i - \langle \bar{Q} \rangle)^2}{N_b} \right)^{1/2};$$

where N_b are the number of bodies in a cluster, N_t is the number of samples at different times, Q_{ij} is the heat load for body i and time j , \bar{Q}_i is the time averaged heat load for body i in a cluster, $\langle \bar{Q} \rangle$ is the ensemble averaged heat load over bodies in a cluster and $\sigma\{\bar{Q}\}$ is the standard deviation of the time averaged heat load over bodies in a cluster.

Numerical schlieren

Figure 4.19 shows the instantaneous numerical schlieren image from the eight cases. The primary bow shock shape varies dramatically depending on the body arrangements. Highly

unsteady wakes are generated with shock interactions and shocklet shedding. The unsteadiness is significant compared to binary body arrangements in Fig. 4.11, despite the same free-stream conditions and wake Reynolds number. Quantitatively, the flow field unsteadiness Fig. 4.20 shows cluster ensemble-averaged heat load over ten flow times, which is normalised by an isolated body's heat load Q_1 . It shows that the normalised time average heat load approximately varies between 1.2 to 0.4. Cases 5 and 6 have the largest heat load fluctuations in time. This agrees with the observed unsteady behaviour based on numerical schlieren in Fig. 4.19. Furthermore, a time average over ten flow times is deemed to be a reasonable approximation of the steady-state heat load.

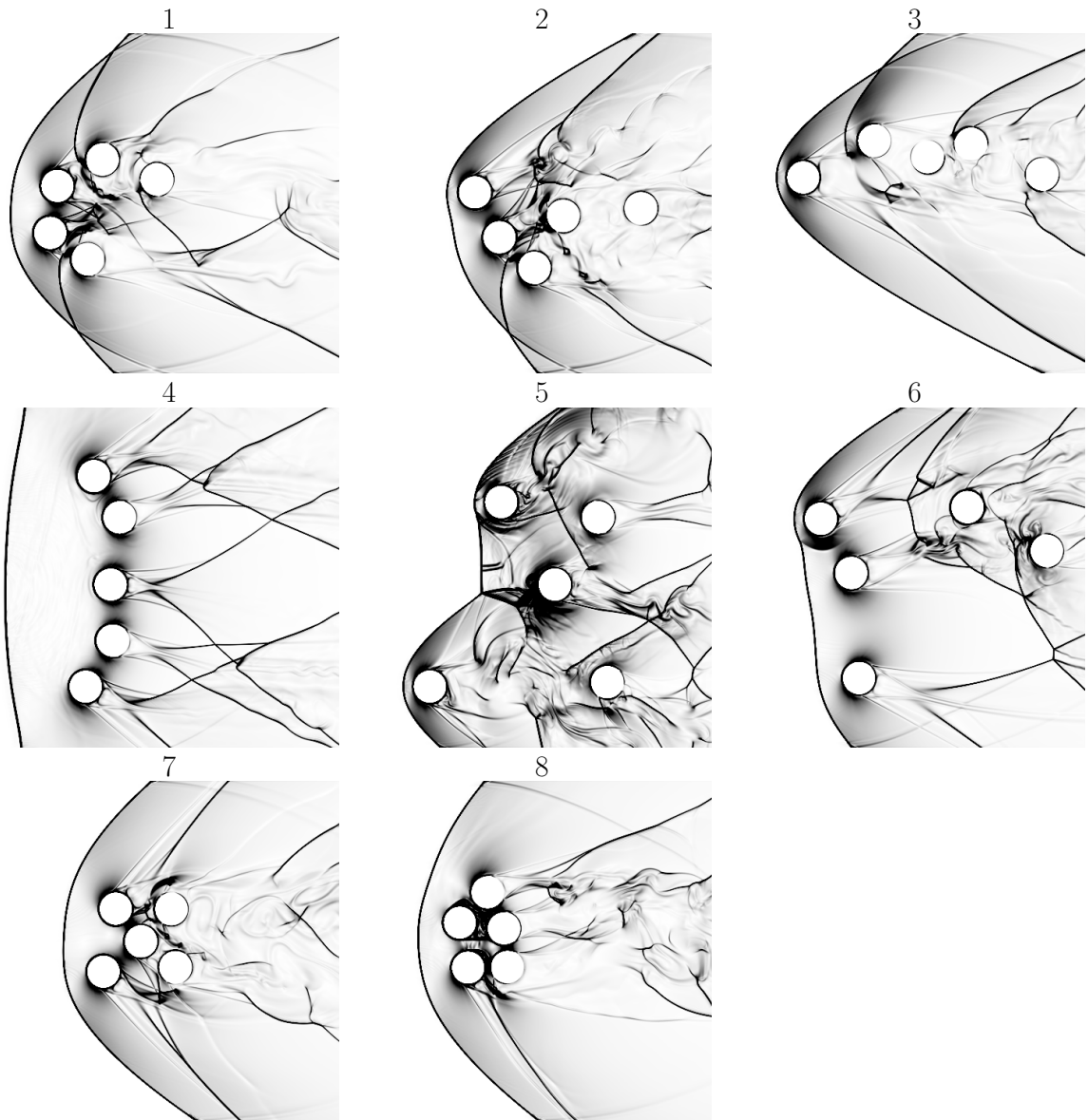


Fig. 4.19 Numerical schlieren of five body clusters at $M = 4$ in eight different arrangements.

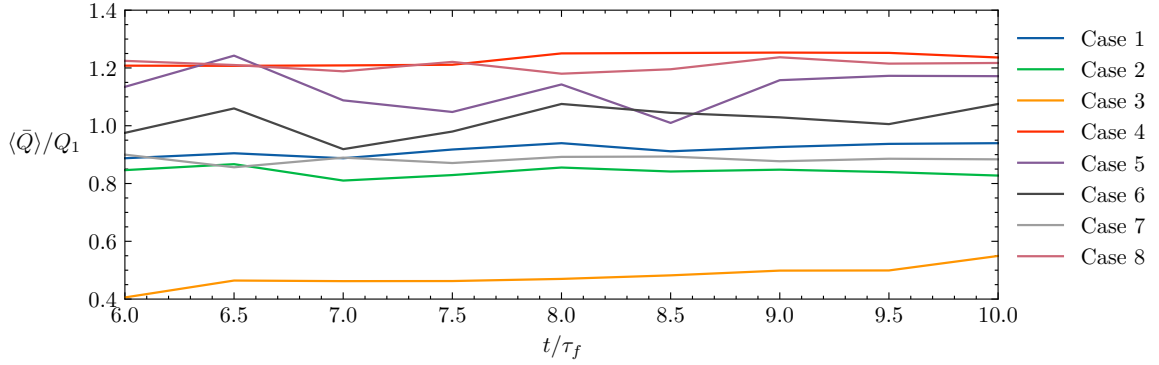


Fig. 4.20 Cluster averaged heat load ($\langle \bar{Q} \rangle$) varying over 6-10 flow times in all cases.

Average heat transfer profiles and heat load scaling

Figure 4.21 shows the time and ensemble averaged over all bodies in a cluster for all cases. All cases have their average stagnation point heat transfer reduced by around 10% to 50% compared to an isolated body. This is because some bodies are shielded from the direct shocked flow, for example some bodies in cases 1, 2, 3 and 7. However, the heat transfer around the sides and the back, for $\pi/4 \lesssim |\theta| < \pi$, is increased in many cases. This increase not only offsets the reduction in heat load around the stagnation region, but also results in a net increased heat load when compared to an isolated body. Considering Fig. 4.20 (also Fig. 4.20), cases 4, 5 and 8 receive a larger heat load than an isolated body. In case 5, the unsteadiness and mixing in the wake is responsible for the increased heat load. But in case 4, the flow is forced to pass in between the cylinders which act as obstacles, increasing the boundary layer gradients on the sides of the cylinders. On the other hand, case 8 has increased heating on the side and back as hot gases from the stagnation region of the combined bow shock linger in the small spaces in between the bodies. Therefore, despite similar increases in heat load in these cases, they seem to be caused by different mechanisms.

Moreover, cases 7 and 8 are visually similar, but there is a significant difference between their average heat load—a factor of ~ 1.2 and ~ 0.85 respectively, compared to an isolated body. The exact reason for this is not clear as the flow fields contain many shocks and expansions, and is unsteady. Lastly, heat load in case 6 is on average the same as an isolated body as the increase in heat transfer to the leading bodies is negated by the reduced heat transfer to the trailing bodies.

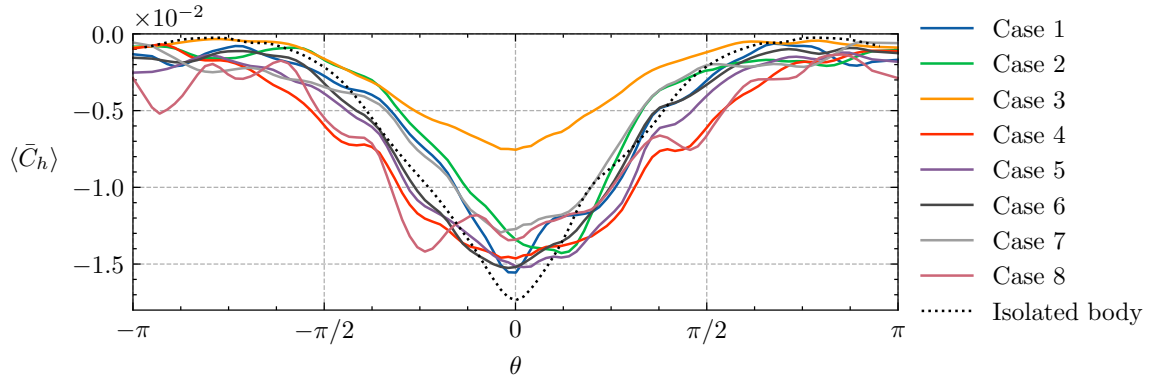


Fig. 4.21 Time and ensemble averaged heat transfer profile around cylinder. Where θ is positive in anti-clockwise direction and negative in clockwise direction.

Figure 4.22 shows the scaling of cluster ensemble time average heat load with cluster properties. Simple cluster properties like standard deviation of body positions in coordinate directions give good correlations with current data. More complex properties like projected area in the flow direction, and for a collection of points (body centres) hamiltonian path, Minkowski distance, do not give improved correlations. Position coordinates standard deviations parallel to the flow vector ($\sigma\{x\}$) and ($\sigma\{y\}$) perpendicular to the flow vector correlate well with the ensemble heat load for different clusters. Increasing $\sigma\{x\}$ decreases the ensemble heat load, whereas increasing ($\sigma\{y\}$) increases the ensemble heat load. The ratio $\sigma\{x\}/\sigma\{y\}$ correlates best with the ensemble heat load. Importantly, it suggests that when $\sigma\{x\}/\sigma\{y\} \gtrsim 1$, the ensemble heat load is less than compared to an isolated body; in other words, thermal shielding occurs. On the other hand, $\sigma\{x\}/\sigma\{y\} \lesssim 1$ results in an increased ensemble heat load compared to an isolated body; in other words, thermal amplification occurs.

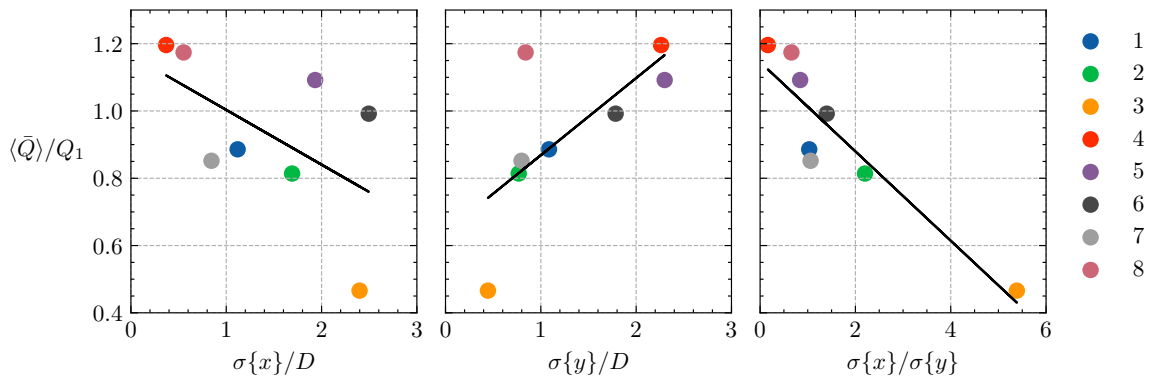


Fig. 4.22 Time and body ensemble averaged heat load ($\langle \bar{Q} \rangle$) scaling with body position standard deviations ($\sigma\{x\}/D$, $\sigma\{y\}/D$, $\sigma\{x\}/\sigma\{y\}$) for all cases.

Note, these scaling parameters are only valid for closely packed clusters with $\sigma\{x\} \lesssim 3D$ and $\sigma\{y\} \lesssim 3D$. For $\sigma\{y\} \gg 3D$, meaning the cluster approaches an essentially isolated limit. Therefore, the current linearly increasing heat load behaviour cannot be sustained for all values of $\sigma\{y\}/D$.

Heat load standard deviation in a cluster is correlated with a variety of parameters, in Fig. 4.23. Strongest (negative) correlation is observed with $\sigma\{y\}$ and the weakest correlation is with $\sigma\{x\}$. Interestingly, $\sigma\{x\}/\sigma\{y\}$ shows a positive correlation. Moreover, $\langle\bar{Q}\rangle/Q_1$ shows a strong correlation, as expected from the negative correlation between $\sigma\{x\}/\sigma\{y\}$ and $\langle\bar{Q}\rangle/Q_1$. Note, increasing $\sigma\{y\}$ cannot decrease $\sigma\{\bar{Q}\}$ beyond 0. This means that for $\sigma\{y\} \gtrsim 3D$, according to the current data, there must be a change in trend. As, intuitively, the heat load variance in a cluster should go to zero as the cluster size increases.

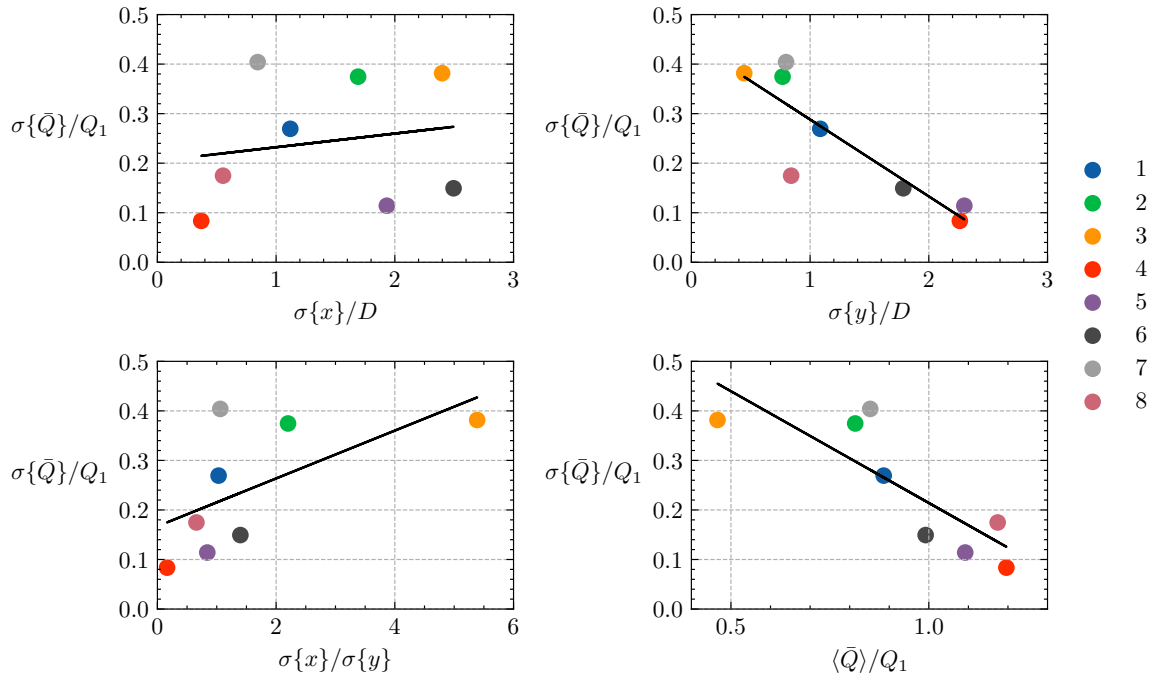


Fig. 4.23 Body time averaged heat load standard deviation ($\sigma\{\bar{Q}\}$) scaling with body position standard deviations ($\sigma\{x\}/D$, $\sigma\{y\}/D$, $\sigma\{x\}/\sigma\{y\}$) and ensemble time average heat load ($\langle\bar{Q}\rangle/Q_1$) for all cases.

4.5 Summary

This chapter studied the heat transfer in proximal cylinders in the near wake, within five diameters of each other. The motivation for the study was that destructive atmospheric entries involve fragmentation and interaction of bodies. The relative velocities of bodies in a cluster are much slower than the flow velocity. Therefore, static body studies to understand surface properties are justified. In particular, the focus of the work was to understand the heat transfer to proximal bodies.

Firstly, binary bodies are considered. The secondary body's positions are systematically varied in the primary body's near wake. Different arrangements are considered at Mach numbers 2, 4 and 8 with constant wall temperature, under calorically perfect gas assumption and without thermochemical relaxation. The key findings from the study are:

- The heat load and peak heat transfer can be augmented for either one or both proximal bodies by +20% to −90% of an isolated body. The magnitude of variation in the heat load and the peak heat transfer is observed to be insensitive to the Mach number. And since the wake topology remains similar even at higher Mach numbers, given similar free-stream Reynolds number, a similar magnitude of variation in heat transfer is also likely for even higher Mach numbers. However, an important parameter governing the magnitude of heat transfer to the secondary body in the primary body's wake maybe the wake Reynolds number.
- Minimum heat load and minimum peak heat transfer (maximum thermal shielding) occurs when the secondary body is in the viscous wake of the primary body. In other words, when the second body is tailgating the primary body. The thermal shielding is due to reduction in heat transfer on the front half of the cylinder ($-\pi/2 < \theta < \pi/2$). The heat transfer is reduced on the front half of the secondary cylinder due to a weaker flow impingement around its stagnation region because of flow shielding from the leading body, leading to larger boundary layer and reduced heat transfer.
- Maximum heat load occurs when the secondary body approaches the primary body's bow shock and stagnation region. The increase in heat load is due to increase to heat transfer on the top ($-\pi/2 < \theta < 0$) or bottom ($0 < \theta < \pi/2$) half of the cylinder due the presence of the other body.

Secondly, multiple bodies near each other are considered. Eight clusters with five semi-randomly arranged cylinders are generated, and the cluster average heat transfer and standard deviation are correlated with cluster properties. The key findings from the study are:

- The average heat load in a cluster ranges between +20% and –60% of an isolated body. The change in heat load is mainly due to the change in heat transfer around the sides and the back, for $\pi/4 \lesssim |\theta| < \pi$, is increased in many cases. However, the average heat load around the stagnation region is also reduced in all clusters, as some bodies are shielded from the direct flow. The increased heat transfer to sides and back is caused by: unsteadiness and mixing in the wake; the flow being forced to pass in between the cylinders; or the hot flow from the stagnation region lingering in the small spaces in between the bodies.
- The average heat load in a cluster shows a negative correlation with the ratio of: standard deviation of body coordinates in direction parallel to the free-stream velocity, to standard deviation of body coordinates in direction perpendicular to the free-stream velocity. In other words, clusters thin in the direction perpendicular to the free-stream velocity and long in the direction parallel to the free-stream velocity have their heat load reduced (thermally shielded). In contrast, thick and short clusters, in directions perpendicular and parallel to the free-stream velocity, feel an increased heat load.
- The heat load standard deviation in a cluster is also negatively correlated with the body position's standard deviation in the free-stream perpendicular direction. This means that heated clusters have a smaller variation of heat load amongst its bodies than cooled clusters.

Although, relatively small Mach numbers ($M < 8$) are tested when compared to sub-orbital Mach numbers ($M \lesssim 30$). The trends observed in the current work are expected to remain valid even at higher Mach numbers in frozen flow. This is because of the following reasons: the Mach number independent non-dimensionalisation of the body positions; normalisation of the heat transfer with an isolated body; and, the fact that wake topology does not change significantly with the Mach number.

The main limitation to the current study is that the current simulations are two-dimensional, which do not account for three-dimensional effects. Nevertheless, the trends and intuition gained in the current work are likely to apply to three-dimensional flows, at least qualitatively. However, the magnitude of the heat transfer augmentation observed in the current work is likely to be different in three dimensions.

Moreover, with high Mach number reacting flows chemical dissociation and ionization can significantly reduce the heat transfer to bodies. The chemical compositional changes also affect the gas transport properties, and most importantly thermal conductivity. For binary body configuration, the compositional changes of the fluid in the primary body's wake could

change the secondary body's wall transport properties significantly. Therefore, future studies should extend the current work to include thermochemical non-equilibrium modelling in three dimensions.

From a numerical perspective, flows with increasing Mach numbers with the current numerical method result in increasingly inefficient computations. This is because large number of refinement levels are required to resolve stagnation point heat transfer. Increasing the refinement ratio between levels is likely to improve the computational efficiency.

5. Hypersonic ablation patterns

Previously, Chapters 2 and 3 developed a numerical method for modelling hypersonic flows around complex geometries. This chapter applies the method to study hypersonic ablation patterns.

5.1 Introduction

Hypersonic ablation is a process in which a material surface erodes at high temperatures, it is driven by energy exchanges at the surface and results in surface mass loss. It is observed during controlled and uncontrolled atmospheric entry of satellites, spacecrafts and meteors. There are various physical mechanisms which cause hypersonic ablation: phase changes (sublimation/evaporation and melting); surface (heterogeneous) chemical reactions; and spallation¹. These result in the surface receding over time and often unevenly in space, generating surface patterns over a range of length scales, as shown in Fig. 5.1. Simple patterns like grooves and cross-hatching are thought to decay towards more complex patterns like regmaglypts (also known as scallops) found in meteorites.

Hypersonic ablation problem is a member of a larger set of ablation problems. In these problems, the boundary's slow movement is driven by faster, local fluid dynamics. Subsonic ablation problems are ubiquitous in nature and have been studied across different research fields (Ristroph, 2018). Ablation patterns which emerge from these disparate scenarios look alike over a range of length scales despite the different physical mechanisms driving them, some of these patterns are shown in Fig. 5.2. The sub-figures (a) and (b) show pattern formation by dissolution mechanism (Cohen et al., 2020), whereas (c) and (d) show patterns formed by granular transport of snow (Amory et al., 2017) and radiative heat transfer to snow (Betterton, 2001; Claudin et al., 2015).

¹The ejection of surface material due to thermal stresses.

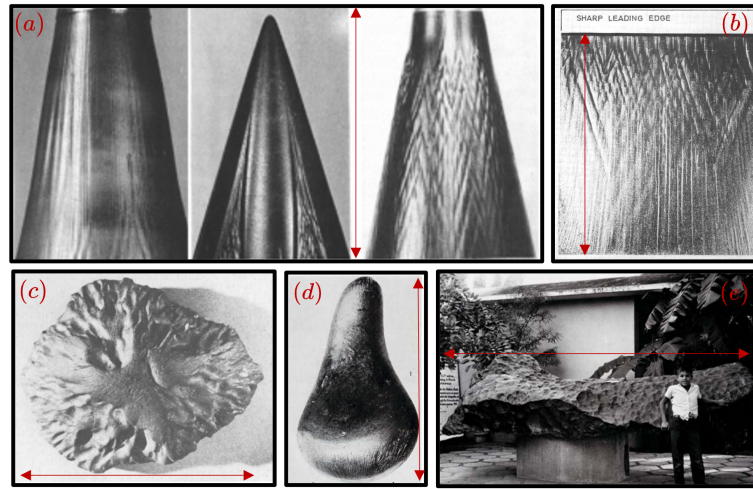


Fig. 5.1 Hypersonic ablation surface patterns with indicated length scales. (a) From left to right, ablation grooves, turbulent wedge and cross-hatching patterns on wax cone (0.1 m) (Stock, 1975). (b) Flat plate cross-hatching pattern on wax ablator (0.15 m) (Stock and Ginoux, 1973). (c) The Middlesbrough stony meteorite, a smooth nose, few large and deep ablation pits followed by regmaglypt surface (0.16 m) (Lin and Qun, 1987). (d) A smooth pear-shaped iron meteorite (0.12 m) (Hodge-Smith, 1939). (e) Bacubirito iron meteorite, world's longest meteorite, covered in regmaglypts (4.2 m) (Terán-Bobadilla et al., 2017).

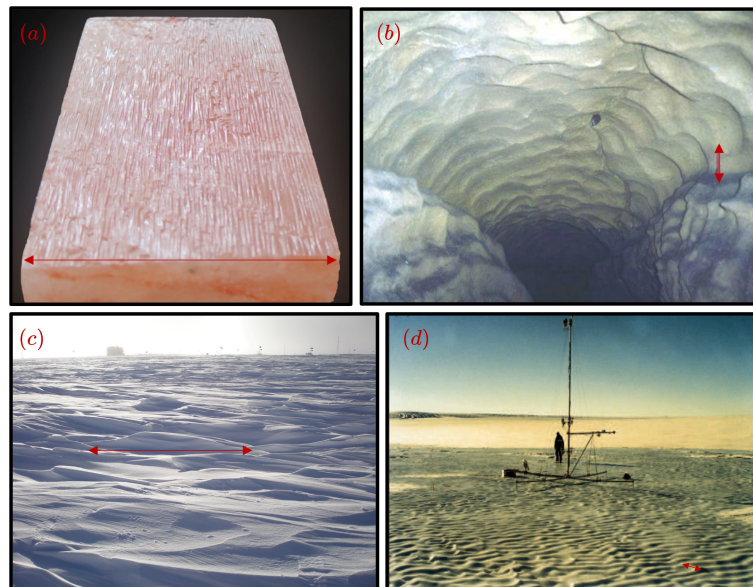


Fig. 5.2 Subsonic ablation surface patterns. (a) Pink salt block with longitudinal grooves (0.1 m) (Cohen et al., 2020). (b) Scalloped Shafts cave walls (0.15 m) (Meakin and Jamtveit, 2010). (c) Sastrugi in snow (1 m) (Amory et al., 2017). (d) Ice ablation waves (0.2 m) (Bordiec et al., 2020).

5.1.1 Existing studies

Most experimental (lab and flight) and theoretical studies in the literature on hypersonic ablation patterns are from around the 1970s and focus on regular cross-hatching patterns. Most of these studies are reviewed and summarised by (Swigart, 1974), which suggests that cross-hatching patterns have been experimentally characterised extensively over a range of Reynolds numbers and Mach numbers. Also, with a variety of materials: low-temperature ablators like camphor, naphthalene, and wood; as well as high-temperature ablators like graphite, and carbon phenolics. The test geometries have been mainly blunted and sharp cones or flat plates. From these experiments, it is clear that cross-hatching occurs with supersonic or hypersonic transitional boundary layers. Laminar subsonic boundary layers do not produce cross-hatching patterns. Moreover, the characteristics of the resulting diamond-shaped elements which form, as shown in Fig. 5.1(b) can be correlated with the flow parameters. However, the mechanism producing these patterns remains unclear.

Another kind of ablation patterns are known as Regmaglypt patterns, as in Fig. 5.1(e). It is known that regular cross-hatching patterns may degrade towards regmaglypts patterns (Stock and Ginoux, 1973). Regmaglypts are also often found on meteors (Lin and Qun, 1987). They are expected to form in turbulent flow and the characteristic pattern's length scale is likely linked to some flow length scale (Bronshen, 2012). However, they are not well understood and have not been characterised.

Only a handful of modern studies exist on hypersonic ablation patterns. (Duffa et al., 2005; Vignoles et al., 2009) study carbon-based materials ablating in subsonic flow experiments and analytically. They find that surface patterns form via a competition between diffusion and heterogeneous reactions. The only computational study (Trevino, 2021) in the literature, was completed independently and in parallel to the current study. They computationally model subliming low-temperature camphor ablators and observe the formation of localised grooves, but more complex patterns like cross-hatching and regmaglypt are not observed.

Other studies focus on ablation shape changes rather than surface patterns. (Simpkins, 1963) study ablation shape change experimentally, beginning with an axis-symmetric Teflon body. They find that the body ablates towards an equilibrium profile. This profile is found to be independent of the initial nose profile obtained. Moreover, (Miller and Sutton, 1966) study the effect of Reynolds number on shape change initially. They find that in low Reynolds number flows an initially hemispherical ablating body will evolve into a somewhat blunter shape. However, with higher Reynolds number conditions, an ogival-shaped nose forms due to increased heating as the flow transitions outside the nose. More recently, (Bianchi et al.,

2021) experimentally and computationally study shape changes in low-temperature ablators, namely Camphor and Naphthalene.

The effect of ablation patterns on the boundary layer is not well explored. Only one study is found in the literature, (Peltier et al., 2016) which investigates the effects of cross-hatching patterns on the boundary layer experimentally and computationally. They observed significant pressure loading on the roughness elements, which results in a wave pattern of alternating shocks and expansions that span the boundary layer. Overall, the boundary layer has increased net swirling and Reynolds stresses in the lower half of the boundary layer.

In summary, the fluid-structure interaction between an ablating surface and the boundary layer is not well understood. The development of hypersonic ablation surface patterns and the effects of the developed patterns on the boundary layer are not well characterised. The current computational study aims to develop, implement and validate a numerical ablation method; and understand some of the mechanisms behind hypersonic ablation patterns.

5.2 Hypersonic ablation modelling

Hypersonic ablation is driven by four mechanisms: melting, sublimation/evaporation, heterogeneous reactions and spallation. The first two are most important and account for the majority of mass loss (Duffa, 2013) in atmospheric entries. Melting and evaporation-driven ablation involves a liquid phase and requires more complex modelling (Bethe and Adams, 1959; Feldman, 1959; Raghunandan et al., 2021) compared to sublimation and spallation. Spallation is the ejection of solid particles from the ablating surface and is generally the least important mode in hypersonic ablation; however, in some cases it can be significant depending on the material structure and induced thermal stresses. For example, the Galileo probe may have had 10-30% of its ablation mass loss by spallation (Davuluri et al., 2016). However, it remains poorly characterised with very few studies on the topic and remains an active research area (Grigat et al., 2020; Price et al., 2020). Heterogeneous reactions include Oxidation and Nitridation reactions and generally cause little mass loss compared with melting/evaporation or sublimation. Furthermore, they are only well characterised for carbon ablators. Current work focuses on ablation by sublimation only, for simplicity

Sublimation (and evaporation) are phase change reactions that are most simply described by the Hertz-Knudsen law (also known as Knudsen-Langmuir law in sublimation-related literature). It is a balance of two terms, the first term represents the sublimation/evaporation flux of gaseous particles from the solid (or the liquid surface), and the second term represents the condensation flux of gaseous particles to the solid surface. The governing equation is

$$\omega_k = \alpha_k \sqrt{M_k / 2\pi RT_w} (p_{e,k} - p_{w,k}); \quad (5.1)$$

where α_k is an accommodation coefficient usually from experimental measurements or molecular dynamics simulations, M_k is the molar mass, T_w is the wall temperature; $p_{w,k}$ is the species wall partial pressure. More detailed modelling of sublimation and evaporation is discussed by Dias (2020) and can include convective effects in a thin layer (also known as the Knudsen layer) around the surface. The equilibrium vapour pressure (p_e) can be estimated by a variety of semi-empirical fits (Poling et al., 2001). The simplest ² fit is known as the Clausius-Claperyon relation,

$$p_{e,k} = p_{a,k} \exp(-h_{sg,k}/R_k T_w) = p_{a,k} \exp(-T_a/T_w); \quad (5.2)$$

²A more complex fit adds curvature to the log-linear Clausius-Claperyon relationship and is of the form $p_a = B \exp(-C/(T_w + D))$. This is called the Antoine equation, where B, C, D are constants.

where $p_{a,k}$ is the activation-like pressure; $h_{sg,k}$ is the enthalpy of sublimation (or evaporation); $T_{a,k} = h_{sg,k}/R_k$ is the activation-like temperature.

Combining Eqs. (5.1) and (5.2):

$$\omega_k = A_k T_w^{-1/2} (\exp(-T_{a,k}/T_w) - p_{w,k}/p_{a,k}), \quad A_k = \alpha_k p_{a,k} \sqrt{M_k/2\pi R}; \quad (5.3)$$

where A_k is a constant. Therefore, sublimation (or evaporation) of a pure substance is a function of three parameters ($A_k, T_{a,k}, p_{a,k}$). For common compounds, numerical values of these parameters are listed in Table 5.1. Carbon (C) commonly found in heat shields as pure graphite or Carbon-Phenolic composites (Duffa, 2013). Iron (II) oxide, Silicon dioxide and Magnesium oxide are the most abundant species found in H-type chondrite meteors, which are the most common type of meteors (Jarosewich, 1990). Naphthalene and Camphor are low-temperature ablators, often used in laboratory experiments where true re-entry conditions are impossible to generate, for example, Bianchi et al. (2021).

Table 5.1 Hertz-Knudsen parameters values (rounded to two significant figures) for some common hypersonic ablation materials.

Material	Reference	A_k	$p_{a,k}$ (pa)	$T_{a,k}$ (K)
Carbon (C) ³	(Mortensen and Zhong, 2014)	28×10^9	13×10^{12}	86×10^3
Iron (II) oxide	(Dias, 2020)	4.4×10^9	120×10^9	52×10^3
Silicon dioxide	(Dias, 2020)	14×10^9	410×10^9	52×10^3
Magnesium oxide	(Dias, 2020)	7×10^9	260×10^9	52×10^3
Camphor	(Haynes, 2014)	4.48×10^9	83×10^9	6400
Naphthalene ⁴	(Linstrom and Mallard, 2001)	320×10^6	74×10^5	1800

³Note, carbon sublimation can also produce C_2, C_3, C_4, C_5 where only C_2 and C_3 sublime significantly, as their equilibrium vapour pressures are of the same magnitude as C with about 10% higher activation temperature (Mortensen and Zhong, 2014)

⁴Naphthalene equilibrium partial pressure is in Antoine equation form, and the additional constant is $D = -61$ K. Since $D \ll T_w$, it is possible to ignore the constant as a first approximation, revealing the simpler Clausis-Claperyon relation.

5.2.1 Multi-species sublimation boundary conditions

Multi-species ablation boundary conditions for subliming non-porous and rigid ablators are simply steady state surface conservation balances (Duffa, 2013), illustrated in Fig. 5.3.

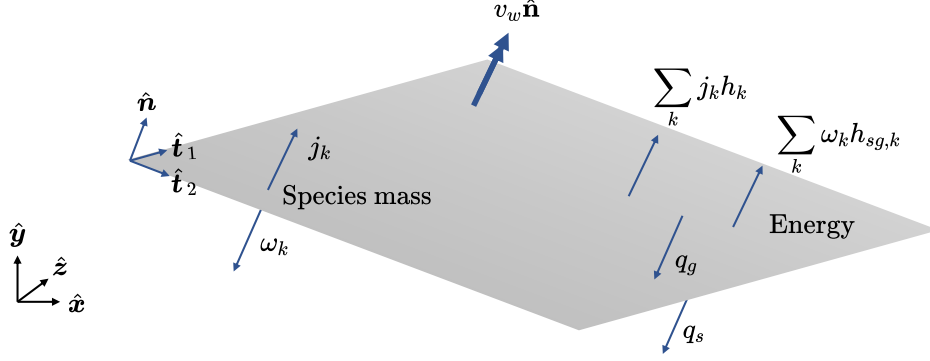


Fig. 5.3 Surface species mass (left) and energy (right) balances with two coordinate systems, global $(\hat{x}, \hat{y}, \hat{z})$ and local $(\hat{n}, \hat{t}_1, \hat{t}_2)$.

The species mass balance involves a diffusive flux j_k balanced by a species ablation rate ω_k . The momentum transfer is trivial as the wall is rigid, and so it is restricted to moving in the wall-normal direction only. Near wall velocities are small, so the dynamic pressure is approximately equal to the static pressure. So, the Navier-Stokes momentum balance in the wall normal direction at steady state leads to a zero wall-normal pressure gradient.

The energy balance is complex, the gas phase heat transfer to the surface (q_g) is balanced by solid-phase heat transfer (q_s), heat transfer by mass transfer ($\sum_k j_k h_k$) and the enthalpy of phase change ($\omega_k h_{sg,k}$), where $h_{sg,k}$ is the phase change enthalpy of species k .

The wall state is defined by thermodynamic $\{\rho_w, Y_{w,k}, v_w, T_w, p_w\}$ and geometric parameters $\{\hat{n}, \hat{t}_1, \hat{t}_2\}$. The number of conservation equations plus the equation of state equals the number of unknowns in the wall state vector. Mass, species mass, energy and wall-normal momentum surface conservation balances are:

$$v_w = \sum_k \omega_k / \rho_s, \quad j_k = \omega_k'', \quad q_g = q_s + \sum_k \omega_k h_{sg,k} + \sum_k j_k h_k, \quad \left. \frac{dp}{dn} \right|_w = 0; \quad (5.4)$$

where v_w is the wall recession velocity in the local coordinate system and can be transformed into a velocity vector in the global coordinate system.

5.2.2 Simple boundary conditions

For a binary system, the boundary conditions can be simplified by taking species 1 as the ablation species and species 2 as the free-stream species. The diffusive fluxes must sum to zero:

$$\sum_k j_k = j_1 + j_2 = 0 \quad \longrightarrow \quad j_2 = -j_1 \quad (5.5)$$

Hence, Eq. (5.4) simplifies to:

$$v_w = \omega_1/\rho_s; \quad j_1 = \omega_1; \quad q_g = q_s + \omega_1(h_{sg,1} + h_1 - h_2); \quad \left. \frac{dp}{dn} \right|_w = 0. \quad (5.6)$$

For single species:

$$v_w = \omega/\rho_s; \quad q_g = q_s + \omega h_{sg}; \quad \left. \frac{dp}{dn} \right|_w = 0. \quad (5.7)$$

Modelling the solid phase heat transfer, q_s , is not trivial. Previous studies [Bianchi et al. \(2021\)](#); [Trevino \(2021\)](#) compute the solid phase heat transfer with the heat equation. However, approximations may be possible considering the physics.

In hypersonic atmospheric re-entries and most hypersonic experiments, the short flow duration and small thermal diffusivities of materials only allow the thermal front to travel small distances, usually much smaller than the body's characteristic length scale. The distance travelled by the thermal front is known as the penetration distance (l_p), where $l_p = \sqrt{4\pi\alpha_s t}$ in a solid which is infinitely large in two-dimensions and finite in one-dimension, with a constant wall temperature ([Bergman et al., 2011](#)).

The thermal diffusivity α (m²/s) of Iron and Camphor⁵ is $O(10^{-5})$. The flow duration (t) for atmospheric re-entries and laboratory experiments with ablation changes is approximately, $O(10) - O(100)$ s. Therefore, $O(10^{-1.5}) < l_p < O(10^{-2})$ m. This means that the heat transfer is essentially to a semi-infinite solid (temperature field only varying in one-direction, normal to the surface) for bodies with characteristic scales much larger than $\sim 10^{-1}$ m. The heat transfer to a semi-infinite solid over time is $q_s = k(T_s - T_i)/l_p$, where T_s is the surface temperature and T_i is the initial surface temperature.

However, this semi-infinite solid assumption becomes inaccurate around surface features with similar length scales to the thermal penetration distance. Moreover, as the shape changes

⁵Solid phase properties estimated from [Bianchi et al. \(2021\)](#); [Linstrom and Mallard \(2001\)](#); [Trevino \(2021\)](#)

due to ablation, the surface temperature changes and this further invalidates the simple approximation. To begin with, and for simplicity, the solid phase heat transfer is assumed to be zero in the present work.

5.2.3 Numerical method

Studying hypersonic ablation computationally is a difficult problem due to the problem's large range of space and time scales. Surface recession rate due to ablation time scales are $O(1) - O(10)$ s, whereas hypersonic simulation times are typically orders of magnitudes shorter, around $O(10^{-3})$ s. However, a computational approach has benefits over an experimental approach. It can de-couple physical mechanisms and may be able to give insights into mechanisms which are difficult to observe experimentally.

All algorithms shown in Section 3.1.1 remain largely the same, except two minor changes:

1. "Apply $bc \rightarrow \phi_{ib}$ " from Algorithm 7 now applies the ablation boundary conditions from Eq. (5.6) or Eq. (5.7). The boundary conditions need to be solved with an iterative procedure as the state variables are non-separable in the energy equation. For example, taking Eq. (5.7), assuming no heat transfer to the solid ($q_s = 0$) and including equation of state:

$$v_w = \omega(T_w, p_w)/\rho_s; \quad q_g(T_w) = \omega(T_w, p_w)h_{sg}; \quad \left. \frac{dp}{dn} \right|_w = 0; \quad \rho_w = p_w/RT_w \quad (5.8)$$

The boundary state variables are p_w, ρ_w, T_w, v_w . The energy equation is non-separable with respect to T_w , so it can be solved with the Newton iteration procedure. The solution values are clipped to maintain stability as the boundary conditions are very sensitive to the wall temperature.

Alternatively, the boundary conditions can be linearised, which adds numerical stability. Considering the boundary movement will be much slower than the computational time step, and the boundary is updated every time step, linearising the boundary conditions is unlikely to affect the accuracy of the simulation. Equation (5.3) can be linearised around the first interpolation point (T_{ip}, p_w) ,

$$\omega(T_w, p_w) \approx \omega(T_{ip}, p_w) + (T_w - T_{ip}) \left. \frac{d\omega}{dT} \right|_{T_{ip}, p_w}. \quad (5.9)$$

For binary species, the linearisation of the ablation function does not lead to a fully linear system, as transport properties (with mixing rules) are also non-linear and non-

separable functions for temperature. Only species mass and energy equations are coupled, and momentum (pressure) is decoupled from other state variables. So, the boundary conditions can be written as

$$\begin{pmatrix} f(Y_w, T_w) \\ g(Y_w, T_w) \end{pmatrix} = \begin{pmatrix} 0 \\ 0 \end{pmatrix}. \quad (5.10)$$

This can also be solved with Newton iteration procedure, taking IP point state as the initial guess.

2. "Move vertices" From Algorithm 10 moves the vertices based on recession velocity v_w in local normal direction.

5.3 Single species subliming sphere test

Extensive validations in Chapter 3 give confidence in the current numerical method's ability to predict surface properties accurately. And so, the validation focus here is on ablating moving boundary problems. A simple single-species subliming sphere is considered. No experiments involving single species ablation in high-speed flow exist in the literature. So, the focus here is comparing with analytical stagnation-point recession approximation and observing the effects of numerical speed-up on shape change.

Alternative validation method. For flows over axis-symmetric or two-dimensional blunt bodies, self-similar boundary layer equations can be solved to calculate shape change analytically. The biggest problem with this method is calculating the boundary layer edge state, even over simple shapes like a parabola or a hyperbola. However, the boundary layer edge state can be calculated, if the bow shock shape is known. The shock shape can be calculated for simple body shapes using [Van Dyke \(1958\)](#). Hence, this method of validation seems possible in theory; however, it is not attempted in the current work due to its complexity.

5.3.1 Numerical setup

The fluid is nitrogen gas with a fictional ablating solid phase of nitrogen. The non-dimensional numbers: the blowing factor (β), material density ($\hat{\rho}_s$), activation-like temperature (\hat{T}_a) and activation-like pressure (\hat{p}_a) link the flow parameters with the material parameters as follows:

$$\beta = \frac{AT_r}{\rho_r u_r}; \quad \hat{T}_a = \frac{T_a}{T_r}; \quad \hat{\rho}_s = \frac{\rho_s}{\rho_r}; \quad \hat{p}_a = \frac{p_a}{p_r}; \quad (5.11)$$

where the subscript r represents the reference state. The reference thermodynamic quantities are from stagnation state and reference velocity is the free stream velocity ($\rho_r = \rho_0; p_r = p_0; T_r = T_0; u_r = u_\infty$).

Camphor experiments of [Bianchi et al. \(2021\)](#) are used as a guide in the current setup to quantify the material properties of the fictional material. The non-dimensional variables used in the current work and from the Camphor experiments are listed in Table 5.2.

Table 5.2 Non-dimensional single species subliming sphere parameters.

	β	\hat{T}_a	\hat{p}_a	$\hat{\rho}_s$	Re_∞	M_∞
Bianchi et al. (2021)	840	13	4	74	10^5	6
Current work	840	10	40	10^{-5}	10^4	4

The Mach and Reynolds numbers are decreased to increase the mesh size required to resolve the flow and reduce the computational cost. The recession rate can be controlled by ρ_s , which is decreased by a factor of 10^{-7} here, to speed up ablation and allow a shorter simulation time. The dimensional parameters for the current case are:

$$A = 8.9 \times 10^4 \text{ kg s}^{-1} \text{ m}^2 \text{ K}^{1/2}; \quad T_a = 6300 \text{ K}; \quad p_a = 2 \times 10^7 \text{ Pa}; \quad \rho_s = 2.6 \times 10^{-5} \text{ kg m}^{-3}; \\ T_\infty = 150 \text{ K}; \quad u_\infty = 998 \text{ m s}^{-1}; \quad p_\infty = 4 \text{ Pa}.$$

The base mesh is 100×100 with up to 4 refinement levels, the domain size is $2 \times 2 \text{ m}$ and the sphere diameter is 1 m . The AMR parameters take their default values as in Section 2.2.3, except `cluster_min_eff` = 0.9. The gas viscosity is modelled by Sutherland's law, specific heat capacity is taken to be constant, and the thermal conductivity satisfies constant Prandtl number ($Pr = 0.7$). The Euler fluxes are calculated using CS4-JST with $C_2 = 1.0$ and $C_4 = 0.016$. The global time step is $5\mu\text{s}$ with CFL around 0.6. The flow timescale based on free-stream velocity and the sphere diameter is around 1 ms . Thus, 200 time steps are equivalent to one flow time. The refinement studies are limited to 2000 steps and 10 flow times. The wake is not fully relaxed, but this does not affect the surface properties significantly. Condensation is prevented during initialisation by enforcing $|\omega| > 0$.

5.3.2 Stationary wall ablation

Effect of the mesh size. A mesh refinement study is conducted with an ablating but stationary wall, for a given body element size. The sphere is constructed with 50K elements, arbitrarily chosen such that the average element size is $\sim 23 \text{ mm}$ ⁶ is visually small compared to the radius. The mesh with 3 levels of refinement is shown in Fig. 5.4. A single level of refinement is added to the shock layer in the stagnation region. Additional levels of refinement are added near the walls in the stagnation region of the sphere. Table 5.3 shows convergence of total ablation rate and stagnation-point ablation rate with increasing mesh resolution.

Table 5.3 Single species subliming sphere mesh refinement results.

Refinement levels	1	2	3	4
Number of points ($\times 10^6$)	3.4	6.0	12.9	39
Computational cost per flow time (CPU hours)	6	12	56	380
Total Ablation rate ($\times 10^{-3} \text{ kg s}^{-1}$)	2.15	3.52	4.93	4.94
Stagnation-point ablation rate ($\times 10^{-3} \text{ kg s}^{-1} \text{ m}^{-2}$)	0.084	0.137	0.192	0.196

⁶Assuming an equilateral triangle, its area is $A = l^2/2$, where l is the element width.

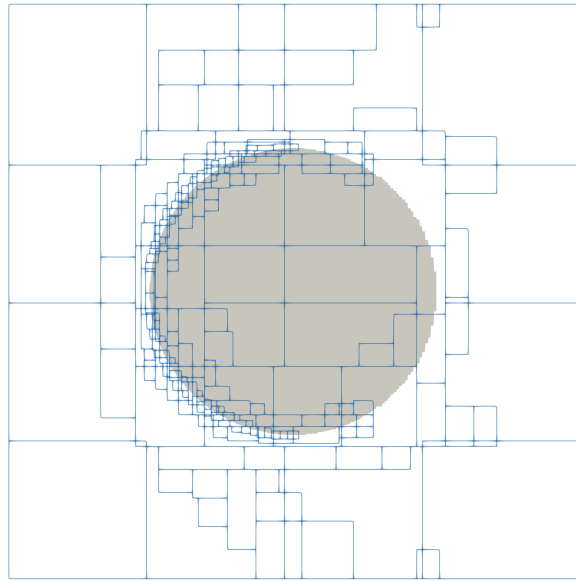
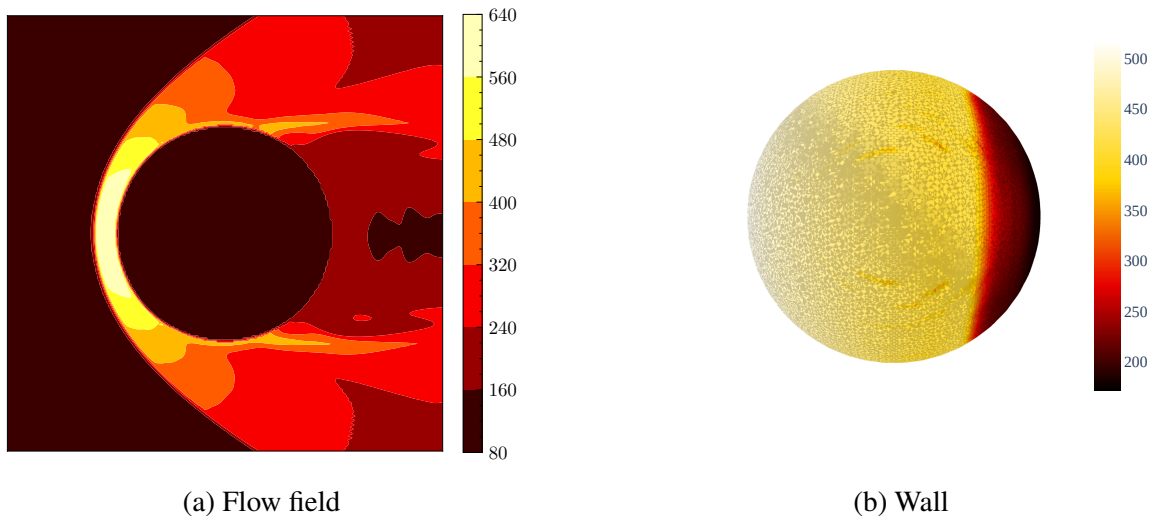


Fig. 5.4 Slice of AMR patches around sphere with 3 refinement levels.



(a) Flow field

(b) Wall

Fig. 5.5 Single species subliming sphere temperature (K) plots.

Analytically, as a first approximation, the stagnation-point ablation rate is simply,

$$q_0 \approx h_{sg} \omega; \quad (5.12)$$

where q_0 is the stagnation-point heat transfer calculated using semi-empirical correlations from Eq. (4.3). The analytical approximate stagnation-point wall temperature and ablation

rate are, 492 K and $0.25 \times 10^{-3} \text{kg s}^{-1} \text{m}^{-2}$ respectively. The stagnation-point wall temperature from simulations is 513 K, irrespective of the mesh resolution, around a 4% larger compared to the analytical approximation. The free-stream stagnation-point temperature is 630 K, so the ablation cooling is evident. The ablation mass flux from simulations is around 60% larger than the analytical approximation. This large error is because of the exponential relationship between the wall temperature and ablation flux, the sensitivity of the ablation flux to the wall temperature can be reduced by increasing β and reducing T_a/T_w .

Effect of body element size. Wall normal gradients in a boundary layer are much larger than wall tangential gradients. Hence, for a simple shape like a smooth sphere, the body element size required is expected to be much larger than the local (wall-normal) mesh size. The number of elements can be very large in three dimensions and can significantly increase the computational cost of moving body algorithms. So it is beneficial to avoid an excessive number of body elements. Table 5.4 shows the effect of body element size on the total ablation rate. And it suggests, that increasing the body element size reduces the total ablation rate, and in the current case, 12.5×10^3 elements give the total ablation rate to 2% accuracy. Moreover, a $\sim 3 \times$ increase in element size only results in $\sim 20\%$ inaccuracy.

Table 5.4 Single species subliming sphere body refinement.

Element size/Radius	65/1000	46/1000	32/1000	23/1000
Elements $\times 10^3$	6	12.5	25	50
Total Ablation rate ($\times 10^{-3} \text{kg s}^{-1}$)	5.63	4.93	4.83	4.82

5.3.3 Moving wall ablation

Effect of ablation speed-up factor on shape change. Ablating wall movement timescales are orders of magnitude smaller than flow timescales. From a computational perspective, hypersonic ablation is prohibitively slow. A wall Damköhler number (Da_w) can be controlled to balance computational cost and accuracy:

$$Da_w = \frac{\tau_f}{\tau_w} = \frac{u_2}{v_w} = \frac{\rho_s u_2}{\omega_0}; \quad \frac{u_2}{u_1} = \frac{M_\infty^2(\gamma - 1) + 2}{M_\infty^2(\gamma + 1)} \quad (5.13)$$

Da_w is defined as the ratio of the post-shock velocity to stagnation-point wall recession velocity. In the current study, $Da_w = [5, 20, 40]$ are selected. These correlate to $\rho_s = [411, 1644, 3288] \times 10^{-6} \text{kg/m}^3$.

Figure 5.6 shows the sphere shape varying with wall timescale (τ_w), where a blunted-sphere shape forms over time. This is expected as the heat transfer increases towards the stagnation region, which ablates faster around the stagnation region than around the sides. Moreover, the surface remains smooth generally, as expected with laminar flow. However, a sharp corner forms around $\tau_w = 4$ and leads to a locally unstable computation. The instability is due to the triangulated mesh tangling. This could be avoided by geometry fairing procedures during runtime. However, their implementation is not trivial.

It is not clear whether the formation of the corner is physical or arises only due to inaccurate physical modelling. As discussed in Section 5.2.3, the limitations of the current physical model are: first, is that the boundary conditions are one-dimensional; and second, the solid phase heat transfer is neglected. In the author's opinion, it is unlikely that the lack of solid phase heat conduction gives rise to the formation of the corner. However, modelling solid phase heat transfer accurately is likely to smooth the corner. This smoothing is also likely to reduce mesh tangling. However, further investigation is required on this issue.

Another important observation is that the shape change depends on Da_w , until a critical value. After this value, the shape change is independent of Da_w . Meaning, that ablation can be artificially sped-up if Da_w is more than the critical value.

Figure 5.7 shows the shape change comparison with ablation due shear stress (Mac Huang et al., 2015), hydrodynamic erosion on clay bodies. The results suggest that the sphere-cone shape, often found in meteors, may not be formed by sublimation alone. The sphere-cone shape is likely to occur by material melting and the melt layer eroding by shear stresses.

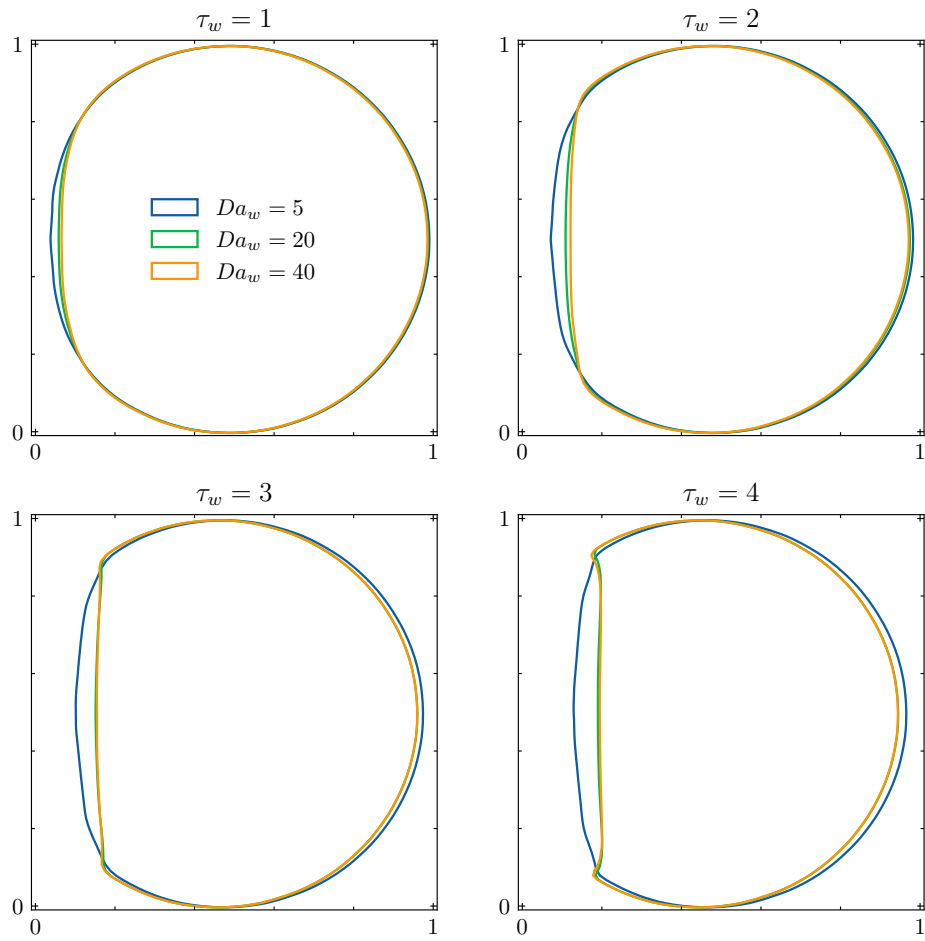


Fig. 5.6 Subliming sphere shape change with material time (τ_w).

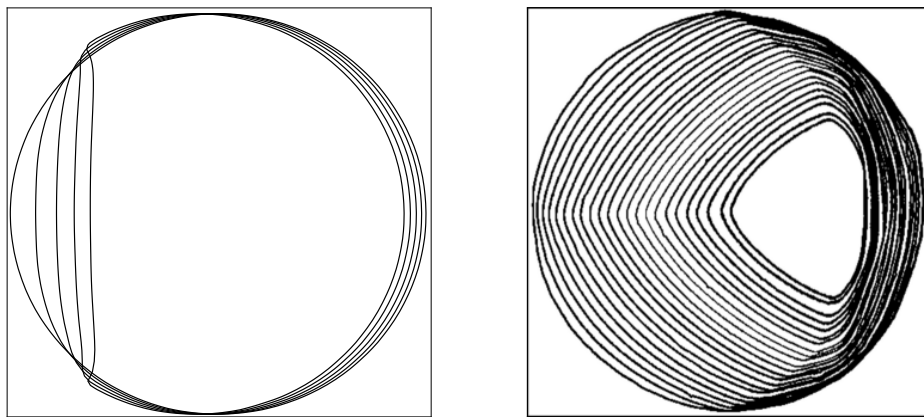


Fig. 5.7 Comparison of shape changes with different ablation modes. Left: Sublimation only (Current work). Right: Shear only (Ristroph et al., 2012).

5.4 Search for ablation patterns

Underlying mechanisms behind cross-hatching patterns are unclear in literature, as briefly discussed in Section 5.1.1. Hypothesised mechanisms can be classified into two categories (Swigart, 1974). First, *visco-elastic solid/liquid layer* mechanisms assume the dominant amplifying effect of surface perturbations is from the shear stress-driven surface perturbations of visco-elastic solid or the thin liquid layer. Second, *differential ablation* mechanisms assume the dominant amplifying effect to be from heat-transfer or pressure perturbations, which affect the local ablation rate. An overwhelming majority of the studies (Swigart, 1974) in the literature suggest streamwise vortices are necessary for developing cross-hatching patterns. In contrast, some studies (Stock and Ginoux, 1973) suggest that streamwise vortices are not necessary for cross-hatching to occur.

This section aims to re-produce the hypersonic ablation patterns numerically. Previously, Trevino (2021) numerically studied cross-hatching patterns. They explored flows over cones and flat plates with roughness with the aim of better understanding cross-hatching patterns. However, they were not able to re-produce cross-hatching patterns.

5.4.1 Backward facing step numerical setup

A backward facing step (BFS) with ablating walls is devised as it can generate multiple streamwise vortices (also referred to as Gortler-like vortices) and trigger a quick transition to turbulence, without any external forcing (Hu et al., 2019). Furthermore, lab experiments often lead to a BFS formation at the interface of the non-ablating and ablative material (Stock and Ginoux, 1973) and the step could be linked to the development of cross-hatching patterns in experimental setups. A channel BFS (internal flow) configuration is more widely studied (Barkley et al., 2002; Rani et al., 2007) than an open BFS (external flow) configuration (Hu et al., 2019, 2020). The two configurations are similar, but no direct comparison studies exist. However, in both cases, post-step boundary layer re-attachment and concave streamlines induce streamwise Gortler-like vortices.

Numerical Setup. Figure 5.8 shows the BFS geometry in terms of the inflow velocity boundary layer thickness (δ_0), the setup is loosely based on Barkley et al. (2002); Hu et al. (2020). The solid is bigger than the computational domain by $\delta_0/2$ in all directions, this is to avoid the solid boundary crossing the domain boundary during run time with moving boundaries. The inflow boundary layer is a polynomial fit of the exact solution of compressible boundary layer equations. The computational domain boundary conditions are periodic in y , zero-gradient in x and z .

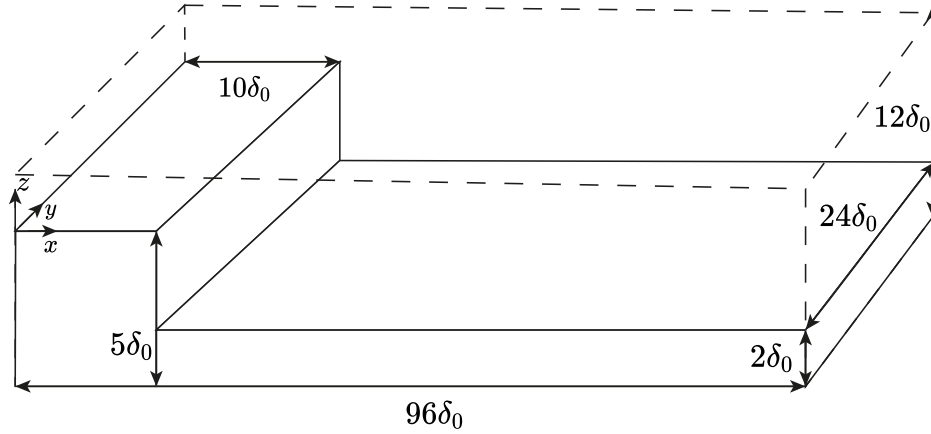


Fig. 5.8 Backward facing step geometry and computational domain.

Table 5.5 summarises the flow conditions.

Table 5.5 Backward facing step flow conditions.

M_∞	T_∞ (K)	P_∞ (Pa)	δ_1 (mm)	δ_0 (mm)	$Re_{\delta_0}/10^3$	δ_v (μm)	x_0 (m)	τ_f (μs)
4	300	3000	0.82	1.56	4.02	17.3	0.15	106

δ_1 is the displacement thickness of the inflow boundary layer, δ_0 is the thickness⁷ of the inflow boundary layer, $Re_{\delta_0} = \rho_\infty u_\infty \delta_0 / \mu_\infty$ and represents the Reynolds number based on displacement thickness, δ_v is the viscous length scale of the inflow boundary layer, x_0 is the inflow boundary layer distance from the start of a flat plate leading edge, and a flow time is defined as $\tau_f = 96\delta_0 / u_\infty$.

The specific heat capacity at constant pressure (C_p) is taken as constant at 400K for camphor at 1040 kJ/kg and air as 1050 kJ/kg. The C_p for camphor varies by a factor of two within the 300-1000K range, much more than air. However, a constant C_p assumption is justified for the current study as fluid temperatures remain below 600K at all times and the variation in C_p will not affect the qualitative behaviour. Polynomial fits as functions of temperature for camphor transport properties (Yaws, 2014), viscosity, thermal conductivity and binary diffusion coefficient are used —whereas Sutherland’s law is utilised for air viscosity and thermal conductivity. Mixture properties are calculated using Wilke’s mixing rule (Wilke, 1950).

⁷Defined using velocity $< 0.99u_\infty$.

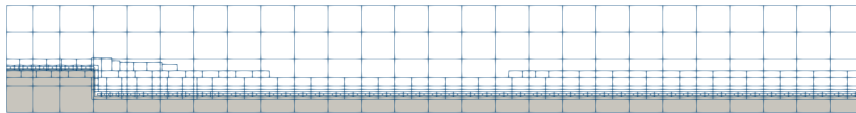
Mesh refinement

A mesh refinement study is conducted with a base mesh of $[512 \times 128 \times 64]$. Resolution is added near walls and in the boundary layer. There are three cases, with an additional refinement level to the previous case. For all cases, the base mesh time-step (Δt) and steps per flow-time (N_τ) are $0.15\mu s$ and 1000 respectively. The maximum CFL is around 0.7.

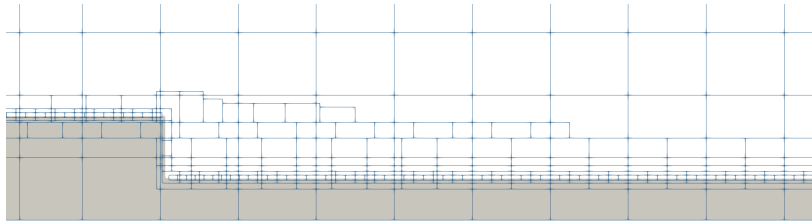
The results are summarised in Table 5.6 and suggest that the integrated heat load is converging, and the high resolution mesh heat load reduces by around 20% compared to the medium resolution mesh. Increasing the mesh resolution decreases the local heat transfer and the total heat load, this can be observed visually as well in Fig. 5.10. Moreover, in all cases, the streamwise vortices generate spanwise variations in heat transfer, as expected. Based on the heat load convergence, as shown in Fig. 5.9, the high-resolution mesh is not well converged by is deemed sufficient to observe qualitative behaviour.

Table 5.6 Backward facing step mesh refinement results.

Resolution	Refinement levels	Points ($\times 10^6$)	$(\Delta y^+)_w$	Heat load (W)
Low	1	13	8	103
Medium	2	35	4	58
High	3	67	2	48

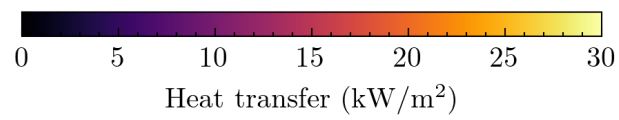
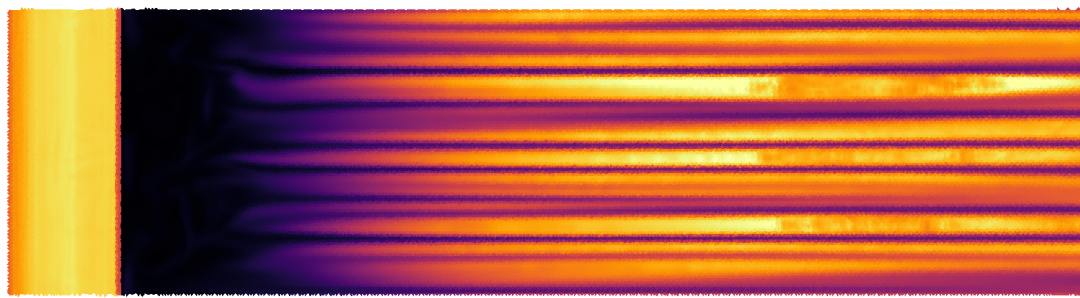


(a) Full mesh.

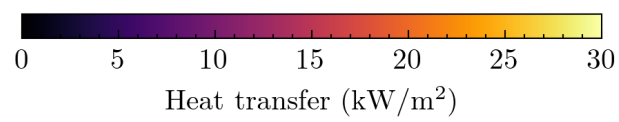
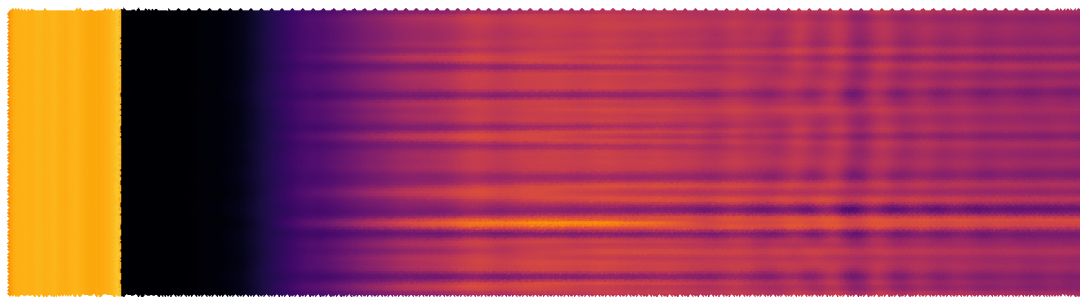


(b) Zoomed near wall mesh.

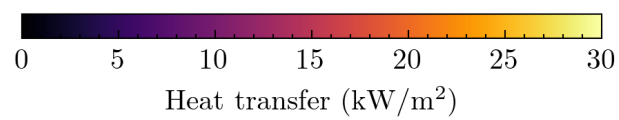
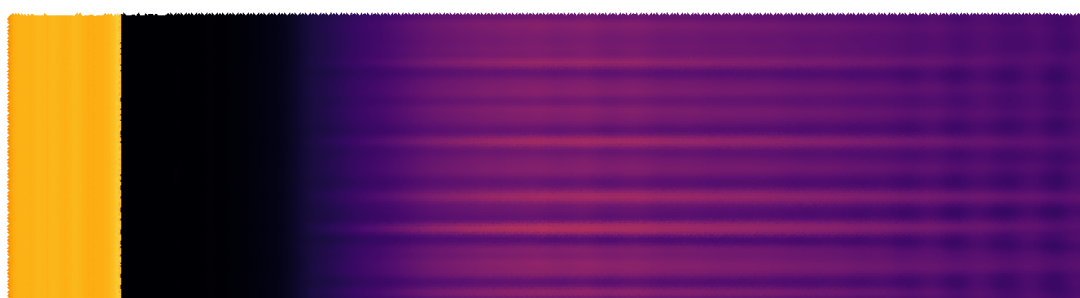
Fig. 5.9 Backward facing step high resolution 3 level mesh patches.



(a) Low



(b) Medium



(c) High

Fig. 5.10 Backward facing step wall steady-state heat transfer with varying mesh resolution.

5.4.2 Results

Three cases are considered, no ablation (A), stationary ablating wall (B) and moving ablating wall (C).

A. No ablation

Figure 5.10 shows transient weak streamwise perturbations, which are amplified naturally and become stronger in the downstream direction. The streamwise perturbation's wavelength is $\sim 4\delta_0$ and is likely to be a Mack mode instability (Mack, 1984). The Gortler-like vortices create spanwise perturbations which also have a similar length scale of $\sim 3\delta_0$. An important observation is that the interaction of streamwise perturbations and Gortler-like instability generates interference heating patterns, which can generate differential ablation patterns and may lead to cross-hatching ablation patterns. However, in the current simulations, the interference pattern does not persist.

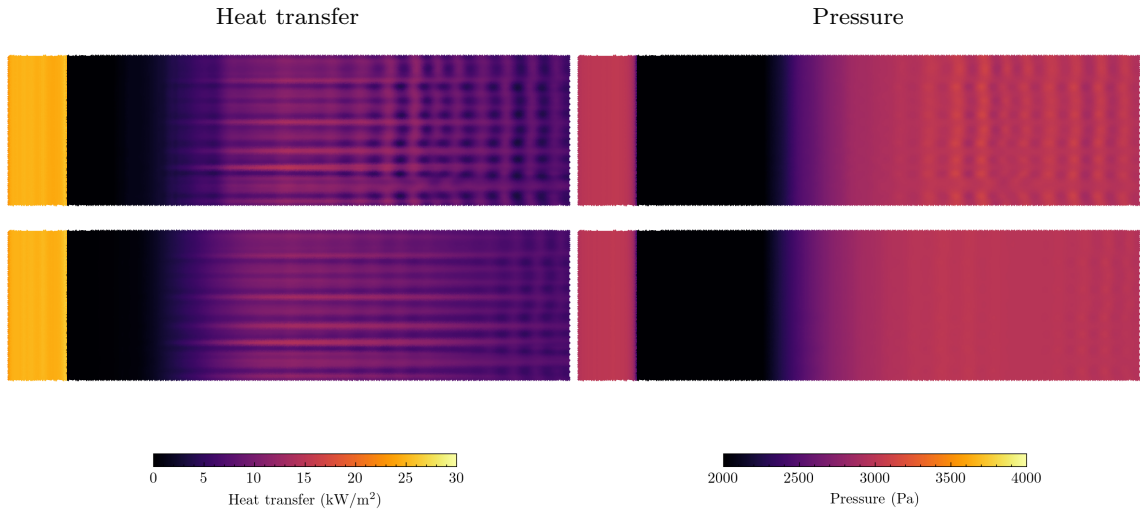


Fig. 5.11 Transient (top row) and steady state (bottom row) surface heat transfer and pressure.

B. Stationary wall ablation

This case aims to observe the boundary layer development with ablating walls without wall recession. The upper step surface is kept at a constant temperature ($T_w = 300\text{K}$), whereas the ablation boundary condition is imposed on the bottom step surface. The steady-state solution from case A initialises the simulation and is computed for around 14 flow times. Figure 5.12 shows that the mass loss rate does not change significantly after 4 flow times. The computation takes 10 hours per flow time with 500 processors.

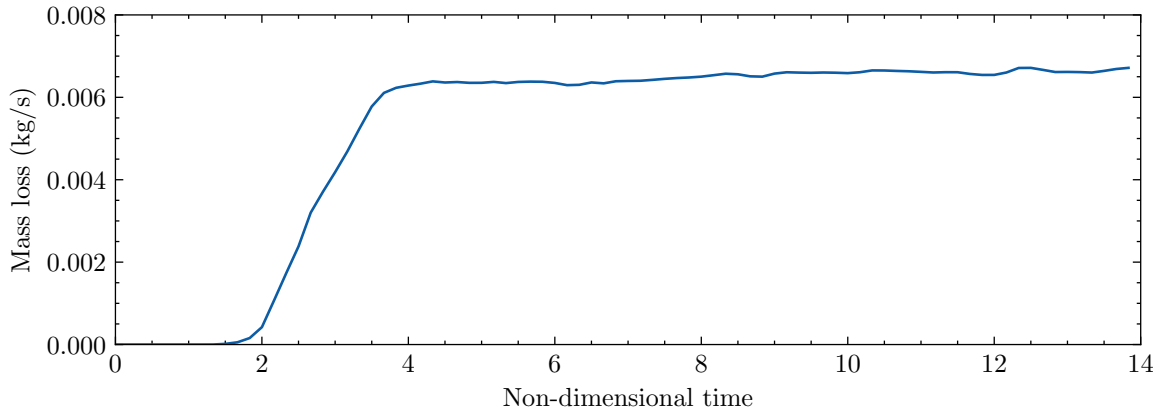


Fig. 5.12 Variation of mass loss with non-dimensional flow time.

Figures 5.13 and 5.14 show the surface properties' variation over time:

- The surface temperature initially follows the spanwise varying heat transfer pattern from Fig. 5.12. However, over time the surface temperature increases and becomes essentially uniform with hotspots sized up to $\sim \delta_0$.
- The surface pressure plots show the streamwise perturbations and the interim interference pattern from Gortler-like vortices and streamwise vortices. Over long times the surface pressure is uniform with small-scale perturbations with length-scale $\ll \delta_0$.
- Surface mass fraction increases initially; as it approaches 1, the boundary layer becomes unstable, and mixing occurs. This can be observed clearly in Fig. 5.15. Moreover, it also shows the interference of streamwise vortices and perturbations result in islands of high and low mass fractions.
- Ablation mass flux is small initially. Once the boundary layer becomes unstable, mixing occurs, and wall temperature increases, the ablation mass flux also increases. The interference of streamwise vorticity and perturbations create islands of low ablation rates. This interference pattern is interim. However, if it were to persist, this could give rise to arrays of raised islands, leading to surface topologies similar to cross-hatching patterns. Over a long time, patches with a high ablation rate form, corresponding to locally increased temperature due to mixing.

Overall, the flow is laminar at the start but seems to become unstable and transition with ablation boundary conditions. The transition is clearer with Q-criterion iso-surface plots in Fig. 5.15. The flow is initially laminar with streamwise perturbations. Then the far downstream flow becomes unstable and transitions, only around half of the bottom step

surface is laminar. Then de-stabilised region grows towards the reattachment point and the boundary layer over the whole bottom step becomes transitional and highly vortical.

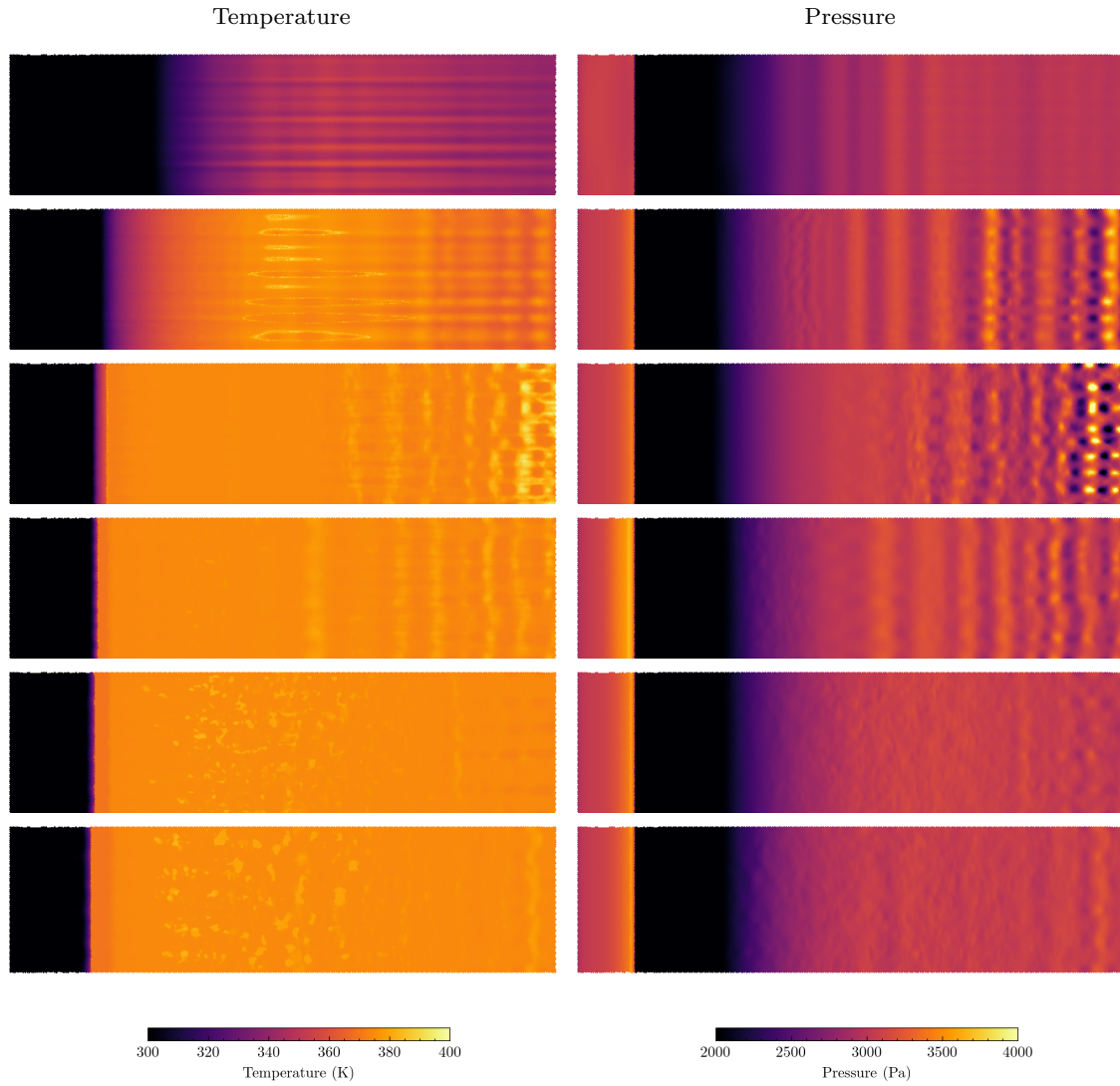


Fig. 5.13 Surface temperature and pressure varying with time. Beginning with $\tau_f = 2$ (top row) and increasing by two flow times for every row below.

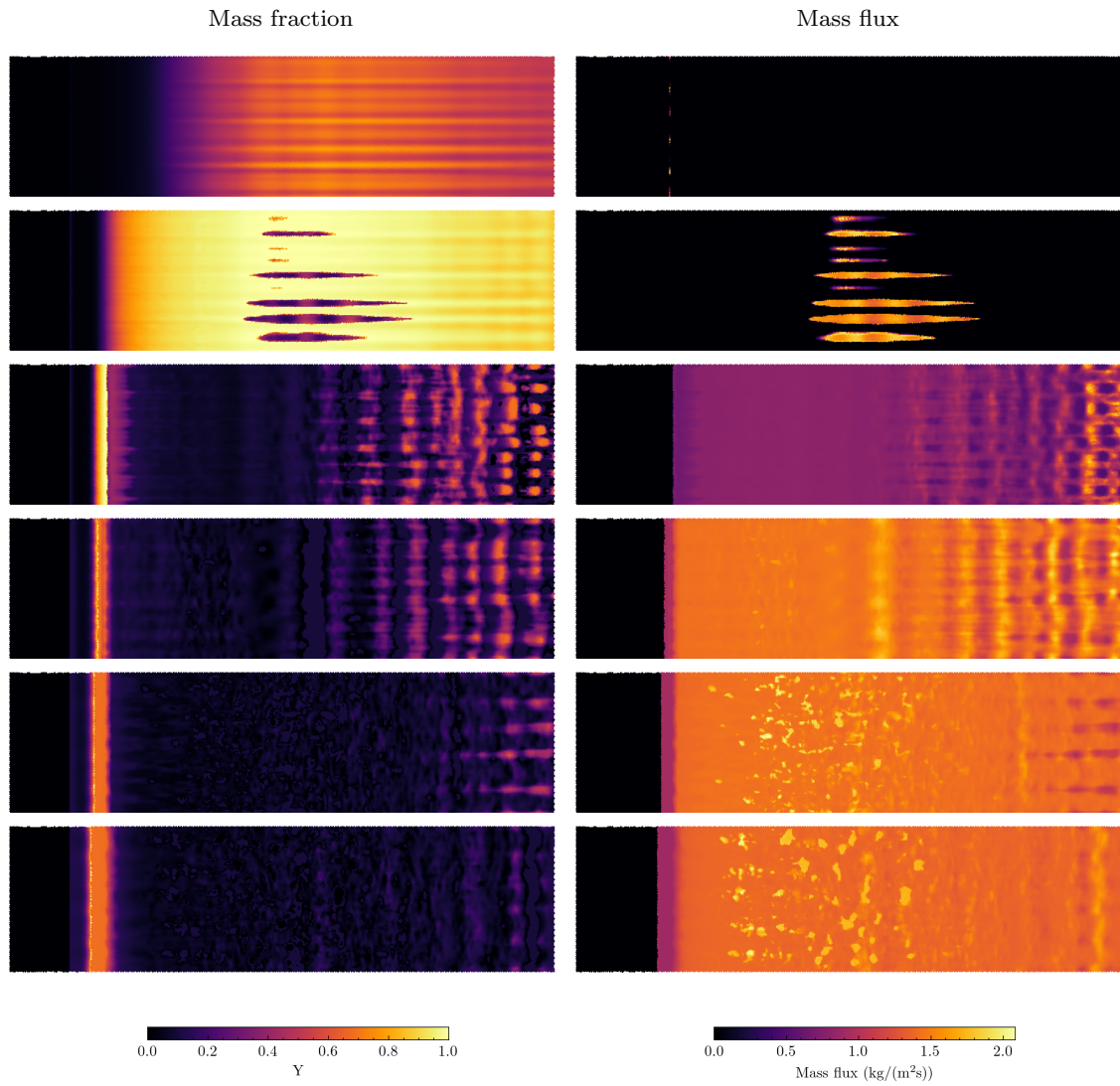
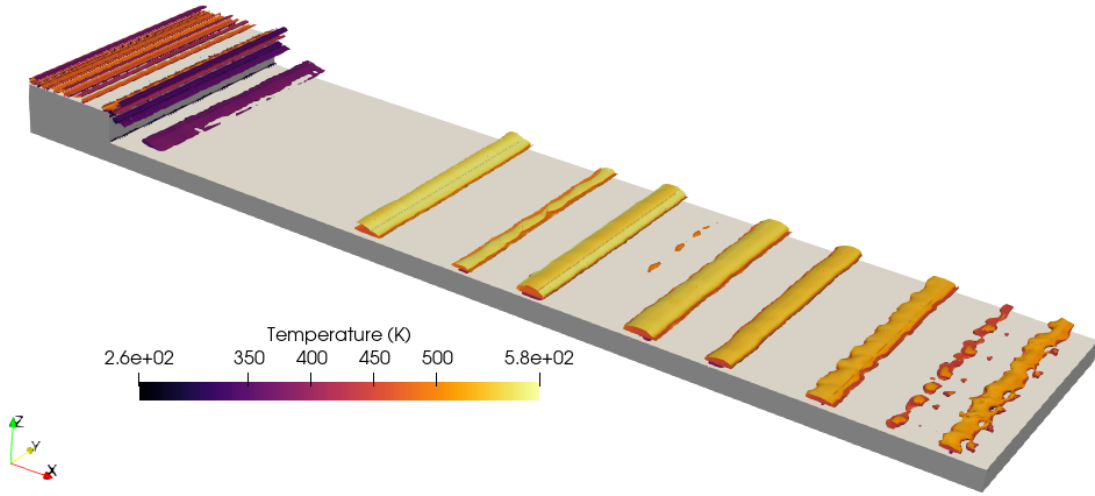
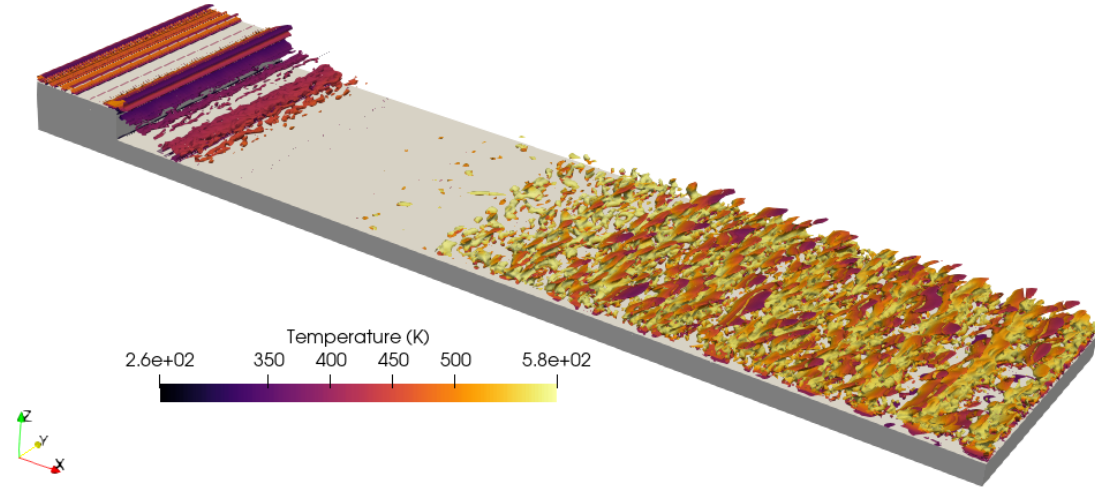


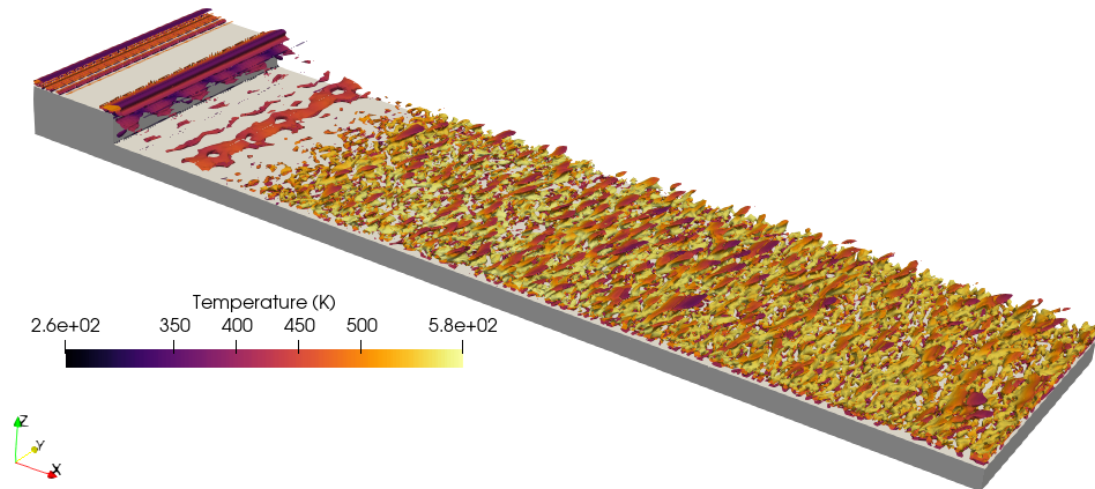
Fig. 5.14 Surface mass fraction and flux varying with time. Beginning with $\tau_f = 2$ (top row) and increasing by two flow times for every row below.



(a) $\tau_f = 0$.



(b) $\tau_f = 4$.



(c) $\tau_f = 10$.

Fig. 5.15 Q-criterion plots at different times with temperature based colour scale.

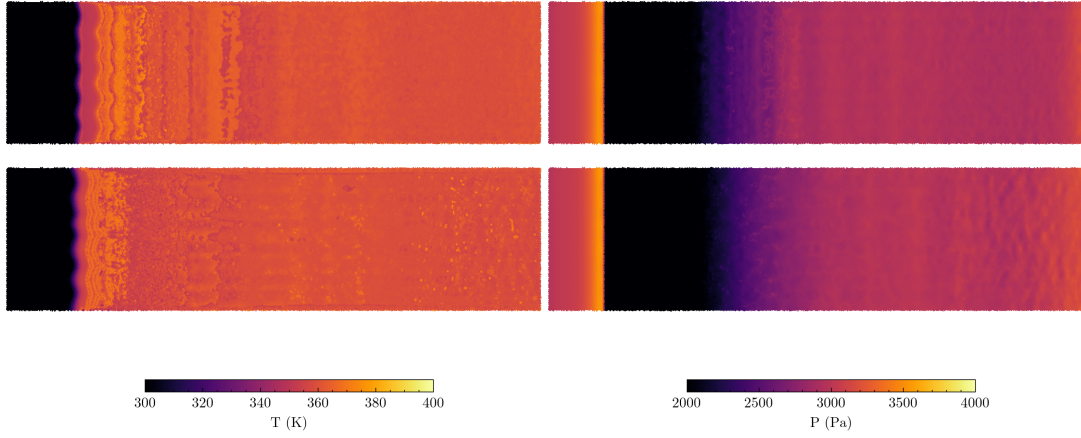
C. Moving wall ablation

This case investigates the BFS with ablating and receding wall, where the local ablation rate controls the wall recession rate. The wall recession is performed by the numerical method described in Section 5.2.3. The simulation is initialised from the transitioned boundary layer flow-field in case B. The ablation boundary condition is only applied on the lower step surface and the upper plate remains at 300K. Re-gridding occurs every 100 steps. The solid is moved every 10 steps and the maximum movement is limited to $\Delta x/2$, for numerical stability. Periodic boundary condition in y for the solid movement is not imposed, as this is not trivial in the current implementation and is considered unimportant for a first study.

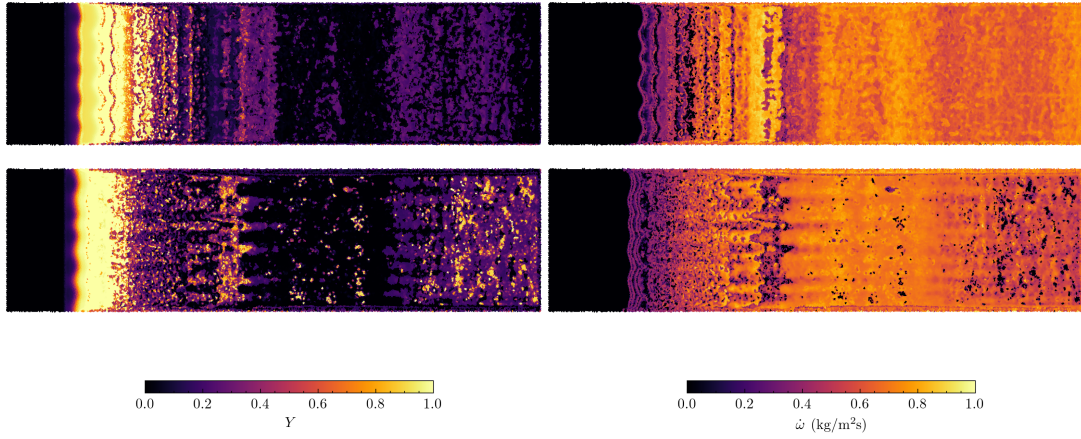
The equilibrium ablation wall temperature is approximately 361K, calculated by assuming the inflow boundary layer heat transfer rate, free-stream pressure and assumed mass fraction of 0.5. This temperature is then used to calculate a reference ablation rate and set solid density, $\rho_s = 0.117 \text{ kg/m}^3$ with $Da_w = 50$. Figure 5.16 shows the instantaneous surface properties at $\tau_f = 1$ and $\tau_f = 2$. The following observations are made:

- Figure 5.16a suggests that the surface temperature is the lowest in the re-circulation region, and increases after the re-attachment line. Surface temperature fluctuations result in uneven surface recession, when compared to Fig. 5.13. The surface pressure fluctuations are stronger in $\tau_f = 2$ than $\tau_f = 1$. These fluctuations affect mass fraction, as seen in Fig. 5.16b
- Figure 5.16b suggests that the mass fraction in the re-circulation region is not zero because of the trapped ablated species within the region. The streamwise vortices induce a spanwise variation in the surface mass fraction, as observed at $\tau_f = 2$. This variation in mass fraction also contributes to the spanwise variation in ablation rate. An arrowhead pattern in ablation mass flux rate due to the streamwise vortices forms.
- Figure 5.16c suggests that the transitional flow over the backward facing step creates uneven surface ablation, and surface roughness develops. The surface ablates to a maximum depth of around $0.8\delta_0$, and the maximum surface height fluctuation is around $\pm 0.2\delta_0$. The surface recession increases with increasing distance downstream of the re-attachment line, and streamwise grooves seem to develop over time. Overall, differential ablation generates surface roughness, but more complex patterns like cross-hatching patterns are not observed in the current simulation.

Also, the simulation becomes unstable after $\tau_f = 2$, due to localised large discrete curvatures. This behaviour is also observed in Section 5.3 and could be avoided by managing the discrete curvature.



(a) Temperature (left) and Pressure (right).



(b) Ablating species mass fraction (left) and mass flux (right).

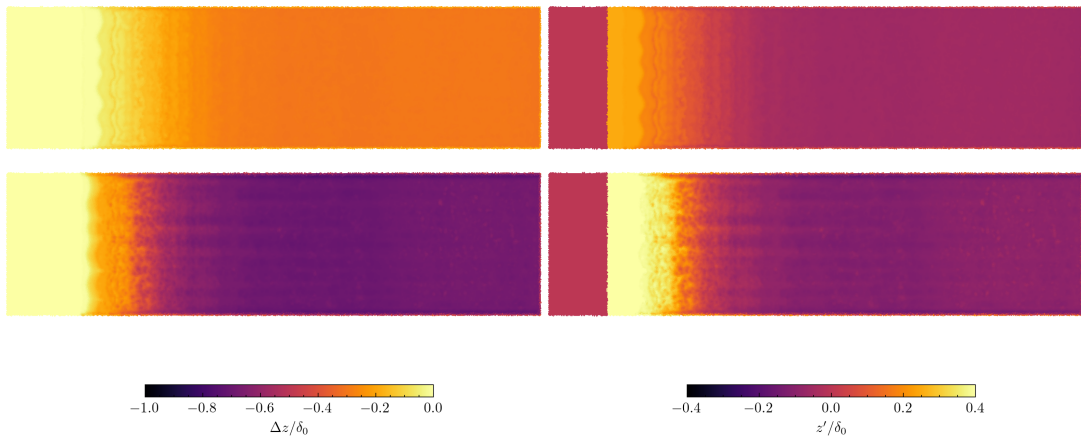

 (c) Surface displacement (left) and surface height fluctuations (right) normalised by inflow boundary layer thickness (δ_0).

 Fig. 5.16 Surface properties with abating and moving wall boundary condition at $\tau_f = 1$ (top) and $\tau_f = 2$ (bottom).

Figure 5.17 shows increased vorticity immediately after re-attachment point when compared to Fig. 5.15 in case B. This suggests that ablation-induced roughness may be important for boundary layer stability and transition. The effect of distributed roughness on boundary layers remains an open problem, especially with roughness generated by ablation (Schneider, 2008).

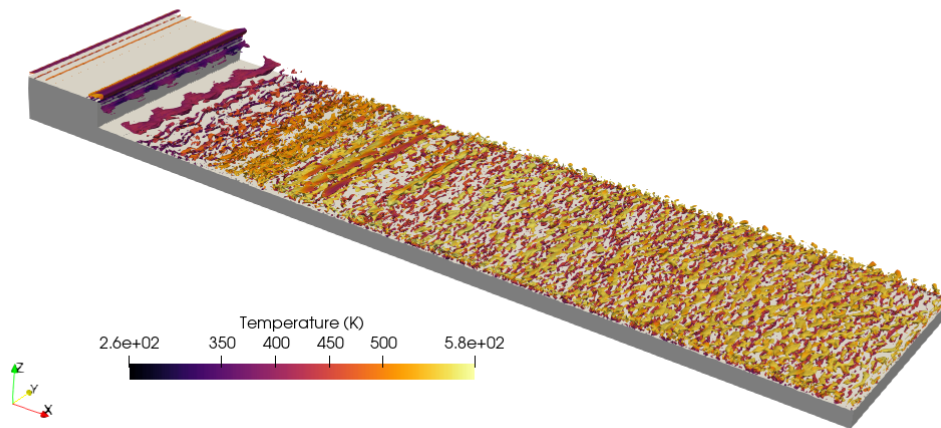
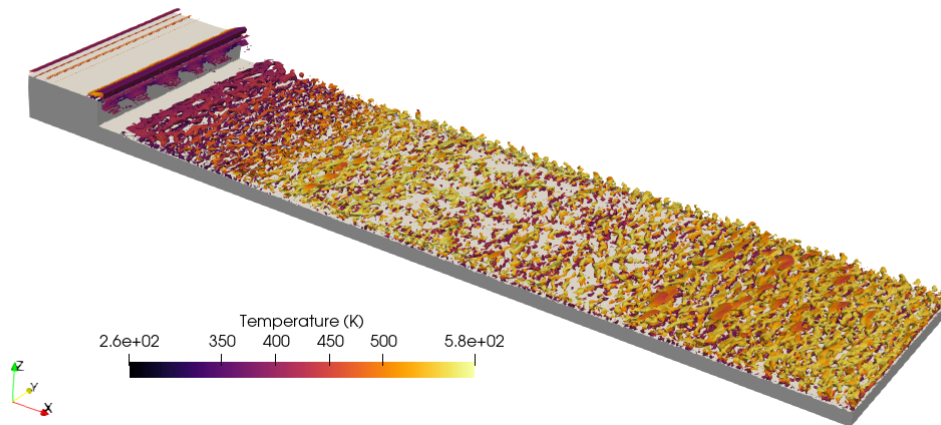
(a) $\tau_f = 1$ (b) $\tau_f = 2$

Fig. 5.17 Q-criterion with temperature field colouring of iso-surfaces.

5.5 Summary

This chapter completed a novel study on hypersonic ablation patterns. Hypersonic ablation was identified as a part of a larger set of slow-moving boundary, fluid-structure interaction problems, which are ubiquitous in nature. The literature was found to lack understanding of the mechanisms behind ablation patterns and the patterns remain largely uncharacterised. Moreover, the pattern's effect on the boundary layer is poorly understood.

First, a simple validation test case is devised. It involves a laminar hypersonic flow ($M = 4$) over a subliming sphere, where the sphere is a fictional solid state of nitrogen allowing a single species simulation. The aim was to minimise modelling complexity whilst preserving qualitative physical behaviours to test the numerical method. Stationary and moving wall ablation boundary conditions were investigated separately:

- A mesh refinement study with the stationary and ablating wall was conducted. The simulation's stagnation-point temperature and ablation rate were compared with an approximation based on semi-empirical heat transfer correlations. Compared with this approximation, the equilibrium surface temperature was around 4% larger, and the ablation mass flux was around 60% larger. The large discrepancy in the ablation mass flux is due to the exponential dependency of the sublimation flux on the wall temperature. Moreover, a body refinement study for a fixed mesh revealed that the body element size can be much smaller than the wall mesh size as the wall tangent gradients are smaller than the wall-normal gradients. In the current case, a $\sim 3\times$ increase in the body element size resulted in surface integrated mass loss rate difference of $\sim 20\%$.
- With the moving wall ablation case, managing a large range of timescales in a fluid-structure interaction ablation problem is a key computational challenge. The ablation timescales are orders of magnitudes larger than flow timescales. To overcome this challenge, an artificial ablation speed-up factor, in the form of a wall Damköhler number is introduced in the ablation boundary conditions. Investigating the effect of wall Damköhler number on shape change revealed, that as the wall Damköhler increases, the error in shape change becomes independent of the Damköhler. In other words, the surface movement due to ablation can be sped-up without affecting the shape change accuracy.
- The subliming sphere's shape is compared with shear ablation experiments. The two ablation modes result in different shapes, sublimation leads to a blunted body; whereas, shear ablation has been shown to result in a sphere-cone body in the literature. The

sphere-cone shape is characteristic of an oriented meteor, and current simulations suggest that ablation by sublimation alone may not be able to reproduce this.

In addition to the outcomes, this work had some limitations. In particular, relating to the current physical model: first, is that the boundary conditions are one-dimensional; and second, the solid phase heat transfer is neglected. Particularly, ablation with solid phase heat transfer modelling should be investigated in future studies. Moreover, comparison of the numerical method with binary species experiments from literature could be performed.

Secondly, to investigate hypersonic ablation patterns, a novel configuration with a transitional flow over a backward facing step (BFS) with binary species ablating boundary is devised. A BFS is selected as it naturally generates streamwise vortices, which can cause localised heating and result in differential ablation, necessary for the development of ablation patterns. Three cases are investigated, no ablation (A), ablation with a stationary wall (B) and ablation with a moving wall (C):

- An interference pattern is generated by the interaction of streamwise perturbations and streamwise vorticity. Although the pattern does not persist with the current flow conditions, the resulting ablation flux from such a pattern could lead to cross-hatching patterns.
- Case B suggests that ablation destabilises the boundary layer forces transitional flow. Initialising case C with the transitioned flow generates surface roughness driven by the unsteady flow. Cross-hatching patterns are not observed in the current simulations, however, differential ablation results in large surface recession of $\sim 0.8\delta_0$ and fluctuations in surface height of $\sim 0.2\delta_0$. This roughness generates vorticity in the boundary layer.

Both tests, subliming sphere and BFS resulted in unstable simulations over a long time with moving wall ablation. The instability is likely due to large discrete curvatures forming in the geometry, also commonly known as mesh tangling, and could be avoided with runtime management of the geometry's discrete curvature. However, implementing such an algorithm is not trivial and is deemed outside the scope of the current work. Nevertheless, current work demonstrates a novel application of SAMR-GPIBM for fluid-structure interaction hypersonic ablation modelling in transitional flows, with potential for future investigations.

6. Conclusions

This thesis aimed to: first, develop a computational fluid dynamics method for modelling hypersonic flows; and second, apply the method to study novel hypersonic flow problems. After developing, validating and testing the numerical method, two independent knowledge gaps in the literature were identified, then particular research questions formed, research planned and conducted. This chapter summarises the thesis and discusses future works.

6.1 Main contributions

Numerical method development

Literature review in Chapter 1 suggested that numerical methods for modelling hypersonic flows are seldom high order of accuracy, low numerical dissipation—especially around complex geometries—and include high-temperature physics.

In Chapter 2, a finite-difference low dissipation computational fluid dynamics solver for hypersonic flows with adaptive mesh refinement was developed. A numerical approach with high-temperature thermochemistry; and low dissipation shock stable methods from weighted essentially non-oscillatory and artificial dissipation families was implemented and tested. Most importantly, CS-JST from the artificial dissipation family was found to be attractive from a cost-to-accuracy perspective when compared to WENO methods.

The developed structured adaptive mesh refinement solver was coupled with the ghost-point forcing immersed boundary method (SAMR-GPIBM), to allow modelling with complex geometries, and tested over a variety of test cases in Chapter 3. The SAMR-GPIBM solver with CS-JST is novel, as WENO methods with IBM in literature are common. The current approach is stable even with high Mach number transients, computationally $\sim 3\times$ less expensive than WENO methods and accurate enough for laminar and turbulent engineering calculations. Moreover, in the author's view, SAMR-GPIBM could be competitive with body-fitted meshes for hypersonic flow modelling, especially with local time stepping strategy and refinement on the local y_w^+ . However, direct comparisons are necessary for quantified cost differences.

Heat transfer to proximal circular cylinders in hypersonic flow

A novel study on the heat transfer to proximal cylinders in hypersonic flow was conducted in Chapter 4. Motivated by the atmospheric entries of meteors, satellites or spacecraft components, which are destructive and involve fragmentation of bodies. This leads to many bodies in proximity to one another. Previous studies on this problem have only focused on aerodynamic forces and heat transfer has not been investigated, despite its importance for demise during atmospheric entry.

First, heat transfer to binary proximal bodies was investigated. The secondary body's position was systematically varied in the near wake (defined as a body being less than five diameters from the other). Flows with Mach numbers 2, 4 and 8 are investigated. It was found, that the heat load and peak heat transfer can be augmented for either or both proximal bodies by +20% to −90% of an isolated body. Minimum heat load (maximum thermal shielding) occurs when the secondary body is in the viscous wake of the primary body. In other words, when the second body is tailgating the primary body. In contrast, maximum heat load occurs when the secondary body approaches the primary body's bow shock and stagnation region. Generally, reduced heat load is due to the reduction of heat transfer on the front half of the cylinder ($-\pi/2 < \theta < \pi/2$); whereas, the increase in heat load is due to the increase to heat transfer on the top ($-\pi/2 < \theta < 0$) or bottom ($0 < \theta < \pi/2$) half of the cylinder due the presence of the other body.

Secondly, the heat transfer to multiple proximal bodies was investigated. Eight clusters with randomly spaced cylinders were generated. The average heat load (per body) in a cluster was found to be between +20% to −60% of an isolated body. The average heat load showed a negative correlation with the ratio of: standard deviation of body coordinates in parallel direction to the free-stream, to standard deviation of body coordinates in perpendicular direction to the free-stream. In other words, clusters thin in the direction perpendicular to the free-stream velocity and long in the direction parallel to the free-stream have low average heat load (thermally shielded). Whereas thick and short clusters, in directions perpendicular and parallel to the free-stream velocity, feel an increased heat load. Moreover, the heat load standard deviation in a cluster is also negatively correlated with the body position's standard deviation in the free-stream perpendicular direction. This means that heated clusters have a smaller variation of heat load amongst its bodies than cooled clusters.

Hypersonic ablation patterns

A novel study on hypersonic ablation patterns was conducted in Chapter 5. This problem was identified as part of a larger set of slow-moving boundary fluid-structure interaction problems. The literature review concluded that the mechanisms behind ablation patterns are not well understood, the patterns remain uncharacterised and the pattern's effect on the boundary layer are not clear.

First, a simple test case was devised and used to validate the numerical method. The case involves a nitrogen laminar hypersonic flow ($M = 4$) over a subliming sphere. A non-dimensionalisation was introduced, which allowed the specification of a fictional solid phase of nitrogen. This simplified the computation as the material ablation parameters could be tuned for a given flow. The test case with stationary ablating walls was compared with a semi-analytical approximation. The stagnation-point equilibrium surface temperature was found to be 4% larger, and the ablation mass flux was around 60% larger than the approximation. Moreover, the computational challenge of managing a large range of timescales in fluid-structure interaction ablation problem was overcome by introducing an artificial ablation speed-up factor - the wall Damköhler number. Artificially changing the ablating material density allows control over the wall Damköhler number. It was shown that, as the Damköhler number increases the error in the shape change becomes independent of it. This means that the surface movement due to ablation can be sped-up whilst managing the shape change accuracy. Furthermore, the sphere's qualitative shape change was in disagreement with the characteristic sphere-cone shape of oriented meteors. This suggested that sublimation alone may not be sufficient for accurate physical modelling of meteors, both sublimation and shear ablation are necessary for accurate shape change modelling of meteors.

Secondly, hypersonic ablation patterns are investigated. A novel configuration with a transitional flow over a backward facing step with binary species ablating boundary was devised. A BFS was selected as it naturally generates streamwise vortices, which can cause localised heating and result in differential ablation, necessary for ablation patterns development. Three cases are investigated, without ablation, ablation with a stationary wall and ablation with a moving wall. The cases highlight an interference pattern, generated by the interaction of streamwise perturbations and streamwise vorticity. The pattern does not persist with the current flow conditions, however, the resulting ablation flux from such a pattern could lead to cross-hatching patterns. Furthermore, the cases showed that ablation destabilises and transitions the boundary layer. And, under a transitional boundary layer, differential ablation generates surface roughness. Around $\lesssim 0.8\delta_0$ of surface recession and fluctuations

in surface height of $\lesssim 0.2\delta_0$ are observed, where δ_0 is the inflow boundary layer thickness. The developed roughness was found to generate vorticity in the boundary layer.

6.2 Future works

Numerical method development

Considering the physical modelling, a separate electron temperature can be added to the system of conservation equations, which can improve electron density predictions with plasmas in thermochemical non-equilibrium. Moreover, electric and/or magnetic field conservation laws can also be added for plasma simulations. In addition, the thermochemical models can be tabulated by machine learning techniques for computational speed-ups.

On the other hand, considering the numerical modelling, future works should implement the AMR framework with anisotropic meshes. Currently, isotropic meshes are extremely limiting in three dimensions and high Reynolds and Mach number flows, as observed in the supersonic turbulent channel flow case. This feature is readily available in the next generation of AMR frameworks. Moreover, the addition of flux limiter for stability at Mach numbers greater than sub-orbital could also be explored. In addition, the performance of hybrid Euler flux calculation method—CS-TENO method—could be investigated. Lastly, addition of a wall model to further reduce computational cost with high Reynold numbers could be explored.

The viscous cases with SAMR-GPIBM suggested that the resolution requirement over a boundary layer is not uniform, and adaptively refining based on local y_w^+ can be computationally more efficient. This is shown by the double compression ramp case, where around 25% reduction in the number of computational points is observed with similar accuracy results. In the author's opinion, efficiently adapted grids could be competitive in computational cost with conformal meshes, especially considering adaptive time-stepping. However, direct comparison with a body-conformal mesh solver should be performed to quantify the cost benefits.

Heat transfer to proximal circular cylinders in hypersonic flow

The main limitation to the current study is that the simulations are two-dimensional, and not three-dimensional; as well as, the lack of thermochemical relaxation, which becomes increasingly relevant in high enthalpy conditions and is common to real atmospheric re-entry flows. Therefore, future studies should investigate the heat transfer to proximal bodies in

three-dimensions and thermochemical relaxation. However, three-dimensional simulations will be computationally challenging due to the large range of spacial length scales which need to be well resolved with increasing Mach and Reynolds numbers.

The second direction for future works is based on exploring the large parameter space. A limitation of the work is that only one flow condition was investigated. Future works should investigate the effect of varying Mach and Reynolds numbers. Furthermore, amongst the cluster parameters, only variations in body positions are investigated. The effect of a range of body sizes, shapes and the number of bodies should also be investigated in future studies.

Hypersonic ablation patterns

A limitation of the current work is the problem of mesh tangling with large surface recession. Which led to the backward facing step simulations to be limited to two flow times as the numerical method becomes unstable soon after, and could be avoided with runtime management of the geometry's discrete curvature. Future works should implement the necessary algorithms to void this issue.

Furthermore, future studies can explore the ablation topology (regmaglypt patterns) on oriented meteors. A motivation for this is to explore the possibility of predicting the meteor entry conditions with just the surface topology of the meteor and its material properties. Such a predictive ability is important as meteor trajectories are rarely known.

From a practical engineering perspective, a future study could focus on the effect of heat transfer augmentation due to micrometeoroid damage, as well as investigate damage growth based on flow conditions. In addition, the effect of ablation-generated roughness on boundary layer stability and transition could be investigated.

References

- Alkandry, H., Boyd, I., and Martin, A. (2013). Comparison of models for mixture transport properties for numerical simulations of ablative heat-shields. In *51st AIAA Aerospace Sciences Meeting including the New Horizons Forum and Aerospace Exposition*, page 303.
- Amory, C., Gallée, H., Naaïm-Bouvet, F., Favier, V., Vignon, E., Picard, G., Trouvilliez, A., Piard, L., Genthon, C., and Bellot, H. (2017). Seasonal variations in drag coefficient over a sastrugi-covered snowfield in coastal east antarctica. *Boundary-Layer Meteorology*, 164(1):107–133.
- Anderson Jr, J. D. (2006). *Hypersonic and high-temperature gas dynamics*. American Institute of Aeronautics and Astronautics.
- Artemieva, N. A. and Shuvalov, V. V. (2016). From Tunguska to Chelyabinsk via Jupiter. *Annual Review of Earth and Planetary Sciences*, 44:37–56.
- Atkins, C. and Deiterding, R. (2020). Towards a strand-cartesian solver for modelling hypersonic flows in thermochemical non-equilibrium. In *23rd AIAA International Space Planes and Hypersonic Systems and Technologies Conference*.
- Barkley, D., Gomes, M. G. M., and Henderson, R. D. (2002). Three-dimensional instability in flow over a backward-facing step. *Journal of Fluid Mechanics*, 473:167–190.
- Bauer, M., Eibl, S., Godenschwager, C., Kohl, N., Kuron, M., Rettinger, C., Schornbaum, F., Schwarzmeier, C., Thönnies, D., Köstler, H., et al. (2021). waLBerla: A block-structured high-performance framework for multiphysics simulations. *Computers & Mathematics with Applications*, 81:478–501.
- Baurle, R. A., White, J. A., Drozda, T. G., and Norris, A. T. (2020). *VULCAN-CFD theory manual: Ver. 7.1.0*. National Aeronautics and Space Administration.
- Behrens, W. (1967). The far wake behind cylinders at hypersonic speeds. I. *AIAA Journal*, 5(12):2135–2141.
- Bell, J., Almgren, A., Beckner, V., Day, M., Lijewski, M., Nonaka, A., and Zhang, W. (2014). Boxlib github repository. <https://github.com/BoxLib-Codes/BoxLib>. Accessed: 01-03-2021.
- Belouaggadia, N., Olivier, H., and Brun, R. (2008). Numerical and theoretical study of the shock stand-off distance in non-equilibrium flows. *Journal of Fluid Mechanics*, 607:167.

- Ben Ameer, F., Balis, J., Vandenhoeck, R., Lani, A., and Poedts, S. (2021). R-adaptive mesh algorithms with high-order flux reconstruction scheme for high-speed flows. In *AIAA Scitech 2021 Forum*, page 1240.
- Berger, M. (2017). Cut cells: Meshes and solvers. In *Handbook of Numerical Analysis*, volume 18, pages 1–22. Elsevier.
- Berger, M. and Giuliani, A. (2021). A state redistribution algorithm for finite volume schemes on cut cell meshes. *Journal of Computational Physics*, 428:109820.
- Berger, M. and Rigoutsos, I. (1991). An algorithm for point clustering and grid generation. *IEEE Transactions on Systems, Man, and Cybernetics*, 21(5):1278–1286.
- Berger, M. J., Colella, P., et al. (1989). Local adaptive mesh refinement for shock hydrodynamics. *Journal of Computational Physics*, 82(1):64–84.
- Bergman, T. L., Lavine, A. S., Incropera, F. P., and DeWitt, D. P. (2011). *Introduction to heat transfer*. John Wiley & Sons.
- Bethe, H. A. and Adams, M. C. (1959). A theory for the ablation of glassy materials. *Journal of the Aerospace Sciences*, 26(6):321–328.
- Betterton, M. (2001). Theory of structure formation in snowfields motivated by penitentes, suncups, and dirt cones. *Physical Review E*, 63(5):056129.
- Bianchi, D., Migliorino, M. T., Rotondi, M., and Turchi, A. (2021). Numerical analysis and wind tunnel validation of low-temperature ablators undergoing shape change. *International Journal of Heat and Mass Transfer*, 177:121430.
- Billig, F. S. (1967). Shock-wave shapes around spherical-and cylindrical-nosed bodies. *Journal of Spacecraft and Rockets*, 4(6):822–823.
- Bordiec, M., Carpy, S., Bourgeois, O., Herny, C., Massé, M., Perret, L., Claudin, P., Pochat, S., and Douté, S. (2020). Sublimation waves: Geomorphic markers of interactions between icy planetary surfaces and winds. *Earth-Science Reviews*, 211:103350.
- Bordner, J. and Norman, M. L. (2018). Computational Cosmology and Astrophysics on Adaptive Meshes using Charm++. *arXiv preprint arXiv:1810.01319*.
- Borges, R., Carmona, M., Costa, B., and Don, W. S. (2008). An improved weighted essentially non-oscillatory scheme for hyperbolic conservation laws. *Journal of Computational Physics*, 227(6):3191–3211.
- Boukharfane, R., Ribeiro, F. H. E., Bouali, Z., and Mura, A. (2018). A combined ghost-point-forcing/direct-forcing immersed boundary method (IBM) for compressible flow simulations. *Computers & Fluids*, 162:91–112.
- Boyd, I. D. and Schwartzentruber, T. E. (2017). *Nonequilibrium gas dynamics and molecular simulation*, volume 42. Cambridge University Press.
- Brehm, C., Barad, M. F., Housman, J. A., and Kiris, C. C. (2015). A comparison of higher-order finite-difference shock capturing schemes. *Computers & Fluids*, 122:184–208.

- Bridel-Bertomeu, T. (2021). Immersed boundary conditions for hypersonic flows using ENO-like least-square reconstruction. *Computers & Fluids*, 215:104794.
- Britt, D. T. and Consolmagno, G. (2003). Stony meteorite porosities and densities: A review of the data through 2001. *Meteoritics & Planetary Science*, 38(8):1161–1180.
- Bronshten, V. A. (2012). *Physics of meteoric phenomena*, volume 22. Springer Science & Business Media.
- Brown, P. G., Assink, J. D., Astiz, L., Blaauw, R., Boslough, M. B., Borovička, J., Brachet, N., Brown, D., Campbell-Brown, M., Ceranna, L., et al. (2013). A 500-kiloton airburst over Chelyabinsk and an enhanced hazard from small impactors. *Nature*, 503(7475):238–241.
- Burstedde, C., Wilcox, L. C., and Ghattas, O. (2011). p4est: Scalable algorithms for parallel adaptive mesh refinement on forests of octrees. *SIAM Journal on Scientific Computing*, 33(3):1103–1133.
- Butler, C., Whalen, T., Sousa, C., and Laurence, S. (2021). Dynamics of a spherical body shedding from a hypersonic ramp. part 2. viscous flow. *Journal of Fluid Mechanics*, 906.
- Calhoun, D. and Burstedde, C. (2017). ForestClaw: A parallel algorithm for patch-based adaptive mesh refinement on a forest of quadrees. *arXiv preprint arXiv:1703.03116*.
- Candler, G. V. (2019). Rate effects in hypersonic flows. *Annual Review of Fluid Mechanics*, 51:379–402.
- Capitelli, M., Colonna, G., Marraffa, L., Giordano, D., Giordano, D., and Warmbein, B. (2005). *Tables of internal partition functions and thermodynamic properties of high-temperature Mars-atmosphere species from 50K to 50000K*. European Space Agency.
- Casseau, V., Espinoza, D. E., Scanlon, T. J., and Brown, R. E. (2016). A two-temperature open-source CFD model for hypersonic reacting flows, part two: multi-dimensional analysis. *Aerospace*, 3(4):45.
- Chaudhuri, A., Hadjadj, A., and Chinnayya, A. (2011). On the use of immersed boundary methods for shock/obstacle interactions. *Journal of Computational Physics*, 230(5):1731–1748.
- Cheatwood, F. M. and Gnoffo, P. A. (1996). *User’s Manual for the Langley Aerothermodynamic Upwind Relaxation Algorithm (LAURA)*. National Aeronautics and Space Administration, Langley Research Center.
- Ching, E. J., Lv, Y., Gnoffo, P., Barnhardt, M., and Ihme, M. (2019). Shock capturing for discontinuous galerkin methods with application to predicting heat transfer in hypersonic flows. *Journal of Computational Physics*, 376:54–75.
- Claudin, P., Jarry, H., Vignoles, G., Plapp, M., and Andreotti, B. (2015). Physical processes causing the formation of penitentes. *Physical Review E*, 92(3):033015.
- Cohen, C., Berhanu, M., Derr, J., and Du Pont, S. C. (2020). Buoyancy-driven dissolution of inclined blocks: Erosion rate and pattern formation. *Physical Review Fluids*, 5(5):053802.

- Colella, P., Graves, D. T., Keen, B. J., and Modiano, D. (2006). A cartesian grid embedded boundary method for hyperbolic conservation laws. *Journal of Computational Physics*, 211(1):347–366.
- Coleman, G. N., Kim, J., and Moser, R. D. (1995). A numerical study of turbulent supersonic isothermal-wall channel flow. *Journal of Fluid Mechanics*, 305:159–183.
- Cook, A. W. and Cabot, W. H. (2004). A high-wavenumber viscosity for high-resolution numerical methods. *Journal of Computational Physics*, 195(2):594–601.
- Cook, A. W. and Cabot, W. H. (2005). Hyperviscosity for shock-turbulence interactions. *Journal of Computational Physics*, 203(2):379–385.
- Coppola, G., Capuano, F., Pirozzoli, S., and de Luca, L. (2019). Numerically stable formulations of convective terms for turbulent compressible flows. *Journal of Computational Physics*, 382:86–104.
- Courant, R., Friedrichs, K., and Lewy, H. (1967). On the partial difference equations of mathematical physics. *IBM Journal of Research and Development*, 11(2):215–234.
- Courant, R., Isaacson, E., and Rees, M. (1952). On the solution of nonlinear hyperbolic differential equations by finite differences. *Communications on Pure and Applied Mathematics*, 5(3):243–255.
- Daily, J. W. (2018). *Statistical Thermodynamics: An Engineering Approach*. Cambridge University Press.
- Damm, K. A., Landsberg, W. O., Mecklem, S., and Veeraragavan, A. (2020). Performance analysis and validation of an explicit local time-stepping algorithm for complex hypersonic flows. *Aerospace Science and Technology*, 107:106321.
- Davuluri, R. S., Zhang, H., and Martin, A. (2016). Numerical study of spallation phenomenon in an arc-jet environment. *Journal of Thermophysics and Heat Transfer*, 30(1):32–41.
- De Vanna, F., Picano, F., and Benini, E. (2020). A sharp-interface immersed boundary method for moving objects in compressible viscous flows. *Computers & Fluids*, 201:104415.
- Deiterding, R. (2003). *Parallel adaptive simulation of multi-dimensional detonation structures*. PhD thesis, Brandenburg University of Technology.
- Deiterding, R. (2011). Block-structured adaptive mesh refinement-theory, implementation and application. In *Esaim: Proceedings*, volume 34, pages 97–150. EDP Sciences.
- Délery, J. M. (2001). Robert Legendre and Henri Werlé: toward the elucidation of three-dimensional separation. *Annual Review of Fluid Mechanics*, 33(1):129–154.
- Di Renzo, M., Fu, L., and Urzay, J. (2020). HTR solver: An open-source exascale-oriented task-based multi-gpu high-order code for hypersonic aerothermodynamics. *Computer Physics Communications*, 255:107262.
- Dias, B. (2020). *Thermal ablation and radiation modeling of meteor phenomena*. PhD thesis, UCL-Université Catholique de Louvain.

- Domingues, M. O., Gomes, S. M., Roussel, O., and Schneider, K. (2009). Space–time adaptive multiresolution methods for hyperbolic conservation laws: applications to compressible Euler equations. *Applied numerical mathematics*, 59(9):2303–2321.
- Doru, C. (2016). Vortex transport by uniform flow. <https://how5.cenaero.be/content/vi1-vortex-transport-uniform-flow>. Accessed: 01-01-2022.
- Dubey, A., Almgren, A., Bell, J., Berzins, M., Brandt, S., Bryan, G., Colella, P., Graves, D., Lijewski, M., Löffler, F., et al. (2014). A survey of high level frameworks in block-structured adaptive mesh refinement packages. *Journal of Parallel and Distributed Computing*, 74(12):3217–3227.
- Dubey, A., Berzins, M., Burstedde, C., Norman, M. L., Unat, D., and Wahib, M. (2021). Structured adaptive mesh refinement adaptations to retain performance portability with increasing heterogeneity. *Computing in Science & Engineering*, 23(5):62–66.
- Ducros, F., Laporte, F., Soulères, T., Guinot, V., Moinat, P., and Caruelle, B. (2000). High-order fluxes for conservative skew-symmetric-like schemes in structured meshes: application to compressible flows. *Journal of Computational Physics*, 161(1):114–139.
- Duffa, G. (2013). *Ablative thermal protection systems modeling*. American Institute of Aeronautics and Astronautics, Inc.
- Duffa, G., Vignoles, G. L., Goyhénèche, J.-M., and Aspa, Y. (2005). Ablation of carbon-based materials: investigation of roughness set-up from heterogeneous reactions. *International Journal of Heat and Mass Transfer*, 48(16):3387–3401.
- Durna, A. and Celik, B. (2019). Time-periodic shock interaction mechanisms over double wedges at mach 7. *Shock Waves*, 29(3):381–399.
- Edney, B. (1968). Anomalous heat transfer and pressure distributions on blunt bodies at hypersonic speeds in the presence of an impinging shock. Technical report, Flygtekniska Forsoksanstalten, Stockholm (Sweden).
- Einfeldt, B. (1988). On godunov-type methods for gas dynamics. *SIAM Journal on Numerical Analysis*, 25(2):294–318.
- Ekaterinaris, J. A. (2005). High-order accurate, low numerical diffusion methods for aerodynamics. *Progress in Aerospace Sciences*, 41(3-4):192–300.
- Energia (2022). Vostok 1 anniversary photo album. <http://www.spaceref.com/news/viewpr.html?pid=4390>. Accessed: 01-03-2022.
- Fay, J. A. and Riddell, F. R. (1958). Theory of stagnation point heat transfer in dissociated air. *Journal of the Aerospace Sciences*, 25(2):73–85.
- Feldman, S. (1959). On the instability theory of the melted surface of an ablating body when entering the atmosphere. *Journal of Fluid Mechanics*, 6(1):131–155.
- Fernando, M., Neilsen, D., Lim, H., Hirschmann, E., and Sundar, H. (2018). Massively parallel simulations of binary black hole intermediate-mass-ratio inspirals. *arXiv preprint arXiv:1807.06128*.

- Fisher, T. B. (2019). *Development of advanced techniques for aerodynamic assessment of blunt bodies in hypersonic flows*. PhD thesis, The University of Manchester.
- Foysi, H., Sarkar, S., and Friedrich, R. (2004). Compressibility effects and turbulence scalings in supersonic channel flow. *Journal of Fluid Mechanics*, 509:207–216.
- Freeman, N. (1958). Non-equilibrium flow of an ideal dissociating gas. *Journal of Fluid Mechanics*, 4(4):407–425.
- Fu, L. (2019). A very-high-order TENO scheme for all-speed gas dynamics and turbulence. *Computer Physics Communications*, 244:117–131.
- Fu, L., Hu, X. Y., and Adams, N. A. (2017). Targeted ENO schemes with tailored resolution property for hyperbolic conservation laws. *Journal of Computational Physics*, 349:97–121.
- Fu, L., Hu, X. Y., and Adams, N. A. (2018). A new class of adaptive high-order targeted ENO schemes for hyperbolic conservation laws. *Journal of Computational Physics*, 374:724–751.
- Gai, S. L. and Khraibut, A. (2019). Hypersonic compression corner flow with large separated regions. *Journal of Fluid Mechanics*, 877:471–494.
- Ghias, R., Mittal, R., and Dong, H. (2007). A sharp interface immersed boundary method for compressible viscous flows. *Journal of Computational Physics*, 225(1):528–553.
- Giovangigli, V. (1991). Convergent iterative methods for multicomponent diffusion. *IMPACT of Computing in Science and Engineering*, 3(3):244–276.
- Godnov, S. (1969). A difference scheme for numerical computation of discontinuous solution of hydrodynamic equations. *Res. Service, JPRS*, 7226:271–306.
- Gokhale, N., Nikiforakis, N., and Klein, R. (2018). A dimensionally split cartesian cut cell method for hyperbolic conservation laws. *Journal of Computational Physics*, 364:186–208.
- Gollan, R. J. and Jacobs, P. A. (2013). About the formulation, verification and validation of the hypersonic flow solver eilmer. *International Journal for Numerical Methods in Fluids*, 73(1):19–57.
- Grasso, F. and Marini, M. (1996). Analysis of hypersonic shock-wave laminar boundary-layer interaction phenomena. *Computers & fluids*, 25(6):561–581.
- Griffin, K. P., Fu, L., and Moin, P. (2021). Velocity transformation for compressible wall-bounded turbulent flows with and without heat transfer. *Proceedings of the National Academy of Sciences*, 118(34):e2111144118.
- Grigat, F., Loehle, S., Zander, F., and Fasoulas, S. (2020). Detection of spallation phenomena on ablator surfaces. In *AIAA Scitech 2020 Forum*, page 1706.
- Grossman, B. and Cinnella, P. (1990). Flux-split algorithms for flows with non-equilibrium chemistry and vibrational relaxation. *Journal of Computational Physics*, 88(1):131–168.
- Gu, S. and Olivier, H. (2020). Capabilities and limitations of existing hypersonic facilities. *Progress in Aerospace Sciences*, 113:100607.

- Guarini, S. E., Moser, R. D., Shariff, K., and Wray, A. (2000). Direct numerical simulation of a supersonic turbulent boundary layer at Mach 2.5. *Journal of Fluid Mechanics*, 414:1–33.
- Guo, S., Feng, Y., Jacob, J., Renard, F., and Sagaut, P. (2020). An efficient lattice boltzmann method for compressible aerodynamics on D3Q19 lattice. *Journal of Computational Physics*, 418:109570.
- Gupta, R. N., Lee, K.-P., Thompson, R. A., and Yos, J. M. (1990). A review of reaction rates and thermodynamic and transport properties for an 11-species air model for chemical and thermal nonequilibrium calculations to 30000 k. *NASA Reference Publication*.
- Hama, F. R. (1968). Experimental studies on the lip shock. *AIAA Journal*, 6(2):212–219.
- Hamzehloo, A., Lusher, D. J., Laizet, S., and Sandham, N. D. (2021). On the performance of WENO/TENO schemes to resolve turbulence in dns/les of high-speed compressible flows. *International Journal for Numerical Methods in Fluids*, 93(1):176–196.
- Hao, J., Wang, J., and Lee, C. (2017). Development of a navier- stokes code for hypersonic nonequilibrium simulations. In *21st AIAA International Space Planes and Hypersonics Technologies Conference*, page 2164.
- Haynes, W. M. (2014). *CRC handbook of chemistry and physics*. CRC press.
- Hermeus (2022). Homepage. <https://www.hermeus.com/>. Accessed: 01-03-2022.
- Hinman, W. S. and Johansen, C. T. (2018). Mechanisms in the hypersonic laminar near wake of a blunt body. *Journal of Fluid Mechanics*, 839:33–75.
- Hirschfelder, J. O., Curtiss, C. F., Bird, R. B., and Mayer, M. G. (1964). *Molecular theory of gases and liquids*, volume 165. Wiley New York.
- Hodge-Smith, T. (1939). Australian meteorites. *Australian Museum Memoir*, 7:1–84.
- Holden, Michael S, J. R. M. (1970). Theoretical and experimental studies of the shock wave-boundary layer interaction on compression surfaces in hypersonic flow. Technical report, Cornell Aeronautical Lab Inc Buffalo NY.
- Hu, W., Hickel, S., and Van Oudheusden, B. (2019). Dynamics of a supersonic transitional flow over a backward-facing step. *Physical Review Fluids*, 4(10):103904.
- Hu, W., Hickel, S., and Van Oudheusden, B. (2020). Influence of upstream disturbances on the primary and secondary instabilities in a supersonic separated flow over a backward-facing step. *Physics of Fluids*, 32(5):056102.
- Jameson, A. (2017). Origins and further development of the Jameson–Schmidt–Tukel scheme. *AIAA Journal*, 55(5):1487–1510.
- Jarosewich, E. (1990). Chemical analyses of meteorites: A compilation of stony and iron meteorite analyses. *Meteoritics*, 25(4):323–337.
- Jiang, G.-S. and Shu, C.-W. (1996). Efficient implementation of weighted ENO schemes. *Journal of Computational Physics*, 126(1):202–228.

- Johnsen, E., Larsson, J., Bhagatwala, A. V., Cabot, W. H., Moin, P., Olson, B. J., Rawat, P. S., Shankar, S. K., Sjögreen, B., Yee, H. C., et al. (2010). Assessment of high-resolution methods for numerical simulations of compressible turbulence with shock waves. *Journal of Computational Physics*, 229(4):1213–1237.
- Kaiser, J. W., Hoppe, N., Adami, S., and Adams, N. A. (2019). An adaptive local time-stepping scheme for multiresolution simulations of hyperbolic conservation laws. *Journal of Computational Physics: X*, 4:100038.
- Kawai, S., Shankar, S. K., and Lele, S. K. (2010). Assessment of localized artificial diffusivity scheme for large-eddy simulation of compressible turbulent flows. *Journal of Computational Physics*, 229(5):1739–1762.
- Kessler, D. J. and Cour-Palais, B. G. (1978). Collision frequency of artificial satellites: The creation of a debris belt. *Journal of Geophysical Research: Space Physics*, 83(A6):2637–2646.
- Keyes, J. W. and Hains, F. D. (1973). Analytical and experimental studies of shock interference heating in hypersonic flows. Technical report, NASA.
- Khalili, M. E., Larsson, M., and Müller, B. (2018). Immersed boundary method for viscous compressible flows around moving bodies. *Computers & Fluids*, 170:77–92.
- Klein, M., Sadiki, A., and Janicka, J. (2003). A digital filter based generation of inflow data for spatially developing direct numerical or large eddy simulations. *Journal of Computational Physics*, 186(2):652–665.
- Knight, D., Chazot, O., Austin, J., Badr, M. A., Candler, G., Celik, B., de Rosa, D., Donelli, R., Komives, J., Lani, A., et al. (2017). Assessment of predictive capabilities for aerodynamic heating in hypersonic flow. *Progress in Aerospace Sciences*, 90:39–53.
- Kravchenko, A. and Moin, P. (1997). On the effect of numerical errors in large eddy simulations of turbulent flows. *Journal of Computational Physics*, 131(2):310–322.
- Kruger, C. H. and Vincenti, W. (1965). *Introduction to physical gas dynamics*. Krieger Publishing Company.
- Laney, C. B. (1998). *Computational gasdynamics*. Cambridge University Press.
- Laurence, S. J. and Deiterding, R. (2011). Shock-wave surfing. *Journal of fluid mechanics*, 676:396–431.
- Laurence, S. J., Deiterding, R., and Hornung, G. (2007). Proximal bodies in hypersonic flow. *Journal of Fluid Mechanics*, 590:209–237.
- Laurence, S. J., Parziale, N. J., and Deiterding, R. (2012). Dynamical separation of spherical bodies in supersonic flow. *Journal of Fluid Mechanics*, 713:159–182.
- Lax, P. (1959). Systems of conservation laws. Technical report, Los Alamos National Lab.
- Lee, J.-H. (1984). Basic governing equations for the flight regimes of aeroassisted orbital transfer vehicles. In *19th Thermophysics Conference*, page 1729.

- Lees, L. (1964). Hypersonic wakes and trails. *AIAA Journal*, 2(3):417–428.
- LeVeque, R. J. (1992). *Numerical methods for conservation laws*, volume 132. Springer.
- LeVeque, R. J. et al. (2002). *Finite volume methods for hyperbolic problems*, volume 31. Cambridge University Press.
- Lighthill, M. (1957). Dynamics of a dissociating gas part i equilibrium flow. *Journal of Fluid Mechanics*, 2(1):1–32.
- Lin, T. and Qun, P. (1987). On the formation of regmaglypts on meteorites. *Fluid dynamics research*, 1(3-4):191–199.
- Linstrom, P. J. and Mallard, W. G. (2001). The NIST Chemistry WebBook: A chemical data resource on the internet. *Journal of Chemical & Engineering Data*, 46(5):1059–1063.
- Liou, M.-S. (2006). A sequel to AUSM, Part II: AUSM⁺ - up for all speeds. *Journal of Computational Physics*, 214(1):137–170.
- Lips, T. and Fritsche, B. (2005). A comparison of commonly used re-entry analysis tools. *Acta Astronautica*, 57(2-8):312–323.
- Liu, X.-D., Osher, S., and Chan, T. (1994). Weighted essentially non-oscillatory schemes. *Journal of Computational Physics*, 115(1):200–212.
- Locatelli, G., Bingham, C., and Mancini, M. (2014). Small modular reactors: A comprehensive overview of their economics and strategic aspects. *Progress in Nuclear Energy*, 73:75–85.
- Lodato, G. (2008). *Tridimensional Boundary Conditions for Direct and Large-Eddy Simulation of Turbulent Flows. Sub-Grid Scale Modeling for Near-Wall Region Turbulence*. PhD thesis, INSA de Rouen.
- Luitjens, J. and Berzins, M. (2011). Scalable parallel regridding algorithms for block-structured adaptive mesh refinement. *Concurrency and Computation: Practice and Experience*, 23(13):1522–1537.
- Luitjens, J., Berzins, M., and Henderson, T. (2007). Parallel space-filling curve generation through sorting. *Concurrency and Computation: Practice and Experience*, 19(10):1387–1402.
- Lusher, D. (2020). *Shock-wave/boundary-layer interactions with sidewall effects in the OpenSBLI code-generation framework*. PhD thesis, University of Southampton.
- Mac Huang, J., Moore, M. N. J., and Ristroph, L. (2015). Shape dynamics and scaling laws for a body dissolving in fluid flow. *Journal of Fluid Mechanics*, 765.
- Macheret, S., Fridman, A., Adamovich, I., Rich, J., and Treanor, C. (1994). Mechanisms of nonequilibrium dissociation of diatomic molecules. In *AIAA/ASME 6th Joint Thermo-physics and Heat Transfer Conference, 1994*, pages AIAA–94.
- Mack, L. M. (1984). Boundary-layer linear stability theory. Technical report, California Inst of Tech Pasadena Jet Propulsion Lab.

- MacNeice, P., Olson, K. M., Mobarry, C., De Fainchtein, R., and Packer, C. (2000). PARAMESH: A parallel adaptive mesh refinement community toolkit. *Computer physics communications*, 126(3):330–354.
- Magin, T. E. and Degrez, G. (2004). Transport algorithms for partially ionized and unmagnetized plasmas. *Journal of Computational Physics*, 198(2):424–449.
- Mandli, K. T., Ahmadi, A. J., Berger, M., Calhoun, D., George, D. L., Hadjimichael, Y., Ketcheson, D. I., Lemoine, G. I., and LeVeque, R. J. (2016). Clawpack: building an open source ecosystem for solving hyperbolic PDEs. *PeerJ Computer Science*, 2:e68.
- Marrone, P. V. and Treanor, C. E. (1963). Chemical relaxation with preferential dissociation from excited vibrational levels. *Physics of Fluids*, 6(9):1215–1221.
- Marwege, A., Willems, S., Gülhan, A., Aftosmis, M. J., and Stern, E. C. (2018). Superposition method for force estimations on bodies in supersonic and hypersonic flows. *Journal of Spacecraft and Rockets*, 55(5):1166–1180.
- Matsuyama, S., Takayanagi, H., and Fujita, K. (2013). Numerical investigation on RCS jet interactions for a mars entry vehicle. In *43rd AIAA Fluid Dynamics Conference*, page 2977.
- McQuaid, J. A., Zibitsker, A., Martin, A., and Brehm, C. (2021a). Heat flux predictions for high speed flows with an immersed boundary method. In *AIAA AVIATION 2021 FORUM*, page 3145.
- McQuaid, J. A., Zibitsker, A. L., Saikia, B., Martin, A., and Brehm, C. (2021b). An immersed boundary method for hypersonic viscous flows. In *AIAA Scitech 2021 Forum*, page 0926.
- Meakin, P. and Jamtveit, B. (2010). Geological pattern formation by growth and dissolution in aqueous systems. *Proceedings of the Royal Society A: Mathematical, Physical and Engineering Sciences*, 466(2115):659–694.
- Miller, I. M. and Sutton, K. (1966). An experimental study of the oxidation of graphite in high-temperature supersonic and hypersonic environments. Technical report, NASA.
- Millikan, R. C. and White, D. R. (1963). Systematics of vibrational relaxation. *The Journal of Chemical Physics*, 39(12):3209–3213.
- Mittal, R. and Iaccarino, G. (2005). Immersed boundary methods. *Annual. Rev. Fluid Mech.*, 37:239–261.
- Morgan Stanley (2022). New space economy on the edge of lift-off. <https://www.morganstanley.com/Themes/global-space-economy>. Accessed: 01-03-2022.
- Mortensen, C. H. and Zhong, X. (2014). Simulation of second-mode instability in a real-gas hypersonic flow with graphite ablation. *AIAA journal*, 52(8):1632–1652.
- NASA (2022). First launch from cape canaveral. https://www.nasa.gov/multimedia/imagegallery/image_feature_765.html. Accessed: 01-03-2022.

- National Post (2022). Russian meteor strike. <https://nationalpost.com/news/it-will-cost-over-33m-to-repair-damage-from-russian-meteor-strike>. Accessed: 01-03-2022.
- Navarro-Martinez, S. (2003). *Numerical simulation of laminar flow over hypersonic compression ramps*. PhD thesis, University of Southampton.
- Nompelis, I., Drayna, T. W., and Candler, G. V. (2006). A parallel unstructured implicit solver for hypersonic reacting flow simulation. In *Parallel Computational Fluid Dynamics 2005*, pages 389–395. Elsevier.
- Nonaka, S., Mizuno, H., Takayama, K., and Park, C. (2000). Measurement of shock standoff distance for sphere in ballistic range. *Journal of Thermophysics and Heat Transfer*, 14(2):225–229.
- Panesi, M. (2009). *Physical models for nonequilibrium plasma flow simulations at high speed re-entry conditions*. PhD thesis, Von Karman Institute.
- Park, C. (1984). Problems of rate chemistry in the flight regimes of aeroassisted orbital transfer vehicles. In *19th Thermophysics Conference*, page 1730.
- Park, C. (1988). Assessment of a two-temperature kinetic model for dissociating and weakly ionizing nitrogen. *Journal of Thermophysics and Heat Transfer*, 2(1):8–16.
- Park, C. (1989). Assessment of two-temperature kinetic model for ionizing air. *Journal of Thermophysics and Heat Transfer*, 3(3):233–244.
- Park, C. (1990). *Nonequilibrium Hypersonic Aerothermodynamics*. Wiley.
- Park, S.-H., Kim, J., Choi, I., and Park, G. (2021). Experimental study of separation behavior of two bodies in hypersonic flow. *Acta Astronautica*, 181:414–426.
- Park, S.-H. and Park, G. (2020). Separation process of multi-spheres in hypersonic flow. *Advances in Space Research*, 65(1):392–406.
- Passey, Q. R. and Melosh, H. (1980). Effects of atmospheric breakup on crater field formation. *Icarus*, 42(2):211–233.
- Peltier, S., Humble, R., and Bowersox, R. (2016). Crosshatch roughness distortions on a hypersonic turbulent boundary layer. *Physics of Fluids*, 28(4):045105.
- Piquet, A. (2017). *Physical analysis and numerical simulation of the separation phenomenon in over-expanded nozzle flow*. PhD thesis, Normandie Université; Imperial College London.
- Pirozzoli, S. (2010). Generalized conservative approximations of split convective derivative operators. *Journal of Computational Physics*, 229(19):7180–7190.
- Pirozzoli, S. (2011). Numerical methods for high-speed flows. *Annual Review of Fluid Mechanics*, 43:163–194.
- Poinsot, T. and Veynante, D. (2005). *Theoretical and numerical combustion*. RT Edwards, Inc.

- Poling, B. E., Prausnitz, J. M., O'connell, J. P., et al. (2001). *The properties of gases and liquids*, volume 5. Mcgraw-hill New York.
- Pope, S. B. (2000). *Turbulent flows*. Cambridge University Press.
- Popinet, S. (2006). The GNU triangulated surface library (GTS). <http://gts.sourceforge.net/>. Accessed: 01-02-2020.
- Popova, O. P., Jenniskens, P., and Others (2013). Chelyabinsk airburst, damage assessment, meteorite recovery, and characterization. *Science*, 342(6162):1069–1073.
- Price, K. J., Hardy, J. M., Borchetta, C. G., Panerai, F., Bailey, S. C., and Martin, A. (2020). Analysis of spallation products using arc-jet experiments. In *AIAA Scitech 2020 Forum*, page 1707.
- Raghunandan, P., Haskins, J. B., Palmer, G. E., Bessire, B. K., and Stern, E. C. (2021). Material response modeling of melt flow-vapor ablation for iron. *AIAA Journal*, pages 1–11.
- Ramjatan, S., Lani, A., Boccelli, S., Van Hove, B., Karatekin, O., Magin, T., and Thoemel, J. (2020). Blackout analysis of mars entry missions. *Journal of Fluid Mechanics*, 904:A26.
- Rani, H., Sheu, T. W., and Tsai, E. S. (2007). Eddy structures in a transitional backward-facing step flow. *Journal of Fluid Mechanics*, 588:43–58.
- Rees, T. W. (2020). *Hypersonic Aerothermodynamics of Satellite Demise*. PhD thesis, Imperial College London.
- Register, P., Aftosmis, M., Stern, E., Brock, J., Seltner, P., Willems, S., Gülhan, A., and Mathias, D. (2020). Interactions between asteroid fragments during atmospheric entry. *Icarus*, 337:113468.
- Reinert, J. D., Candler, G. V., and Komives, J. R. (2020). Simulations of unsteady three-dimensional hypersonic double-wedge flow experiments. *AIAA journal*, 58(9):4055–4067.
- Ren, X., Yuan, J., He, B., Zhang, M., and Cai, G. (2019). Grid criteria for numerical simulation of hypersonic aerothermodynamics in transition regime. *Journal of Fluid Mechanics*, 881:585–601.
- Ren, Y.-X., Zhang, H., et al. (2003). A characteristic-wise hybrid compact-WENO scheme for solving hyperbolic conservation laws. *Journal of Computational Physics*, 192(2):365–386.
- Renzo, M. D. and Urzay, J. (2021). Direct numerical simulation of a hypersonic transitional boundary layer at suborbital enthalpies. *Journal of Fluid Mechanics*, 912.
- Ristroph, L. (2018). Sculpting with flow. *Journal of Fluid Mechanics*, 838:1–4.
- Ristroph, L., Moore, M. N., Childress, S., Shelley, M. J., and Zhang, J. (2012). Sculpting of an erodible body by flowing water. *Proceedings of the National Academy of Sciences*, 109(48):19606–19609.
- Roe, P. L. (1981). Approximate riemann solvers, parameter vectors, and difference schemes. *Journal of Computational Physics*, 43(2):357–372.

- Rudy, D. H., Thomas, J. L., Kumar, A., Gnoffo, P. A., and Chakravarthy, S. R. (1991). Computation of laminar hypersonic compression-corner flows. *AIAA journal*, 29(7):1108–1113.
- Sawant, N., Dorschner, B., and Karlin, I. (2021). A lattice boltzmann model for reactive mixtures. *Philosophical Transactions of the Royal Society A*, 379(2208):20200402.
- Scalabrin, L. and Boyd, I. (2006). Numerical simulation of weakly ionized hypersonic flow for reentry configurations. In *9th AIAA/ASME Joint Thermophysics and Heat Transfer Conference*, page 3773.
- Schneider, S. P. (2008). Effects of roughness on hypersonic boundary-layer transition. *Journal of spacecraft and rockets*, 45(2):193–209.
- Schneiders, L., Hartmann, D., Meinke, M., and Schröder, W. (2013). An accurate moving boundaries formulation in cut-cell methods. *Journal of Computational Physics*, 235:786–809.
- Schwamborn, D., Gerhold, T., and Heinrich, R. (2006). The dlr tau-code: recent applications in research and industry. In *European Conference on Computational Fluid Dynamics*.
- Sciacovelli, L., Passiatore, D., Cinnella, P., and Pascazio, G. (2021). Assessment of a high-order shock-capturing central-difference scheme for hypersonic turbulent flow simulations. *Computers & Fluids*, 230:105134.
- Scoggins, J. (2017). *Development of numerical methods and study of coupled flow, radiation, and ablation phenomena for atmospheric entry*. PhD thesis, PhD thesis, Université Paris-Saclay and VKI.
- Scoggins, J. B., Leroy, V., Bellas-Chatzigeorgis, G., Dias, B., and Magin, T. E. (2020). Mutation++: Multicomponent thermodynamic and transport properties for ionized gases in c++. *SoftwareX*, 12.
- Sekhar, S. K. and Ruffin, S. M. (2013). Predictions of convective heat transfer rates using a cartesian grid solver for hypersonic flows. In *44th AIAA Thermophysics Conference*, page 2645.
- Shu, C.-W. (1988). Total-variation-diminishing time discretizations. *SIAM Journal on Scientific and Statistical Computing*, 9(6):1073–1084.
- Shu, C.-W. (1997). Essentially non-oscillatory and weighted essentially non-oscillatory schemes for hyperbolic conservation laws. *NASA Technical Report*.
- Shu, C.-W. and Osher, S. (1988). Efficient implementation of essentially non-oscillatory shock-capturing schemes. *Journal of Computational Physics*, 77(2):439–471.
- Simpkins, P. G. (1963). On the stable shape of subliming bodies in a high-enthalpy gas stream. *Journal of Fluid Mechanics*, 15(1):119–132.
- Smith, A. J. D. (1993). *The dynamic response of a wedge separated hypersonic flow and its effects on heat transfer*. PhD thesis, University of Southampton.

- Sousa, C., Deiterding, R., and Laurence, S. J. (2021). Dynamics of a spherical body shedding from a hypersonic ramp. part 1. inviscid flow. *Journal of Fluid Mechanics*, 906.
- Spiegel, S. C., Huynh, H., and DeBonis, J. R. (2015). A survey of the isentropic euler vortex problem using high-order methods. In *22nd AIAA computational fluid dynamics conference*, page 2444.
- Steger, J. L. and Warming, R. (1981). Flux vector splitting of the inviscid gasdynamic equations with application to finite-difference methods. *Journal of Computational Physics*, 40(2):263–293.
- Stock, H. W. (1975). Surface patterns on subliming and liquefying ablation materials. *AIAA Journal*, 13(9):1217–1223.
- Stock, H. W. and Ginoux, J. J. (1973). Hypersonic low temperature ablation an experimental study of cross-hatched surface patterns. In *Astronautical Research 1971*, pages 105–120. Springer.
- Sutton, K. and Gnoffo, P. (1998). Multi-component diffusion with application to computational aerothermodynamics. In *7th AIAA/ASME Joint Thermophysics and Heat Transfer Conference*, page 2575.
- Swantek, A. (2012). *The role of aerothermochemistry in double cone and double wedge flows*. University of Illinois at Urbana-Champaign.
- Swigart, R. J. (1974). Cross-hatching studies-a critical review. *AIAA Journal*, 12(10):1301–1318.
- Tauber, M. E. (1989). A review of high-speed, convective, heat-transfer computation methods. *NASA Technical Report*.
- Terán-Bobadilla, E., Abundis-Patiño, J., Añorve, C., Moraila, C., Ortega-Gutiérrez, F., and Aragón-Calvo, M. (2017). On a novel geometric analysis of the bacubirito meteorite. *Earth, Moon, and Planets*, 120(2):101–111.
- Teunissen, J. and Ebert, U. (2018). Afivo: A framework for quadtree/octree AMR with shared-memory parallelization and geometric multigrid methods. *Computer Physics Communications*, 233:156–166.
- Toro, E. F. (2013). *Riemann solvers and numerical methods for fluid dynamics: a practical introduction*. Springer Science & Business Media.
- Toro, E. F., Spruce, M., and Speares, W. (1994). Restoration of the contact surface in the HLL-Riemann solver. *Shock waves*, 4(1):25–34.
- Trevino, L. (2021). *Numerical Simulation of Surface Patterns on Sublimating Ablative Materials*. PhD thesis, University of Minnesota.
- Tseng, Y.-H. and Ferziger, J. H. (2003). A ghost-cell immersed boundary method for flow in complex geometry. *Journal of Computational Physics*, 192(2):593–623.
- Urzay, J. (2020). The physical characteristics of hypersonic flows. http://web.stanford.edu/~jurzay/hypersonicsCh2_Urzay.pdf. Accessed: 02-08-2021.

- Urzay, J. and Di Renzo, M. (2021). Engineering aspects of hypersonic turbulent flows at suborbital enthalpies. *Annual Research Briefs, Center for Turbulence Research*, pages 7–32.
- Van Dyke, M. D. (1958). The supersonic blunt-body problem-review and extension. *Journal of the Aerospace Sciences*, 25(8):485–496.
- van Leer, B. (1982). Flux-vector splitting for the euler equations. *Numerical Methods in Fluid Dynamics*, 170:507–512.
- Vandenhoeck, R. and Lani, A. (2019). Implicit high-order flux reconstruction solver for high-speed compressible flows. *Computer Physics Communications*, 242:1–24.
- Vignoles, G. L., Lachaud, J., Aspa, Y., and Goyh  n  che, J.-M. (2009). Ablation of carbon-based materials: multiscale roughness modelling. *Composites Science and Technology*, 69(9):1470–1477.
- VonNeumann, J. and Richtmyer, R. D. (1950). A method for the numerical calculation of hydrodynamic shocks. *Journal of Applied Physics*, 21(3):232–237.
- Wang, X., Deiterding, R., Liang, J., Cai, X., and Zhao, W. (2022). A second-order-accurate immersed boundary ghost-cell method with hybrid reconstruction for compressible flow simulations. *Computers & Fluids*, 237:105314.
- Wen, C.-Y. and Hornung, H. (1995). Non-equilibrium dissociating flow over spheres. *Journal of Fluid Mechanics*, 299:389–405.
- Wen, C.-Y., Massimi, H. S., and Shen, H. (2018). Extension of ce/se method to non-equilibrium dissociating flows. *Journal of Computational Physics*, 356:240–260.
- Whalen, T. J. and Laurence, S. J. (2021). Experiments on the separation of sphere clusters in hypersonic flow. *Experiments in Fluids*, 62(4):1–19.
- Wilke, C. (1950). A viscosity equation for gas mixtures. *The Journal of Chemical Physics*, 18(4):517–519.
- Williamson, C. H. (1988). Defining a universal and continuous Strouhal–Reynolds number relationship for the laminar vortex shedding of a circular cylinder. *Physics of fluids*, 31(10):2742–2744.
- Wilson, L. (1967). Far wake behavior of hypersonic spheres. *AIAA Journal*, 5(7):1238–1244.
- Wong, M. L. and Lele, S. K. (2019). *High-Order Shock-Capturing Methods for Study of Shock-Induced Turbulent Mixing with Adaptive Mesh Refinement Simulations*. PhD thesis, Stanford University.
- Wright, M. J., Bose, D., Palmer, G. E., and Levin, E. (2005). Recommended collision integrals for transport property computations part 1: Air species. *AIAA journal*, 43(12):2558–2564.
- Wright, M. J., White, T., and Mangini, N. (2009). *Data Parallel Line Relaxation (DPLR) Code User Manual: Acadia Version 4.01. 1*. National Aeronautics and Space Administration, Ames Research Center.

- Xie, Z.-T. and Castro, I. P. (2008). Efficient generation of inflow conditions for large eddy simulation of street-scale flows. *Flow, Turbulence and Combustion*, 81(3):449–470.
- Yaws, C. L. (2014). *Transport properties of chemicals and hydrocarbons*. William Andrew.
- Yee, H. (1989). A class of high-resolution explicit and implicit shock-capturing methods. *NASA Technical Report*.
- Yee, H. and Sjögren, B. (2018). Recent developments in accuracy and stability improvement of nonlinear filter methods for dns and les of compressible flows. *Computers & Fluids*, 169:331–348.
- Yee, H. C., Sandham, N. D., and Djomehri, M. J. (1999). Low-dissipative high-order shock-capturing methods using characteristic-based filters. *Journal of Computational Physics*, 150(1):199–238.
- Zhang, W., Almgren, A., Day, M., Nguyen, T., Shalf, J., and Unat, D. (2016). Boxlib with tiling: An adaptive mesh refinement software framework. *SIAM Journal on Scientific Computing*, 38(5):S156–S172.
- Zhang, W., Myers, A., Gott, K., Almgren, A., and Bell, J. (2021). AMReX: Block-structured adaptive mesh refinement for multiphysics applications. *The International Journal of High Performance Computing Applications*, page 10943420211022811.
- Zhao, G., Sun, M., Memmolo, A., and Pirozzoli, S. (2019). A general framework for the evaluation of shock-capturing schemes. *Journal of Computational Physics*, 376:924–936.
- Zhao, G.-Y., Sun, M.-B., and Pirozzoli, S. (2020). On shock sensors for hybrid compact/WENO schemes. *Computers & Fluids*, 199:104439.

A. Conservation equations and non-dimensional numbers

A.1 Knudsen number

Knudsen number (Kn) can be written as a function of Mach (M) and Reynolds (Re) numbers for a gas with specific heat capacities ratio (γ). Beginning from the definitions of the non-dimensional numbers

$$Kn = \frac{\lambda}{L}, \quad M = \frac{u}{\sqrt{\gamma k_B T / m}}, \quad Re = \frac{\rho u L}{\mu}, \quad (\text{A.1})$$

where k_B is the Boltzmann constant, T is the temperature, ρ is the gas density and m is the molecular mass. Then, introducing hard sphere model kinetic theory results¹ for dynamic viscosity (μ), the mean free path length (λ) and the average velocity from the Maxwell-Boltzmann distribution (\bar{c})

$$\bar{c} = \sqrt{\frac{8k_B T}{\pi m}}, \quad \mu = \frac{\rho \bar{c} \lambda}{2}, \quad \lambda = \frac{\mu}{\rho} \sqrt{\frac{\pi m}{2k_B T}}. \quad (\text{A.2})$$

Combining Eqs. (A.1) and (A.2),

$$Kn = \frac{M}{Re} \sqrt{\frac{\gamma \pi}{2}}. \quad (\text{A.3})$$

¹Found in standard molecular transport theory texts like [Hirschfelder et al. \(1964\)](#).

A.2 Energy equation heat flux term

Beginning from Fourier's law of conduction for each mode separately and heat transfer by mass diffusion via Fick's law of diffusion,

$$\mathbf{q} = -\lambda_{tr} \nabla T_{tr} - \lambda_{ve} \nabla T_{ve} - \sum_k h_k \rho D_{km} \nabla Y_k. \quad (\text{A.4})$$

Then, recalling that $h(T_{tr}, T_{ve}, Y_k) = \sum_k Y_k h_k = \sum_k Y_k (h_{tr,k} + h_{ve,k})$, the enthalpy gradient is

$$\nabla h = c_{p,tr} \nabla T_{tr} + c_{ve} \nabla T_{ve} + \sum_k \nabla Y_k h_k. \quad (\text{A.5})$$

Rearranging Eq. (A.5) leads to an expression for the vibrational temperature gradient

$$\nabla T_{tr} = \frac{1}{c_{ve}} \nabla h - \frac{c_{ve}}{c_{p,tr}} \nabla T_{ve} - \frac{1}{c_{ve}} \sum_k \nabla Y_k h_k. \quad (\text{A.6})$$

Substituting Eq. (A.6) in Eq. (A.4) gives

$$\begin{aligned} \mathbf{q} &= -\lambda_{tr} \nabla T_{tr} - \frac{\lambda_{ve}}{c_{ve}} \left(\nabla h - c_{p,tr} \nabla T_{tr} - \sum_k h_k \nabla Y_k \right) - \sum_k h_k \rho D_{km} \nabla Y_k \\ &= -\frac{\lambda_{tr}}{c_{p,tr}} \nabla h + \left(\frac{\lambda_{tr} c_{ve}}{c_{p,tr}} - \lambda_{ve} \right) \nabla T_{ve} + \frac{\lambda_{tr}}{c_{p,tr}} \sum_k h_k \nabla Y_k \left(1 - \frac{\rho D_{km} c_{p,tr}}{\lambda_{tr}} \right) \\ &= \frac{\lambda_{tr}}{c_{p,tr}} \left[-\nabla h + \left(c_{ve} - c_{p,tr} \frac{\lambda_{ve}}{\lambda_{tr}} \right) \nabla T_{ve} + \sum_k h_k \nabla Y_k \left(1 - \frac{\rho D_{km} c_{p,tr}}{\lambda_{tr}} \right) \right] \end{aligned} \quad (\text{A.7})$$

Introducing non-dimensional variables:

$$\alpha = \frac{\lambda_{tr}}{\rho c_{p,tr}}, \quad \Lambda = \frac{c_{p,tr} \lambda_{ve}}{c_{ve} \lambda_{tr}}, \quad Le_k = \frac{\lambda_{tr}}{\rho D_{km} c_{p,tr}}; \quad (\text{A.8})$$

leads to

$$\mathbf{q} = \rho \alpha \left(-\nabla h + \sum_k h_k \nabla Y_k \left(1 - \frac{1}{Le_k} \right) + (1 - \Lambda) \nabla T_{ve} \right). \quad (\text{A.9})$$

A.3 Non-dimensional conservation equations

The reference quantities are denoted by subscript r and non-dimensional quantities are denoted by $\hat{\cdot}$. Common variables to all conservation laws,

$$\hat{\nabla} = l_r \nabla, \quad \hat{\rho} = \frac{\rho}{\rho_r}, \quad \hat{\mathbf{u}} = \frac{1}{u_r} \mathbf{u}, \quad \hat{t} = \frac{t}{t_r}, \quad t_r = \frac{u_r}{l_r}. \quad (\text{A.10})$$

Variables from species mass conservation,

$$\hat{\omega}_i = \frac{\tau_k^c}{\rho_r} \omega_k, \quad \hat{\mathbf{j}}_k = \frac{l_r}{D_{kr} \rho_r} \mathbf{j}_k, \quad Da_k = \frac{t_r}{\tau_k^c}, \quad Pe_k = \frac{u_r l_r}{D_{kr}} = Re Sc_k. \quad (\text{A.11})$$

Variables from momentum conservation,

$$\hat{\boldsymbol{\tau}} = \frac{l_r}{u_r \mu_r} \boldsymbol{\tau}, \quad \hat{p} = \frac{p}{\rho_r u_r^2}, \quad Re = \frac{\rho_r u_r l_r}{\mu_r}. \quad (\text{A.12})$$

Variables from total energy conservation,

$$\hat{T} = \frac{T}{T_r}, \quad \hat{\mathbf{q}} = \frac{l_r}{\alpha T_r} \mathbf{q}, \quad \hat{h}_k = \frac{h_k}{e_r}, \quad e_r = a_r^2, \quad M_r = \frac{u_r}{a_r}, \quad Pe_t = \frac{u_r l_r}{\alpha} = Re Pr_t, \quad \alpha = \frac{\lambda_r}{\rho c_{p,r}}. \quad (\text{A.13})$$

Variables from vibrational energy conservation,

$$\hat{e}_{ve} = \frac{e_{ve}}{e_r}, \quad \hat{\mathbf{q}}_{ve} = \frac{l_r}{\lambda_{ve} T_r} \mathbf{q}_{ve}, \quad Pr_v = \frac{\mu}{\rho} c_{ve}, \quad Da^I = \frac{t_r}{\tau_{vt}}, \quad Da^{II} = \frac{t_r}{\tau_{vc}}. \quad (\text{A.14})$$

τ_k^c is the chemical timescale for species k ; a_r is reference speed of sound. Species mass fraction (Y_k) is already a non-dimensional quantity. Note, the transport properties are field variables. So the non-dimensional numbers, Schmidt number (Sc), Prandtl number (Pr) and Damköhler (Da) are not constants, but are also field variables.

Equation (2.7), system of conservation laws for a two-temperature thermochemically relaxing flow in non-dimensional form is

$$\frac{\partial}{\partial \hat{t}} \begin{pmatrix} \hat{\rho} Y_1 \\ \vdots \\ \hat{\rho} Y_n \\ \hat{\rho} \\ \hat{\rho} \hat{\mathbf{u}} \\ \hat{\rho} \hat{e}_t \\ \hat{\rho} \hat{e}_{ve} \end{pmatrix} + \hat{\nabla} \cdot \begin{pmatrix} \hat{\rho} Y_1 \hat{\mathbf{u}} \\ \vdots \\ \hat{\rho} Y_n \hat{\mathbf{u}} \\ \hat{\rho} \hat{\mathbf{u}} \\ \hat{\rho} \hat{\mathbf{u}} \otimes \hat{\mathbf{u}} + \hat{p} \mathbf{I} \\ \hat{\rho} \hat{\mathbf{u}} \hat{h}_t \\ \hat{\rho} \hat{\mathbf{u}} \hat{e}_{ve} \end{pmatrix} + \frac{1}{Re} \hat{\nabla} \cdot \begin{pmatrix} \frac{1}{Sc_1} \hat{\mathbf{j}}_1 \\ \vdots \\ \frac{1}{Sc_n} \hat{\mathbf{j}}_n \\ 0 \\ -\hat{\boldsymbol{\tau}} \\ \frac{1}{Pr_t} \hat{\mathbf{q}} - M_r^2 (\hat{\boldsymbol{\tau}} \cdot \hat{\mathbf{u}}) \\ \frac{1}{Pr_v} \hat{\mathbf{q}}_{ve} \end{pmatrix} = \begin{pmatrix} Da_1 \hat{\omega}_1 \\ \vdots \\ Da_n \hat{\omega}_n \\ 0 \\ 0 \\ 0 \\ Da^I \hat{\omega}_{vt} + Da^{II} \hat{\omega}_{vc} \end{pmatrix}, \quad (\text{A.15})$$

where the primitive state variables are $\{Y_k, P, T_{tr}, T_{ve}, \mathbf{u}\}$.

For frozen flow, the non-dimensional system of conservation law is

$$\frac{\partial}{\partial \hat{t}} \begin{pmatrix} \hat{\rho} \\ \hat{\rho} \hat{\mathbf{u}} \\ \hat{\rho} \hat{e}_t \end{pmatrix} + \hat{\nabla} \cdot \begin{pmatrix} \hat{\rho} \hat{\mathbf{u}} \\ \hat{\rho} \hat{\mathbf{u}} \otimes \hat{\mathbf{u}} + \hat{p} \mathbf{I} \\ \hat{\rho} \hat{\mathbf{u}} \hat{h}_t \end{pmatrix} + \frac{1}{Re} \hat{\nabla} \cdot \begin{pmatrix} 0 \\ -\hat{\boldsymbol{\tau}} \\ \frac{1}{Pr_t} \hat{\mathbf{q}} - M_r^2 (\hat{\boldsymbol{\tau}} \cdot \hat{\mathbf{u}}) \end{pmatrix} = \begin{pmatrix} 0 \\ 0 \\ 0 \end{pmatrix}, \quad (\text{A.16})$$

where the primitive state variables are $\{P, T, \mathbf{u}\}$.

B. Three-dimensional immersed geometry handling verification

This case aims to test the performance of the numerical method with complex geometry; so far, test cases have involved only simple geometries, cylinders, spheres, ramps and plates. The test case involves viscous flow around a horse-shaped body in hypersonic flow.

The flow parameters are $M = 6$, $Re = 10^5$, and $T_\infty = 300K$. The flow is over a horse body, composed of 1.08×10^5 triangular elements. The domain size is $(6m)^3$, and the base mesh is 128^3 with 1 level of refinement. Re-gridding occurs every 50 steps, and resolution is added in the wake and around the solid body. There are around 7×10^6 computational points once the bow shock is fully developed. Figure B.1 shows the mesh, which is not fine enough to resolve the flow scales fully, but this is acceptable as accuracy is not important here. The time step is $20\mu s$, CFL is around 1, and the simulation run length is 2000 time steps. Computation for each time step takes around 16s with 8 processors, around 72 total CPU hours. CS4-JST is used, and the flow is initialised at half the free-stream velocity; otherwise, the initialisation is unstable; and, adiabatic wall boundary conditions are enforced.

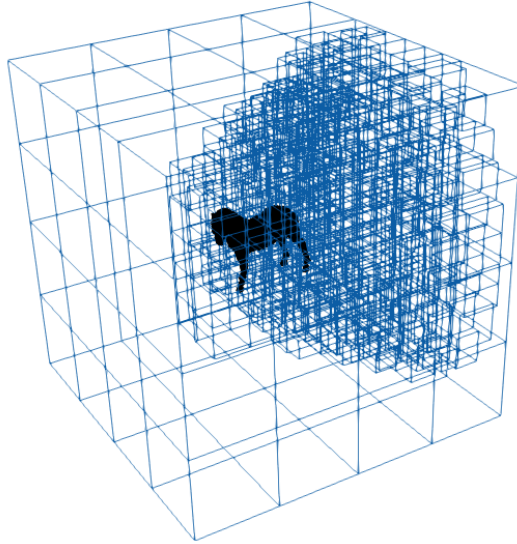


Fig. B.1 Mesh patches with 1 level of refinement around horse body and wake.

Quantitative comparisons are not considered here; instead, qualitative behaviour is of main concern. Figure B.2 shows the velocity field projections from the side and top, where the bow shock, shock layer and wake can be seen clearly. Figure B.3 shows the elemental surface temperature and pressure, generally increasing towards the front of the body.

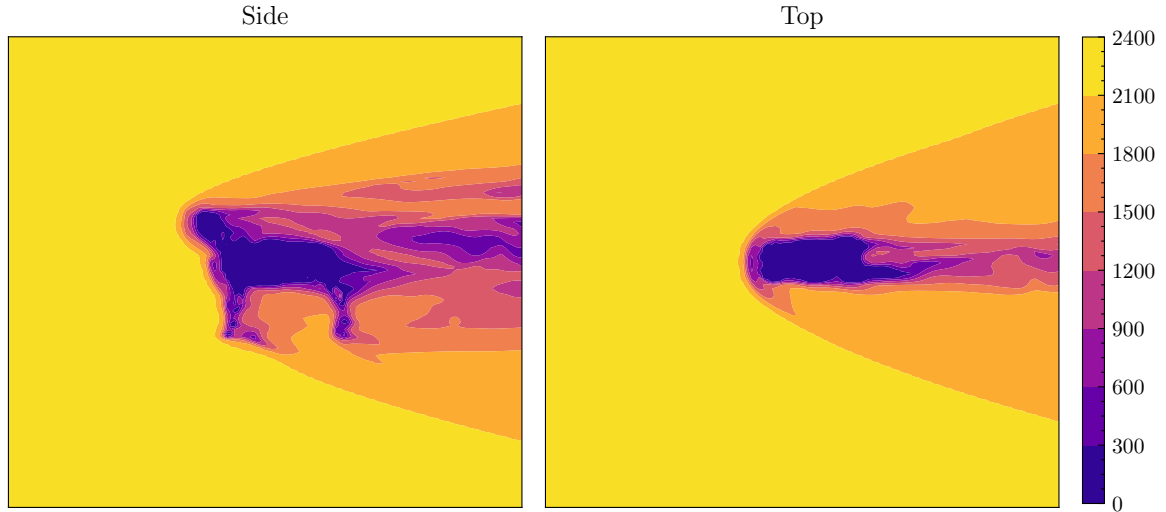


Fig. B.2 Velocity (m/s) field side and top projections of horse geometry in $M = 6$ flow.

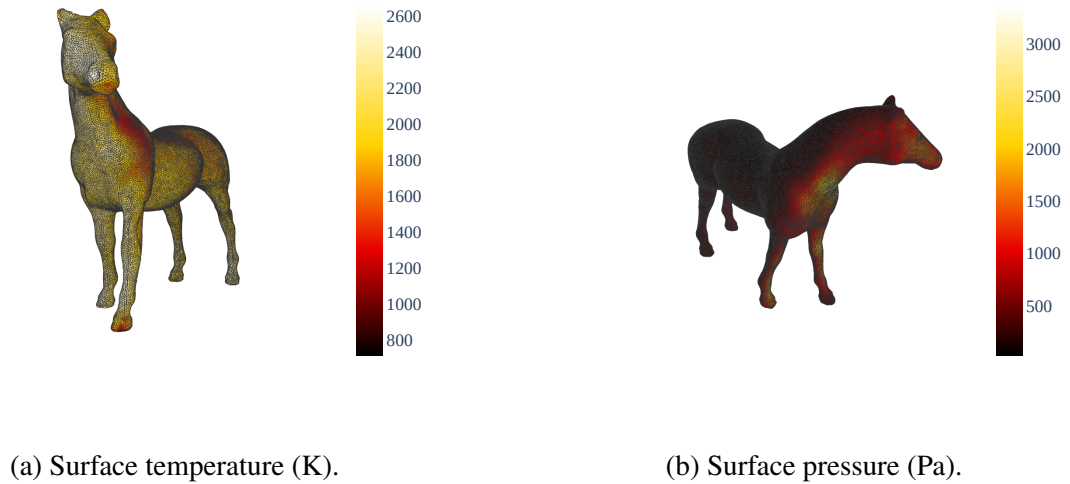


Fig. B.3 Horse geometry handling verification surface temperature and pressure in $M = 6$ flow and in three-dimensions.